



UNIVERSITÀ  
DEGLI STUDI  
DI PADOVA

Head Office: Università degli Studi di Padova

Department  
GEOSCIENCES

Ph.D. COURSE IN: GEOSCIENCES  
SERIES: XXXV

**SEISMIC RISK ASSESSMENT AT A TERRITORIAL SCALE  
BASED ON MACHINE LEARNING**

**Coordinator:** Prof. Claudia Agnini

**Supervisor:** Prof. Francesca da Porto

**Ph.D. student :** Pietro Carpanese



# TABLE OF CONTENTS

<b>TABLE OF CONTENTS .....</b>	<b>3</b>
<b>LIST OF FIGURES .....</b>	<b>7</b>
<b>LIST OF TABLES.....</b>	<b>11</b>
<b>ABSTRACT .....</b>	<b>13</b>
<b>1 INTRODUCTION .....</b>	<b>15</b>
<b>1.1. State of the problem .....</b>	<b>15</b>
<b>1.2. Research aims and methodology .....</b>	<b>16</b>
<b>1.3. Thesis structure .....</b>	<b>16</b>
<b>2 STATE OF THE ART .....</b>	<b>19</b>
<b>2.1. Seismic risk .....</b>	<b>19</b>
2.1.1. Seismic hazard .....	20
2.1.2. Seismic vulnerability .....	23
2.1.3. Exposure .....	30
<b>2.2. Assessment of seismic losses and consequences.....</b>	<b>34</b>
<b>2.3. Seismic risk calculation platforms.....</b>	<b>36</b>
<b>2.4. Machine learning techniques in earthquake engineering .....</b>	<b>37</b>
2.4.1. Machine learning in seismic hazard analysis .....	39
2.4.2. Machine learning in seismic vulnerability assessment.....	41
2.4.3. Machine learning in system identification and damage detection.....	42
2.4.4. Machine learning in structural control for seismic effect mitigation .....	45
<b>2.5. Automatic retrieval of building features.....</b>	<b>46</b>
2.5.1. OpenStreetMap (OSM).....	47
2.5.2. Google Street View (GSV).....	50
2.5.3. Building detection, class and typology.....	52
2.5.4. Building height .....	53
2.5.5. Building material .....	54
2.5.6. Building age.....	54
2.5.7. Urban fabric.....	55
<b>2.6. Research gaps .....</b>	<b>55</b>

<b>3</b>	<b>FRAGILITY CURVES FOR ITALIAN RESIDENTIAL MASONRY BUILDINGS ...</b>	<b>57</b>
3.1.	Method of derivation of fragility curves .....	57
3.2.	Macro-typologies and sampling of Italian masonry buildings.....	59
3.2.1.	Definition of building macro-typologies and representativeness criteria .....	59
3.2.2.	Sampling of buildings assumed as case studies .....	62
3.3.	Vulnus-based seismic fragility model for moderate to severe damage .....	64
3.4.	Multi-damage seismic fragility model .....	68
3.5.	Reliability assessment based on the observed damage .....	73
3.6.	Fragility curves with retrofit interventions .....	78
3.6.1.	Seismic retrofit interventions .....	79
3.6.2.	Mitigated fragility results .....	88
3.7.	Final remarks.....	93
<b>4</b>	<b>AUTOMATIC DETECTION AND CHARACTERIZATION OF BUILDINGS AT A TERRITORIAL SCALE .....</b>	<b>95</b>
4.1.	OpenStreetMap module to retrieve building footprints.....	95
4.2.	Google Street View module to retrieve street-level images .....	99
4.3.	Deep Learning for the recognition of building features .....	102
4.3.1.	Convolutional Neural Networks (CNNs): a brief history .....	102
4.3.2.	Theory of Convolutional Neural Networks.....	105
4.4.	Database of images of Italian residential buildings.....	108
4.4.1.	Images retrieved from the CARTIS web application.....	110
4.4.2.	Images retrieved from Da.D.O. ....	115
4.4.3.	Training, evaluation, and validation sets.....	117
4.5.	Training of the CNNs for the prediction of height, material, and construction period.....	120
4.5.1.	Google Colaboratory .....	120
4.5.2.	Transfer learning and fine-tuning.....	121
4.5.3.	Outline of the script to train the Convolutional Neural Networks .....	122
4.5.4.	Comparison of the CNN predictions with an on-site survey .....	134
<b>5</b>	<b>SEISMIC RISK CALCULATION PLATFORM .....</b>	<b>147</b>
5.1.	Structure of the platform.....	147
5.2.	Seismic hazard module .....	148

---

<b>5.3.</b>	<b>Seismic vulnerability module .....</b>	<b>150</b>
<b>5.4.</b>	<b>Exposure module and consequence matrices .....</b>	<b>152</b>
<b>6</b>	<b>RESULTS .....</b>	<b>157</b>
<b>6.1.</b>	<b>Damage maps.....</b>	<b>157</b>
6.1.1.	Conditional damage maps .....	157
6.1.2.	Unconditional damage maps .....	166
6.1.3.	Damage maps validation .....	174
<b>6.2.</b>	<b>Risk maps.....</b>	<b>177</b>
6.2.1.	Conditional risk maps.....	178
6.2.2.	Unconditional risk maps.....	185
6.2.3.	Risk maps validation .....	191
6.2.4.	Risk assessment in case of retrofitted scenarios .....	193
<b>7</b>	<b>CONCLUSIONS AND FUTURE DEVELOPMENTS .....</b>	<b>197</b>
<b>7.1.</b>	<b>Conclusions .....</b>	<b>197</b>
<b>7.2.</b>	<b>Future developments.....</b>	<b>198</b>
	<b>ACKNOWLEDGEMENTS .....</b>	<b>200</b>
	<b>REFERENCES .....</b>	<b>201</b>



## LIST OF FIGURES

Figure 2.1 – Modified Mercalli (MM) scale, with the description of each intensity level ....	21
Figure 2.2 – European macro-seismic EMS98 scale (Grünthal, 1998).....	21
Figure 2.3 - Seismic hazard map for Italy (MPS04) in terms of PGA (Peak Ground Acceleration) with a 10% probability of exceedance in 50 years .....	22
Figure 2.4 - Example of fragility curves .....	23
Figure 2.5 - Damage Probability Matrix format proposed by Whitman et al. (1973).....	25
Figure 2.6 - DPM in the European Macro-seismic Scale EMS98 (Grünthal, 1998).....	25
Figure 2.7 - Vulnerability curves for the EMS98 vulnerability classes (Lagomarsino and Cattari, 2014).....	26
Figure 2.8 - Sections from the II level GNDT form (a) and from the AeDES form (b).....	27
Figure 2.9 – Cover and first sections of the CARTIS form .....	33
Figure 2.10 - Example of Italian building typologies according to the TABULA project ....	34
Figure 2.11 – User interface of the IRMA platform (Borzi et al., 2021b) .....	37
Figure 2.12 - Towns, cities and villages mapped in OpenStreetMap (Moosavi, 2017).....	48
Figure 2.13 - Fraction of streets for each country in the OSM database (Barrington-Leigh and Millard-Ball, 2017).....	48
Figure 2.14 - Google Street View worldwide coverage ( <a href="https://en.wikipedia.org/wiki/Coverage_of_Google_Street_View">https://en.wikipedia.org/wiki/Coverage_of_Google_Street_View</a> ).....	51
Figure 3.1 - Distribution of buildings by number of stories (n), within each macro-typology, according to ISTAT data and the database of sampled buildings. (a) $n \leq 2$ ; (b) $n \geq 3$ .....	61
Figure 3.2 - Distribution of buildings by number of housing units, per number of stories, according to ISTAT data and the database of sampled buildings .....	62
Figure 3.3 - Examples of some representative Italian URM buildings by construction age and number of stories .....	64
Figure 3.4 - Example of Vulnus curves and those obtained from lognormal fit.....	65
Figure 3.5 - Dependence of the fragility curves on the sample size, for three building macro-typologies .....	65
Figure 3.6 - Procedure to define fragility models. Example of White fragility for Pre-1919 buildings .....	67
Figure 3.7 - Vulnus model of White fragility for all building macro-typologies.....	67
Figure 3.8 - White, Upper- and Lower-Bound fragility of all building macro-typologies ....	68
Figure 3.9 - Procedure to define multi-damage fragility models and LUW model. Example for Pre-1919, $n \geq 3$ .....	71
Figure 3.10 - Optimal fit of combined DS2-3 curves (reference model) on White curves (Vulnus model).....	71
Figure 3.11 - Comparison between LUW curves and associated White, Upper- and Lower-Bound curves.....	72
Figure 3.12 - Fragility sets (from DS1 to DS5) of LUW model of all building macro-typologies .....	73
Figure 3.13 – (a) % of surveyed buildings of all municipalities; (b) ShakeMap of L'Aquila 2009 .....	76
Figure 3.14 - Simulated and observed damage scenarios of the 2009 L'Aquila earthquake. 77	
Figure 3.15 - Comparison of damage scenarios simulated by the LUW, Upper- and Lower-Bound models.....	78
Figure 3.16 - Reinforced concrete jackets (a) and example of application of FRP-SRG (b, c) .....	82
Figure 3.17 - Example of connection floor-to-wall (a) and of external anchors (b, c) .....	84
Figure 3.18 - Positioning of tie-beams: three-dimensional scheme (b) and disposition in plan (a) .....	85

Figure 3.19 - Reinforced timber floor with double planking crossed at +45° and -45° (a) and addition of composite slab in r.c. floors (b)..... 87

Figure 3.20 - Mitigated fragility curves for TR, MSN1+TR, MSN2+TR, CR, and MSN+CR compared to the as built model..... 90

Figure 3.21 – Mitigated fragility curves for FLR, MSN1+FLR, MSN2+FLR, and MSN+FLR compared to the as built model..... 91

Figure 3.22 - Percentage of increase of  $\mu$  calculated for DS2..... 92

Figure 4.1 - Satellite images for a) the town of Padova, b) an area centered in the point of coordinates (45.409605, 11.888727) with a radius of 300 meters ..... 97

Figure 4.2 - Building footprints for a) the town of Padova, b) an area centered in the point of coordinates (45.409605, 11.888727) with a radius of 300 meters ..... 97

Figure 4.3 - Building footprints and their labels for the area centered in (45.409605, 11.888727) with a radius of 300 meters ..... 98

Figure 4.4 - Building footprints and their labels for the area centered in (45.965009, 12.653791) with a radius of 500 meters ..... 98

Figure 4.5 - Building footprints and their labels for the area centered in (45.409605, 11.888727) with a radius of 300 meters, where only residential buildings are kept..... 99

Figure 4.6 - Building footprints and their labels for the area centered in (45.965009, 12.653791) with a radius of 500 meters, where only residential buildings are kept..... 99

Figure 4.7 - Examples of street view images obtained from the coordinates of the building footprints for the area centered in (45.409605, 11.888727) with a radius of 300 meters .... 101

Figure 4.8 - Examples of street view images obtained from the coordinates of the building footprints for the area centered in (45.965009, 12.653791) with a radius of 500 meters .... 101

Figure 4.9 - Examples of handwritten digits from the MNIST dataset ([https://it.wikipedia.org/wiki/MNIST\\_database](https://it.wikipedia.org/wiki/MNIST_database)) ..... 103

Figure 4.10 - Example images from the ImageNet dataset (<https://becominghuman.ai/transfer-learning-part-3-datasets-and-repositories-cebc644007f4>) ..... 105

Figure 4.11 - Convoluting a 5x5x1 image with a 3x3x1 kernel to get a 3x3x1 convolved feature..... 106

Figure 4.12 - The two main types of pooling: max pooling and average pooling ..... 107

Figure 4.13 - Example of scheme of a CNN ..... 108

Figure 4.14 - 3D Convolutional Neural Network visualization (Harley, 2015)..... 108

Figure 4.15 - Administration panel of the CARTIS web portal (<http://cartis.plinivs.it/backoffice/login.php>)..... 111

Figure 4.16 - User interface for the second level CARTIS forms in the CARTIS web application ..... 111

Figure 4.17 - Examples of images downloaded from the CARTIS online database..... 113

Figure 4.18 - Examples of masonry buildings in Pordenone: a) and b), pre-1919; c) and d), 1919-1945; e) and f), post-1945 ..... 114

Figure 4.19 – User login of Da.D.O. ([http://egeos.eucentre.it/danno\\_osservato/web/danno\\_osservato](http://egeos.eucentre.it/danno_osservato/web/danno_osservato)) ..... 116

Figure 4.20 – User interface of the Da.D.O. web portal ..... 116

Figure 4.21 – Comparison of building distribution between ISTAT 2011 and our dataset considering the features height, material, and construction period..... 119

Figure 4.22 - Precision, recall, and F1 score for the parameter "height" after the warmup training..... 129

Figure 4.23 - Precision, recall, and F1 score for the parameter "material" after the warmup training..... 129

Figure 4.24 - Precision, recall, and F1 score for the parameter "construction period" after the warmup training..... 129

Figure 4.25 - Precision, recall, and F1 score for the parameter "height" after the unfrozen training..... 131

Figure 4.26 - Precision, recall, and F1 score for the parameter "material" after the unfrozen training..... 131



Figure 4.27 - Precision, recall, and F1 score for the parameter "construction period" after the unfrozen training .....	132
Figure 4.28 - Examples of outputs of the three CNNs for the parameters height, material, and construction period.....	133
Figure 4.29 - Comparison between direct survey (a) and CNN predictions (b) for the parameter "height", for Pordenone city center .....	135
Figure 4.30 - Comparison between direct survey (a) and CNN predictions (b) for the parameter "material", for Pordenone city center .....	135
Figure 4.31 - Comparison between direct survey (a) and CNN predictions (b) for the parameter "construction period", for Pordenone city center .....	136
Figure 4.32 - Comparison between direct survey (a) and CNN predictions (b) for the parameter "height", for Pordenone northern area.....	136
Figure 4.33 - Comparison between direct survey (a) and CNN predictions (b) for the parameter "material", for Pordenone northern area.....	137
Figure 4.34 - Comparison between direct survey (a) and CNN predictions (b) for the parameter "construction period", for Pordenone northern area.....	137
Figure 4.35 – Percentages of correct and wrong predictions of the CNNs for the parameters height (a), material (b), and construction period (c) for the Municipality of Pordenone, when compared to the direct survey .....	139
Figure 4.36 – Percentages of correct predictions and predictions with 1, 2, 3, or 4 epochs difference for the Municipality of Pordenone, when compared to the direct survey.....	140
Figure 4.37 - CNN predictions for the parameter "height" for the whole Municipality of Pordenone.....	143
Figure 4.38 - CNN predictions for the parameter "material" for the whole Municipality of Pordenone.....	144
Figure 4.39 - CNN predictions for the parameter "construction period" for the whole Municipality of Pordenone.....	145
Figure 5.1 – Example of definition of the probability of occurrence for each damage state, given a PGA of 0.2g .....	152
Figure 5.2 - General framework for risk assessment.....	155
Figure 6.1 - Damage maps DS1, DS3, and DS5 for $T_r = 475$ years in Pordenone city center .....	159
Figure 6.2 - Average damage map for $T_r = 475$ years in Pordenone city center .....	159
Figure 6.3 - Damage maps DS1, DS3, and DS5 for $T_r = 475$ years in Pordenone northern area .....	161
Figure 6.4 - Average damage map for $T_r = 475$ years in Pordenone northern area.....	161
Figure 6.5 - Damage maps DS1, DS3, and DS5 for $T_r = 475$ years in the Municipality of Pordenone.....	164
Figure 6.6 - Average damage map for $T_r = 475$ years in the Municipality of Pordenone ...	165
Figure 6.7 - Damage maps DS1, DS3, and DS5 for a time window of 50 years in Pordenone city center .....	167
Figure 6.8 - Average damage map for a time window of 50 years in Pordenone city center .....	168
Figure 6.9 - Damage maps DS1, DS3, and DS5 for a time window of 50 years in Pordenone northern area.....	169
Figure 6.10 - Average damage map for a time window of 50 years in Pordenone northern area .....	169
Figure 6.11 - Damage maps DS1, DS3, and DS5 for a time window of 50 years in the Municipality of Pordenone.....	172
Figure 6.12 - Average damage map for a time window of 50 years in the Municipality of Pordenone.....	173
Figure 6.13 – Damage in Castelsantangelo sul Nera assessed during a direct survey (a) and predicted by the algorithm (b).....	176
Figure 6.14 – Percentages of damage states in Castelsantangelo sul Nera assessed during a direct survey (a) and predicted by the algorithm (b).....	176

Figure 6.15 - Percentages of correct predictions and predictions with 1 or 2 damage states difference for the Municipality of Castelsantangelo sul Nera when compared to the direct survey ..... 177

Figure 6.16 – Economic losses for  $T_r = 475$  years in Pordenone city center..... 179

Figure 6.17 - Economic losses for  $T_r = 475$  years in Pordenone northern area ..... 179

Figure 6.18 - Economic losses for  $T_r = 475$  years in the Municipality of Pordenone ..... 180

Figure 6.19 - Usability of buildings for  $T_r = 475$  years in Pordenone city center ..... 181

Figure 6.20 - Usability of buildings for  $T_r = 475$  years in Pordenone northern area..... 181

Figure 6.21 - Usability of buildings for  $T_r = 475$  years in the Municipality of Pordenone . 182

Figure 6.22 - Displaced people for  $T_r = 475$  years in Pordenone city center..... 183

Figure 6.23 - Displaced people for  $T_r = 475$  years in Pordenone northern area ..... 183

Figure 6.24 - Displaced people for  $T_r = 475$  years in the Municipality of Pordenone ..... 184

Figure 6.25 - Economic losses for a time window of 50 years in Pordenone city center ... 185

Figure 6.26 - Economic losses for a time window of 50 years in Pordenone northern area 185

Figure 6.27 - Economic losses for a time window of 50 years in the Municipality of Pordenone ..... 186

Figure 6.28 – Usability of buildings for a time window of 50 years in Pordenone city center ..... 187

Figure 6.29 - Usability of buildings for a time window of 50 years in Pordenone northern area ..... 187

Figure 6.30 - Usability of buildings for a time window of 50 years in the Municipality of Pordenone ..... 188

Figure 6.31 - Displaced people for a time window of 50 years in Pordenone city center ... 189

Figure 6.32 - Displaced people for a time window of 50 years in Pordenone northern area 189

Figure 6.33 - Displaced people for a time window of 50 years in the municipality of Pordenone ..... 190

Figure 6.34 - Effect on economic losses, victims, and injuries for different retrofit strategies in Pordenone (50 years)..... 195

Figure 6.35 - Effect on economic losses, victims, and injuries for different retrofit strategies in Pordenone (50 years) as percentage of the as built configuration..... 196

## LIST OF TABLES

Table 3.1 - Macro-typologies of Italian residential URM buildings and number of sampled buildings.....	60
Table 3.2 - Summary of reference information for each construction age.....	63
Table 3.3 - Mean ( $\mu$ ) and standard deviation ( $\beta$ ) values of reference fragility model .....	69
Table 3.4 - Optimal combination coefficients of vulnerability classes of reference model fitting Vulnus model.....	71
Table 3.5 - $\mu$ and $\beta$ values of LUW fragility model.....	72
Table 3.6 - $d_i$ and $e_i$ coefficients associated with AeDES information (Lagomarsino et al., 2015).....	75
Table 3.7 - $\alpha_i$ weights associated with building elements (Lagomarsino et al., 2015).....	75
Table 3.8 - Conversion of AeDES damage information to EMS98 damage scale (Rota et al., 2008).....	75
Table 3.9 - Selected retrofit interventions for different construction periods.....	80
Table 3.10 - Multiplicative coefficients applied by type of masonry and construction period .....	83
Table 3.11 - $\mu$ and $\beta$ values of the fragility model for the as built and retrofitted configuration of historical buildings.....	88
Table 3.12 - $\mu$ and $\beta$ values of the fragility model for the as built and retrofitted configuration of modern buildings .....	89
Table 4.1 - Number of second level CARTIS forms obtained from the CARTIS web platform .....	112
Table 4.2 - Splitting of images into training, validation, and evaluation for the 3 features.	118
Table 4.3 - Graphic representation of the meaning of true positive, false negative, false positive and true negative.....	127
Table 5.1 - Description of soil types according to Italian code (Ministry of Public Works, 2018).....	150
Table 5.2 - $\mu$ and $\beta$ values of the fragility model from Rosti et al. (2021b) .....	151
Table 5.3 - Damage ratios: percentages used for the computation of economic losses .....	153
Table 5.4 - Percentages used for the computation of casualties (fatalities and injuries) .....	154
Table 5.5 - Percentages used for the computation of building usability .....	155
Table 6.1 - PGAs associated with each return period for the town of Pordenone.....	166
Table 6.2 - Difference of exposure in Pordenone between the risk calculation platform and IRMA .....	192
Table 6.3 - Difference of conditional risk ( $T_r=475$ years) in Pordenone between the risk calculation platform and IRMA .....	192
Table 6.4 - Difference of unconditional risk (time window 50 years) in Pordenone between the risk calculation platform and IRMA.....	193



## ABSTRACT

### *English*

Seismic risk assessment is a major challenge in countries with a significant seismic hazard and a highly vulnerable built heritage, such as Italy. Especially when the risk needs to be analyzed at a large scale, the assessment can entail very time-consuming and costly studies, since it is necessary to define numerous variables that can influence seismic exposure and vulnerability.

In this thesis, a mechanically based seismic fragility model has been developed for Italian masonry residential buildings. This model is based on the classification of the building stock into macro-typologies, also considering possible seismic retrofit measures.

Also exposure needs to be properly assessed: artificial intelligence techniques can be helpful to evaluate it in a quick and efficient way. Specifically, satellite images are used to automatically collect building data, street view photos are extracted for each building and Convolutional Neural Networks are trained to recognize specific features of interest from pictures, particularly the same ones on which the vulnerability model is based.

The following step of this work consists in combining vulnerability and exposure with the seismic hazard within a seismic risk calculation platform that can evaluate seismic damage and risk, expressed as repair or reconstruction costs, number of unusable buildings, casualties, and displaced people.

This information can be important for carrying out targeted investigations and establishing priority criteria for seismic retrofit measures. These seismic risk prevention and mitigation tools can be used by emergency authorities to manage resources in the pre- and post-earthquake phases, as well as to select effective emergency response and recovery plans.

## **Italiano**

La valutazione del rischio sismico rappresenta una sfida in Paesi con una significativa pericolosità sismica e un patrimonio edilizio vulnerabile come l'Italia. Soprattutto quando il rischio deve essere analizzato su larga scala, la sua stima può comportare analisi costose in termini economici e di tempo, a causa della necessità di definire numerose variabili che possono influenzare l'esposizione e la vulnerabilità.

In questo lavoro è stato sviluppato un modello di fragilità su base meccanica per gli edifici residenziali italiani in muratura. Il modello si basa sulla classificazione del patrimonio edilizio in macro-tipologie, simulando inoltre la possibile presenza di interventi anti-sismici.

Anche l'esposizione deve essere correttamente valutata: tecniche di intelligenza artificiale possono rivelarsi utili per effettuare stime in modo rapido ed efficiente. In particolare, le immagini satellitari possono essere utilizzate per raccogliere automaticamente i dati degli edifici, per poi estrarre foto street view per ogni edificio e allenare reti neurali convoluzionali a riconoscere specifiche caratteristiche di interesse dalle immagini, in particolare le stesse su cui si basa il modello di vulnerabilità.

La fase successiva di questo lavoro consiste nel combinare la vulnerabilità e l'esposizione con la pericolosità sismica all'interno di una piattaforma di calcolo in grado di valutare il rischio sismico, espresso come costo di riparazione, numero di edifici inutilizzabili, vittime e sfollati.

Queste informazioni sono fondamentali per condurre indagini mirate e stabilire criteri di priorità per le misure di adeguamento sismico. Gli strumenti proposti possono essere utilizzati per gestire risorse nelle fasi pre e post-terremoto e per elaborare piani di recupero efficaci.

# 1 INTRODUCTION

## 1.1. State of the problem

Italy is historically one of the European countries with the highest seismic activity and related number of victims, around 160,000 in the last two centuries (with 85,000 victims in the 1908 Messina earthquake of magnitude  $M_w$  7.1). In the twentieth century, earthquakes with a value of  $M_w \geq 6.5$  were at least seven and, only in the last ten years, four events have reached or exceeded a magnitude of 6.0.

Over the last 50 years, earthquakes forced the Italian country to sustain emergency management, recovery and reconstruction costs amounting to around 180 billion euros, of which 130 billion for earthquakes from 1968 to 2003 and 45 billion for the recent events of L'Aquila 2009, Emilia 2012 and Central Italy 2016. Therefore, without considering casualties, impairment of historical and artistic heritage, loss in tourist flow and the high indirect consequences on the production sector, the cost of Italian earthquakes can reach 3.6 billion euros per year.

For all the reasons mentioned so far, seismic risk assessment at a territorial scale is widely recognized to play a crucial role in addressing emergency planning and mitigation policies.

This is also in line with the “Sendai Framework for Disaster Risk Reduction 2015-2030” (United Nations, 2015), adopted in March 2015 at the Third World Conference of the United Nations in Sendai (Japan), which provides indications on the measures to be implemented for the priority actions number 3 (investing in disaster risk reduction for resilience) and number 4 (enhancing disaster preparedness for effective response, and to “Building Back Better” in recovery, rehabilitation and reconstruction). The urgency to address the aforementioned issues, as well as priority 1 (understanding disaster risk) and priority 2 (strengthening disaster risk governance to manage disaster risk) of the Sendai Framework called for an updating of risk assessments by many countries. In this regard, the Italian Civil Protection Department recently released the “*National Risk Assessment*” (DPC 2018), a document that provides an overview of potential major natural disasters in Italy, with a particular focus on seismic risk and on the seismic vulnerability assessment of the residential building heritage in Italy.

In spite of the considerable progress achieved for more accurate seismic risk assessments, often risk management institutions (both public and private) do not have detailed and sufficiently articulated information that can lead to appropriate risk estimations. Particularly, when the aim is to carry out large-scale analyses, the evaluation of the total exposure prone to risk often relies on public data available at municipal, regional, or national scale (e.g., ISTAT national census data, cadastral data, etc.), which are, however, often incomplete or inaccurate. On the other hand, a more appropriate estimation of exposure can be hindered by the need to collect a volume of data that only slow and expensive surveys can provide. Moreover, even when the exposure is correctly assessed, it is not trivial to provide an estimate of vulnerability

to the buildings involved in the analysis, given the heterogeneity of residential building typologies at the national scale.

This work therefore addresses the issue of faster and more accurate seismic risk assessments at a large scale.

## **1.2. Research aims and methodology**

The aim of this thesis is to develop a systematic methodology that can lead to seismic risk assessments at a territorial scale. To fulfil this task, a risk calculation algorithm is implemented: the algorithm is meant to operate remotely, which means that no direct on-site survey of the area of interest is required, and automatically, meaning that seismic risk estimates can be elaborated for any location in Italy and without the need for manual input throughout the computational steps.

Firstly, since the methodology is supposed to be valid for any place in Italy, a vulnerability model is developed for different Italian building typologies (with a particular focus on masonry buildings), so that every building can be associated with an estimate of seismic vulnerability.

With regard to exposure, the distribution of buildings in the area of interest is detected through satellite images, and their typology can be identified thanks to street view pictures. As a matter of fact, modern technologies allow us to derive quite smoothly street view images of buildings, and with a very wide coverage, thus simulating the external survey of an urban area. From the pictures collected, machine learning techniques (specifically, neural networks) are deployed to recognize specific features of buildings exposed to risk, so that it is possible to associate them with the correct vulnerability model previously defined.

Lastly, a seismic risk calculation platform is developed, in order to carry out risk assessments for different seismic scenarios. The results provided by the platform can respond to the needs mentioned in the previous section, since they can give a solid baseline for increasing preparedness and planning mitigation actions at large scales.

## **1.3. Thesis structure**

The thesis is structured as follows. Chapter 2 presents an overview of the state of the art regarding the topic of seismic risk assessment. In this chapter, the main methods for evaluating seismic hazard, vulnerability, and exposure are discussed, and subsequently particular focus is placed on the literature that concerns the application of machine learning techniques to solve earthquake engineering problems. Chapter 3 discusses the methodology adopted to derive a vulnerability model that can describe the seismic behavior of buildings. Particularly, fragility curves are elaborated for macro-typologies of Italian residential masonry buildings. Chapter 4 proves how it is possible to automatically detect buildings and some of their geometrical characteristics from satellite images, as well as their street view pictures, and then describes the procedure adopted to automatically predict building features from the photos



previously obtained. Lastly, the structure of the risk calculation platform is presented in chapter 5, and some examples of possible results in terms of risk assessment that can be derived through the platform are shown in chapter 6.



## 2 STATE OF THE ART

This chapter is intended to review the literature that is relevant for this thesis related to the field of study, pointing out all the work that has been carried out so far and highlighting any research gaps or shortcomings.

The first part of this chapter is dedicated to the definition of seismic risk and of its components: seismic hazard, vulnerability, and exposure. Since one of the key points of this project is the creation of a fragility model that can be representative for Italian buildings at a national scale, this section pays particular attention on the methods that evaluate seismic vulnerability, with a focus on simplified approaches that allow the definition of fragility at territorial scales. Then, this chapter reviews the studies that have been carried out regarding the topic of seismic losses and consequences, and the main seismic risk calculation platforms are listed. Subsequently, the field of machine learning is explored. Indeed, artificial intelligence in general has proven successful in providing various methods that can solve particular problems related to the field of earthquake engineering, whether by simplifying or speeding up the solution processes, or by giving answers to problems that could not be addressed by classical methods. Furthermore, particular attention is paid to the retrieval of information about building taxonomy and exposure, which is indeed another main goal of this thesis. Particularly, new approaches that allow a remote and automatic acquisition of building data are presented. The chapter finally concludes with some considerations on the gaps found in the literature reviewed, which motivated the proposal and the development of this thesis. These gaps will find answers in the following chapters.

### 2.1. Seismic risk

Seismic risk can be defined as the probability of occurrence of economic, social, and environmental potential losses due to an earthquake within a given time period in a given area. It can be considered as a combination of three main parameters: hazard, exposure, and vulnerability.

Seismic hazard is defined as the probability of occurrence of a seismic event at a given location within a given time period, typically expressed by the ratio between the level of seismic ground shaking (indicated by strong motion parameters such as peak ground acceleration PGA, peak ground velocity PGV, spectral acceleration PSA) and the probability of occurrence.

Seismic vulnerability indicates the probability of expected damage suffered by a building when exposed to a specific seismic event. It is often represented by correlations between seismic input and damage probability.

Exposure is the quantification of the number of people and buildings potentially at risk in case of a seismic event in the assessed area, and takes into account the value of the exposed assets.

The assessment of seismic risk can be expressed as a function of seismic hazard, vulnerability, and exposure. Therefore, for an appropriate estimation of seismic risk, it is preliminarily crucial to define these three components. The following sections elaborate on the definition of these three variables and describe the main methods for evaluating them that can be found in the literature.

### 2.1.1. Seismic hazard

Seismic hazard represents the probability that a selected strong-motion parameter (peak ground acceleration, velocity, spectral acceleration, etc.) is exceeded in a given time interval at a target location. It is related to the probability of occurrence of an earthquake and to the geological characteristics of the area where the event occurs. The intensity of an earthquake can be measured in different ways. Some of the most popular scales and intensity measures are here presented.

Firstly, earthquake magnitude is an objective quantitative measure of the size and amplitude of an earthquake, and it can be described by several seismic magnitude scales. The main differences among these scales depend on which aspects of the seismic waves are measured and how they are measured, as well as on the purpose of the measurement. One of the most used scales is the local Richter magnitude scale ML (Richter, 1935), defined as the logarithm (base 10) of the maximum trace amplitude (in microns) recorded by a Wood-Anderson seismograph, measured at a distance of 100 km from the epicenter of the earthquake. It is often adopted for local earthquakes up to 600 km away. Another widely used magnitude scale is the surface-wave magnitude MS, which is based on the amplitude of Rayleigh waves with a period of about 20 seconds. MS is most commonly used to describe the magnitude of shallow (less than 70 km focal depth), distant (farther than about 1000 km), moderate to large earthquakes.

Also macro-seismic intensity is a very helpful tool for evaluating ground shaking. Intensity scales have been historically used, since no instruments are required and useful measurements can be made by an unequipped observer. They are based on the observed effects of the earthquake, such as damage to structures and human responses (Kramer, 1996). Among the different macro-seismic intensity scales, the most known and frequently adopted ones are the modified Mercalli intensity (MM, MMI, or MCS, Richter, 1958; Figure 2.1), the European macro-seismic scale EMS98 (Grünthal, 1998; Figure 2.2), which has replaced the Medvedev-Spoonheuer-Karnit (MSK) and Mercalli-Cancani-Sieberg scales for European measurements (MCS), and the Japan Meteorological Agency (JMA) scale. The main difference among these scales lies in the number and range of degrees that they propose: for example, the MM and EMS98 scales are characterized by 12 levels, while the JMA scale has 9 levels, with a “Lower” and “Upper” distinction for the V and VI intensities. For a deeper insight on a comparison among the different macro-seismic intensity scales, reference can be made to specific studies (Musson et al., 2010).

Intensity	Shaking	Description/Damage
I	Not felt	Not felt except by a very few under especially favorable conditions.
II	Weak	Felt only by a few persons at rest, especially on upper floors of buildings.
III	Weak	Felt quite noticeably by persons indoors, especially on upper floors of buildings. Many people do not recognize it as an earthquake. Standing motor cars may rock slightly. Vibrations similar to the passing of a truck. Duration estimated.
IV	Light	Felt indoors by many, outdoors by few during the day. At night, some awakened. Dishes, windows, doors disturbed; walls make cracking sound. Sensation like heavy truck striking building. Standing motor cars rocked noticeably.
V	Moderate	Felt by nearly everyone; many awakened. Some dishes, windows broken. Unstable objects overturned. Pendulum clocks may stop.
VI	Strong	Felt by all, many frightened. Some heavy furniture moved; a few instances of fallen plaster. Damage slight.
VII	Very strong	Damage negligible in buildings of good design and construction; slight to moderate in well-built ordinary structures; considerable damage in poorly built or badly designed structures; some chimneys broken.
VIII	Severe	Damage slight in specially designed structures; considerable damage in ordinary substantial buildings with partial collapse. Damage great in poorly built structures. Fall of chimneys, factory stacks, columns, monuments, walls. Heavy furniture overturned.
IX	Violent	Damage considerable in specially designed structures; well-designed frame structures thrown out of plumb. Damage great in substantial buildings, with partial collapse. Buildings shifted off foundations.
X	Extreme	Some well-built wooden structures destroyed; most masonry and frame structures destroyed with foundations. Rails bent.

Figure 2.1 – Modified Mercalli (MM) scale, with the description of each intensity level

EMS intensity	Definition	Description of typical observed effects (abstracted)
I	Not felt	Not felt.
II	Scarcely felt	Felt only by very few individual people at rest in houses.
III	Weak	Felt indoors by a few people. People at rest feel a swaying or light trembling.
IV	Largely observed	Felt indoors by many people, outdoors by very few. A few people are awakened. Windows, doors and dishes rattle.
V	Strong	Felt indoors by most, outdoors by few. Many sleeping people awake. A few are frightened. Buildings tremble throughout. Hanging objects swing considerably. Small objects are shifted. Doors and windows swing open or shut.
VI	Slightly damaging	Many people are frightened and run outdoors. Some objects fall. Many houses suffer slight non-structural damage like hair-line cracks and fall of small pieces of plaster.
VII	Damaging	Most people are frightened and run outdoors. Furniture is shifted and objects fall from shelves in large numbers. Many well built ordinary buildings suffer moderate damage: small cracks in walls, fall of plaster, parts of chimneys fall down; older buildings may show large cracks in walls and failure of fill-in walls.
VIII	Heavily damaging	Many people find it difficult to stand. Many houses have large cracks in walls. A few well built ordinary buildings show serious failure of walls, while weak older structures may collapse.
IX	Destructive	General panic. Many weak constructions collapse. Even well built ordinary buildings show very heavy damage: serious failure of walls and partial structural failure.
X	Very destructive	Many ordinary well built buildings collapse.
XI	Devastating	Most ordinary well built buildings collapse, even some with good earthquake resistant design are destroyed.
XII	Completely devastating	Almost all buildings are destroyed.

Figure 2.2 – European macro-seismic EMS98 scale (Grünthal, 1998)

Furthermore, physical-mechanical parameters are extensively used to express the intensity of an earthquake. The most common parameter that describes the amplitude of ground motion is peak ground acceleration (PGA), which is defined as the maximum ground acceleration that occurs during an earthquake at a given location. PGA does not actually provide information on the dynamic behavior of structures, which can, however, be obtained by using response spectra. Response spectra give the maximum response of a system with one degree of freedom (SDOF) when subjected to a given input motion as a function of the natural frequency (or natural period) and the damping ratio of the SDOF. Response can be expressed in terms of acceleration,

velocity, or displacement, and their maximum values are referred to as spectral acceleration ( $S_a$ ), spectral velocity ( $S_v$ ), and spectral displacement ( $S_d$ ). Empirical relationships between macro-seismic intensity and PGA have also been developed to compare macro-seismic observations with recorded ground motions. Since it is troublesome to propose correlation laws of general validity, most of the studies carried out so far take into account the seismicity of specific countries or geographic areas, such as the USA (Wald et al., 1999; Trifunac and Brady, 1975; Neumann, 1954; Hershberger, 1956; Gutenberg and Richter, 1942, 1956), Japan (Kawasumi, 1951), the Mediterranean region, including Italy (Margottini et al., 1992; Theodulis and Papazachos, 1992; Panza et al., 1997; Faccioli and Cauzzi, 2006), or the collection of different areas around the world (Murphy and O'Brien, 1977). All the measuring tools mentioned so far have given the opportunity to systematically collect data about earthquake intensities over the years. This has helped in the creation of seismic hazard maps, especially in countries with a high seismicity. In Italy, for example, a national probabilistic seismic hazard map known as MPS04 (Figure 2.3) was developed in 2004 (Stucchi et al., 2004), thanks to the Decree OPCM 3274/2003 (OJ No. 108, May 8, 2003). It then became the reference hazard map on April 6, 2004 (Decree PCM 3519/2006, OJ No. 105, May 11, 2006). This Italian hazard map was developed by the INGV Group (National Institute of Geophysics and Volcanology) in collaboration with Italian universities and research centers.

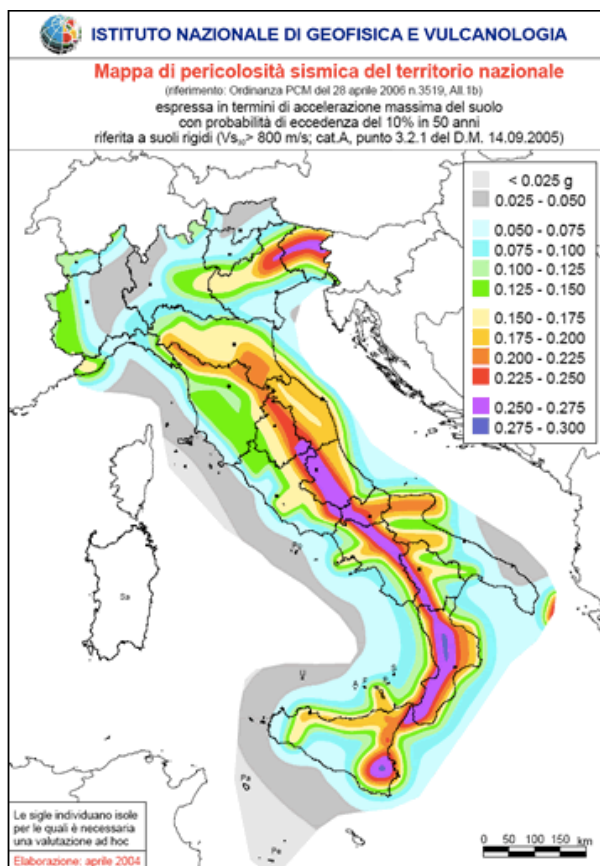


Figure 2.3 - Seismic hazard map for Italy (MPS04) in terms of PGA (Peak Ground Acceleration) with a 10% probability of exceedance in 50 years

The MPS04 gives the 10% probability of exceeding a given ground motion parameter (such as for example PGA) in 50 years, taking into account rigid soils. Seismic hazard was assessed for grid points at  $0.05^\circ$  intervals and for a finer grid at  $0.02^\circ$  intervals in latitude and longitude, covering the entire national territory (except for Sardinia and some smaller islands, for which ad hoc studies were required).

### 2.1.2. Seismic vulnerability

Seismic vulnerability is the tendency of a structure to be damaged and collapse when subjected to ground motion of a certain intensity. It depends on many factors, including the type of structure, quality of construction materials, construction methods, maintenance, and the possible presence of anti-seismic retrofit intervention. When performing vulnerability assessments, the aim is to determine the probability that a particular building will reach a given level of damage during an earthquake scenario. For this reason, the ground motion evaluated through one of the seismic hazard analyses presented before must be correlated with the damage caused to the building. In order to do so, among the various tools that have been developed in the field of seismic vulnerability, fragility models are definitely some of the most popular.

Fragility models (expressed by fragility curves) correlate seismic intensity parameters (e.g. the Peak Ground Acceleration, PGA) with the probabilities of exceeding some damage states (DSs) of buildings, and are frequently described by lognormal cumulative density functions (an example of a graphic representation of fragility curves is shown in Figure 2.4). Many methods to derive fragility sets are found in the literature (Calvi et al., 2006), which are based on two main approaches: empirical, which calibrate fragility curves based on damage information surveyed in the aftermath of the event; and analytical (or mechanics-based), which define fragility based on structural models and analyses to simulate the seismic behavior of buildings. Other methods widely used are the hybrid ones, which use information from both empirical and analytical methods, as well as judgement-based methods, which are based on the statistical evaluation of information provided by teams of experts or based on field inspections.

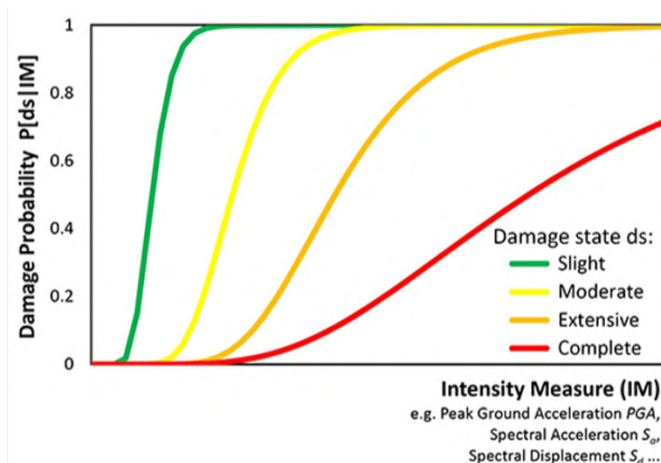


Figure 2.4 - Example of fragility curves

In general, there is no method that is better than the others, as they all have advantages and disadvantages. For example, an empirical fragility model is calibrated on specific areas affected by the earthquake (therefore on specific building types and on a particular seismic scenario) and includes a series of uncertainties on surveys and measurements of seismic damage and ground shaking intensity that are responsible for increasing the dispersion of fragility curves. On the other hand, a mechanics-based fragility model requires the retrieval of a significant amount of geometric and design information, through time-consuming surveys and cognitive studies; moreover, its reliability is strongly related to that of the structural models and analyses, as well as to the quantity and quality of the information collected. In summary, both approaches can lead to significantly accurate results, but often not without drawbacks or limitations in their implementation and use.

Among all building typologies for which seismic vulnerability must be evaluated, masonry buildings make up a large portion of the world's building stock, especially in countries with a significant amount of historical buildings such as Italy. Seismic vulnerability assessment of such structures is a key issue in the context of seismic risk. For this reason, this thesis focuses on the vulnerability assessment of Italian residential masonry buildings, and therefore an insight on some methods that have proven successful for defining fragility curves for this building typology is presented below.

#### *2.1.2.1. Empirical and observational methods*

Empirical methods for vulnerability assessment are mainly based on the distribution of recorded damage collected and statistically analyzed during post-earthquake surveys. They can provide damage probability matrices (DPM), i.e., matrices expressing the probability of suffering a damage condition at a given seismic intensity for a macro-class of buildings. The first use of DPMs as a tool for the probabilistic prediction of damage to buildings subjected to seismic actions was realized by Whitman et al. (1973), after the San Fernando earthquake of 1971 (Figure 2.5). The use of these matrices was first introduced in Italy after the 1980 Irpinia earthquake (Braga et al., 1982) as a tool to perform vulnerability analysis and predict the expected damage. In addition, a binomial distribution was proposed as representative of the damage distribution for a fixed class of buildings with different macro-seismic intensity. In that study, buildings were divided into three vulnerability classes (A, B, and C) and the MSK macro-seismic scale was adopted as a reference (Kárník et al., 1984). In subsequent Italian studies (Di Pasquale et al., 2005), the DPMs were further developed starting from the MCS macro-seismic scale. Specific applications of this method to masonry structures have also been widely used in countries and regions with extensive historical seismicity records (Corsanegro and Petrini, 1990; Askan and Yucemen, 2010; Zobin et al, 2010).



Damage State	Structural Damage	Non-structural Damage	Damage Ratio (%)	Intensity of Earthquake				
				V	VI	VII	VIII	IX
0	None	None	0-0.05	10.4	-	-	-	-
1	None	Minor	0.05-0.3	16.4	0.5	-	-	-
2	None	Localised	0.3-1.25	40.0	22.5	-	-	-
3	Not noticeable	Widespread	1.25-3.5	20.0	30.0	2.7	-	-
4	Minor	Substantial	3.5-4.5	13.2	47.1	92.3	58.8	14.7
5	Substantial	Extensive	7.5-20	-	0.2	5.0	41.2	83.0
6	Major	Nearly total	20-65	-	-	-	-	2.3
7	Building condemned		100	-	-	-	-	-
8	Collapse		100	-	-	-	-	-

Figure 2.5 - Damage Probability Matrix format proposed by Whitman et al. (1973)

However, DPMs have the major limitations of defining damage levels in a discrete way, and depending on a specific seismic scenario. In order to overcome this problem, a macro-seismic heuristic method was proposed by Lagomarsino and Giovinazzi (2006) to derive vulnerability curves, i.e. expected mean damage based on macro-seismic intensity, directly from "qualitative" DPM in the European Macro-seismic Scale EMS98 (Grünthal, 1998), where the expected damage frequency is expressed by linguistic terms (e.g. "few", "most", as shown in Figure 2.6). In this case, vulnerability classes are associated with seismic behavior before being attributed to specific structural classes. The macro-seismic method was refined in 2014 (Figure 2.7) by Lagomarsino and Cattari (2014) with the derivation of fragility curves using peak ground acceleration (PGA) as an intensity measure, and finally, further developments of the model were presented in a recent publication (Lagomarsino et al., 2021).

Class A					
Damage Intensity	1	2	3	4	5
V	Few				
VI	Many	Few			
VII			Many	Few	
VIII				Many	Few
IX					Many
X					Most
XI					
XII					

Class B					
Damage Intensity	1	2	3	4	5
V	Few				
VI	Many	Few			
VII		Many	Few		
VIII			Many	Few	
IX				Many	Few
X					Many
XI					Most
XII					

Class C					
Damage Intensity	1	2	3	4	5
V					
VI	Few				
VII		Few			
VIII		Many	Few		
IX			Many	Few	
X				Many	Few
XI					Many
XII					Most

Class D					
Damage Intensity	1	2	3	4	5
V					
VI					
VII	Few				
VIII		Few			
IX		Many	Few		
X			Many	Few	
XI				Many	Few
XII					Most

Class E					
Damage Intensity	1	2	3	4	5
V					
VI					
VII					
VIII					
IX		Few			
X		Many	Few		
XI			Many	Few	
XII					

Class F					
Damage Intensity	1	2	3	4	5
V					
VI					
VII					
VIII					
IX					
X		Few			
XI		Many	Few		
XII					

Figure 2.6 - DPM in the European Macro-seismic Scale EMS98 (Grünthal, 1998)

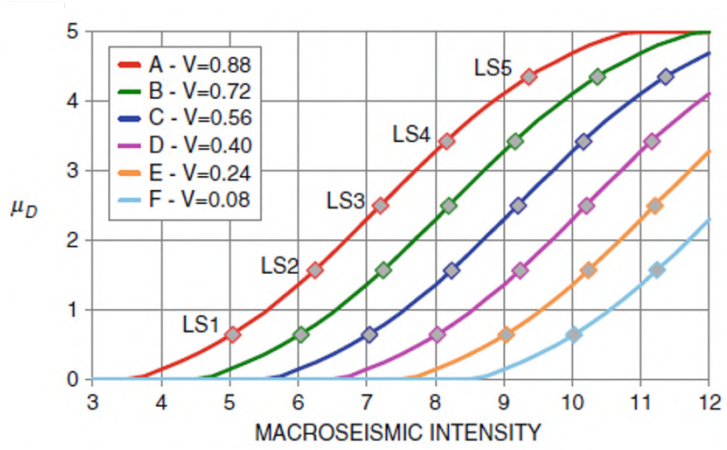


Figure 2.7 - Vulnerability curves for the EMS98 vulnerability classes (Lagomarsino and Cattari, 2014)

Other studies developed different empirical vulnerability and fragility relationships from post-earthquake data, and they usually depend on the seismic scenarios from which damage data are retrieved (Rosti et al., 2021a; Zuccaro et al., 2021; Rota et al., 2008; Rosti et al., 2018; Menichini et al., 2022).

Due to the wide variety of building typologies and the lack of sufficient historical data on earthquake damage, surveys rarely provide a complete set of information. Nevertheless, this type of vulnerability assessment is representative of the physical and real response of exposed buildings, taking into account many variables such as ground motion, topography, soil-structure interaction, and structural features.

#### 2.1.2.2. Judgement-based methods

Judgement-based methods have been largely used for collecting and evaluating data on building vulnerability and on building damage. The forms issued by the GNDT (National Group for Earthquake Protection), particularly the GNDT form and the AeDES form, allow the assessment of post-earthquake damage found during field inspections. These first-level forms are typically used for assessing entire urban areas, thus being useful for developing damage scenarios and conducting empirical vulnerability analyses after the data collection.

The GNDT form is divided into two levels and covers masonry and reinforced concrete buildings (Benedetti and Petrini, 1984; GNDT-SSN, 1994; Ferrini et al., 2003). For both materials, the second-level GNDT form allows a rapid assessment of the seismic vulnerability of existing buildings by assigning a class to a certain number of vulnerability factors (Figure 2.8a). Each assigned class corresponds to a rating value ( $p_i$ ), while each vulnerability factor is assigned a weighting value ( $w_i$ ). The vulnerability index  $I_v$  is then calculated as the weighted sum of the assessment values for all vulnerability factors. This index increases with increasing vulnerability.

For what concerns the collection of data on observed damage after a seismic event, the main tool used in Italy is the on-site form AeDES (*Usability and Damage in Seismic Emergencies*, Baggio et al., 2007, 2014). The intensity and extent of seismic damage to structural and nonstructural elements is assessed and recorded on the form, as well



the box-like behavior is not achieved, local failures may occur, due to the lack of proper connections between orthogonal walls, the absence of connecting ties, insufficiently rigid floor diaphragms, the presence of low strength and deteriorated materials, and the presence of openings. Recurrent mechanisms that can occur under seismic loading are the overturning of masonry walls (Casapulla et al., 2016) and corners (Casapulla et al., 2019).

Mechanics-based methods require simulations of the seismic response of a building macro-class by a prototype building or building datasets. Simulations can be based on either detailed modelling (Rota et al., 2010, Barbat et al., 2008; Simões et al., 2015; Rota et al., 2014) or simplified methods. The latter can be grouped into capacity spectrum-based methods, such as the U.S. Federal Emergency Management Agency (FEMA, 2003) HAZUS approach, collapse mechanism-based methods, including *Vulnus* by Bernardini et al. (1990), and displacement-based methods, among which we find the approach proposed by Calvi (1999) and its further development (MeBaSe) proposed by Restrepo-Velez and Magenes (2004), the SP-BELA approach (Borzi et al., 2008), and the DBV masonry method (Lagomarsino and Cattari, 2014). The simplified methods for masonry buildings cited above are discussed more in details in the following paragraphs.

The mechanism-based method *Vulnus* (Bernardini et al., 1990; Valluzzi et al., 2009) performs vulnerability assessment by considering both the in-plane (IP) and out-of-plane (OOP) response of masonry structures. Specifically, *Vulnus* evaluates the building's IP shear resistance (assuming that all masonry walls reach their maximum shear capacity without premature failure) and the initiation of potential OOP mechanisms, considering overturning, flexural failure, and vault failure, as well as a qualitative estimate of building vulnerability according to the second level GNDT form (see section 2.1.2.2). Since *Vulnus* is actually the method that is used in this thesis for the development of fragility curves for masonry buildings, the specific procedure proposed by *Vulnus* is further described in the dedicated chapter (chapter 3), where the most recent application proposed by Donà et al. (2021) is presented.

Another method based on collapse mechanisms called FaMIVE was proposed by D'Ayala and Speranza (2003) to evaluate the seismic vulnerability of unreinforced masonry (URM) buildings, based on the susceptibility of the facades to local mechanisms. The FaMIVE (Failure Mechanism Identification and Vulnerability Evaluation) method is based on a set of input parameters, most of which can be collected from an external survey. The procedure identifies the possible collapse mechanisms among those that have been observed during post-event damage detection surveys. A story-by-story analysis is performed to determine how many of them are involved in each failure mechanism, including an estimate of restraining forces provided by transverse walls and possible reinforcing devices, as well as frictional forces. For each possible mechanism, an index is calculated to express the Equivalent Shear Capacity (ESC) as a percentage of gravity acceleration.

Moreover, Calvi (1999) proposed a displacement-based approach for vulnerability assessment of building macro-classes classified by their construction material (i.e., unreinforced masonry or reinforced concrete), number of floors, and level of seismic

design. The evaluation is based on the estimation of displacement and energy dissipation capacities. This methodology was further developed for masonry buildings by Restrepo-Velez and Magenes (2004) and called MeBaSe (Mechanics-Based Seismic Risk Assessment Method). MeBaSe evaluates the seismic vulnerability of masonry buildings classes using a displacement-based approach. The URM building under study is modelled in a simplified way as a single degree of freedom (SDOF) system, and different displacement profiles related to different failure mechanisms and limit states are considered. The maximum displacement for a given limit state results from two contributions: a yield displacement and a plastic displacement. In addition, the MeBaSe method includes the evaluation of a number of out-of-plane failure modes, in particular for simple overturning, overturning of double-leaf walls, and vertical flexure. In addition, the major sources of uncertainty (i.e., seismic demand, capacity response, and damage thresholds) are evaluated and included in the fragility assessment.

Later, Borzi et al. (2008) proposed another displacement-based procedure called SP-BELA (Simplified Pushover-Based Earthquake Loss Assessment), which was originally developed for deriving vulnerability curves of r.c. bare frame buildings designed for gravity loads only. The method was then adapted for URM buildings, considering the in-plane failure mode and assuming the deformed shapes associated with different global failure mechanisms according to Calvi (1999). In this case, a collapse multiplier for each story is calculated according to Benedetti and Petrini (1984), as also proposed by Restrepo-Velez and Magenes (2004). A thorough evaluation of out-of-plane mechanisms is not included in SP-BELA for masonry because the data required for this purpose are often not available at a very large scale, for which the method was developed. The latest developments and results of this method are included in Borzi et al. (2021a) for what concerns r.c. buildings.

Specifically for masonry buildings, a simplified displacement-based mechanical model was developed by Lagomarsino and Cattari (2014). The method determines the capacity curve of a based on the pseudo-elastic period, the spectral acceleration at yielding, and the ultimate capacity in terms of displacement. When evaluating shear strength, it is assumed that all masonry piers fail simultaneously, which is reasonable if they have similar dimensions and the building presents regularity in plan; otherwise, correction coefficients are applied. Then, four limit states (LS) are determined on the capacity curve. The analysis is performed for the two main horizontal directions, assuming for the fragility analysis the most vulnerable direction, which can differ for different LSs and seismic intensities.

As part of the ASSESS project 2008-2011 (Grimaz et al., 2011), two new simplified mechanical methods were developed to evaluate the seismic capacity of buildings made of reinforced concrete and masonry, respectively. Both simplified methods, called FIRSTSTEP-RC and FIRSTSTEP-M, provide a capacity acceleration of the building defined as the resistive acceleration on the ground  $A$  in the weakest principal direction (Gattesco et al., 2011). Specifically, the simplified procedure FIRSTSTEP-M allows the evaluation of both masonry and mixed masonry-r.c. buildings. It is assumed that only

the in-plane resistance of the vertical structural elements contributes to the seismic capacity.

Lastly, a simplified analytical model called RE.SIS.TO was proposed by Mazzotti et al. (2013). This method was developed for the estimation of the collapse peak ground acceleration for masonry and r.c. buildings. The acceleration is evaluated based on the minimum ratio between shear capacity and shear demand in the weakest direction.

#### *2.1.2.4. Hybrid methods*

This final section is meant to give an insight on hybrid methods for evaluating seismic vulnerability. Among the main ones, Kappos et al. (2006) propose a method for deriving derivation of vulnerability and fragility curves expressed as a function of PGA, as well as spectral displacement ( $S_d$ ) and also includes the estimation of capacity curves for different r.c. and URM building typologies. The vulnerability assessment methodology is based on the hybrid approach that combines statistical data from earthquake-damaged Greek buildings with processed results from nonlinear dynamic or static analyses. The latter allow extrapolation of the statistical data for PGAs and/or spectral displacements for which data are not available. Another method that combines post-earthquake damage statistics with mathematical models is the macro-seismic method proposed by Giovinazzi and Lagomarsino (2004). This macro-seismic method was developed starting from the definition of the EMS98 and is based on classical probability theory and fuzzy set theory. It allows the vulnerability assessment of buildings or classes of buildings. Vulnerability is defined by evaluating a vulnerability index  $V$  and a ductility index  $Q$ : both indices depend on the structural characteristics and typology of building analyzed. Damage levels are also considered according to the ones provided by EMS98 (0-no damage, 1-light damage, 2-moderate damage, 3-heavy damage, 4-very heavy damage, 5-destruction). Also Sandoli et al. (2021) provide a hybrid seismic fragility model for territorial-scale seismic vulnerability assessment, by combining expert judgement and mechanical approaches to derive typological fragility curves for Italian masonry residential buildings. The first one classifies Italian masonry buildings into five different typological classes as a function of building age, structural typology and seismic behavior and damage observed after the most severe earthquakes in Italy. The second part is based on the results of numerical analyses carried out on building prototypes and provides all the parameters necessary for the development of fragility functions.

#### **2.1.3. Exposure**

The exposure of an area refers to the type, quality, and quantity of assets that can be subjected to risk. Thus, exposure assessment involves quantifying the structures (buildings, infrastructures, etc.) and the number of people likely to be affected by a seismic event.

In literature, we can find many definitions of the concept of “exposure”: even though most of them share the same key points, some differences can be perceived. For

example, in “Risk Assessment, Modeling and Decision Support” by Bostrom et al., (2008), exposure takes into account “*humans, animals, property, business operations and other items of value whose reduction in value (loss) is a concern. In general, the economy and built, social and natural environments that may be affected by an earthquake. Similar terms include asset, inventory, and portfolio. Note that assets include intangibles such as intellectual property and reputation*”. Furthermore, the “Sendai Framework for Disaster Risk Reduction 2015-2030” (United Nations, 2015) define exposure as “*people, property, systems, or other elements present in hazard zones that are thereby subject to potential losses. Measures of exposure can include the number of people or types of assets in an area*”. Another possible definition of exposure can be found in Fundamentals of Earthquake Engineering (Elnashai and Di Sarno, 2015), which states that “*exposure comprises the assets that are subjected to the hazard; thus, it is a count of the exposed systems and their value*”.

The definitions provided above imply that, in order to properly define exposure as an essential component of seismic risk, it is necessary to analyze the distribution, structure, and socioeconomic conditions of the population residing in a given area, the quantity and functions of the building stock (residential, public, industrial), the infrastructure system, the existing activities, and the possible relationships with surrounding areas. It is clear that estimating exposure can be very cumbersome, especially in urban areas where large-scale surveys are generally expensive and require a lot of resources; yet it is in urban areas that most assets are at stake in the event of a disaster. In order to face this challenge, particularly when the aim is to survey large building inventories, forms for rapid visual-screening have been developed, which often also include the identification of structures that require more in-depth evaluation in the first instance.

For example, CARTIS (Typological-Structural Characterization of the urban compartments) represents a valid tool to evaluate exposure at large scales. CARTIS is a project carried out by the ReLUIIS consortium (Network of the University Laboratories of Seismic Engineering) and funded by the Italian Civil Protection Department (DPC) which proposes a procedure that involves the construction of regional inventories, obtained through the typological-structural characterization of buildings. This project was created with the intention of investigating the national building panorama and identifying local building characteristics. In fact, over the entire national territory, building techniques have differed over the centuries, due to local influences, which in some cases have significantly affected the characteristics and quality of construction, determining substantial differences even in terms of response to natural phenomena such as earthquakes. Through appropriate processing, the data collected through the CARTIS form can provide indications for a regionalization of the seismic vulnerability currently used throughout the Italian territory (Zuccaro et al., 2016). As for 2022, the total number of municipalities surveyed within CARTIS amounts to 506, and it includes smaller and bigger towns in different regions of Italy. The use of the CARTIS form in a significant number of municipalities in Italy aims to improve the building taxonomy to provide a

regionalized characterization of the building stock and to allow more accurate risk assessments at the national level.

The CARTIS form is composed of a first level sheet and a second level sheet. The first level sheet includes the typological-structural definition of urban compartments, called districts (Figure 2.9). Districts are homogeneous areas characterized by the presence of buildings that are similar from a typological point of view and by construction period. The sheet refers only to ordinary buildings, such as those mainly for housing and services. The characterization therefore excludes typologies attributable to monumental assets (religious buildings, historical buildings, etc.), special structures (industrial warehouses, shopping centers, etc.) or strategic structures (hospitals, schools, barracks, prefectures, civil protection offices, etc.), whose characteristics often do not fall within those of ordinary buildings. For each municipality investigated, the form is filled in by an expert from one of the research units belonging to the ReLUIS consortium. The CARTIS form is divided into the following four sections:

- Section 0, for the identification of the municipality under examination and of the districts detected in it;
- Section 1, for the identification of each typology characterizing the district of the municipality;
- Section 2, for the identification of the general characteristics of the typologies under examination;
- Section 3, for the characterization of the structural elements of the typologies under consideration.

The identification of the prevailing typologies in each compartment is carried out with particular reference to the fields of Sections 2 and 3, considered fundamental in the characterization of different seismic behaviors: total number of floors, building age, characteristics of the masonry/r.c./mixed structure, characteristics of the floors, presence of separation joints, presence of floor infills, characteristics of the roof, and structural interventions.

The second level CARTIS form (issued on 2016) goes more in-depth as it analyzes a particular type of building (Polese et al., 2019, Sbrogiò et. al, 2022). The filling of the sheets concerns both reinforced concrete and masonry buildings. Various parameters are defined in the sheet for the correct assessment of buildings. For masonry, the following are considered: type and organization of the resistant system, quality of the resistant system, position of the building and foundation, orientations, planimetric configuration, configuration in elevation, roofing, non-structural elements, among others. The section concerning reinforced concrete, on the other hand, includes as parameters: type and organization of the resistant system, distribution of infills, planimetric configuration, and irregularities in elevation.

All these survey methods and projects have proven very successful in the analysis of exposure and vulnerability at a large scale. However, most of these ongoing projects still need time to collect an adequate amount of data in order to derive meaningful and representative results that can be extended at larger scales.



The image shows the cover and the first sections of the CARTIS 2014 form. The cover is red and features the title "MANUALE PER LA COMPILAZIONE DELLA SCHEDA CARTIS 2014" and "SCHEDA DI 1° LIVELLO PER LA CARATTERIZZAZIONE TIPOLOGICO-STRUTTURALE DEI COMPARTI URBANI COSTITUITI DA EDIFICI ORDINARI". The form sections include:

- SEZIONE 0: Identificazione Comune e Comparti** (PARTE A)
- a. DATI DI LOCALIZZAZIONE**: Region, Province, Comune, Municipalità/Frazione/Localtà (denominazione ISTAT).
- b. DATI GENERALI COMUNE**: Numero totale residenti del Comune, Anno di prima classificazione sismica, Anno di approvazione Piano Regolatore Generale, Anno di approvazione Programma di fabbricazione, Numero totale abitazioni, Numero totale edifici.
- c. NUMERO ZONE OMOGENEE (COMPARTI)**
- d. DATI IDENTIFICATIVI UNITÀ DI RICERCA (UR) RELIUS**: Codice UR, Ente di appartenenza, Qualifica, Titolo di studio, Indirizzo, Tel. ufficio, Compilatore, Firma del Compilatore.
- e. DATI IDENTIFICATIVI TECNICO INTERVISTATO**: Referente del Comune, Nominativo, Ente di appartenenza, Qualifica, Titolo di studio, Indirizzo, Mail, Tel. ufficio, Cell.

Figure 2.9 – Cover and first sections of the CARTIS form

Furthermore, research has focused not only on the elaboration of methodologies for the evaluation of building exposure to perform risk assessments, but also on the definition of building taxonomy. When we talk about taxonomy, we refer to the practice of categorization or classification in which objects are organized into groups or types. Indeed, the development of a robust risk model requires a solid methodological foundation and consistent terminology to achieve a common understanding of the building stock under consideration.

In this view, the vision of the GEM Building Taxonomy is to create a unique description for a building or building typology (Brzev et al., 2013; Silva et al. 2022), defined by several attributes. Typical attributes are material, lateral load restraint system, and building height. To develop this taxonomy, the GEM project set as its goal to review existing taxonomies, and verify it at the global level.

Moreover, the project TABULA (Typology Approach for Building stock energy Assessment, 2009-1012), funded by the European program *Intelligent Energy Europe*, has the goal to create a harmonized structure of European building types (Corrado et al., 2014; Ballarin et al., 2014). The focus is on residential buildings, but other building categories are also considered. Each participating country has developed a “National Building Typology” consisting of a set of sample residential buildings with typical energy characteristics. Each building type represents a specific region or climatic zone, a class of construction period, and a class of building size. The elements that contribute to the classification of the building typology form the axes of the so-called “building typology matrix”. Each cell of the matrix accommodates a “building type” that is considered representative of the condition (climate zone/building age/size). The Italian building type matrix was developed for climate zone E (medium climate zone), which includes 4,250 Italian municipalities. In this way, a common structure for building typologies has been developed, based on the typical construction characteristics of the

national residential building stock (Figure 2.10). Moreover, two levels of building type retrofits are analyzed: a “typical retrofit” by applying measures that are common in each country, and an “advanced retrofit” by introducing measures that correspond to the best available technologies. The project is aimed at experts working on scenario analyzes and policy makers at different levels (regional, national, municipal).

**Generic Building Types - Middle Climatic Zone**




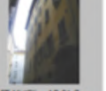




























Region	Construction Year Class	Additional Classification	SFH	TH	MFH	AB
			Single-Family House	Terraced House	Multi-Family House	Apartment Block
1	Middle Climatic Zone (Zona climatica media - ZONA E) ... 1900	generic	 IT.MidClim.SFH.01.Gen	 IT.MidClim.TH.01.Gen	 IT.MidClim.MFH.01.Gen	 IT.MidClim.AB.01.Gen
2	Middle Climatic Zone (Zona climatica media - ZONA E) 1901 ... 1920	generic	 IT.MidClim.SFH.02.Gen	 IT.MidClim.TH.02.Gen	 IT.MidClim.MFH.02.Gen	 IT.MidClim.AB.02.Gen
3	Middle Climatic Zone (Zona climatica media - ZONA E) 1921 ... 1945	generic	 IT.MidClim.SFH.03.Gen	 IT.MidClim.TH.03.Gen	 IT.MidClim.MFH.03.Gen	 IT.MidClim.AB.03.Gen
4	Middle Climatic Zone (Zona climatica media - ZONA E) 1946 ... 1960	generic	 IT.MidClim.SFH.04.Gen	 IT.MidClim.TH.04.Gen	 IT.MidClim.MFH.04.Gen	 IT.MidClim.AB.04.Gen
5	Middle Climatic Zone (Zona climatica media - ZONA E) 1961 ... 1975	generic	 IT.MidClim.SFH.05.Gen	 IT.MidClim.TH.05.Gen	 IT.MidClim.MFH.05.Gen	 IT.MidClim.AB.05.Gen
6	Middle Climatic Zone (Zona climatica media - ZONA E) 1976 ... 1990	generic	 IT.MidClim.SFH.06.Gen	 IT.MidClim.TH.06.Gen	 IT.MidClim.MFH.06.Gen	 IT.MidClim.AB.06.Gen
7	Middle Climatic Zone (Zona climatica media - ZONA E) 1991 ... 2005	generic	 IT.MidClim.SFH.07.Gen	 IT.MidClim.TH.07.Gen	 IT.MidClim.MFH.07.Gen	 IT.MidClim.AB.07.Gen
8	Middle Climatic Zone (Zona climatica media - ZONA E) 2006 ...	generic	 IT.MidClim.SFH.08.Gen	 IT.MidClim.TH.08.Gen	 IT.MidClim.MFH.08.Gen	 IT.MidClim.AB.08.Gen

Figure 2.10 - Example of Italian building typologies according to the TABULA project

**2.2. Assessment of seismic losses and consequences**

The correct definition of seismic hazard, vulnerability and exposure can lead to accurate estimates of seismic damage. However, when the aim is to assess seismic risk, specific correlations need to be defined in order to express damage as risk indicators such as impact on people (casualties and displaced people), buildings (economic losses and usability), cultural heritage, and social and economic disruption. This operation is not trivial at all, since many of these aspects include indirect (or consequential) losses or even losses related to people or artistic assets that can be difficult to quantify.

Nevertheless, research on the assessment of earthquake-related damage and consequences has been carried out, often by processing data from past seismic events. Since these aspects are strongly linked to the local context in terms of observed events, structural assets, and emergency management, a particular focus is placed here on Italy-specific studies.

One of the reference events in this field in Italy was L'Aquila earthquake (2009). The main shaking, which occurred on April 6, caused extensive damage to buildings in the municipality of L'Aquila and neighboring municipalities; 309 people were killed and 67,459 people were displaced (Mannella et al., 2017). After the earthquake, the usability and damage of residential buildings were assessed using the AeDES form (already described in section 2.1.2.2). Three classes of usability were considered in the reconstruction process, i.e., usable buildings (A), short-term unusable buildings (B-C), and long-term unusable buildings (E). The principle of "building back better" was applied: therefore, reconstruction included both repair and seismic strengthening. Reconstruction of buildings in categories B-C, i.e., buildings with light damage (Di Ludovico et al., 2017a) was performed before the reconstruction of building that had suffered severe damage (Di Ludovico et al., 2017b), so that slightly damaged buildings could be quickly reoccupied by people that were displaced. Technical and economic data were obtained for 5,775 residential buildings located in the municipality of L'Aquila (outside the historic center) or in one of the 63 neighboring municipalities belonging to the area struck by the earthquake. The repair costs processed for the assessment of direct damages included emergency response, demolition and debris removal, repair and reinforcement works, as well as safety costs, professional fees, and relocation costs (Del Vecchio et al., 2020; Del Vecchio et al., 2018).

Recently, Di Ludovico et al. (2022), assuming a reference cost for a residential building of 1,350 €/m<sup>2</sup> (Dolce et al., 2021), processed actual repair costs to evaluate probability density functions of direct economic losses, expressed as a percentage of total cost for r.c. and masonry buildings according to their usability and damage condition. Similarly, the cost for supporting the displaced population was calculated, including the different types of shelter established during the emergency and reconstruction phases.

Furthermore, Del Vecchio et al. (2020) processed these data for damaged buildings, distinguishing between direct repair costs and retrofit costs, and then further distinguishing between direct repair costs for structural and nonstructural building components. A more complex earthquake-related consequence to assess is the business interruption in the productive sector (Donà et al., 2019), which causes significant losses to businesses and may also affect the national GDP (gross domestic product).

Moreover, strong earthquakes have tragically shown how much they can be a threat for human lives. The factors affecting earthquake mortality were discussed by Coburn et al. (1992), particularly deaths from building collapses, which are estimated to cause 75% of earthquake casualties. The authors propose a calculation to estimate the number of people killed by an earthquake, which mainly depends on the number of collapsed buildings (DS5), on the average number of people per building and the

occupancy rate at the time of the event (which can vary during the day, as well as weekly and seasonally), on the building type and extent of the collapse, as well as on the effectiveness of search and rescue efforts. The casualty estimation models available in the literature were reviewed by Spence and So (2011), who pointed out the large uncertainties that characterize this estimation. As part of the development of the Global Earthquake Model (GEM), estimates of human casualties at the national level were based on empirical casualty models at country-level (Silva et al., 2014). Communities are also affected by earthquakes in the form of displaced people who are likely to require public shelters and emergency housing. Mannella et al. (2017) used data on reconstruction after the L'Aquila earthquake to investigate the timing of assistance to the population and the return times of displaced people to their homes.

### 2.3. Seismic risk calculation platforms

Certainly, the estimation of seismic hazard, vulnerability, and exposure are of utmost importance when assessing seismic risk. However, it must not be forgotten that these three elements ultimately need to find a connection among each other in a pipeline that integrates them, for an appropriate seismic damage and risk analysis.

During these years, several research groups around the world have developed earthquake risk assessment tools to estimate seismic damage and loss. A number of existing risk software applications are reviewed in Crowley et al. (2010). SELENA, SEismic Loss Estimation using a logic tree Approach (Molina et al., 2010) is a software tool for seismic risk and loss assessment based on the HAZUS methodology (National Institute of Building Sciences, 1999; FEMA, 2003). Another open-source earthquake hazard and risk assessment tool is the EarthQuake Risk Model (EQRM) (Robinson et al., 2005), developed by Geoscience Australia and applicable to the Australian country. In addition, Earthquake Loss Estimation Routine (ELER) (Hancilar et al., 2010) is a stand-alone application that provides rapid estimation of earthquake shaking and damage in the Euro-Mediterranean region. Two tools whose source code is available upon request are CEDIM (CEDIM Risk Estimation Tool) (Köhler et al., 2006) and Central America Probabilistic Risk Analysis (CAPRA, Gill et al., 2009). The CEDIM software was developed by the Center for Disaster Management and Risk Reduction Technology in Potsdam, Germany, but has also been used for damage and risk analysis in other earthquake-prone areas of the world. On the other hand, CAPRA is a multi-hazard damage estimation software, elaborated under a World Bank initiative aimed at strengthening institutional capacity for disaster risk assessment, understanding, and communication, with the ultimate goal of integrating disaster risk information into development policies and programs. CANRISK (Ploeger et al., 2016) is a seismic vulnerability assessment tool for buildings in Canada. The model combines the HAZUS method with its own method to estimate the number of injuries, and it is designed to test the benefits of mitigation strategies. Lastly, Mesgar and Jalilvand (2017) developed a scenario-based model to estimate seismic damage to residential buildings in Iran, focusing on the city of Sari as a case study.

The European Centre for Training and Research in Earthquake Engineering (Eucentre) has also developed tools implemented in WebGIS platforms for earthquake risk and loss scenario assessment, with funding from the Italian Civil Protection Department. These platforms consider residential buildings (Faravelli et al., 2017, 2018), school buildings (Borzi et al., 2013; Faravelli et al., 2017, 2018), transportation network infrastructures (Di Meo et al., 2018; Faravelli et al., 2018), and dams (Bozzoni et al., 2015; Bozzoni and Lai, 2017). Among the many platforms elaborated by Eucentre, the Italian Risk Maps (IRMA) (Borzi et al., 2021b; Figure 2.11) was specifically designed upon request of the Italian DPC to provide researchers with an open, common and verified risk assessment tool that allows implementing user-defined models of fragility, cost and casualties (Dolce et al., 2021). IRMA can evaluate risk by producing risk maps in terms of direct economic losses, unusable buildings, and casualties, both considering conditional damage (i.e., for a specified return period) or unconditional damage (i.e., for a specified time window). In addition, IRMA contains information on the ground shaking accelerations (ShakeMaps) of some recent and significant Italian earthquakes, and thus allows simulating specific seismic events.



Figure 2.11 – User interface of the IRMA platform (Borzi et al., 2021b)

## 2.4. Machine learning techniques in earthquake engineering

Machine learning (ML) has played a central role in many areas of science, finance, and engineering (Xie et al., 2020; Salehi and Burgueño, 2018). By definition, ML is a field of research that gives computers the ability to learn without being explicitly programmed (Samuel, 1959). ML Algorithms can be divided into two main types: supervised learning and unsupervised learning. Supervised learning uses prior

knowledge about the labeled data set to learn a function that best approximates the relationship between input and labeled output in the data. On the other hand, unsupervised learning aims to infer the natural structure of a set of data points that have no target labels. Depending on the data characteristics (i.e., discrete or continuous) and the goals of the task, supervised learning can be further divided into classification and regression, while unsupervised learning includes clustering and dimensionality reduction.

Previous studies have explored the applications of ML and other advanced soft computing tools in civil engineering, including earthquake engineering. Earthquake engineering is an interdisciplinary branch of engineering that describes earthquake hazards at the source, describes site impacts and structural response, evaluates seismic risk and vulnerability, and assesses seismic protection measures. The numerous topics covered by the branch of earthquake engineering that have been covered with the help of artificial intelligence (AI) in recent years can be grouped into four categories: seismic hazard analysis, system identification and damage detection, seismic vulnerability assessment, and structural control for earthquake mitigation. In seismic hazard analysis, ML tools are used not only to assess seismic hazard itself, but also to evaluate the liquefaction potential of soils and to predict lateral spreading. The second topic includes a collection of studies that use ML to replicate a structural system and predict its deterministic seismic response, as well as to detect, classify, and evaluate seismic damage to civil structures. Third, ML techniques have proven promising in seismic fragility assessment (task that typically involves multiple sources of uncertainty, as shown in section 2.1.2): in this field, ML methods have been used to develop probabilistic seismic demand models (PSDM) and parameterized fragility functions. The fourth topic area includes studies related to ML-equipped structural control systems that are meant to mitigate the adverse effects of seismic hazard.

For what concerns the main ML methods used in the field of earthquake engineering, the most used are Artificial Neural Networks (ANN), Support Vector Machines (SVM), Response Surface Methodology (RSM), Logistic Regression (LR), Decision Tree and Random Forests (DT/RF), and hybrid methods that couple ANN with other soft computing algorithms, such as fuzzy logic and wavelet analysis.

An ANN typically consists of three types of layers: input layer, hidden layer, and output layer (Perlovsky, 2000). In particular, model variables in the input layer are weighted and fed into the hidden layer that consists of a series of nonlinear relationships such as sigmoidal functions, which are further weighted and fed into the output layer to provide a regression or classification model. Connection weights are learned in the forward propagation and updated through a training process that minimizes the prediction error, which is typically propagated in the backward direction (Bishop, 2006; Murphy, 2012). On the other hand, SVM is a binary classification algorithm that uses kernel functions to enable an implicit mapping of the data into a high-dimensional feature space. Usually, an optimum margin classifier is carried out to construct a separating hyper-plane that maximizes the margin between the hyperplane and the support vectors, which comprise the data points that lie closest to the hyperplane (Vapnik, 1998). Furthermore, RSM was originally developed as a

statistical method that explores the relationship of explanatory variables of a system and its responses (Box and Hunter, 1957), and it has been commonly applied in various areas because of its simplicity, transparency, and transferability features. The main idea of the RSM is to conduct a series of planned experiments to obtain an optimal answer, using for example a second-degree polynomial model to accomplish this. Also LR is widely used in this field, since it represents one of the most basic methods to measure the relationship between the categorical dependent variable and one or more independent variables through a logistic distribution function. Namely, the sigmoid function is used to estimate the probability that a new data point belongs to one of the two classes (Hosmer and Lemeshow, 2000). DT, also named as classification and regression tree (CART), is a ML algorithm that recursively partitions the input space and defines a local model in each resulting region. A simple regression model can be fit to each sub-space in case of regression, while a class can be assigned to each subspace in case of classification. A cost function is applied to find the optimal partitioning of the data. To overcome the potential overfitting and instability issues associated with a single tree, RF constructs a multitude of DTs at training and outputs the mean predictions of individual trees (Ho, 1995). As mentioned before, ML methods (particularly ANNs) can be combined with other soft computing techniques to deal with the complexity and ambiguity in earthquake engineering problems. Such a combination provides integrated systems to overcome the limitations of individual techniques. ANNs can be for example coupled with fuzzy logic algorithms to take advantage of the computational capabilities from both algorithms. For instance, imprecise data information, such as linguistic statements, can be transformed into numerical data through a fuzzy logic interface in order to train an ANN and make decisions (Alvanitopoulos et al., 2010). Moreover, wavelet transform can analyze the different frequency components of an earthquake signal with varying levels of details, which has emerged as an effective technique that can be embedded in an ANN for system identification and damage detection (Adeli and Jiang, 2006; Hung et al., 2003). In the following paragraphs, the implementation of different ML techniques in each one of the earthquake engineering fields mentioned above is discussed.

#### **2.4.1. Machine learning in seismic hazard analysis**

In the field of seismic hazard, ground motion prediction has always received much interest from the scientific community. Due to the complex nature of seismic events, it is challenging to efficiently extract indicative features even from continuously acquired seismic data. This has serious implications for the performance of conventional seismic prediction models and hinders the development of seismology in general. Conventional empirical methods rely on regression analyses to derive attenuation equations for various measures of ground motion intensity as functions of source, path, and site parameters (Boore and Atkinson, 2008; Boore et al., 2014; Douglas, 2003) through ground motion prediction equations (GMPEs). GMPEs usually take into account the influence of magnitude, distance, and site effects. Selecting an appropriate functional form for the parameters that define a GMPE is not

straightforward because it requires not only appropriate identification and inclusion of significant independent variables, but also appropriate parametric quantification of the relationship between these input variables and the outcome. In this regard, AI techniques can be used as powerful statistical tools to overcome these problems (Jiao and Alavi, 2020): particularly, the recent implementation of ML methods can remove the limitations of these predefined mathematical structures. Studies that use ML to predict GMPEs benefited from the availability of the strong-motion database in Taiwan, Turkey (Gülkan and Kalkan, 2002), Iran (Amiri et al., 2010), Europe (Akkar et al., 2014), the western United States (Ancheta et al., 2014; Chiou et al., 2008), and Central America for induced earthquakes (Khosravikia et al., 2018). In general, a group of independent parameters can be identified as significant predictors of time-domain intensity measurements, such as peak ground acceleration (PGA), peak ground velocity (PGV), and peak ground displacement (PGD), and frequency-domain measurements, such as pseudo-spectral acceleration (PSA). Significant predictors include earthquake moment magnitude, source-to-site distance, site average shear wave velocity, fault mechanism, and focal depth. Among the ML tools used in GMPEs is ANN (Bakhshi et al., 2014; Derras et al., 2014; Dhanya and Raghukanth, 2018; Güllü and Erxcelebi, 2007; Kerh and Ting, 2005; Khosravikia et al., 2019), SVR (Tezcan and Cheng, 2012; Thomas et al., 2017), DT and CART (Hamze-Ziabari and Bakhshpoori, 2018; Kaveh et al., 2016), and hybrid methods (Gandomi et al., 2011; Alavi and Gandomi, 2011; Mohammadnejad et al., 2012; Akhane et al., 2019).

Significant improvements have been made in several aspects to increase the accuracy and generalizability of ML models in GMPEs. Particularly, of fundamental importance was the creation of a comprehensive ground motion database, namely the NGA Project (Next Generation of Ground-Motion Attenuation Models) strong motion database (Chiou et al., 2008), which contains 3,551 ground motion records of 173 earthquakes with magnitudes ranging from 4.2 to 7.9. Many works made use of the NGA database, which allowed a better validation and testing (Alavi et al., 2011; Alavi and Gandomi, 2011), a separate testing procedure on a different motion database to check the generalization ability of the model (Gandomi et al., 2011; Thomas et al., 2016, 2017), and a significant improvement to ML model performance (Akhane et al., 2019; Alavi and Gandomi, 2011; Gandomi et al., 2011; Hamze-Ziabari and Bakhshpoori, 2018; Mohammadnejad et al., 2012; Thomas et al., 2016).

In contrast to GMPEs, other studies have focused on the use of ML algorithms for probabilistic seismic hazard analysis. Alimoradi and Beck (2015) used principal component analysis PCA (Jolliffe, 2002) to extract a set of orthonormal basis vectors that capture the predictive variations in earthquake wave time histories.

Not only has ground motion prediction been investigated with the help of ML techniques, but also soil liquefaction, since significant structural damage has been caused by this phenomenon during historical earthquake events (Bird et al., 2006; Cubrinovski et al., 2014). Particularly, research includes work that use pattern recognition (PR) tools to classify the occurrence or non-occurrence of soil liquefaction, as well as regression techniques to predict liquefaction-induced lateral spreading over a free surface. Traditionally, empirical approaches have used two-



dimensional plots to visually identify the boundary curve separating liquefaction and non-liquefaction (Boulanger and Idriss, 2014; Idriss and Boulanger, 2006; Moss et al., 2006). In this context, the techniques of ML can surpass these empirical studies by more objectively capturing the nonlinear and multidimensional relationship between critical inputs and soil liquefaction initiation. Significant studies in this area include implementations of SVM (Goh and Goh, 2007; Pal, 2006), ANN (Goh, 1994, 1996; Hanna et al., 2007; Juang and Chen, 1999; Ramakrishnan et al., 2008; Ülgen and Engin, 2007), a combination of kernel discriminant analysis with SVM (Hoang and Bui, 2018), a combination of ANN and RSM (Pirhadi et al., 2018), and RF (Kohestani and Ardakani, 2015). Another related issue of soil liquefaction is the liquefaction-induced lateral spread: predicting the magnitude of lateral displacement during soil liquefaction is a complex problem. A variety of influencing factors play a role in lateral spreading, including earthquake magnitude, distance between fault and site, and local soil profile information such as soil slope and the particle sizes of liquefiable sediments (Bartlett and Youd, 1995). Following Youd et al. (2002), who first used multilinear regression (MLR) to develop predictive equations, several ML models have been developed to improve the prediction of lateral displacement. These models use ANN (Baziar and Ghorbani, 2005; Chiru-Danzer et al., 2001; Wang and Rahman, 1999), a hybrid neuro-fuzzy method (García et al., 2008), SVR (Oommen and Baise, 2010), RF (Liu and Tesfamariam, 2012), and multilayer perceptrons (MLPs) with adaptive neuro-fuzzy inference systems (ANFIS) (Kaya, 2016).

#### **2.4.2. Machine learning in seismic vulnerability assessment**

In the field of seismic vulnerability, ML methods have proved promising in facilitating the development of fragility curves. Especially for articulated analytical methods, time and effort can be saved as fewer numerical simulations are required to cover the distribution ranges for a large number of uncertain parameters. In this regard, many works have made use of RSMs, including response surface with random block effects (Buratti et al., 2010), dual response surface (Perotti et al., 2013), and RSM with polynomial basis functions (De Felice and Giannini, 2010; De Grandis et al., 2009; Liel et al., 2009; Pan et al., 2007; Park and Towashiraporn, 2014; Rajeev and Tesfamariam, 2012; Ravi Kiran et al., 2019; Ricci et al., 2013; Saha et al., 2016; Seo et al., 2012; Seo and Linzell, 2010, 2012, 2013; Seo and Park, 2017; Verderame et al., 2014). Stepwise regression and other regularization algorithms also have been used in conjunction with RSMs to identify the most informative predictors. For example, Ebad Sichani et al. (2018) use a stepwise RSM to create probabilistic models to be used in seismic fragility analyses for dry concrete tanks that are prone to sliding, shaking, and swaying during seismic events. Xie and DesRoches (2019) tested regression models for probabilistic seismic demand analysis of California freeway bridges. In addition to RSMs, multi-predictor models have been developed using ANNs (Calabrese and Lai, 2013; Lagaros et al., 2009; Lagaros and Fragiadakis, 2007; Liu and Zhang, 2018; Mitropoulou and Papadrakakis, 2011; Pang et al., 2014; Wang et al., 2018; Ferrario et al., 2017), SVM (Ghosh et al., 2018; Huang et al., 2017; Mahmoudi and Chouinard,

2016), Bayes classifiers (Hariri-Ardebili and Pourkamali-Anaraki, 2018), and RF (Mangalathu and Jeon, 2019b).

Subsequently, Monte Carlo simulations can be used to develop multidimensional fragility functions. Such fragility models usually do not have an explicit mathematical expression and cannot be easily reproduced. To address this problem, researchers have used an alternative approach to compare demand to capacity and generate binary survival and failure samples from which additional models are trained (often using the LR model) to develop a parameterized fragility model. Relevant studies in this area have developed LR-based fragility models for: highway bridges (Dukes et al., 2018; Ghosh et al., 2013, 2014; Ghosh and Sood, 2016; Jeon et al., 2019; Kameshwar and Padgett, 2014, 2018; Mangalathu et al., 2018a, 2018b), single degree-of-freedom structures on liquefiable sand (Koutsourelakis, 2010), rigid blocks with safety features (Contento et al., 2017), and r.c. shear walls (Yazdi et al., 2016). In particular, fragility models based on LR are expressed through functions that explicitly quantify the influences of the earthquake and other significant structural parameters, enabling fragility analysis across multiple scales.

Other studies have worked specifically on the refinement of machine learning tools to produce rapid vulnerability assessments of existing buildings, also at territorial scales. Particularly, Ruggieri et al. (2021) proposed a machine learning based framework called VULMA (VULnerability analysis using MACHine-learning), which is supposed to foster vulnerability analysis of existing buildings with the aim to provide an indication of seismic vulnerability by using available photographs properly processed. In order to do so, images of buildings are collected, which are then labelled and stored. Machine learning models are then trained for image classification, and subsequently for assigning a vulnerability index to the buildings that are analyzed. Cardellicchio et al. (2021) also created *View VULMA*, a dataset specifically designed to support vulnerability analyses of existing buildings. *View VULMA* is meant to be used as a training set for a transfer-learning-based automated tool to rapidly assess the vulnerability of existing buildings based on individual images. Such automatic tools are becoming more and more popular in the research world, and they are opening new scenarios in the field of vulnerability assessment procedures and risk mitigation strategies.

#### **2.4.3. Machine learning in system identification and damage detection**

The field of system identification and damage detection consists of a variety of studies that address problems ranging from classifying failure from laboratory tests to detecting structural damage using satellite imagery. The topic area of system identification encompasses a broad branch of studies that develop ML-based models to emulate a structural system and predict its seismic response. The existing literature applies various ML methods to data sets from laboratory tests and numerical simulations to determine the seismic response of both structural components and structural systems. First, laboratory tests on reinforced concrete structures have provided a source of data that allow ML to determine failure modes, strength,

capacities, and constitutive behavior. In this regard, many studies have focused on the prediction of failure modes and shear strength for beam-column connections. For example, Mitra et al. (2011) use LR to categorize the non-ductile shear failure of connections versus ductile failure of beam-column connections internally. Mangalathu and Jeon (2018) apply a group of ML tools such as LR, K-nearest neighbors, Bayes classification, SVM, and RF for classification and regression to classify failure to predict shear strength. A similar group of ML tools is used by Mangalathu and Jeon (2019a) to predict the bending, bending-shear, and shear failure modes of bridge piers. Furthermore, image processing algorithms involving image segmentation, feature extraction, and nonlinear regression analysis are developed by Lattanzi et al. (2015) to estimate the peak drift of bridge piers using lateral load test data. Recently, a multi-output least squares support vector machine algorithm (MLS-SVMR) has been implemented by Luo and Paal (2018) to construct bilinear force-displacement constitutive relationships for r.c. columns. A similar study has been conducted by Luo and Paal (2019) to predict the drift capacity of r.c. columns using a locally weighted least square (SVR) approach. In addition, a group of six ML algorithms is used by Huang and Burton (2019) to classify the in-plane failure modes of r.c. frame structures with masonry infill, and 114 test results of infill frame specimens are examined. Apart from r.c. structures, Farfani et al. (2015) use the centrifuge test data of a soil-pile-structure system to train, test, and validate ANN and SVM models to predict the dynamic properties and earthquake behavior of the pile structure. Moreover, data sets from dynamic cyclic tests and shake table tests are used to develop ML models for an actively controlled frame (Bani-Hani et al., 1999a, 1999b), a full-scale nonlinear viscous damper (Yun et al., 2008), and a five-story structure (Zhang et al., 2008). Hybrid methods combining ANN with wavelet analysis and fuzzy logic have also been investigated to simulate the seismic behavior of building frames (Adeli and Jiang, 2006; Hung et al., 2003).

A second group of studies in the area of system identification deals with datasets from numerical simulations where the data inputs (structural parameters and ground motions) and outputs (structural responses) allow ML methods to create a relational map that replicates the structural behavior. To this end, ANNs have proven to be an effective substitute for finite element modeling of civil structures since they can approximate complex structures without being constrained by specific shapes. Starting from Conte et al. (1994), who use an ANN to learn and simulate the linear elastic behavior of multistory buildings, ANNs have been used in the identification of a variety of structures, including building frames (Joghataie and Farrokh, 2008; Xu et al., 2004), concrete gravity dams (Karimi et al., 2010), prestressed concrete bridges (Jeng and Mo, 2004), embankments (Tsompanakis et al., 2009), and column splices in steel frames of different heights (Akbas et al., 2011).

In the last decades, also the topic of damage detection has gained a lot of popularity, going so far as to include a group of studies that develop ML models to detect, classify, and evaluate seismic damage to structures. Firstly, several studies rely on post-earthquake linguistic or photographic records to predict seismic damage. A major challenge in this case is addressing damage information in linguistic forms. To this

end, De Stefano et al. (1999) use ANN and Bayesian classification to predict seismic damage mechanisms on churches. Fuzzy logic models have been used in a variety of studies that convert physical descriptions of seismic damage into mathematical model parameters (Allali et al., 2018; Alvanitopoulos et al., 2010; Carreño et al., 2010; Demartinos and Dritsos, 2006; Elwood and Corotis, 2015; Silva and Garcia, 2001). Recently, the linguistic damage datasets from the 2014 South Napa earthquake has been used to develop a building damage classification method (Mangalathu and Burton, 2019). Moreover, the damaged r.c. column images collected after the 2010 Haiti earthquake have been used by German et al. (2012) to develop a method that automatically detects spalled areas on the column surface and measures the characteristics of the spalls. This damage detection method has been integrated into a comprehensive framework that links column damage to the residual bearing capacity and fragility curves of r.c. structures after an earthquake (German et al., 2013; Paal et al., 2014). In addition, ML methods have been implemented to allow the detection and classification of building damage from satellite imagery and digital maps (Gong et al., 2016; Peyk-Herfeh and Shahbahrami, 2014). Gao and Mosalam (2018) also created an image database called "Structural ImageNet" on which ML is applied to detect building damage caused by earthquakes and other natural hazards. Much of the existing literature uses test data to detect seismic damage to buildings. In particular, ANNs are often trained with respect to the reference system in its undamaged state, while the response data from the damaged state of the same system is fed into the same model. As a result, the variation of the prediction error between the two states can serve as a reference to quantify the structural damage in a non-parametric way (Huang et al., 2003; Nakamura et al., 1998). Some other studies have improved this approach to allow parametric quantification of structural damage, e.g., damage quantified by changing stiffness values (Wu et al., 2002; Xu et al., 2005). In a broader context, ANN models have been developed to predict the seismic response for a variety of structures in order to draw conclusions about their damage states. Related studies in this area include the rapid determination of earthquake damage to ordinary wood-frame houses in Japan (Molas and Yamazaki, 1995), the assessment of earthquake susceptibility of industrial chemical plants with different topologies (Aoki et al., 2002), the prediction of the damage index of r.c. frames (De Lautour and Omenzetter, 2009; Morfidis and Kostinakis, 2017, 2018), the evaluation of earthquake damage to concrete shear walls (Vafaei et al., 2013) and cantilevered structures (Vafaei et al., 2014), and lastly global damage classification of r.c. slab-column frames by combining ANN with SVM (Kia and Sensoy, 2014). ML has also been used by Burton et al. (2017), by Zhang and Burton (2019), and by Zhang et al. (2018) to link building seismic damage patterns to residual bearing capacity indices (i.e., the capacity ratio between intact and damaged buildings). Their proposed framework integrates seismic demand analysis, building component damage simulation, and residual bearing capacity estimation for both intact and damaged buildings. Furthermore, Ferreira et al. (2017) discuss the use of artificial intelligence-based techniques for seismic damage estimation as a means of improving the accuracy of empirical methods. To this end, damage data collected after the 1998 earthquake in the Azores (Portugal) are used to perform a comparative analysis

between damage levels obtained with a classical damage formulation and an innovative approach based on ANNs. Harirchian et al. (2021) investigate earthquake susceptibility by combining six building performance variables that can be used for optimal prediction of damage state of reinforced concrete buildings using ANNs. For this purpose, a multilayer perceptron network is trained and optimized using a database of 484 damaged buildings from the Düzce earthquake in Turkey and two different databases of damaged buildings from the Nepal and Ecuador earthquakes. Hansapinyo et al. (2020) developed a new approach using an artificial intelligence system, called adaptive neuro-fuzzy inference system to predict building damage at urban scale considering input uncertainties. In Xu et al. (2022), an accurate real-time seismic damage prediction method based on machine learning algorithms and multiple intensity measures is proposed.

#### **2.4.4. Machine learning in structural control for seismic effect mitigation**

Previous studies have demonstrated the effectiveness of control devices in mitigating earthquake-induced structural vibrations (Housner et al., 1997). Essentially, structural control requires the identification and analysis of various components of the controlled system: this includes the assessment of actuator dynamics, of structure non-linearities, and of real-time measurements. Compared to conventional control methods that are programmed to perform a specific task, the inclusion of ML allows controllers to deal with nonlinear mappings, incorporate delays, and recover from partial system failure (Wen et al., 1995). These new methods can thus make structural control more effective in mitigating the adverse effects of earthquake hazards.

Numerous studies have investigated the usefulness of ANNs in developing active control systems to mitigate seismic effects on buildings. For example, studies have elaborated a neural controller (i.e., the actuator controlled by the neural network instead of an *ad hoc* control algorithm) which learns the transfer function between the signal of the actuator and the output of the sensors that measure the response of the structure (Bani-Hani et al., 1999a, 1999b; Bani-Hani and Ghaboussi, 1998; Ghaboussi and Joghataie, 1995). After the neural controller is well trained, it can generate appropriate signals for the actuator based on the feedback from the sensors. The concept of this neuro-controller has been further developed in several studies that improve the efficiency and robustness of the active control system (Brown and Yang, 2001; Khodabandolehlou et al., 2018; Rao and Datta, 2006; Subasri et al., 2014; Yakut and Alli, 2011). On the other hand, semiactive control devices can adapt to changing loading conditions during earthquakes similarly to fully active systems, but without requiring access to large energy sources. In this field, there has been a surge of interest in the use of ANNs. Contributions include ANN models to represent the nonlinear differential equations and simulate the dynamic behavior of dampers (Chang and Roschke, 1998), ANN models that predict the required stress at the desired force of dampers (Xia, 2003), as well as the use of ANNs to mimic the dynamics of the damper and induce the control of the seismic shaking of non-isolated and isolated structures (Bani-Hani and Sheban, 2006; Xu et al., 2003). In a study by Lee et al. (2006), a neuro-

controller is trained to minimize the cost function that includes both structural responses and control signals, and an algorithm is used to activate the damper and produce the desired control force. This work has then been modified to use modal coordinates as inputs to the neuro-controller, which facilitate controller design (Lee et al., 2008). In addition, a hybrid neuro-fuzzy control strategy for dampers has been proposed by Xu and Guo (2008): the algorithm tackles the time delay problem using an ANN and reduces the response time of the control currents by fuzzy control. The control efficiency and robustness of the implementation of neuro-controllers for dampers has been further verified by Bozorgvar and Zahrai (2019) by combining the fuzzy inference system with ANNs. In addition to dampers, ANNs have been used to model elastomer isolators (Fu et al., 2016) and to control the response of a structure isolated by a curved surface device (Krishnamoorthy et al., 2017).

The last sections explored the relevance of various ML techniques to earthquake engineering applications. It has been shown that ML techniques are able to learn and derive relationships between parameters, thus enabling to address various problems in earthquake engineering that are difficult or impossible to solve using traditional methods. As stated before, the blending of the two fields of ML and earthquake engineering is a new but increasingly dynamic area for high-impact research in which a wide range of topics can be explored. Despite the growing number of studies each year, the application of ML in earthquake engineering is still at an early stage compared to other disciplines. However, supported by the next generation of data exchange and sensor technologies, ML has great promise to revolutionize the earthquake engineering field.

## **2.5. Automatic retrieval of building features**

Even though direct surveys represent valid tools for a complete and accurate exposure analysis (as presented in section 2.1.3), the fact that these are often not sustainable in terms of economic resources and time limits has already been pointed out.

Therefore, some studies are trying to retrieve the same data that can be gathered through direct surveys with the help of new technological tools and artificial intelligence methods. The general concept is that these new methods are to some extent able to simulate expeditious surveys from the outside for individual buildings but also at very large scales, thus making it possible to overcome the limitations that those surveys often pose. Remote sensing and artificial intelligence techniques can indeed be used to extract building information from street or satellite imagery, in order to generate building inventories of cities and to provide the data needed for disaster and risk management planning and simulation.

In the following sections, particular attention is paid to tools that allow the remote inspection of urban areas, such as OpenStreetMap and Google Street View, as well as previous studies for the automatic retrieval of building characteristics from images with the help of machine learning techniques. The studies presented below do not necessarily refer to projects belonging to the field of earthquake engineering or risk

assessment; however, they all have in common the aim of evaluating the building exposure of an area, or at least specific features that contribute to the definition of exposure, which is in any case essential in the risk calculation process.

### 2.5.1. OpenStreetMap (OSM)

OpenStreetMap (OSM) is a collaborative project that has the aim to create a freely editable geographic database of the world. Thousands of members around the world work together to create an accurate, detailed, and up-to-date map characterized by continuous contribution: the OSM community collects data on roads, railroads, trails, waterways, bicycle routes, as well as on features along the roads, such as businesses, buildings (private and public), parks and natural areas, land use, cultural resources, and recreational facilities. There are more than 43 categories and hundreds of individual types of data. Users can collect data using manual surveys, GPS equipment, aerial photography and other free sources, or use their own local knowledge of the area. This crowdsourced data is then made available under the Open Database License. Once collected, the data is entered into the database by uploading it to the project's website along with the appropriate attribute data. Some contributors take on the task of mapping entire cities, while a large number of other users contribute with corrections and small additions to the map.

OpenStreetMap uses a topological data structure with four core elements (also known as data primitives). Firstly, *nodes* are points with a geographic location stored as coordinates (latitude and longitude) according to WGS 84. They are used to represent map features of no size, such as points of interest or mountain peaks. Secondly, *ways* are ordered lists of nodes that represent a polyline or a polygon if they form a closed loop. They are used to represent linear features such as roads and rivers, as well as areas such as forests, parks, parking lots, and lakes. Thirdly, *relationships* are ordered lists of nodes or paths. Examples include turn restrictions on roads, routes that span multiple existing paths, and areas with holes. Lastly, *tags* are key-value pairs which are used to store metadata about map objects (e.g., their type, name, and physical properties). Tags are not free-standing, but are always bound to an object, i.e., to a node, a way, or a relationship. A comprehensive ontology of map features is maintained on the wiki page [https://wiki.openstreetmap.org/wiki/Map\\_features](https://wiki.openstreetmap.org/wiki/Map_features), where all the meanings of tags can be found.

OpenStreetMap was developed in 2004 by Steve Coast in the United Kingdom: based on [https://www.openstreetmap.org/stats/data\\_stats.html](https://www.openstreetmap.org/stats/data_stats.html), OSM now counts more than 8.3 million registered users (dated January 10, 2022), 7.4 billion nodes (dated January 10, 2022), approximately 4 million map changes per day (year 2021) and 1.75 million different contributors (year 2021). Some examples of OSM map completeness are shown worldwide in Figure 2.12 and Figure 2.13.



Figure 2.12 - Towns, cities and villages mapped in OpenStreetMap (Moosavi, 2017)

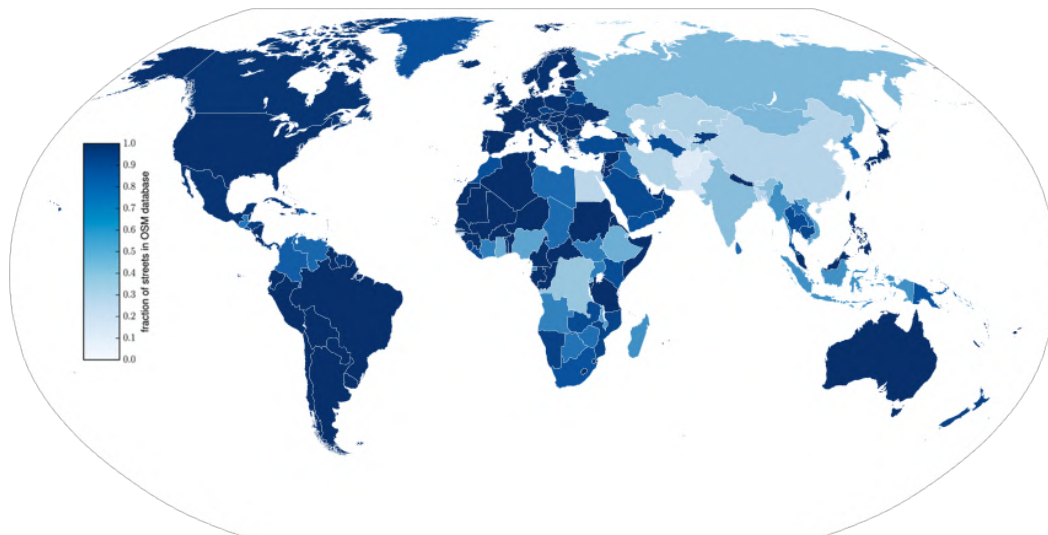


Figure 2.13 - Fraction of streets for each country in the OSM database (Barrington-Leigh and Millard-Ball, 2017)

OpenStreetMap has proved to be an extremely useful tool in many academic and research fields. Indeed, OSM has been taken into consideration by universities and other research institutions, particularly in the fields of geomatics, neogeography, volunteered geo-information (VGI), digital cartography, participatory geoinformatics, and many others. This interest is mainly due to the volume and variety of data offered by OSM products, that can lead to a wide range of their uses. As a matter of fact, many publications that leverage information retrieved and gathered through OSM services have been issued. Some examples of papers are presented here. For instance, Albert et al. (2017) analyze patterns in land use in urban neighborhoods using large-scale satellite imagery data available from OSM, Biljecki et al. (2017) show that it is possible to predict the height of buildings from 2D data from their footprints and attributes available in OpenStreetMap, while Castagno and Atkins (2018) propose a method to automatically label a building roof shape from publicly available OpenStreetMap data. Furthermore, Fleischmann et al. (2020) present the so-called



Morphological Tessellation (MT), a method that derives a spatial unit named Morphological Cell (MC) from available data on building footprints extracted from OpenStreetMap and tests its informational value to capture spatial properties of urban form, and this led Fleischmann (2019) to develop *momepy*, an open-source and expandable Python toolkit which enables a systematic in-depth analysis of urban form, including a wide range of measurable features. Hecht et al. (2015) compare different topographic databases, including OpenStreetMap, to automatically identify building types. Iannelli and Dell'Acqua (2017) propose a system for large-scale, systematic scanning of street-level pictures intended to map height in urban buildings, starting from footprints retrieved from OSM, while Kang et al. (2018) combine street view pictures with remote sensing and OpenStreetMap images to classify façade structures. Maragno et al. (2020) developed and tested a methodology for heat stress vulnerability and risk assessment at the neighborhood scale to support designers, planners, and decision makers in developing and implementing adaptation strategies and measures at the local level, combining high-resolution spatial information and crowdsourcing geospatial data derived from OSM to define sensitivity, vulnerability, exposure, and risk indicators. Moosavi (2017) takes advantage of the urban data collections contained in OpenStreetMap and the advancements in machine learning methods to automatically investigate the hierarchical structures of urban forms. Pittore and Wieland (2013) propose an approach based on different imaging technologies, including OpenStreetMap images, and a Bayesian integration scheme to characterize exposure and vulnerability models, to carry out seismic risk assessments. Raimbault and Perret (2019) propose a method to analyze urban configurations at a large scale, typically for districts generated as OpenStreetMap layout samples, with morphogenesis models, and they compare them to real configurations according to morphological indicators. In another paper, Rosser et al. (2019) demonstrate that in urban areas OpenStreetMap building footprints can have a high-level of completeness and geometric similarities to official map data, making them suitable to be used to infer the age of buildings. Schirmer and Axhausen (2016) give an overview of quantitative descriptions of urban morphology, basing their work on a data model that can be reproducible in any study area. Their model relies on objects representing the built environment in the form of built structures and the connecting street networks, which are available in OpenStreetMap. Wang et al. (2021) present a framework for regional scale building information generation and gathering to support regional risk analyses, by acquiring different types of data from multiple sources and fusing them to semantically profile each building in a city. In this framework, basic information of individual buildings, such as address, footprint, number of stories, construction year, structure type, and occupancy is collected from available sources that include crowd sourcing platforms, such as OpenStreetMap. Wieland et al. (2012) use freely available georeferenced street data from OpenStreetMap as a basis for estimating building inventories and carrying out rapid seismic vulnerability assessments, which can be applied to different urban environments and be efficiently scaled depending on the desired level of detail. In Zhang et al. (2018), a data-driven machine learning approach

is proposed to measure how people perceive a place in a large-scale urban region, based on the road network descriptions obtained from the OpenStreetMap.

Furthermore, OpenStreetMap-based projects are currently being developed all over the world. For example, the special business project “An Open-source System for Building-height Estimation using Street-view Images, Deep Learning, and Building Footprints” carried out by Ala’a Al-Habashna was released on December 8, 2020 and published by Statistics Canada. Within this project, an open-source system for automatically estimating building heights from OpenStreetMap using Deep Learning advanced image processing techniques and geospatial data was developed, with the aim of enriching the Open Database of Buildings (ODB) published by Statistics Canada as part of the Linkable Open Data Environment (LODE). Another example is represented by the European project BELICE (Building Experience to Lead Initial Assessment in Challenging Emergency), started in 2018. This project uses OSM data when census ones are missing, in order to sectorize different areas that need to be studied and examined for the purposes of emergency management in case of earthquakes.

The fact that so many studies have used OSM maps is explained by its competitiveness both in terms of data completeness and update status. This can be verified through different metrics like the amount of road distance mapped, or the number of objects (points of interest, buildings, etc.) detected. The fact that these maps are globally crowd-sourced ensures continuous improvements and updates, and reflects things like neighborhood development, ongoing constructions, or even the results of recent natural disasters.

### **2.5.2. Google Street View (GSV)**

Google Street View is a feature of Google Maps and Google Earth that provides 360° horizontal and 160° vertical panoramic views along streets. The pictures are captured each 10-20 meters, and they allow users to see parts of cities around the world at ground level. It was launched in 2007 in several cities in the United States and has since then expanded worldwide. The list of currently supported cities for Street View is available at <https://www.google.com/streetview/explore/>. Even though other possible services that offer street view pictures are available, such as for example Mapillary and OpenStreetCam, Google Street View remains the most widespread tool, especially in terms of coverage. As a matter of fact, in May 2017 Google announced that it had captured more than 16 million kilometers of street view imagery in 83 countries all over the world (Figure 2.14). As far as Italy is concerned, this service has been available since October 29, 2008, when the cities of Rome, Milan, Florence, Como and the lake of Como were included. Since March 18, 2009, Street View has been available in Irpinia, the central part of Lazio, the western part of Lombardia, and the coastal part of Campania, including Naples, the Amalfi Coast, Salerno and the Irno Valley, as well as the cities of Avellino, Benevento (historic center only), Turin, Genova, Udine, Parma, Bologna, Livorno, Arezzo, Perugia, L'Aquila, Bari, Brindisi, Lecce, Gallipoli, Reggio Calabria, Catania, and Cagliari. Since January 21, 2010, the

Italian coverage of Street View has expanded exponentially: almost all the regions of Southern Italy (Sicilia, Sardinia, Calabria, Basilicata, Apulia, Campania, Abruzzo, and Molise) are available, as well as many areas of Friuli-Venezia Giulia and Veneto, in particular roads and motorways, part of the towns of Jesolo and Verona and the Venetian towns of Mestre and Marghera, and the state roads of the Marche Region. Since July 1, 2011, coverage has also extended to the province of Viterbo in the northern part of Lazio. Since November 14, 2013, the city of Venice, including the islands, has been completely covered. Since 2015, the coverage of Italy is total and also includes some closed places such as museums and commercial activities.

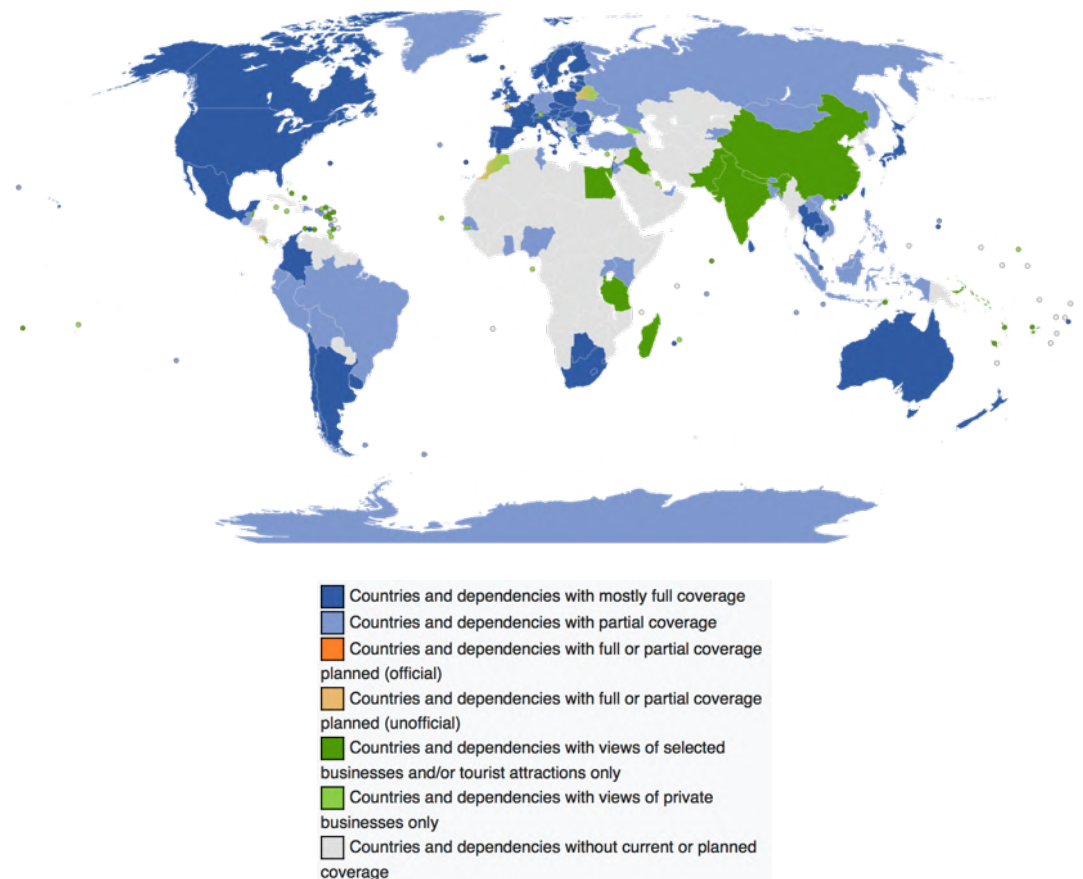


Figure 2.14 - Google Street View worldwide coverage  
([https://en.wikipedia.org/wiki/Coverage\\_of\\_Google\\_Street\\_View](https://en.wikipedia.org/wiki/Coverage_of_Google_Street_View))

Street-view images have already been used for data extraction in multiple applications. In Smith et al. (2013), machine learning and computer vision techniques are used to extract information about the presence and quality of sidewalks in cities. Geometric context and presence of lanes are implemented within a random forest classifier to identify sidewalk segments from Google Street View images, in order to support urban planners in creating pedestrian-friendly and sustainable cities. Many studies have then exploited Google Street View images to gather information about building heights (Mou and Zhu, 2018; Díaz et al., 2016; Yuan and Cheriyyadat, 2016; Zhao et al., 2019; Iannelli and Dell'Acqua, 2017). Cai et al. (2018) perform the quantification of street-level urban greenery by collecting 500 street images from Google Street View and

other 500 images of cityscapes from vehicle-mounted cameras. Other work has used a considerable amount of Google Street View images to identify urban elements (Zhang et al., 2018) or to classify images of building façades into different utility classes (Laupheimer and Haala, 2018). Yan and Huang (2022) derive information on building height from openly available Google Street View images by using single view metrology. This method takes advantage of deep neural networks to extract a set of features – such as vanishing points, line segments, and semantic segmentation maps – and then estimates the height from single street view images, allowing large-scale estimations of building height, especially in areas in which conventional remote sensing data are difficult to obtain. Many other studies that leverage Google Street View pictures are also presented in the following sections

### **2.5.3. Building detection, class and typology**

Automatic extraction of building characteristics from remote sensing data is an attractive research topic useful for various applications such as risk assessment and urban planning. One of the main goal of the research that can be found in this field is the automatic classification of buildings from their images (satellite images or street view pictures), in order to label buildings at the individual scale or more often at a territorial scale.

In this framework, Kang et al. (2018) propose a method to elaborate land-use classification maps based on the functionality of individual buildings. The method is based on Convolutional Neural Networks (CNNs) that classify façade structures from street views in addition to remote sensing images that show roof structures. Maltezos et al. (2017) use a similar approach for building data extraction, yet considering orthoimages. Moreover, Wen et al. (2019) propose an improved Mask Region Convolutional Neural Network (Mask R-CNN) method that can detect bounding boxes of buildings and delineate them from complex backgrounds. Laupheimer and Haala (2018) have developed an approach for classifying images of building façades into different use classes using CNNs to provide semantic information for 3D city models in an automated way, while Llamas et al. (2017) apply CNNs to the classification of architectural heritage images. In addition, supervised machine learning-based methods are employed to identify buildings from high-resolution remote sensing images (Guo et al., 2016; Bezak, 2016). Hecht et al. (2015) propose a data-driven approach to automatically classify building footprints using pattern recognition and machine learning techniques, while Castagno and Atkins (2018) propose a method to automatically label roof shapes of buildings from publicly available data from GIS, using satellite imagery and airborne LiDAR data to train and test CNNs. Also Hermosilla et al. (2011) use high spatial resolution images and LiDAR data, in this case to automatically detect and localize buildings. Dubois et al. (2016) focus on the detection and extraction of building overlays in interferometric synthetic-aperture radar (InSAR) images. In particular, geometric shapes are analyzed to determine geometric parameters such as length, width and height. Fabris et al. (2013) use aerophotogrammetry (i.e., photographs taken from aircraft for land surveying) to

detect building roofs and therefore to retrieve information for estimating their structural characteristics, such as wall thicknesses and other geometric features. Taffarel et al. (2016) and Campostrini et al. (2018) have worked on large-scale a priori estimation of building parameters that cannot be measured directly from the outside of the buildings by elaborating values that can be measured from the outside. By using a Bayesian approach, the original hypotheses can be updated based on new data collected during the field surveys.

#### **2.5.4. Building height**

Another important feature that past and ongoing studies have been trying to retrieve automatically is building height, in terms of number of stories or meters. Elevation data are indeed an essential but often unavailable component for creating 3D city models that may allow city reconstruction, urban planning, navigation, and emergency management.

There have been studies that have used image processing techniques in order to retrieve height information: for example, Yuan and Cheriadat (2016) propose a method that integrates two widely available data sources, building footprints from 2D maps and street imagery, to derive building heights and façade masks. Also Biljecki et al. (2017) manage to create 3D city models from 2D data with machine learning techniques (random forests). Díaz and Arguello (2016) estimate the average height of buildings from Google Street-View pictures using the single view measurement technique (Criminisi et al., 2000). Fully automated 3D building reconstruction from spaceborne point cloud data is explored by Partovi et al. (2014), in order to achieve high quality Digital Surface Models (DSM). Similarly, Misra et al. (2018) investigate the feasibility of using open DSMs, such as the AW3D30, ASTER, and SRTM datasets, for digital building height model extraction. Furthermore, Iannelli and Dell'Acqua (2017) use Deep Learning algorithms to develop a system for large-scale, systematic scanning of street-level images to detect the number of floors in urban buildings. Zhao et al. (2019) propose CBHE (Corner-based Building Height Estimation), a building height estimation algorithm that considers both building corners and roof lines from 2D maps and street view images. Also the detection of windows can be crucial for the computation of the number of floors: as a matter of fact, the detection of the rows of doors or windows can lead to a good estimate of the building height. In this context, Neuhausen et al. (2018) propose a system for detecting windows in façade images, which consists in a sliding detector that employs a cascade classifier to detect windows in image patches.

Another way to retrieve information about the number of stories of a building is considering its shadow, which can be seen in satellite images. The shadows cast by buildings in urban scenes can be processed and used to estimate building heights. Several papers have used this technique: among others, Liasis and Stavrou (2016) use the spectral and spatial features of the satellite image to develop a filter to detect the shadows, whose length is then used to approximate the building height. Also Abdelrahim et al. (2017) use shadow detection along with geo-referenced information

to estimate the structural dimension of man-made infrastructure, as well as Kadhim and Mourshed (2019), who automatically estimate building heights from their shadows in very high resolution (VHR) multispectral images. Furthermore, Arevalo et al. (2006) and Saadi and Bensaibi (2014) developed an automatic building height detection technique based on the analysis of building shadows from Quick Bird imagery (high-resolution commercial Earth observation satellite). Other studies that use shadow detection in satellite images to estimate building heights can be found in Comber et al. (2012), Raju et al. (2014), and Zhou et al. (2019).

### **2.5.5. Building material**

The recognition of semantic information such as building materials is also fundamental, particularly for the monitoring of construction progress, for building information modeling, and for the evaluation of vulnerability. Recent studies have investigated the possibility of detecting building materials from images. Specifically, Dimitrov and Golpavar-Fard (2014) propose an image processing-based method for material classification from single images, where material is classified using SVM. In addition, Rashidi et al. (2015) have conducted a comparative study to evaluate the performance of different machine learning methods (Multilayer Perceptron, Radial Basis Function, and SVM) for recognizing common categories of building materials.

### **2.5.6. Building age**

The age of a building affects its shape and the composition of its building fabric, and this is crucial for drawing conclusions about its vulnerability and efficiency. Furthermore, determining the service life of a structure is a critical step for the evaluation of the possible measures that might be necessary for its maintenance. However, often these data are unknown. Therefore, past work has developed methods to recognize the age of buildings from satellite images and street view photos.

For example, Rosser et al. (2019) present a method for automatically determining the building age of residential buildings, by extracting measures of neighborhood morphology and features from readily available topographic maps, a high-resolution digital surface model, and statistical boundary data. These measures are then used as features in a random forest classifier to derive an age category for each building. The use of random forests has also been coupled with airborne Light Detection and Ranging (LiDAR) data to predict building age (Tooke et al., 2014). The study proposed by Zeppelzauer et al. (2018) has even proved that the analysis of visual patterns at the patch level in building photographs can potentially outperform human evaluators in age estimation. Other studies have also shown that the large amount of building images accessible online via Google Street View and the rapid development of image processing techniques has made it possible to extract information from images to enrich building databases. Particularly, Li et al. (2018) propose a method for building age estimation based on CNNs to extract image features and SVM to regress building year. Moreover, obsolescence assessment to predict the age of a

building is presented by Mahajan et al. (2019) using machine learning, thus reducing manual calculation and increasing the accuracy of predictions.

### **2.5.7. Urban fabric**

Urban planning and morphology have relied for centuries on analytical cartography and visual communication tools to illustrate spatial patterns, conceptualize design proposals and compare alternatives. Besides, all the operations needed to manually extract features are very tedious and time-consuming.

Nowadays, the rapid growth of remote sensing and Big Data storage capacities, combined with the ever-increasing computational power of modern machines, has enabled an evident increase in the use of ML algorithms in the field of urban studies. New spatial technology platforms indeed offer new perspectives for understanding, assessing, monitoring, and managing urban forms and developments. Moreover, the integration with new communication and information technologies (smartphones, GIS, drones, IoT, sensors, etc.) has helped to raise the level of knowledge of urban patterns and to address the challenges of modern cities in various domains (health, safety, mobility, etc.). ML Algorithms have been proposed to model urban indicators, proving to be more powerful than traditional methods and opening up new possibilities for the automatic study of urban forms on a global scale.

As an example, urban Morphometrics (UMM) is an expanding field of urban studies that aims to represent and measure the physical form of cities to support evidence-based research. Particularly, studies have shown that it is possible to capture the spatial properties of urban form at the plot level by exploring urban structural patterns and spatial order (Fleischmann et al., 2020; Boeing, 2021; Schirmer and Axhausen, 2015; Jumlesha et al., 2012), also with a focus on residential areas (Hecht et al., 2013).

Also Deep Learning is leveraged to detect and analyze features in urban patterns. Specifically, Yao et al. (2017) use a Convolutional Neural Network (CNN) to recognize land use patterns in cities by applying a transfer learning-based approach to remote sensing images to extract and classify features. Also Albert et al. (2017) analyze land use patterns in urban neighborhoods using large-scale satellite imagery data and computer vision techniques based on deep convolutional neural networks. Moosavi (2017) gathers a large dataset of street networks in more than one million cities and villages around the world to train a deep convolutional autoencoder that automatically learns the hierarchical structures of urban shapes. The potential of machine learning algorithms in the context of object-based image analysis has also been explored to optimize their use for urban pattern recognition tasks (Wieland and Pittore, 2014; Wieland et al., 2016).

## **2.6. Research gaps**

Each section of this chapter has described the state of the art of the different aspect that concur to the definition and the evaluation of seismic risk, particularly seismic vulnerability and exposure. Furthermore, specific attention has been paid to the use of

machine learning approaches in the fields of earthquake engineering and feature recognition.

For what concerns seismic vulnerability, the research in Italy is moving towards the definition of fragility models that are able describe different building typologies and represent vulnerability at a national scale. The reason why this is considered of paramount importance is the need to have a better understanding of the vulnerability of our built stock, as well as to address national mitigation policies. This thesis is in line with this trend and aims to create a national fragility model for both as built and retrofitted masonry building typologies.

Also the quantification and evaluation of exposure for risk assessments is one of the main topics that research is covering in these years. In this chapter, it has been shown that other studies have already tried to implement machine learning procedures to automatically detect buildings at territorial scales and to recognize specific building characteristics, in order to overcome the economic and time challenges that conventional surveys pose. The benefit that artificial intelligence can bring into this field is evidenced by the surge of works dealing with these issues in recent years. However, there is still the lack of a framework that can remotely and automatically evaluate exposure and associate buildings with their appropriate vulnerability, since many studies usually focus on individual features that are not adequate or sufficient for the definition of seismic vulnerability. Therefore, this project has the goal of developing an algorithm for the automatic identification of buildings and building features, with the help of neural networks.

Lastly, all the information produced and gathered about seismic vulnerability and exposure must find a suitable collocation in a platform that performs risk calculations at large scales, which is indeed the final aim of this thesis. The platform needs to be designed so that it can take as input data the results of vulnerability and exposure deriving from the previous steps. For this purpose, a modular platform is here developed.

The following chapters will describe in detail the novel contributions of this work.



### 3 FRAGILITY CURVES FOR ITALIAN RESIDENTIAL MASONRY BUILDINGS

Seismic risk assessments require a deep knowledge about the components of this risk, starting from the evaluation of vulnerability of the built heritage. Here, a mechanics-based seismic fragility model for Italian residential masonry buildings has been developed. This model is based on the classification of the building stock in macro-typologies, defined by age of construction and number of stories, and it allows the simulation of damage scenarios and risk analyses at a territorial scale. The model is developed on the fragility of over 500 buildings, analyzed through the *Vulnus\_4.0* software. The fragility functions are then extended on the basis of a reference model available in the literature, which provides fragilities on five damage states. Lastly, seismic retrofit interventions are simulated, in order to build mitigated fragility models. The results thus obtained allow the evaluation of the possible improvement in terms of seismic behavior brought by different retrofit interventions.

The work presented in this chapter has been developed under the ReLUIIS 2018 and ReLUIIS 2019-2021 frameworks, and some results have already been published in journal and conference papers (Donà et al., 2019; Donà et al., 2020; Donà et al., 2021; Follador et al., 2021; Carpanese et al., 2021; Carpanese et al., 2022; da Porto et al., 2022; Carpanese et al., 2022).

#### 3.1. Method of derivation of fragility curves

The research group of the University of Padova has been active for years on the themes of seismic vulnerability assessment of the built heritage, with special focus on vulnerability and fragility assessment of unreinforced masonry (URM) buildings in historical centers (Bernardini, 2000; Munari, 2009), comparison of methods for vulnerability assessment (Valluzzi et al., 2007), analysis and interventions on clustered buildings (da Porto et al., 2013), development of methods based on Bayesian inference for territorial analyses (Taffarel, 2016), and emergency management and structural interventions (Modena et al., 2010), among others. One of the outcomes of this research activity has been the development of a calculation tool, called *Vulnus* (Bernardini et al., 1990, Bernardini et al., 2008), initially used for the seismic safety checks of URM buildings by means of linear kinematic analyses, which subsequently evolved into a seismic vulnerability assessment tool, introducing also the fuzzy set theory (Bernardini and Tonon, 2004), and then updated to the latest version *Vulnus\_4.0* (Valluzzi et al., 2009).

For load-bearing URM buildings, *Vulnus\_4.0* processes information on building geometry (in plan and elevation), material properties, types of resistant system, floors and roof and their features, lack or presence of wall-to-wall connections and their effectiveness, and also other qualitative information. Based on this information, *Vulnus\_4.0* first calculates the horizontal accelerations ( $a$ ) that activate the main in-plane (IP) and out-of-plane (OOP) mechanisms, respectively through resistance

checks and linear kinematic analyses; then, on the basis of these values, it derives the IP and OOP critical triggering accelerations that, normalized to gravity acceleration  $g$  ( $a/g$ ), define the resistance indexes  $I_1$  and  $I_2$  respectively.

Specifically,  $I_1$  represents the shear resistance of the building in its weakest direction, normalized to its total weight, and is obtained by assessing the total shear resistance offered by wall systems in that direction. Parallel walls in each direction are analyzed as rigidly coupled. In the case of irregular buildings, the effects of the uneven distribution of stresses on the shear strength are taken into account by applying appropriate corrective factors to  $I_1$  (Valluzzi et al., 2009).

$I_2$  is a parameter that depends on the possible out-of-plane mechanisms associated with the vertical and horizontal masonry portions of each wall (taken one meter wide). The mechanisms assessed for vertical strips, whose triggering accelerations define  $I_2'$ , are: overall overturning of walls and overturning and flexural failure of the top story. Those for the horizontal strips, who define  $I_2''$ , are: flexural and arching mechanism failure at the top story, overturning and flexural collapse of the arch shoulders at the top story and detachment of the transverse walls still at the top story. For each wall, *Vulnus\_4.0* calculates the sum of  $I_2'$  and  $I_2''$ , whose minimum value defines  $I_2$  (Valluzzi et al., 2009).

Subsequently, *Vulnus\_4.0* computes and returns another index,  $I_3$ , which takes into account other relevant vulnerability information, although qualitative, relating to the types of resistant system, floors, roof and foundations, the configuration and regularity in elevation of the building, the state of preservation, the presence of structural interventions and, furthermore, the quality of the information. Specifically,  $I_3$  is based on the vulnerability parameters identified by the Second Level GNDT form (Ferrini et al., 2003; see section 2.1.2.2. for further details on this form) and is calculated as a weighted average of the scores assigned to these parameters with expert judgment (Valluzzi et al., 2009).  $I_3$  ranges from 0 to 1, with 0 indicating a building design that fulfills anti-seismic criteria.

Based on the  $I_1$ ,  $I_2$ , and  $I_3$  indices and the Fuzzy set theory, *Vulnus\_4.0* finally provides estimates of expected seismic damage, in the form of fragility curves for incremental values of Peak Ground Acceleration (PGA). The Fuzzy theory is used to convert  $I_1$ ,  $I_2$ , and  $I_3$  into fuzzy subsets, thus allowing the statistical evaluation of the influence of parameters that cannot be quantified exactly (such as those summarized by  $I_3$ ), and the uncertainties on the quantifiable parameters not carefully measured (i.e., associated with a poor information quality) or characterized by high variability (such as the material properties). Further information can be found in Valluzzi et al. (2009) and Munari (2009).

In particular, *Vulnus\_4.0* computes three cumulative probability distributions (fragility curves) associated with the triggering of IP and/or OOP mechanisms. One of these curves, referred to as White, represents the average building vulnerability, whereas the other two, referred to as Lower- and Upper-Bound, define a range of vulnerability due to the various sources of uncertainty and therefore to the quality of information.

These fragility curves, considering the definition of the  $I_1$  and  $I_2$  indexes, and the damage associated to the corresponding mechanisms, were associated with an

intermediate DS between the “moderate” and “severe” ones of the EMS98 scale, which defines the following DSs: slight damage DS1, moderate damage DS2, severe damage DS3, partial collapse DS4 and complete collapse DS5 (Munari, 2009). An equivalence of Vulnus fragility curves with a DS2-3 is a reasonable assumption considering that the triggering acceleration of a certain out-of-plane mechanism, assessed by linear analysis, is a necessary condition for the mechanism activation and the onset of damage (DS2), whereas the definition of the shear resistance of the building in its weakest direction, taking into account the overall shear capacity of all of the walls in that direction, can be very close to the maximum system capacity (DS3), although none of these two mechanisms are yet a sufficient condition to turn the out-of-plane or in-plane mechanism into a partial or total collapse (DS4-5).

## **3.2. Macro-typologies and sampling of Italian masonry buildings**

### **3.2.1. Definition of building macro-typologies and representativeness criteria**

As already mentioned, territorial-level vulnerability assessments carried out on a mechanical basis require a substantial effort to collect the numerous data necessary for calibrating the various structural models and methods of analysis. Therefore, considering the relatively low number of buildings that can be reasonably analyzed, in order to obtain vulnerability results as much representative as possible, it is first necessary to define appropriate building macro-typologies and subsequently perform a representative sampling of the built heritage for each typological class, with the ultimate goal of deriving typological fragility curves representing the average vulnerability of the various classes.

The criteria for defining macro-typologies should obviously be based on those factors that most influence the vulnerability; however, the parameters required to define these criteria should decrease as much as the extent of the analysis increases at a territorial level. On the contrary, the limits in acquiring knowledge of so much information on a large territorial scale would impair the possibility of effectively using the developed typological fragility curves for the sought vulnerability assessment purposes.

To date, the main information on the building stock available for rapid vulnerability estimates, collected by ISTAT throughout the national territory during census, and returned up to the level of the single municipality, regards the type of material (reinforced concrete, masonry or “other”), the age of construction and the number of stories. Although such information may seem limited, careful use allows to rationally address the problem of seismic vulnerability estimates on a national scale, albeit in a simplified way. Indeed, the main geometric factors (such as arrangement of resistant systems, presence of structural irregularities and contiguous buildings), typological-constructive factors (i.e., types of lateral resistant systems, foundations, floors and roofs), as well as the main material properties (weight and resistance) and construction details, are strongly correlated with the construction age, although they may show some variability. Clearly, this is due to the evolution of scientific and technological

knowledge, manufacturing and construction techniques, materials, as well as the drafting and updating of construction standards. In addition, the number of stories in the building is another significant information, as it is associated with the dynamic behavior and seismic demand of the building.

Therefore, based on the main information provided by ISTAT and expert judgment, a macro-typology classification was proposed (Table 3.1) for URM buildings of the Italian built heritage, based on construction age and building height. In particular, the adopted ranges of construction ages are a compromise between the years in which a new census, with updated data, was carried out (i.e., 1919, 1945, 1961, 1971, 1981, 1991, 2001, 2011), and the periods in which important changes in construction methods, due to technological developments and the delivery of construction standards, can be identified. This is a simplified classification, consistent with the relevant significant uncertainties; however, the resulting ages are coherent with those defined in AeDES form (Baggio et al., 2007; section 2.1.2.2).

Table 3.1 - Macro-typologies of Italian residential URM buildings and number of sampled buildings

<b>Construction age</b>	<i>Pre-1919</i>	<i>1919-1945</i>	<i>1946-1960</i>	<i>1961-1980</i>	<i>Post-1980</i>
<b>No. stories (<i>n</i>)</b>	$\leq 2$	$\leq 2$	$\leq 2$	$\leq 2$	$\leq 2$
	$\geq 3$	$\geq 3$	$\geq 3$	$\geq 3$	$\geq 3$
No. sampled buildings	205	80	80	80	80

As regards the sampling of buildings for the various macro-typologies, i.e., the case studies to derive the typological fragility curves, the following criteria were considered.

- Representativeness with respect to the variability of the building heritage with the geographical position. Indeed, in the same historical period, and especially for the most ancient and less industrialized ages, a great variety of construction techniques can be found in Italy, depending on the geographical areas (not necessarily corresponding to administrative boundaries). Differences and peculiarities are noticeable up to the municipal level; the reasons are historical, related to the complex morphology and climatic variability of the country, the presence of local building materials and other reasons of opportunity. The knowledge of this rich building diversity and of its significance on a territorial scale is essential for its appropriate inclusion in vulnerability assessment.
- Representativeness with respect to the typological variability of the buildings, in terms of number of stories and global dimension (single houses, terraced houses, small or medium-sized apartment buildings, etc.), for each construction age.

The first criterion, i.e., geographical representativeness, was taken into account through a nationwide diffused sampling, carefully selecting representative buildings belonging to 65 municipalities and nine regions, located in Southern, Central and Northern Italy. As can be seen from Table 3.1, 525 buildings were sampled in total,

with 80 case studies for each construction age, except for the Pre-1919 period, where the buildings are over 200. In this period, indeed, the local variability of construction practices was definitely higher than in later periods, due to the absence of any industrialized construction process, material and method, and to the absence of relevant construction manuals or standards, which started spreading in Italy during the first decades of the XX Century. In addition, according to ISTAT, Pre-1919 macro-typology holds the largest share of residential masonry buildings, which corresponds to 30% of the total.

Future studies on the geographical characterization of the Italian residential heritage will surely be useful both to improve the representativeness of the current sample and to define further typological classes of buildings based on their location, for more precise vulnerability estimates. This type of studies, which relies on the survey of the main typological-constructive characteristics of the built heritage at the municipal level, are currently underway through the CARTIS project by some research groups of Italian universities, in coordination with the DPC and ReLUIIS (Cacace et al., 2018). As regards the second criterion, i.e. typological representativeness, the sampling was aimed at satisfying as much as possible the statistical distributions of buildings obtained by processing ISTAT data: distribution by number of stories, within the same macro-typology; distribution by number of housing units, within buildings having the same number of stories. In the second case, ISTAT database did not allow to process the information on construction ages and material types together; therefore, this distribution represents the variability of the total built heritage. Nevertheless, in the absence of other information, it was assumed to be enough representative to calibrate our database. Figure 3.1 and Figure 3.2 show the comparison between these ISTAT statistical distributions and the database of sampled buildings.

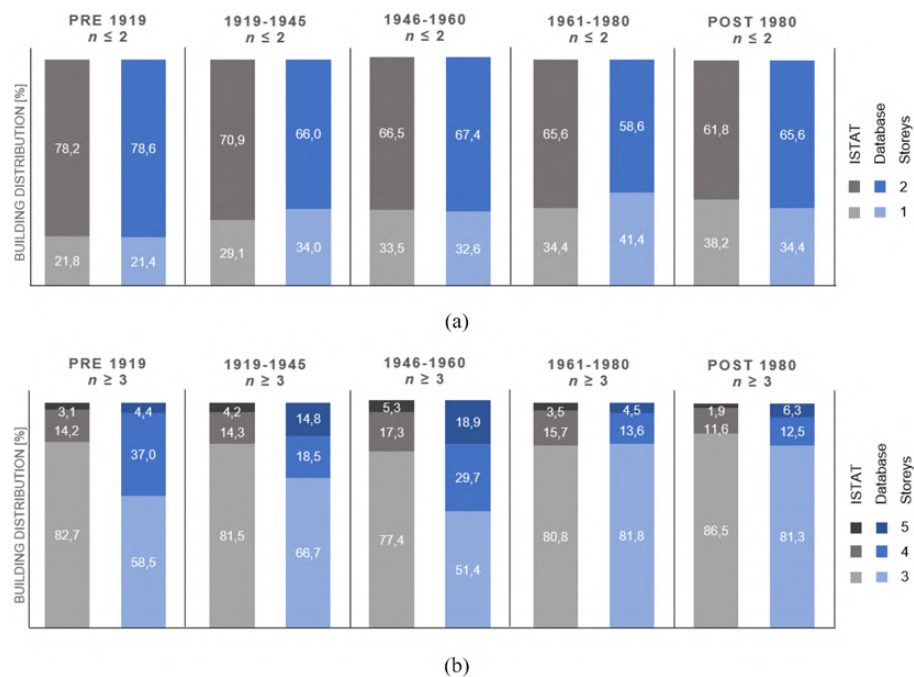


Figure 3.1 - Distribution of buildings by number of stories (n), within each macro-typology, according to ISTAT data and the database of sampled buildings. (a)  $n \leq 2$ ; (b)  $n \geq 3$

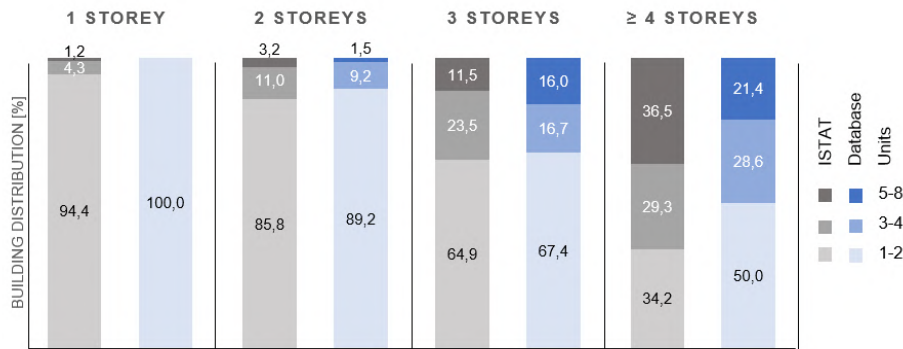


Figure 3.2 - Distribution of buildings by number of housing units, per number of stories, according to ISTAT data and the database of sampled buildings

### 3.2.2. Sampling of buildings assumed as case studies

It is understandable that a detailed sampling of geometric, constructive and material information for over 500 buildings (to calibrate the various models in *Vulnus\_4.0*) would be too expensive for the purpose of this project, if exclusively based on direct surveys. So, to create the database of case studies, various sources of information were used and integrated in order to obtain information as complete as possible in a sustainable and cost-effective way. One of the main sources of building case-studies, which contributed to about 50% of the database, consists in surveys directly carried out by the research group of the University of Padova in recent years, in the aftermath of seismic events, for preliminary assessment of buildings and centers, or for other research purposes. The integration of various information sources made it possible to obtain more robust global information, in relation to the many uncertainties implied in this study and to the possibility of using only the very specific data collected for certain case studies.

In particular, for the different construction periods, the main technical architecture manuals (e.g., Cantalupi, 1862; Curioni, 1868; Donghi, 1905; Arosio, 1941; Ormea, 1951; Carbonara, 1954; Guenzi, 1981; Di Sivo, 1981) and Italian construction standards (e.g., Italian Royal Decree RD 193/1909; RD 2089/1924; RD 640/1935; Italian Government, 1962; Italian Ministry of Infrastructures DM 1986; DM 1987; DM 1996) were examined in order to identify the most recurring typological-constructive characteristics, as well as the typical properties of building materials for each period. In addition, useful information was obtained from the results of the TABULA project (Corrado et al., 2014; see section 2.1.3), which summarizes at national level the main material and constructive information by age and type of building (i.e., single houses, multi-family houses, terraced houses and apartment buildings) and from the “Circolare no. 617” (Italian Ministry of Infrastructures and Transports, 2019), which provides (in Table C8A.2.1) indications about material properties.

This was essential to create a strong basis for performing the most representative sampling possible (relying on representative documents and expert judgments) and to integrate the missing information for the case studies through the reference information identified for each construction age. Table 3.2 summarizes the reference

information of each construction typology, in the form used for implementation in *Vulnus\_4.0*. Type and properties of materials, type of floors, effectiveness of wall-floor connections (represented in a simplified manner through a friction coefficient) and presence of tie-beams are some of the main data.

Table 3.2 - Summary of reference information for each construction age

	<i>Pre-1919</i>		<i>1919-1945</i>	
<i>Material</i>	Stones	Solid bricks	Solid bricks	Solid bricks
Compressive strength [MPa]	2,6	4,0	4,0	4,0
Tensile strength [MPa]	0,085	0,14	0,14	0,14
Specific density [kg/m <sup>3</sup> ]	2100	1800	1800	1800
<i>Floor type</i>	Wood	Wood	Wood Precast RC	Hourdis hollow-tile
Friction coefficient [-]	0,3	0,3	0,3	0,3
Ring-beams	No	No	No	No
<i>Typical building typologies</i>	All	All	Single house	Terraced house Apartment building
	<i>1946-1960</i>		<i>1961-1980</i>	<i>Post-1980</i>
<i>Material</i>	Solid bricks	Hollow bricks	Hollow bricks	Hollow bricks
Compressive strength [MPa]	4,0	3,7	3,7	3,0
Tensile strength [MPa]	0,14	0,27	0,3	0,33
Specific density [kg/m <sup>3</sup> ]	1800	1500	1500	1200
<i>Floor type</i>	r.c. and hollow-tile	r.c. and hollow-tile	r.c. and hollow-tile	r.c. and hollow-tile
Friction coefficient [-]	0,6	0,6	0,6	0,6
Ring-beams	Every floor	Every floor	Every floor	Every floor
<i>Typical building typologies</i>	Single house Public housing	Terraced house Apartment building	All	All

Whereas for the construction age Pre-1919 the main source of geometrical schemes for representative buildings was constituted by direct surveys and design project for structural interventions, due to the very high local variability of construction practices (as above-mentioned), for the following ages it was possible to resort to a broader series of sources.

For the period 1919-1945, many designs (with geometric, typological-constructive and material information) were organized in some project collection books (in Italian), such as "*Villas - 68 Examples of villas and country houses*" (Moretti, 1946), "*Dwelling houses in Italy*" (Moretti, 1947) and others.

In the following period, 1946-1960, public housing projects became very popular, therefore much information was selected from the projects related to the State intervention plan "*INA-Casa*", aimed at increasing the post-war workers' occupation, collected in the "*Ridolfi Fund*" (collection of documents about the professional activity

of the Architect M. Ridolfi, from 1923 to 1984, preserved at the National Academy of Saint Luca, in Rome; some of these documents are also available online, at [www.fondoridolfi.org](http://www.fondoridolfi.org)). Still for the period 1946-1960, as well as for the following one, 1961-1980, many private residential building projects were collected from the digital archive of the technical offices of some Italian municipalities.

For the last construction age, Post-1980, many case studies were defined based on the significant information available on the websites of the leading Real Estate Agencies. Then, to complete the sample and meet the representativeness criteria, some projects were specifically searched, based on the age and type of building, and identified thanks to the valuable support of some engineering companies and design firms. Lastly, other useful documents include the many editions of the manual "*Composition of the house*" (Ceccarini, 1952 and subsequent editions up to 1985), which provide typological examples of Italian buildings throughout the first eight decades of the twentieth century.

As an example, Figure 3.3 shows some of the typical URM buildings of the Italian residential heritage, for some construction periods and number of stories.

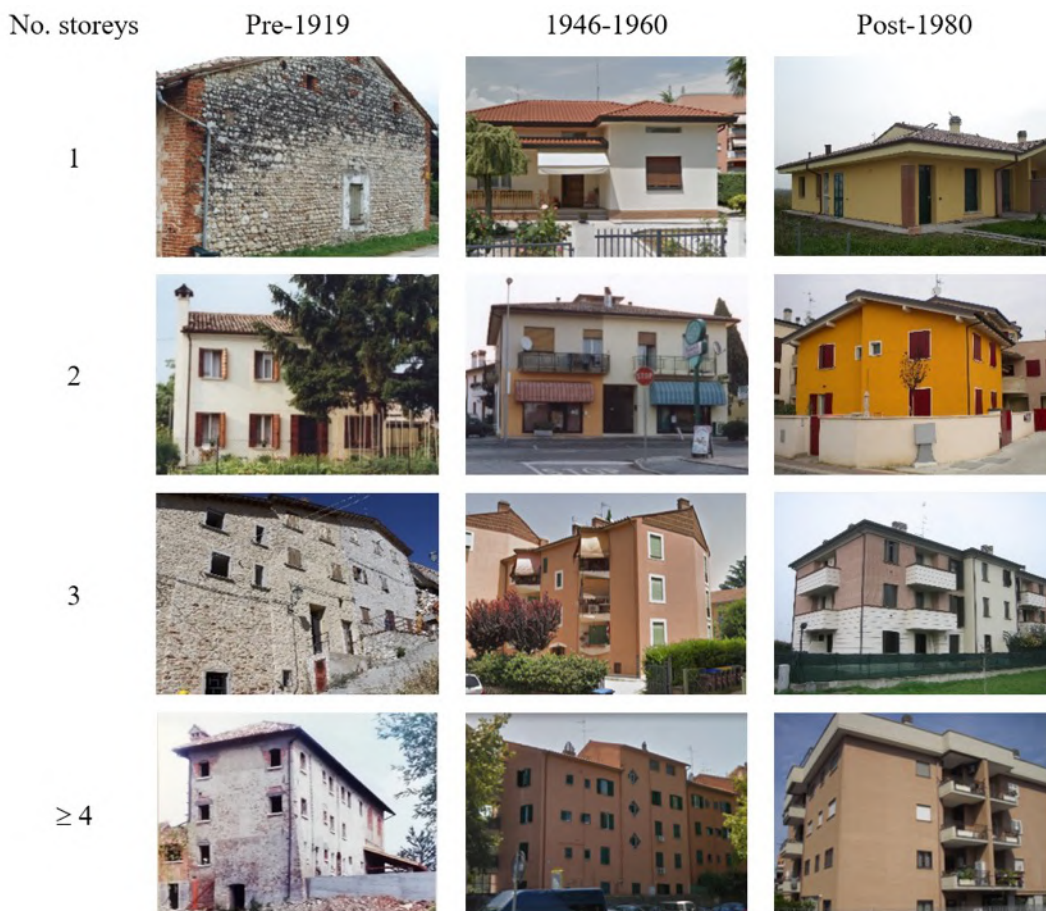


Figure 3.3 - Examples of some representative Italian URM buildings by construction age and number of stories

### 3.3. **Vulnus-based seismic fragility model for moderate to severe damage**



The relevant information for each case study was implemented in *Vulnus\_4.0*. As this software calculates fragility on discrete points, the discrete curves were replaced with cumulative probability lognormal functions – typically used to describe fragility and defined by only two parameters, i.e., mean ( $\mu$ ) and standard deviation ( $\beta$ ) – through the maximum likelihood method, as shown in Figure 3.4 for a case study.

A first analysis based on these curves was aimed at assessing the adequacy of the database size. In particular, the effect of the sample size on the fragility curves was assessed by analyzing, separately for each building macro-typology, ten random subsets of buildings with an increasing size, equal to 25%, 50% and 75% of the database. Some results (for three macro-typologies) are shown in Figure 3.5, in terms of variation in both fragility curves and  $\mu$  values, and show a clear convergence as the number of buildings analyzed increases; more importantly, the maximum variation obtained with 75% of the database is relatively small for the purposes of this study, proving the adequacy of the database size.

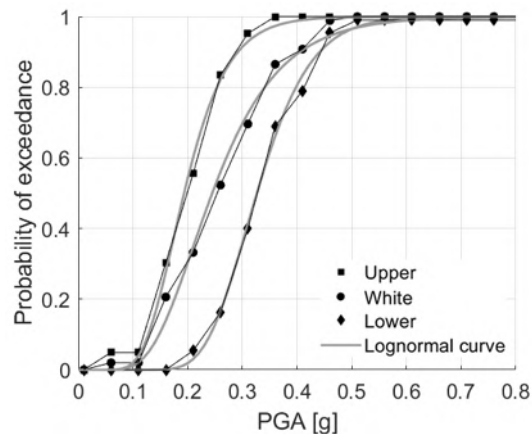


Figure 3.4 - Example of Vulnus curves and those obtained from lognormal fit

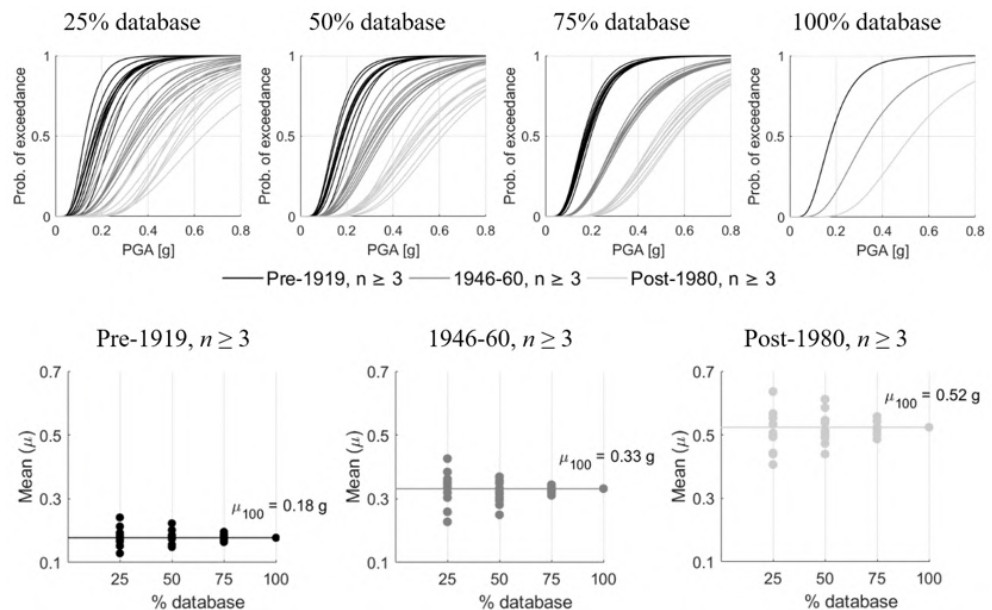


Figure 3.5 - Dependence of the fragility curves on the sample size, for three building macro-typologies

Then, to determine the fragility of all building macro-typologies (Table 3.1), associated with a DS2-3 damage, the following procedure based on the lognormal curves of each building was followed:

- *Step 1.* Calculation of the average fragility curves for buildings classified by construction age (according to Table 3.1) and number of stories (from one to five) at individual municipality level, for all the municipalities involved in the sampling.
- *Step 2.* Determination of the average fragility curves for buildings with the same construction age and number of stories, through the simple average of the previous curves obtained for individual municipalities. This step, necessary to derive a model of general validity within the national territory, provides the same importance to the various construction typologies – within each building macro-typology – regardless of the actual number of buildings that for practical reasons were sampled in each municipality.
- *Step 3.* Derivation of the average fragility curves for all macro-typologies by weighted average of previous fragility curves (defined by period and number of stories), separately for cases with buildings up to and with more than two stories. The weights, depending on the number of stories, are those derived from ISTAT data and shown in Figure 3.1. This step is therefore essential to provide the fragility model with the characteristic of typological representativeness per macro-typology.

These steps were repeated separately for the White, Upper- and Lower-Bound curves. The described procedure is shown as an example in Figure 3.6, which provides all the lognormal curves for the White fragility of buildings of the Pre-1919 period.

Figure 3.7 shows the complete model, i.e. considering all the building macro-typologies, for the White fragility. As can be seen, these macro-typologies allowed the definition of a fairly distributed fragility model, with probability of exceeding the given damage level that increases with increasing age and height of buildings. In particular, the greatest discontinuity in terms of fragility occurs between the periods 1919-1945 and 1946-1960, justified by the significant evolution of technology, construction techniques and material performances that occurred after the Second World War. Furthermore, the reduction of fragility due to the reduction in building height is more evident for more recent periods (1961-1980 and Post-1980), and this is reasonable considering the lower vulnerability of the most recent and newly designed buildings, which emphasizes their actual dynamic behavior.

The complete model, with the White, Upper- and Lower-Bound fragility, is shown in Figure 3.8, separately for each macro-typology. As can be seen, the dispersion range defined by the Upper- and Lower-Bound curves increases after 1946 and, in particular, is wider for the less vulnerable macro-typologies. This is related to a strong reduction in the Lower-Bound fragility, which is demonstrated by the optimal seismic behavior that recent URM buildings have, if properly designed and detailed for lateral loads (Penna et al., 2014; Sorrentino et al., 2019). The extent of dispersion is a useful information for territorial-scale risk assessments and, therefore, it will be taken into account.

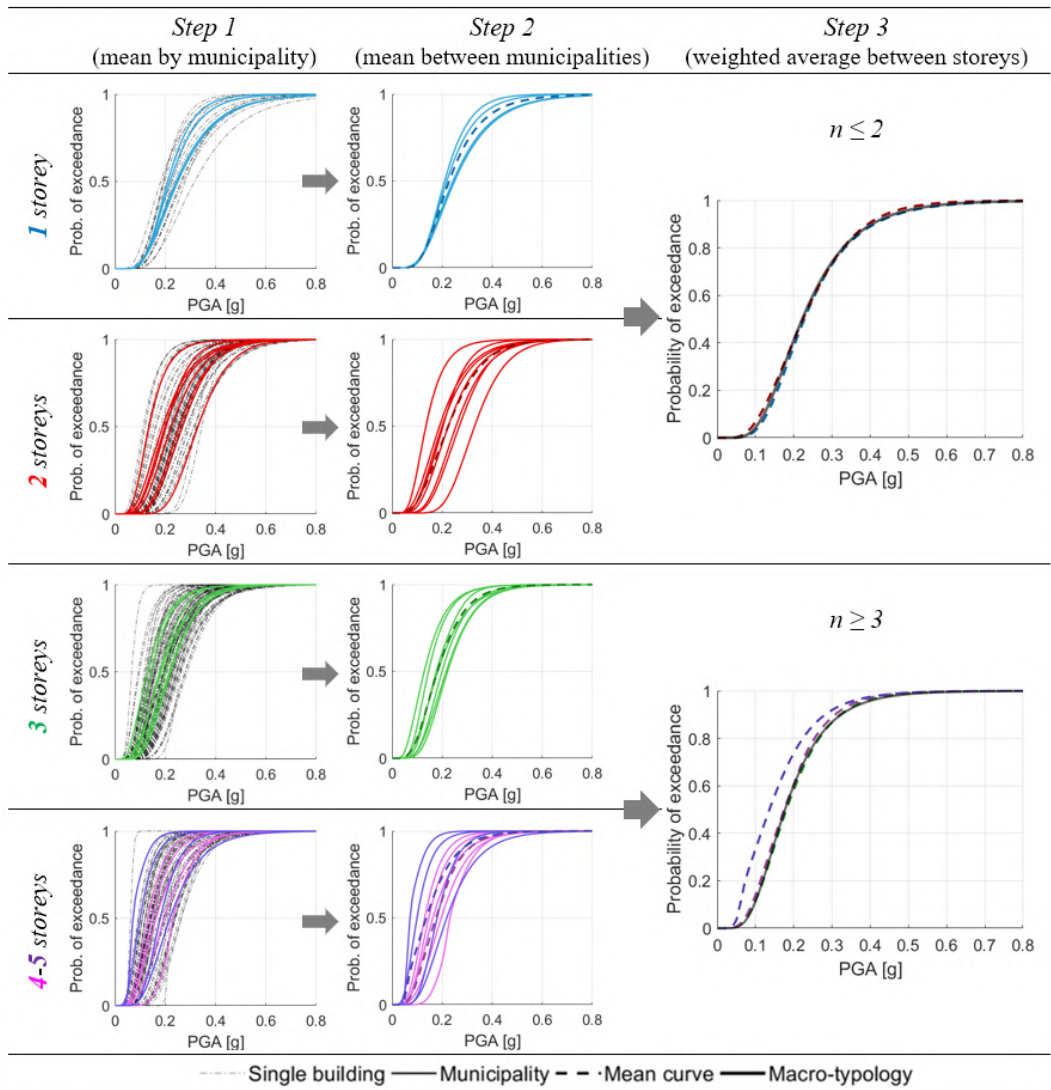


Figure 3.6 - Procedure to define fragility models. Example of White fragility for Pre-1919 buildings

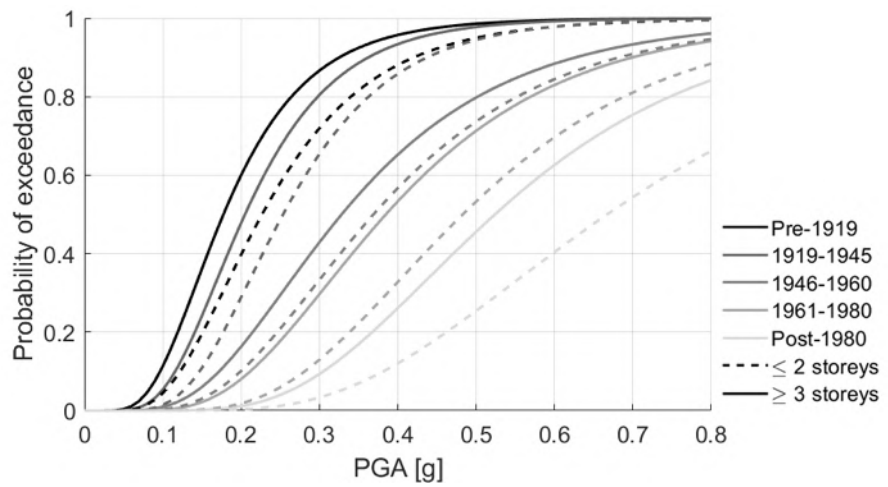


Figure 3.7 - Vulnus model of White fragility for all building macro-typologies

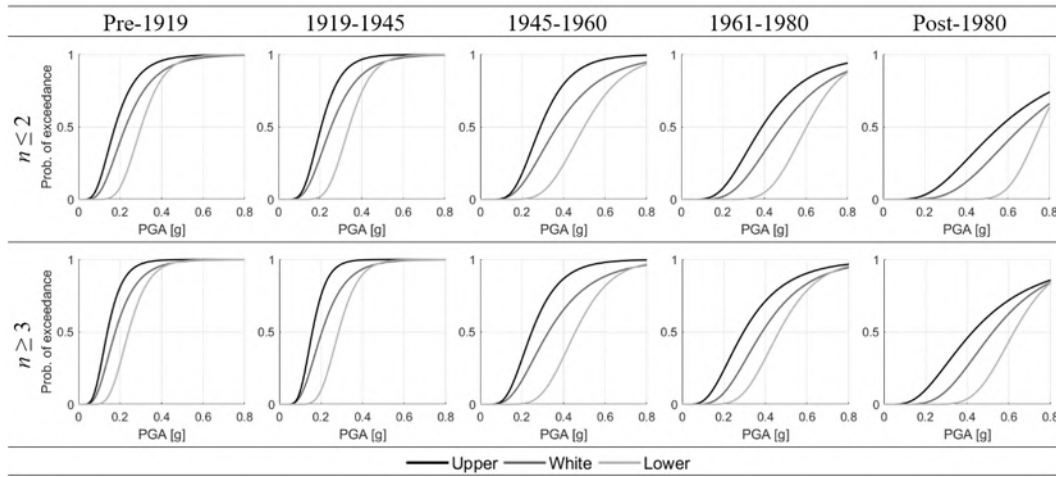


Figure 3.8 - White, Upper- and Lower-Bound fragility of all building macro-typologies

### 3.4. Multi-damage seismic fragility model

The seismic risk management on a territorial scale requires accurate assessments of this risk (economic losses and casualties) to support the Civil Protection decision-making processes; therefore, it is necessary to provide fragility models that allow damage simulations with fairly distributed estimates. To this end, multi-damage fragility models, providing the exceeding probability for multiple damage levels (from the slight one to the building collapse) are desirable. For this reason, the Vulnus fragility model presented above was extended over the entire EMS98 damage scale (from DS1 to DS5) by using a heuristic approach based on previous relevant studies. In particular, the fragility model proposed by Lagomarsino and Cattari (2014), which derives from the macro-seismic approach of Lagomarsino and Giovinazzi (2006), was taken as a reference, as it is particularly suitable for our purposes (see section 2.1.2.1). Indeed, it provides a distributed fragility based on the five DSs and the six vulnerability classes (from A to F) defined in EMS98, and therefore has general validity, referring to seismic performance categories rather than specific structural types.

Specifically, this model is based on the generic vulnerability curve proposed by Bernardini et al. (2010), which provides the mean damage  $\mu_D$  as a function of the macroseismic intensity  $I$  according to the following expression:

$$\mu_D = 2.5 + 3 \tanh \left( \frac{I + 6.25V - 12.7}{Q} \right) \quad (0 \leq \mu_D \leq 5) \quad (\text{Eq. 3.1})$$

In Equation 3.1,  $V$  is a vulnerability index whose values are provided in Lagomarsino and Cattari (2014) as confidence intervals for the six vulnerability classes, and  $Q$  is a ductility parameter assumed equal to 3 by the same authors. Thus, assuming the binomial distribution, the fragility curves can be defined on the basis of  $\mu_D$  and  $I$  as:

$$p_{LSk} = \sum_{i=k}^5 p_{DSi} \quad (k = 1, \dots, 5) \quad (\text{Eq. 3.2})$$

$$p_{DSk} = \frac{5!}{k!(5-k)!} \left(\frac{\mu_D(I)}{5}\right)^k \left(1 - \frac{\mu_D(I)}{5}\right)^{5-k} \quad (k = 0, \dots, 5) \quad (\text{Eq. 3.3})$$

where  $P_{DSk}$  is the probability of experiencing and  $P_{LSk}$  the probability of exceeding the various damage states. To obtain the related fragility curves in terms of PGA, many correlation laws between PGA and  $I$  are available in the literature, usually in the form:

$$\log(PGA) = c_1 + c_2 I \quad (\text{Eq. 3.4})$$

In this study, the mean values of  $V$  were used for all vulnerability classes, and the parameters of the correlation law were assumed as  $c_1 = 0.525$  and  $c_2 = 0.22$ , according to Margottini et al. (1992).

The main advantage to refer to such a model is the possibility of exploiting the fragility distribution with respect to the damage level, which is intrinsically defined by the EMS98 scale for each vulnerability class. Table 3.3 reports the mean ( $\mu$ ) and standard deviation ( $\beta$ ) values of this reference model.

Table 3.3 - Mean ( $\mu$ ) and standard deviation ( $\beta$ ) values of reference fragility model

Vulnerability class	DS1 (slight)		DS2 (moderate)		DS3 (severe)		DS4 (partial collapse)		DS5 (complete collapse)	
	$\mu$ [g]	$\beta$ [-]	$\mu$ [g]	$\beta$ [-]	$\mu$ [g]	$\beta$ [-]	$\mu$ [g]	$\beta$ [-]	$\mu$ [g]	$\beta$ [-]
A	0.0420	0.5110	0.0746	0.5331	0.1204	0.5278	0.1943	0.5332	0.3449	0.5120
B	0.0693	0.5111	0.1230	0.5331	0.1986	0.5279	0.3209	0.5358	0.5822	0.5710
C	0.1144	0.5111	0.2030	0.5331	0.3278	0.5285	0.5305	0.5411	0.9707	0.5859
D	0.1887	0.5110	0.3349	0.5331	0.5408	0.5288	0.8732	0.5384	1.5693	0.5715
E	0.3112	0.5092	0.5517	0.5293	0.8883	0.5230	1.4173	0.5257	2.452	0.5448
F	0.5088	0.4881	0.8934	0.5060	1.4175	0.4984	2.1972	0.4951	2.3782	0.5358

Therefore, this reference model was calibrated on the derived Vulnus model to define the White, Upper- and Lower-Bound distributed fragility sets of each analyzed building macro-typology. The main steps of the analysis are listed below and shown in Figure 3.9.

- *Step 1.* For each vulnerability class (from A to F), an average fragility curve between those of DS2 and DS3 (DS2-3) was determined, which is consistent with the type of fragility described by the Vulnus model.
- *Step 2.* For each mechanical fragility curve of the Vulnus model (White, Upper- and Lower-Bound), the linear combination coefficients of the DS2-3 curves of the vulnerability classes were calculated, which provide the best fit of the combined curve on the mechanical one. To this end, a multi-objective problem was defined with the following aims: minimization of the absolute error between the curves, according to the Least Squares Method, and minimization of the relative error, expressed as the difference between positive and negative areas bounded by the curves. The resolution of this problem was carried out through the NSGA-II genetic algorithm (Deb et al., 2002), obtaining a set of optimal solutions (or Pareto fronts). The final choice of the

combination coefficients was made with expert judgment, evaluating the variability of the two types of error in the range of optimal solutions. Clearly, the optimization procedure is sensitive to the assumed range of PGA, as the latter influences the evaluation of errors between the curves. This range was extended up to 0.8 g, which is a reasonable limit for the ground shaking in Italy, agreed in the project unanimously with the DPC. As an example, Figure 3.10 shows the best match obtained between the White curves of the Vulnus model and the combined DS2-3 curves of the reference model. Table 3.4 reports all the optimal combination coefficients calculated.

- *Step 3.* Based on the parameters  $\mu$  and  $\beta$  (Table 3.3) and the combination coefficients (Table 3.4) of vulnerability classes, the White, Upper- and Lower-Bound fragility sets, defined on all DSs from DS1 to DS5, were derived for each building macro-typology.

The fragility sets thus obtained allow elaborating scenarios of distributed damage that can be considered as the most probable, when derived from White fragility, or extreme, when based on Upper- or Lower-Bound fragility.

Furthermore, the Upper- and Lower-Bound fragility sets define the dispersion of vulnerability information for each building macro-typology, which depends on the uncertainties at the individual building level (quantified through the Fuzzy theory as discussed in Section 2) and on the variability and extent of the sampled building stock. This information is very important, because the mechanics-based fragility curves are generally characterized by relatively low standard deviations ( $\beta$ ) in relation to the needs of large-scale vulnerability assessment. Indeed, the values of  $\beta$  are generally lower than those of empirical approaches, calibrated on extended databases of observed damage. However, the empirical approaches include other sources of uncertainty, in addition to those relating to the variability of the building stock (e.g., uncertainties on the damage surveys and the ground acceleration measures), and could therefore provide overestimates of  $\beta$ .

Based on this, and considering the aim of providing a practical tool for large-scale risk assessments, a single fragility set for each building macro-typology, named LUW, was finally derived by using the main information of the White, Upper- and Lower-Bound fragility sets. The criterion used was to calibrate the mean fragility on that of the White set and the standard deviation on the maximum dispersion provided by the Upper- and Lower-Bound sets, thus obtaining a more suitable model to describe the fragility of the built heritage. The procedure is described below and shown in Figure 3.9.

When the White probability is:

- lower than 2.5%, fragility is assumed equal to the Upper-Bound one;
- between 2,5% and 50%, fragility is calculated as a linear combination of Upper-Bound (from 100% to 0%) and White (from 0% to 100%) fragility;
- between 50% and 97.5%, fragility is calculated as a linear combination of White (from 100% to 0%) and Lower-Bound (from 0% to 100%) fragility;
- greater than 97.5%, fragility is assumed equal to the Lower-Bound one.

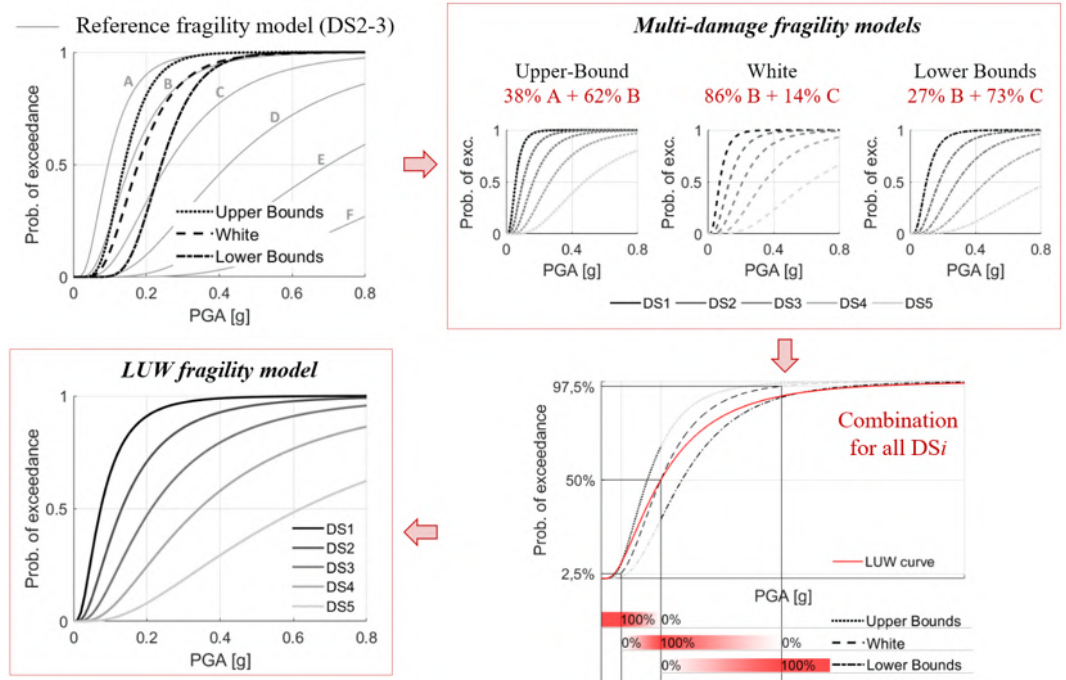


Figure 3.9 - Procedure to define multi-damage fragility models and LUW model. Example for Pre-1919,  $n \geq 3$

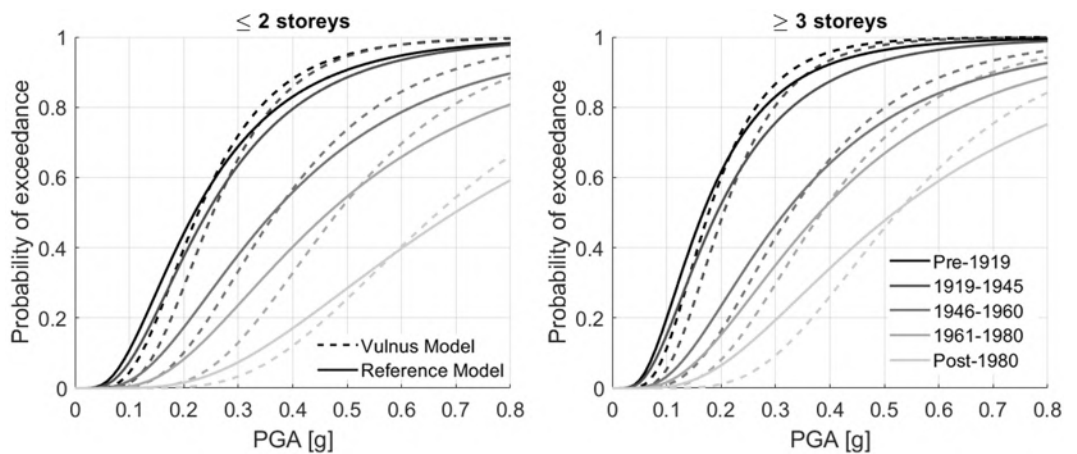


Figure 3.10 - Optimal fit of combined DS2-3 curves (reference model) on White curves (Vulnus model)

Table 3.4 - Optimal combination coefficients of vulnerability classes of reference model fitting Vulnus model

Building macro-typologies	Upper-Bound					White				Lower-Bound				
	A	B	C	D	E	B	C	D	E	B	C	D	E	F
Pre-1919	$\geq 3$	0.38	0.62				0.86	0.14			0.27	0.73		
	$\leq 2$		0.87	0.13			0.33	0.67			0.92	0.08		
1919-1945	$\geq 3$	0.15	0.85				0.58	0.42			0.03	0.97		
	$\leq 2$		0.62	0.38			0.13	0.87			0.62	0.38		
1946-1960	$\geq 3$		0.16	0.84				0.58	0.42			0.95	0.05	
	$\leq 2$			0.94	0.06			0.32	0.68			0.77	0.23	
1961-1980	$\geq 3$			0.77	0.23			0.23	0.77			0.92	0.08	
	$\leq 2$			0.2	0.8				0.81	0.19		0.17	0.83	
Post-1980	$\geq 3$				1				0.6	0.4		0.04	0.96	
	$\leq 2$				0.44	0.56			0.01	0.99			0.22	0.78

The LUW curves were first obtained by discrete points, and subsequently converted into lognormal curves by applying the criterion of maximum likelihood in the PGA range of interest, i.e. from 0 to 0.8 g. As an example, Figure 3.11 shows some comparisons between the proposed LUW model and the White, Upper- and Lower-Bound fragility sets, from which it derives. Table 3.5 lists the  $\mu$  and  $\beta$  values of the entire LUW model, i.e. for all building macro-typologies and DSs; the related fragility curves are shown in Figure 3.12.

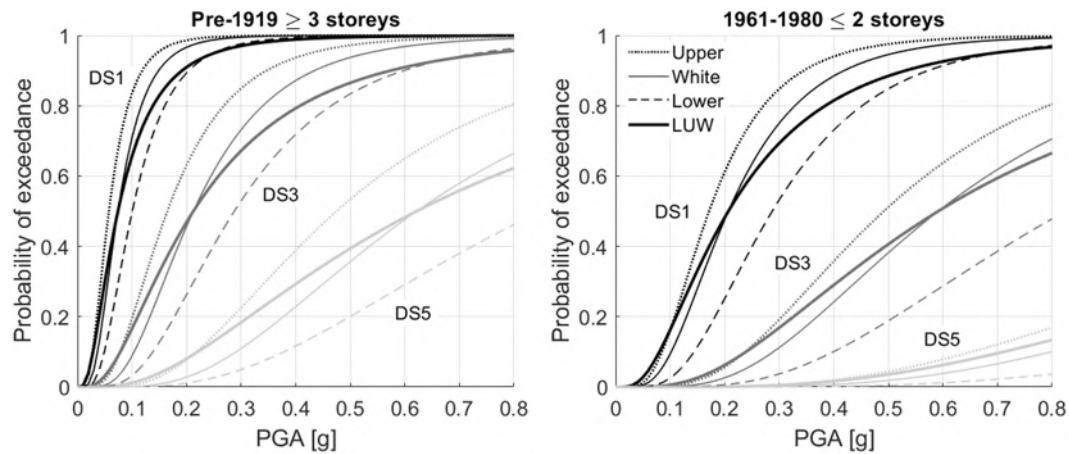


Figure 3.11 - Comparison between LUW curves and associated White, Upper- and Lower-Bound curves

Table 3.5 -  $\mu$  and  $\beta$  values of LUW fragility model

Building macro-typologies		DS1		DS2		DS3		DS4		DS5	
		$\mu$ [g]	$\beta$ [-]	$\mu$ [g]	$\beta$ [-]	$\mu$ [g]	$\beta$ [-]	$\mu$ [g]	$\beta$ [-]	$\mu$ [g]	$\beta$ [-]
Pre-1919	$n \geq 3$	0.0741	0.7414	0.1315	0.7671	0.2123	0.7759	0.3430	0.7736	0.6215	0.8090
	$n \leq 2$	0.0973	0.6929	0.1726	0.7084	0.2787	0.7192	0.4507	0.7499	0.8217	0.7936
1919-1945	$n \geq 3$	0.0854	0.7293	0.1516	0.7431	0.2447	0.7479	0.3955	0.7700	0.7168	0.8204
	$n \leq 2$	0.1076	0.7388	0.1908	0.7533	0.3082	0.7474	0.4988	0.7563	0.9140	0.7924
1946-1960	$n \geq 3$	0.1409	0.7489	0.2501	0.7780	0.4039	0.7789	0.6526	0.7975	1.1840	0.7452
	$n \leq 2$	0.1613	0.7651	0.2862	0.7791	0.4625	0.7818	0.7496	0.8015	1.3660	0.6933
1961-1980	$n \geq 3$	0.1689	0.6770	0.2996	0.7070	0.4842	0.7388	0.7855	0.7875	14.350	0.6997
	$n \leq 2$	0.2067	0.7366	0.3669	0.7367	0.5913	0.7069	0.9499	0.6916	1.6930	0.6764
Post-1980	$n \geq 3$	0.2301	0.6945	0.4083	0.7120	0.6580	0.6874	1.0550	0.6240	1.8690	0.5982
	$n \leq 2$	0.3098	0.7918	0.5492	0.7429	0.8849	0.7393	14.160	0.6780	24.700	0.6132



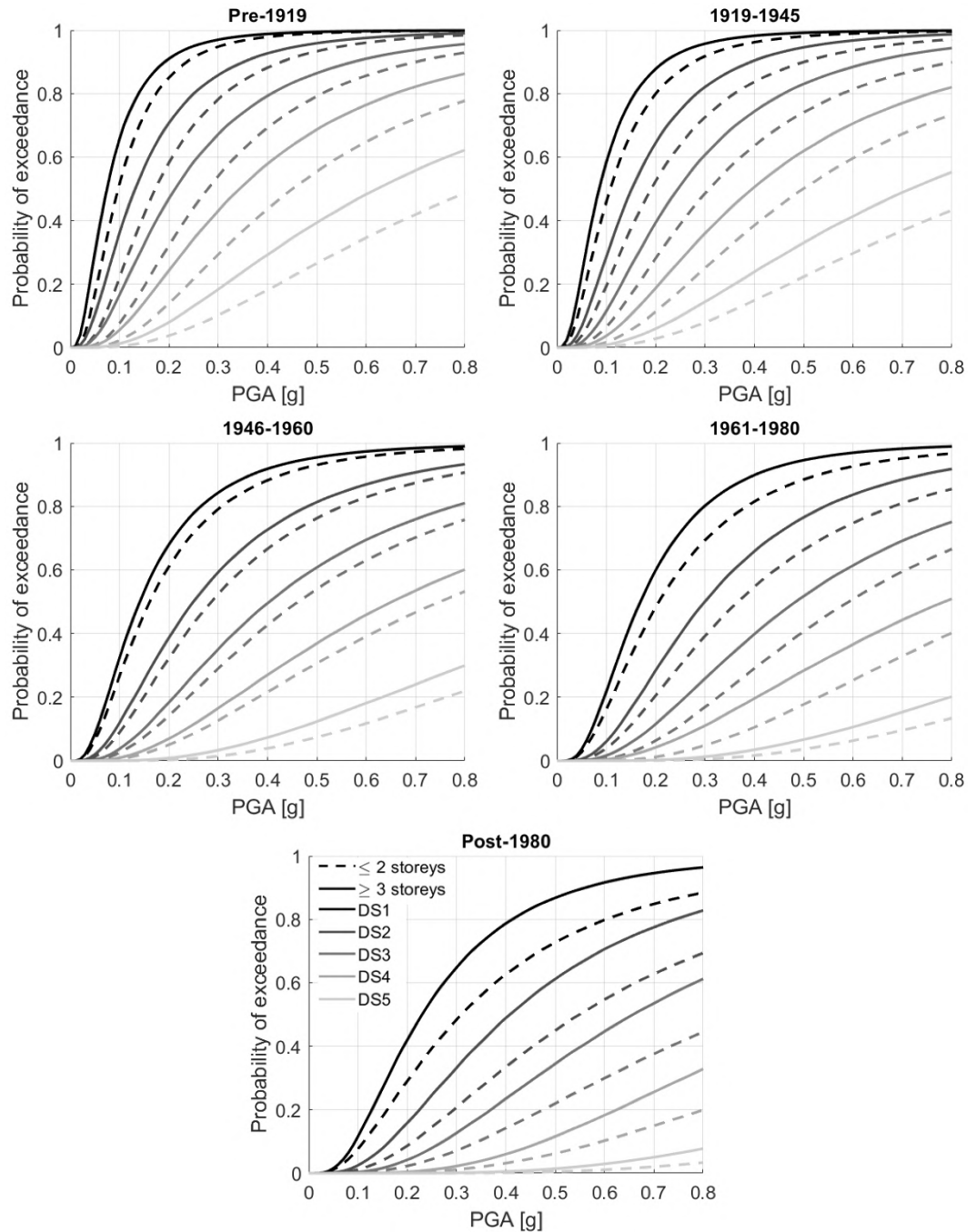


Figure 3.12 - Fragility sets (from DS1 to DS5) of LUW model of all building macro-typologies

### 3.5. Reliability assessment based on the observed damage

For damage simulation and risk assessment in a given territory, it is necessary to know data about its building stock, in terms of belonging to a certain macro-typology and location, and its seismic hazard. These data can be provided by ISTAT at national level for what concerns the building stock, and by INGV (National Institute of Geophysics and Volcanology) for what concerns the hazard. The information is collected and organized in the IRMA platform (Borzi et al., 2021b), developed by the European Centre for Training and Research in Earthquake Engineering (Eucentre) in

collaboration with the DPC and already described in section 2.3. Particularly, IRMA contains information on the ground shaking accelerations (ShakeMaps) of some recent and significant Italian earthquakes, and thus allows simulating specific seismic events and calculating a posteriori damage and costs. This is a very useful tool for validating or even calibrating the various fragility models to be implemented in IRMA.

Therefore, to assess the reliability of the fragility model proposed in this study, the model was implemented in IRMA and was applied to simulate the 2009 L'Aquila earthquake, obtaining the related damage scenarios. Besides being one of the most devastating Italian events in recent years, the L'Aquila earthquake is the most suitable for validation purposes, due to the completeness and reliability of data on observed damage and ground shaking.

Damage data relating to this event was obtained from Da.D.O. (Dolce et al., 2019), a database of the DPC that collects, in a digital form, the damage information detected in the aftermath of Italian earthquakes. In particular, for the 2009 L'Aquila earthquake and afterwards, the damage surveys were based on the latest review of the AeDES form (Baggio et al., 2007), which has been presented in section 2.1.2.2. This form requires, in addition to the main information on the building (age, material, purpose of use, etc.), the identification of the DSs and of their extension – with respect to the entire building, parameter “ $e$ ” – for the main structural and non-structural elements. In addition, a judgment on safety and usability, based on the damage detected, is required. The damage metric is based on the EMS98 scale but the DSs are merged as follow: DS0 (no damage), DS1 (slight), DS2-DS3 (moderate), DS4-DS5 (severe). As for the extent of damage, the metric is:  $e < 1/3$ ,  $1/3 < e < 2/3$ ,  $e > 2/3$ .

Based on the AeDES information, various methods were developed in recent years to define a single and equivalent level of damage per inspected building, to evaluate and represent damage scenarios and to support calibrations of empirical fragility models. In general, two methodologies can be distinguished: one is based on the weighted average of damage of the various building elements (Di Pasquale and Goretti, 2001; Lagomarsino et al., 2015), whereas the other rewards the maximum damage among these elements (Rota et al., 2008; Dolce and Goretti, 2015). To validate the fragility model, both methodologies were considered, applying the methods of Lagomarsino et al. (2015) and Rota et al. (2008).

The method of Lagomarsino et al. (2015) first requires calculating the equivalent damage  $d_j$  for the main building elements (vertical structures, floors, roof), according to Equation 3.5, where the coefficients of intensity  $d_i$  and extension  $e_i$  – defining the possible damage suffered by a given element – are assumed as in

Table 3.6, based on the AeDES information. Then, the overall building damage  $D_b$  is obtained as a weighted average of the previous  $d_j$  according to Equation 3.6, where the weights  $\alpha_i$  are given in Table 3.7. These weights vary depending on whether the damage survey is complete or partial (only external). In the case of partial survey but complete information, albeit indirect, Lagomarsino et al. (2015) suggest using both sets of  $\alpha_i$  and taking the highest  $D_b$ . The obtained  $D_b$  values were rounded to the next unit, and thus converted into the EMS98 scale.

$$d_j = \sum_i d_i e_i \quad (\text{Eq 3.5})$$

$$D_b = \sum_j \alpha_j d_j \quad (\text{Eq 3.6})$$

Table 3.6 -  $d_i$  and  $e_i$  coefficients associated with AeDES information (Lagomarsino et al., 2015)

Damage intensity (AeDES)	DS0	DS1	DS2-DS3	DS4-DS5
$d_i$	0	1	2.5	4.5
Damage extension (AeDES)		$e < 1/3$	$1/3 < e < 2/3$	$e > 2/3$
$e_i$		0.33	0.66	1

Table 3.7 -  $\alpha_i$  weights associated with building elements (Lagomarsino et al., 2015)

Elements ( $j$ )	Complete survey	Partial (external) survey
Vertical structures	0.6	0.8
Floors	0.2	0
Roof	0.2	0.2

The method of Rota et al. (2008) consists in converting the AeDES damage information into the EMS98 metric, according to Table 3.8, separately for vertical structures, floors and roof. Subsequently, the damage levels of all building elements are compared and the maximum is taken as the overall building damage.

Table 3.8 - Conversion of AeDES damage information to EMS98 damage scale (Rota et al., 2008)

AeDES	DS0	DS1	DS2-DS3			DS4-DS5		
to			$e < 1/3$	$1/3 < e < 2/3$	$e > 2/3$	$e < 1/3$	$1/3 < e < 2/3$	$e > 2/3$
EMS98	DS0	DS1	DS2	DS3	DS3	DS4	DS4	DS5

As mentioned above, the AeDES information relating to the 2009 L'Aquila earthquake was analyzed according to these two methods. It is important to point out that, although the damage survey was extensive, it was not complete in all the municipalities affected by the seismic event. In addition, some AeDES forms did not provide specifications on the type of use and construction material of the building, therefore they were excluded from the creation of damage scenarios for residential masonry buildings.

Hence, the available information was assessed with respect to the total number of residential buildings of each municipality (according to ISTAT information), to provide an indication of reliability. In particular, Figure 3.13a identifies the municipalities where damage surveys were available for less than 30%, between 30% and 90% and more than 90% of buildings. As can be seen, the municipalities near the epicenter were almost completely surveyed, thus providing robust and reliable information; moving away from the epicenter, the percentage of inspected buildings is clearly smaller, and information is less reliable. For the purpose of this study, the share

of uninspected buildings was associated with DS0. This assumption seems to be reasonable for the L'Aquila earthquake, where the lack of surveys may be related to the absence of damage on the building. However, some of these buildings may have suffered minor damage, not surveyed via the AeDES form, and this represents a source of uncertainty. Figure 3.13b shows the ShakeMap of the main event of April 6<sup>th</sup>, 2009 (available on the INGV website).

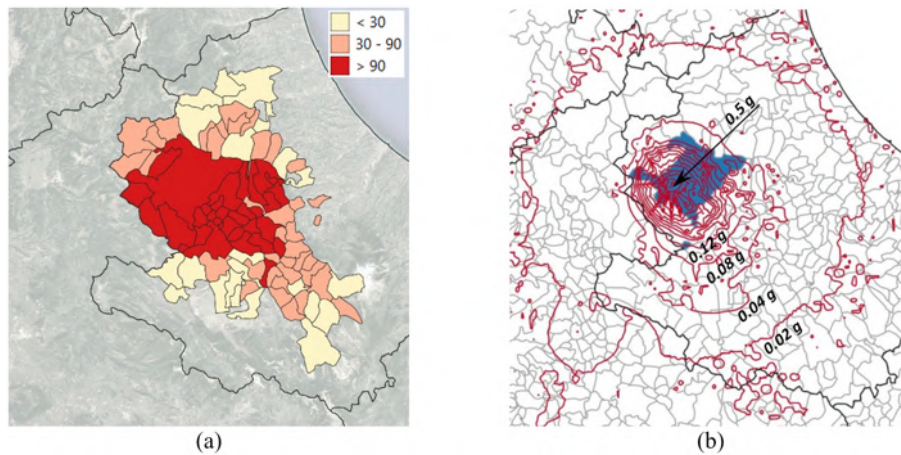


Figure 3.13 – (a) % of surveyed buildings of all municipalities; (b) ShakeMap of L'Aquila 2009

Figure 3.14 shows the comparison between the simulated damage scenarios, obtained with the proposed fragility model, and the observed damage scenarios, elaborated with the above-mentioned methods. In particular, these scenarios provide the percentage of buildings that reach or exceed a given DS for each municipality affected by the earthquake. The following considerations can be drawn.

- For all DSs, the trend of the simulated damage is similar to that of the observed damage; in addition, the damage values predicted by the proposed fragility model are substantially in-between the observed damage values measured with the two methods of Lagomarsino et al. (2015) and Rota et al. (2008), with the exception of some epicentral municipalities that show a slightly conservative damage prediction, in particular for DS1.
- The two methods for measuring the observed damage reasonably led to quite different scenarios, as that of Lagomarsino et al. (2015) rewards average building damage whereas that of Rota et al. (2008) rewards the damage peaks detected in the building. This aspect is interesting and underlines the practical difficulty of describing the overall damage of a building in a univocal and simplified way (i.e., with a single parameter), being able also to rely on an accurate damage survey.
- The proposed fragility model returns damage estimates that most closely resemble those obtained with the method that rewards maximum damage, near the epicenter (i.e., for high PGA values) and those obtained with the method that rewards average damage, moving away from the epicenter (i.e., for lower PGA values). This is due to the intrinsic characteristics of mechanics-based fragility, i.e. to the relatively low standard deviation of lognormal curves, an aspect taken into account in this study and mitigated using the dispersion given by the Upper- and Lower-Bound fragility curves.

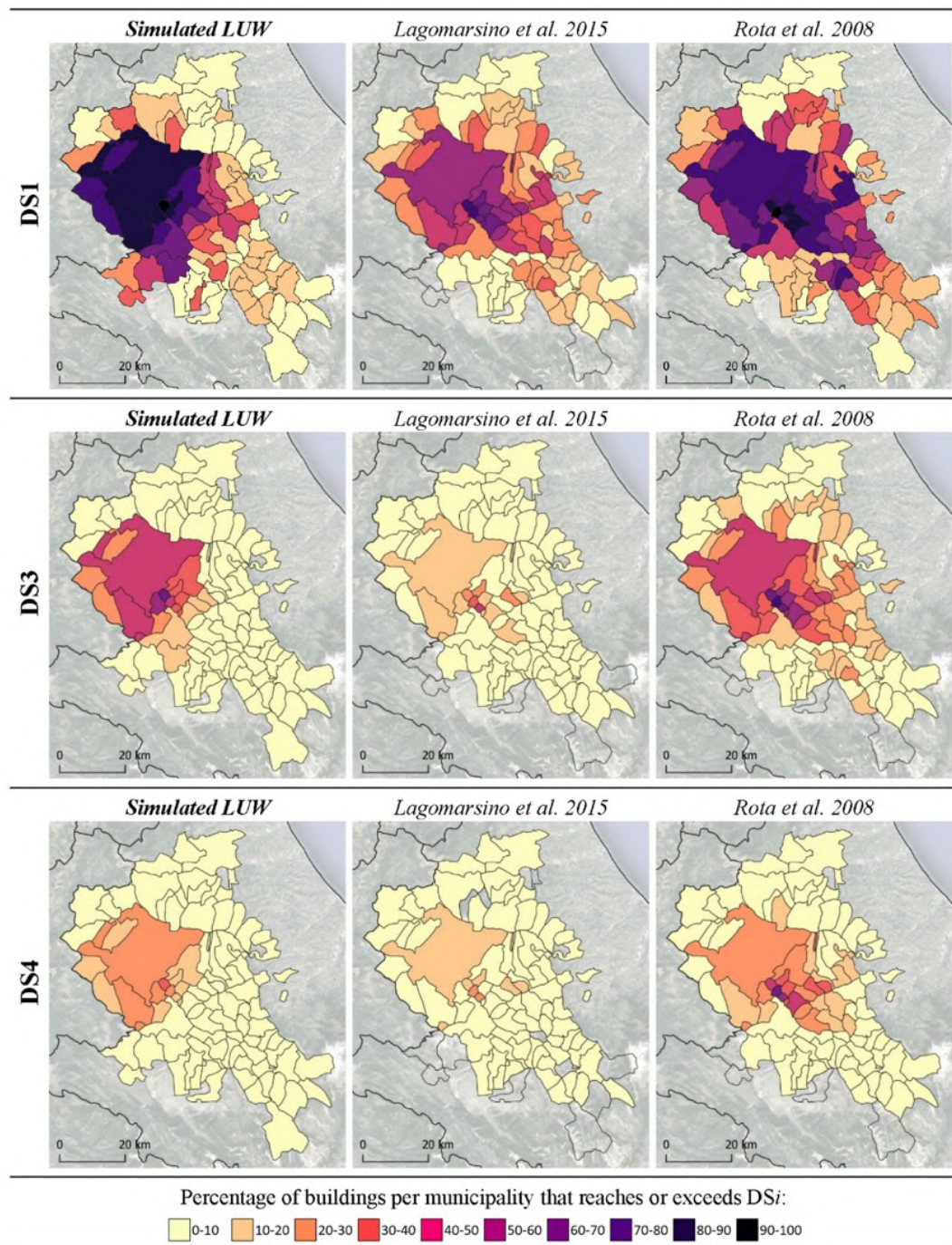


Figure 3.14 - Simulated and observed damage scenarios of the 2009 L'Aquila earthquake

It is worth noticing that some differences between simulated and observed damage are also due to the reasonable limitation of IRMA to use the PGA recorded in the centroid of the municipality for the whole municipal territory, which could be particularly limiting for larger municipalities or for any municipality having strong variations in soil characteristics. Finally, Figure 3.15 shows the comparisons between the most likely damage scenarios, simulated with the LUW model, and those obtained by applying the Upper- and Lower-Bound fragility models, which allow to evaluate the maximum expected damage interval due to the various uncertainties at stake.

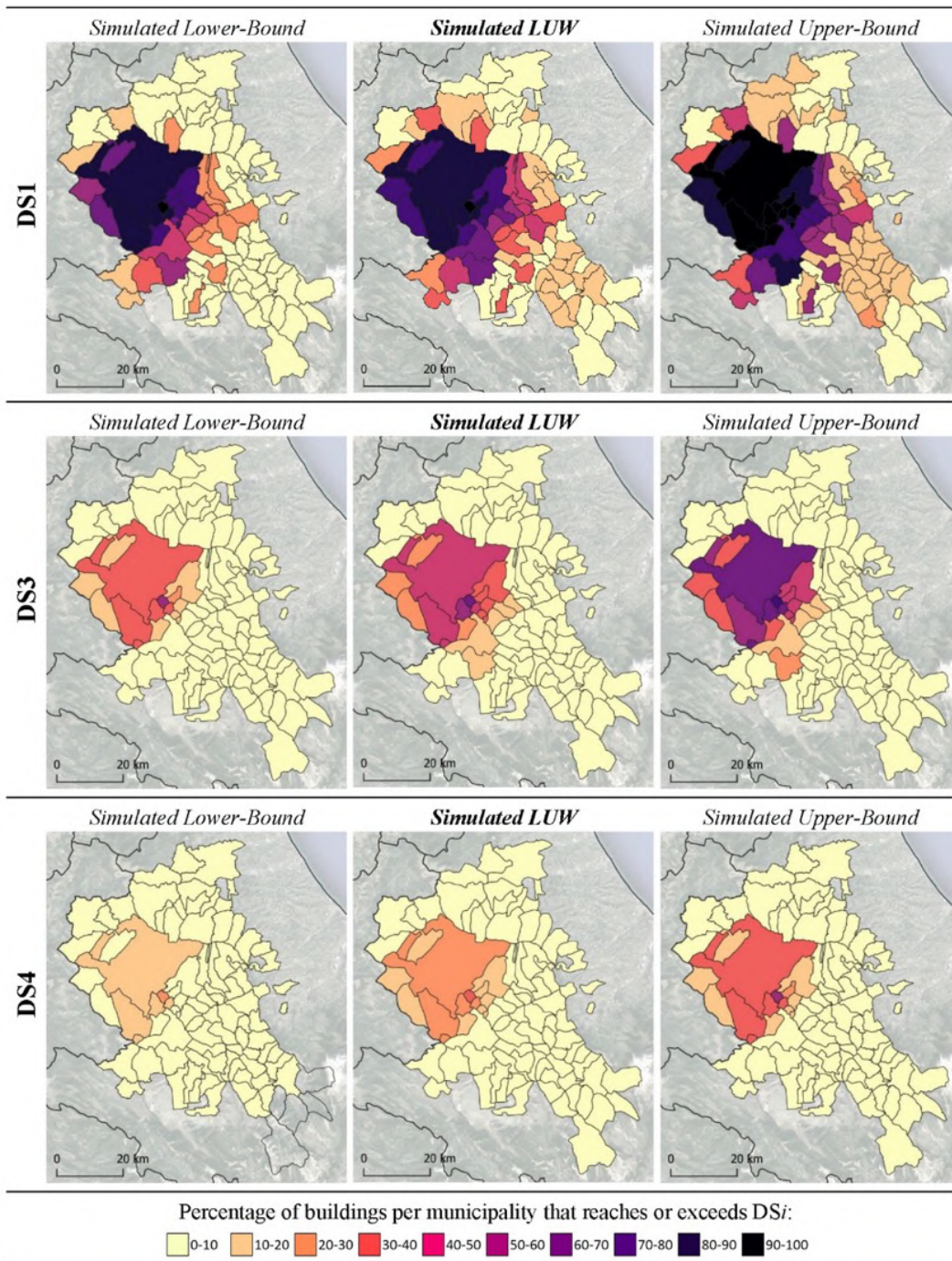


Figure 3.15 - Comparison of damage scenarios simulated by the LUW, Upper- and Lower-Bound models.

Although the results are encouraging, the awareness of the complexity of this study and the uncertainties characterizing all the steps to derive the proposed model suggest using it with due care, highlighting its great potential for improvement.

### 3.6. Fragility curves with retrofit interventions

The seismic events occurred in Italy during the last decades have shown the high vulnerability of the residential built heritage, making it necessary to plan seismic risk mitigation strategies at large scale. In this paragraph, the literature related to possible

seismic retrofit interventions is reviewed. These interventions are then simulated on a database of 445 buildings through *Vulmus\_4.0*, and fragility curves are elaborated and processed, so that a fragility model for four different building typologies (Pre-1919, 1919-1945, 1946-1960, and 1961-1980) is obtained for the various seismic retrofit possibilities.

The database considered has already been analyzed in its as built condition in section 3.2. Out of the 525 buildings belonging to the original database, only the ones associated with the older construction periods have been considered, leading to the selection of 445 residential masonry buildings. The most modern buildings, i.e. those built after 1980, have been excluded from this study since they usually show better design and construction details, following on one hand the improvement of masonry building design occurred after the Friuli (1976) and Irpinia (1980) earthquakes, and on the other hand, the more recent construction techniques widely available since the eighties, including the use of industrialized masonry units and of r.c. and hollow-tile rigid floors. In addition, the first specific regulation for the calculation of masonry structures, listing very significant construction rules to improve the overall building behavior (such as the presence of ring-beams, the use of rigid floors, the geometry, position, and arrangement of masonry walls, among the others) entered into force with a Ministry of Infrastructures Decree in 1987 (DM 1987). For these reasons, and although DM 1987 regulated the design under static loads only, the masonry buildings built after 1980 generally demonstrated a much better behavior than the older ones in recent earthquakes (Penna et al. 2014; Sorrentino et al. 2019) and, when properly designed according to the rules in force at that age, can be considered not to require any specific seismic retrofit intervention, at least at a large scale.

### 3.6.1. Seismic retrofit interventions

Before carrying out vulnerability analyses through *Vulmus\_4.0*, possible retrofit interventions must be selected as the most significant and effective for each building macro-typology. To do this, the reference literature was taken into account together with direct field observations (Vettore et al., 2022; Saretta et al., 2021a,b; Valluzzi et al., 2021a). In particular, due to the typological similarities among buildings erected in time periods that are close to each other, two blocks of interventions were selected, one for the so-called “historical” buildings (i.e. built before 1945) and one for more modern buildings (i.e., built after 1945). Specifically, the interventions have been grouped into three categories, depending on the kind of improvement that they are supposed to bring:

- a) intervention to increase the strength and quality of masonry (MSN);
- b) intervention to improve the wall-to-wall and wall-to-floor connections and to guarantee the box-like behavior (TR, CR);
- c) interventions to increase the stiffness of the horizontal diaphragms (FLR) (Modena et al., 2011; Circular 2019/01/21).

These interventions can be applied individually or they can be combined to optimize their effectiveness. In Table 3.9, the interventions selected for the two building macro-

classes are shown. Four possible interventions are proposed for the two macro-typologies of buildings designed before 1919 and between 1919 and 1945, combined in 4 different ways, for a total of eight possible interventions. On the other hand, the interventions selected for buildings designed between 1945 and 1980 are three, and their possible combinations lead to a total of five possible strategies.

Table 3.9 - Selected retrofit interventions for different construction periods

<i>Before 1945</i>	<i>individual interventions</i>	MSN1	1 <sup>st</sup> stage of masonry strengthening (one intervention)
		MSN2	2 <sup>nd</sup> stage of masonry strengthening (combined interventions)
		TR	addition of tie-rods
		FLR	stiffening of floors (light intervention)
	<i>combined interventions</i>	MSN1+TR	1 <sup>st</sup> stage of masonry strengthening + addition of tie-rods
		MSN1+FLR	1 <sup>st</sup> stage of masonry strengthening + stiffening of floors
		MSN2+TR	2 <sup>nd</sup> stage of masonry strengthening + addition of tie-rods
		MSN2+FLR	2 <sup>nd</sup> stage of masonry strengthening + stiffening of floors
<i>After 1945</i>	<i>individual interventions</i>	MSN	masonry strengthening (reinforced plaster)
		CR	addition of confining rings
		FLR	stiffening of floors (heavy intervention)
	<i>combined interventions</i>	MSN+CR	masonry strengthening + addition of confining rings
		MSN+FLR	masonry strengthening + stiffening of floors

In the following paragraphs, a detailed explanation of the most common interventions summarized in Table 3.9 and of their implementation through Vulnus software is given, taking into account the significant differences between the macro-typologies and the specific features of every single building. Due to the simplified modelling procedures of the software, the implementation process can be divided into two parts. The first part relates to the interventions that can be implemented through the available software options and are generally connected to changes in the mechanical parameters. Some of them could be implemented directly in Vulnus, even though most of them had to be implemented indirectly, by means of reproducing their effect on the overall behavior of the building. The second part of the implementation process refers to the improvement of qualitative building features and impact on the seismic performance, namely the qualitative parameters of the Second Level GNDT form (see section 2.1.2.2). In particular, a qualitative class from A to D (where A is the best condition) is assigned to each one of the 11 parameter of the form, on the basis of several specific characteristics of the building analyzed. The improvements of each intervention have been investigated, and a higher qualitative class has been assigned to the parameters affected by the interventions, with reference to the technical manual of the form (Ferrini et al., 2003).

### 3.6.1.1. Masonry strengthening and compacting

To ensure a good seismic performance of a masonry building, the quality and state of preservation of masonry is of paramount importance. If masonry is not sufficiently



strong and compact, the application of seismic actions leads to stone disaggregation or severe in-plane shear failure. Several techniques can be applied to improve the performance of masonry, depending on the typology and quality of masonry itself (Modena et al., 2000), as also demonstrated by recent post-earthquake field observations (Saretta et al., 2021a). Therefore, a careful evaluation of the as built state of masonry is necessary to select the most suitable intervention.

As presented in Table 3.9, two stages of retrofit interventions on masonry are proposed in case of historical buildings (MSN1, MSN2), while only one stage is taken into consideration in case of modern buildings (MSN), because of their better as built performance. The first stage of masonry intervention on historical buildings (MSN1) considers the application of lighter or single strengthening techniques, whereas the second one (MSN2) implies the concurrent application of two techniques or the extensive implementation of an heavier single technique, to achieve the best retrofit results.

The techniques to improve the quality and strength of masonry proposed in this study vary according to the type of masonry. For what concerns historical buildings, the load-bearing structure is usually composed of stone or solid brick masonry. Specifically, the first usually consists of rubble stones and can show an irregular pattern and the presence of many voids, or it is made of better shaped (ashlar) and coursed stone; the latter being generally of higher quality and more performing than the previous. Brick masonry is generally more regularly coursed. Both stone and brick masonry can be composed of two or three leaves, that are often not properly connected, particularly in the case of rubble, multi-leaf, stone masonry. Conversely, modern load-bearing masonry buildings (built after 1945), generally use industrialized solid or hollow bricks and blocks or, to a smaller extent, better shaped stones.

In case of inconsistent random stone masonry, grout injections are some of the most common and effective interventions (Mazzon et al., 2009; Oliveira et al., 2012; Silva et al., 2014; Quelhas et al., 2014). This technique consists in grouting the wall core, by filling the voids through a regular pattern of drilled holes. Injections are performed from the bottom to the top of the walls under controlled pressure, after cleaning the holes with water or compressed air. Nowadays, natural hydraulic lime based grouts are usually preferred, as their composition is more similar to that of historic mortars, making them more compatible with masonry, and ensuring a better homogenization with existing materials (Valluzzi et al., 2004; Vintzileou and Miltiadou-Fezans, 2008; Kalagri et al 2010; Oliveira et al., 2012;).

Nonetheless, even in masonry composed of more regular elements (i.e. stone ashlar and solid brick) the mechanical characteristics (compressive and tensile strength) can be improved. For this masonry typology, reinforced concrete jackets made of cement or lime-based mortars and a steel mesh can be added (Modena et al., 2009, Figure 3.16a). Another technology developed is the FRP (Fiber Reinforced Polymer) and SRG (Steel Reinforced Grout) (Figure 3.16b,c). These types of intervention consist of strips made of glass, carbon, aramid, or polypropylene fiber meshes and they allow to spread the reinforcement to the entire surface of the walls or to apply it locally (Tomažević et al., 2009; Borri et al., 2011; Capozucca, 2010). As an evolution of these

kinds of interventions, FRCM-TRM (Fibre Reinforced Cementitious Mortar – Textile Reinforced Mortars) plasters can be applied on both sides of the wall, anchored by transversal connections (da Porto et al., 2018; Giaretton et al., 2018; Valluzzi et al., 2021b; CNR-DT 215/2018, 2020; Borri et al. 2019, ACI 549.6R-20, 2020, De Felice et al., 2014; Corradi et al., 2014). Similarly to FRP strips, this type of intervention consists of fiber meshes, which in this case are coated in inorganic matrices based on lime or cement mortar. FRCM-TRM plasters can be applied on the entire surface of the walls; the outcome is similar to that of reinforced concrete jackets, but it comes with a lighter load and stiffness increase. This type of intervention is suitable also for more modern buildings, characterized by more regular masonry, where it is not necessary to fill internal voids, avoid masonry disaggregation, or improve the bond among different masonry leaves, but it is generally needed to produce a light but widespread strength increase.

The most suitable intervention in case of masonry with multiple leaves not adequately connected to each other is the insertion of artificial transverse elements with an anti-expulsion function. These can be stone or reinforced concrete elements, metal profiles, metal tie-rods made of smooth or threaded bars, inserted in dry or injected conditions, or fiber ropes or profiles which can be applied only if the masonry is consistent enough to ensure the coupling between the faces, and thus the overall functioning of the wall (Valluzzi et al., 2004; Corradi et al., 2017; Giaretton et al. 2017; Cascardi et al. 2020). Lastly, when the resistant elements are mostly regular and performing, but the mortar is of very poor quality or in a deteriorated state, it is possible to act with bed-joint repointing (Corradi et al., 2008). This intervention consists of removing part of the old mortar in the joints and replacing it with a new mortar with improved properties and durability. It is also possible to opt for reinforced repointing, adding steel or fiber reinforced polymer (FRP) bars into the newly pointed mortar joints, in order to increase not only the shear capacity, but also the behavior in case of relevant dead loads and creep phenomena (D’Ayala 1998; Valluzzi et al., 2005, Oliveira et al., 2012).

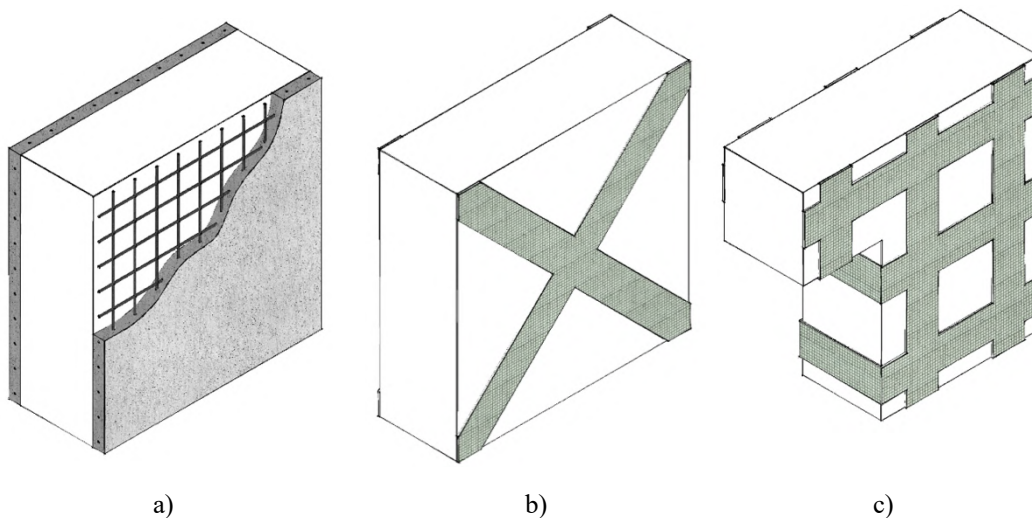


Figure 3.16 - Reinforced concrete jackets (a) and example of application of FRP-SRG (b, c)

To summarize, the 1<sup>st</sup> stage masonry interventions proposed in this study, according to the type of masonry, includes injections on random multi-leaf stone, and the application of reinforced plaster or FRCM-TRM in case of stone ashlar, solid and hollow brick masonry. These interventions can be integrated, as 2<sup>nd</sup> stage intervention, with bed-joint repointing or reinforced bed-joint repointing (in case of regularly coursed masonry) and transversal connection elements (in case of multi-leaf stone masonry).

To simulate these types of intervention through *Vulnus\_4.0*, the corrective coefficients shown in Table 3.10 are applied to the mechanical characteristics of the materials composing the building. The coefficients are averaged on those of table C8.5.II available in the Italian Circular 2019/01/21 (Italian Ministry of Infrastructures and Transports, 2019), and depend on the type of intervention and on the construction material. In case of historical masonry, the first step of intervention brings a similar improvement for different masonry types. Instead, the implementation of more invasive and heavy interventions on stone masonry, characterized by values of the mechanical parameters lower than the ones associated to brick masonry, gives greater improvements, although it does not exceed the values of the mechanical characteristics of brick masonry. Moreover, the improvement in case of hollow brick masonry is very low, since the performance level in the as built state is already high. Lastly, since these interventions require addition of material, an average increase of masonry specific weight was estimated by 5% in case of stone masonry and 4% in case of solid and hollow brick masonry.

Table 3.10 - Multiplicative coefficients applied by type of masonry and construction period

<b><i>Before 1945</i></b>	MSN1	MSN2
<i>Stone masonry</i>	1.7	2.4
<i>Solid brick masonry</i>	1.5	1.8
<i>Tuff masonry</i>	1.6	1.9
<b><i>After 1945</i></b>	MSN	
<i>Solid brick masonry</i>	1.7	
<i>Hollow brick masonry</i>	1.3	

As concerns the modification of the class assigned to the GNDT qualitative parameters, the improvement of masonry quality is related to four parameters: parameter n.1 “type and organization of the resistant system”; parameter n.2 “quality of the resistant system”; parameter n.3 “conventional resistance”; and parameter n.11 “state of preservation”. The parameters n.1 and n.3 are excluded from the calculation of the qualitative index I3 by *Vulnus\_4.0* because the former is considered to be completely integrated in the OOP index I2, and the latter in the IP index I1 (Valluzzi et al., 2009). For this reason, only parameters n.2 and n.11 have been modified after the strengthening interventions. The parameter n.2, “quality of the resistant system”, depends on the homogeneity of the wall fabric, and it is assigned to an A class for particularly good masonry structures, or in presence of masonry consolidated according to current seismic standards (Ferrini et al., 2003). The class of parameter n.2

has been thus changed to A either for MUR1, MUR2 and MUR, regardless of the as built masonry type and original quality class. The parameter n.11 is classified on the basis of the maintenance state of the masonry, and an A class is assigned to masonry in good condition, without visible damage, which can be also obtained after a well realized strengthening intervention. Therefore, also the class of parameter n.11 has been changed to A after the application of interventions.

### 3.6.1.2. Improvement of connections and box-like behavior

Connections between structural elements are necessary to ensure a box-like behavior of masonry buildings, which is the ability to act as an ensemble of all structural components, activating the in-plane response of the walls and resulting in a higher resistance of the structure to the horizontal actions caused by an earthquake.

Wall-to-wall and wall-to-floor/wall-to-roof connections are often inadequate in ancient buildings (Saretta et al., 2021a,b), causing a not adequate distribution of the shear loads in the masonry walls and the possibility of activating out-of-plane collapse mechanisms.

Interventions to improve wall-to-wall connections can be implemented by masonry corner reconstruction or by locally inserting steel or composite elements (Tomažević et al., 1996; Moreira et al., 2012; Araújo et al., 2014; Moreira et al., 2015; Cescatti et al., 2016). Interventions to improve the wall-to-floor connections can be carried out, for example, by locally inserting inclined steel bars in grouted holes drilled in the masonry, or by inserting fasteners (for example steel plates) at the ends of the beams, anchored on the external face of the wall or injected in holes in the wall (Giuriani et al., 2005; Dizhur et al., 2021). The latter solution is particularly efficient in case of wooden floors (Figure 3.17). Nevertheless, the most effective and popular solution to obtain a box-like behavior is the insertion of steel tie-rods (TR) or confining rings (CR) (Modena et al., 2011; Modena et al., 2009).

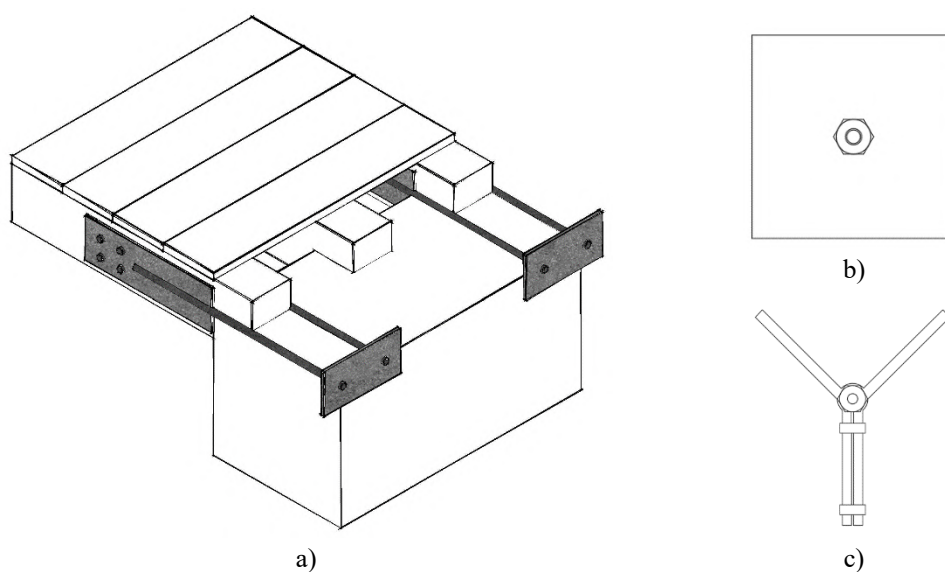


Figure 3.17 - Example of connection floor-to-wall (a) and of external anchors (b, c)

The most traditional and popular solution to obtain a box-like behavior is the insertion of steel tie-rods (TR) or confining rings (CR) (Modena et al., 2011; Modena et al., 2009; Calderini et al., 2016; AlShawa et al., 2019; Podestà and Scandolo, 2019; Rinaldin et al., 2019). Tie-rods (TR) are steel bars connecting parallel opposite walls, that allows preventing the out-of-plane overturning of walls and, when placed parallel to façade walls, allowing a better in-plane load redistribution and behavior of piers and spandrel walls (Figure 3.18a). This technique is one of the most traditional, thus it is highly compatible and very frequently implemented in historical buildings. Usually, tie-rods are placed at floor level in conjunction with masonry corners or T-junctions, along external and internal load-bearing walls, in the two main directions of the building (Figure 3.18b). Tie-rods can be directly implemented in *Vulnus\_4.0*, that considers the presence of this type of element. The number of ties was calculated for each building by placing, along each main direction of the building, an adequate number of rods (two rods, one per side, placed parallel to the internal partitions, and one rod close to the perimeter walls).

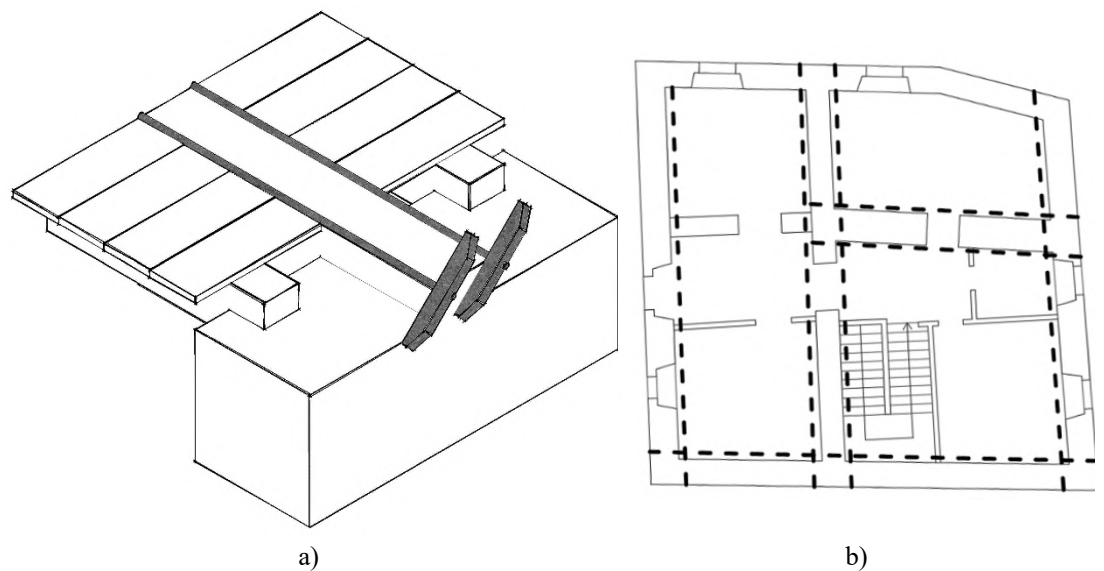


Figure 3.18 - Positioning of tie-beams: three-dimensional scheme (b) and disposition in plan (a)

As for the confining rings (CR), these have the same function of tie-rods, but they are applied on the external face of the walls. They consist of steel bars or bands of FRP (Fiber Reinforced Polymer) placed all around the buildings (CNR-DT 215/2018, 2020; ACI 549.6R-20, 2020). The intervention of confining rings has been considered as the equivalent of TR for modern buildings, useful when modern buildings are not provided with perimetral r.c. tie-beams or the r.c. tie-beams are very lightly (i.e., insufficiently) reinforced, as the result of placing the confining rings is to counteract the OOP mechanisms of walls and to improve the overall box-like behavior of the building. In this case, as *Vulnus\_4.0* does not explicitly consider the presence of this type of element, confining rings are simulated with the insertion of two tie-rods in each direction, in correspondence of the horizontal diaphragms of the building.

For the intervention to be successful, both tie-rods and confining rings need to be used when masonry is sufficiently compact and resistant to sustain the local force applied by the anchors. If this is not the case, it is necessary to apply local or global masonry strengthening interventions such as grout injections, reinforcement or replacement of individual degraded elements (Valluzzi et al., 2021b). For the purpose of this study, this condition was considered to be originally verified (when only TR or CR interventions were applied), or to be satisfied with the application of a combined intervention, where a global masonry strengthening intervention is also foreseen and applied.

The GNDT form takes into account the presence of these elements with particular reference to the issue of OOP thrusts at the roof level (parameter n.9 “roof”). With reference to the manual (Ferrini et al., 2003), the addition of tie-rods or other confining elements can improve the roof of one class. Consistently with the GNDT form, the implementation of TR and CR interventions brings an upgrade of one class to parameter n.9.

### *3.6.1.3. Strengthening and stiffening of horizontal diaphragms*

The horizontal diaphragms of masonry buildings have a crucial role on their seismic behavior, since they redistribute horizontal loads among load-bearing walls, thanks to sufficient stiffness and adequate connections to the vertical structure (load-bearing walls).

In general, there is a significant difference among the floor typologies in historical and modern buildings, resulting in different kinds of floor interventions (FLR) to be applied in the two cases. The horizontal diaphragms in ancient buildings often do not satisfy stiffness and connection conditions. Indeed, in this building typology it is common to find timber floors made with a single planking layer, usually not connected to the walls. In this case, interventions should aim at decreasing the in-plan deformability, and at strengthening the connections between horizontal structures and walls, as already mentioned in the previous sub-section (Branco and Tomasi, 2014). The floor intervention applied in this study, in case of historical building, considers the presence of wooden floors and consists in wooden planking reinforcement, which has proven to be very successful when applied to existing timber floors, as it helps increasing the in-plane stiffness without overloading (Piazza et al., 2008; Valluzzi et al., 2008, 2010; Magenes et al., 2014; Senaldi et al., 2014). This intervention consists of adding single or double wooden planks over the existing one, preferably using tongue-and-groove joints with nails or screws as connectors placed in orthogonal direction or at 45° (Figure 3.19a). Other strategies may be the insertion of diagonal metallic belts or composite material strips (Valluzzi et al., 2007). These interventions can be executed on the floor intrados or on the extrados, depending on the structure configuration and on the presence of valuable floors or elements (da Porto et al., 2018). In case of modern buildings, floors are typically made of reinforced lattice joist, during the turn of the century steel beams, and hollow tiles, and usually completed with a concrete slab. The steel used as reinforcement is not always enough and, in particular,

during the first evolutions of steel/hollow tiles and r.c. joist/hollow tiles floor systems, the connection between the joists and the slab was often inadequate or even absent, as well as the connections to the walls are often inadequate, due to the absence or poor reinforcement of r.c. tie-beams along the building (Neves and Giongo, 2021; Marini et al., 2018). In case of poor r.c. and hollow-tile floors, a concrete slab can be replaced or even added (Figure 3.19b), with the insertion of adequate connections to the joists and to the walls around the building perimeter.

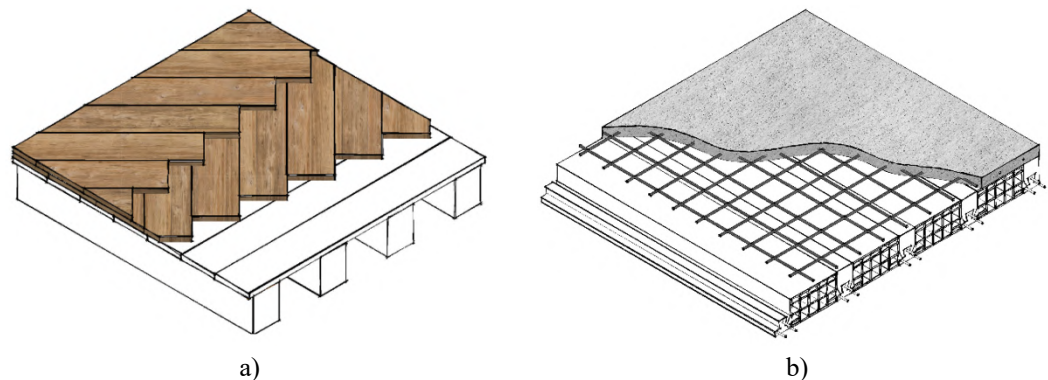


Figure 3.19 - Reinforced timber floor with double planking crossed at +45° and -45° (a) and addition of composite slab in r.c. floors (b)

Regarding the implementation phase, *Vulnus\_4.0* does not provide a way to implement intervention on the floors automatically, but it is necessary to simulate the effect of the intervention indirectly. Indeed, the implementation of the installation of double wooden planks in *Vulnus\_4.0* has been carried out by inserting ties to simulate the improved box-like behavior when floors are stiffened. Then, to further increase the reaction of the diaphragms in the model, the floor-to-wall friction coefficient is increased to take into account the improved connection brought by the intervention. For modern buildings, the replacement or the addition of the collaborating slab is simulated in *Vulnus\_4.0* with the insertion of adequate connections with the walls around the entire perimeter. In addition, the floor-to-wall friction coefficient has not been increased, as in the historical buildings, as it already had non-negligible values due to the type of simulated floors, but tie-beams have been inserted at each floor, when they were not already present. By doing so, the insertion of tie-beams has not been considered as a stand-alone intervention, because of its difficult application, especially at the intermediate floor levels of historical buildings (Borri et al., 2016, Vettore et al., 2022; Saretta et al., 2021a). Also, an average increase of floor specific weight has been estimated by  $1.2 \text{ kN/m}^2$ , in case of newly added collaborating slabs. The GNDT parameters concerned by the floor improvements are n. 5 “floor” and n.9 “roof”. The class of the parameter n. 5 is assigned based on the floor stiffness and the quality of the wall-to-floor connections. The interventions implemented in this study are attributed to an A or B class, based on the presence (class B) or absence (class A) of unaligned floors (Ferrini et al., 2003). Instead, parameter 9 considers stiffness and quality of connections, but also the presence of pushing actions, in case of heavy or

light roofs, and in this case the intervention leads to an improvement of only one class, similar to what happens for tie-rods and confining rings.

### 3.6.2. Mitigated fragility results

The procedure presented in paragraph 3.3 and 3.4 has been repeated for each of the 445 buildings included in the database of constructions built before 1980, and for each intervention considered, as described in paragraph 3.6.1. As a result, the fragility sets related to the building macro-typologies Pre-1919, 1919-1945, 1946-1960, and 1961-1980, for the two height classes Low-Rise (1 and 2 stories) and Mid-Rise (3, 4 and 5 stories), are obtained and are here listed in Table 3.11 and Table 3.12, in terms of median  $\mu$  and standard deviation  $\beta$  of the lognormal cumulative fragility curve. The results are also graphically presented in Figure 3.20 and Figure 3.21, where the fragility sets are compared to the as built ones.

The model obtained allows capturing the overall vulnerability reduction caused by the application of different interventions, but not the variations in individual damage states (e.g., reduction of severe damage but not of slighter ones). So, the fragility model presented in this work is considered reliable for large scale analyses, but it is considered to be only indicative of efficiency of the interventions, when applied at the detailed building scale.

Table 3.11 -  $\mu$  and  $\beta$  values of the fragility model for the as built and retrofitted configuration of historical buildings

		DS1		DS2		DS3		DS4		DS5		
		$\mu$ [g]	$\beta$ [-]	$\mu$ [g]	$\beta$ [-]	$\mu$ [g]	$\beta$ [-]	$\mu$ [g]	$\beta$ [-]	$\mu$ [g]	$\beta$ [-]	
Pre-1919	AB	$n \leq 2$	0,098	0,693	0,173	0,715	0,280	0,718	0,453	0,751	0,825	0,793
		$n \geq 3$	0,073	0,747	0,129	0,776	0,209	0,784	0,337	0,781	0,612	0,808
	MSN1	$n \leq 2$	0,132	0,707	0,234	0,732	0,378	0,725	0,611	0,725	1,110	0,716
		$n \geq 3$	0,111	0,756	0,197	0,786	0,317	0,774	0,514	0,785	0,942	0,816
	MSN2	$n \leq 2$	0,154	0,694	0,274	0,726	0,442	0,735	0,715	0,758	1,301	0,684
		$n \geq 3$	0,127	0,748	0,225	0,780	0,363	0,767	0,587	0,772	1,068	0,767
	TR	$n \leq 2$	0,112	0,740	0,198	0,768	0,320	0,755	0,517	0,766	0,948	0,804
		$n \geq 3$	0,078	0,736	0,139	0,757	0,224	0,761	0,362	0,770	0,656	0,806
	FLR	$n \leq 2$	0,126	0,737	0,223	0,760	0,360	0,749	0,582	0,753	1,059	0,758
		$n \geq 3$	0,091	0,681	0,162	0,702	0,262	0,706	0,424	0,735	0,770	0,774
	MSN1+	$n \leq 2$	0,168	0,692	0,298	0,718	0,481	0,737	0,780	0,778	1,425	0,698
		$n \geq 3$	0,119	0,744	0,212	0,768	0,342	0,756	0,553	0,756	1,009	0,778
	MSN1+	$n \leq 2$	0,205	0,702	0,365	0,703	0,588	0,683	0,945	0,677	1,685	0,670
		$n \geq 3$	0,148	0,671	0,262	0,694	0,423	0,699	0,684	0,717	1,241	0,672
	MSN2+	$n \leq 2$	0,190	0,730	0,338	0,737	0,545	0,729	0,879	0,761	1,579	0,711
		$n \geq 3$	0,142	0,701	0,253	0,729	0,408	0,733	0,659	0,747	1,196	0,697
	MSN2+	$n \leq 2$	0,264	0,737	0,469	0,738	0,758	0,726	1,223	0,653	2,172	0,611
		$n \geq 3$	0,184	0,686	0,327	0,700	0,529	0,709	0,856	0,752	1,554	0,708



1919-1945	AB	$n \leq 2$	0,107	0,753	0,190	0,767	0,307	0,765	0,496	0,785	0,910	0,813
		$n \geq 3$	0,084	0,719	0,149	0,746	0,241	0,751	0,390	0,768	0,707	0,819
	MSN1	$n \leq 2$	0,142	0,705	0,253	0,733	0,408	0,742	0,660	0,764	1,197	0,712
		$n \geq 3$	0,118	0,784	0,209	0,814	0,338	0,802	0,547	0,802	0,999	0,809
	MSN2	$n \leq 2$	0,162	0,701	0,287	0,734	0,465	0,754	0,753	0,791	1,373	0,694
		$n \geq 3$	0,138	0,728	0,245	0,760	0,395	0,770	0,638	0,790	1,159	0,749
	TR	$n \leq 2$	0,116	0,771	0,206	0,798	0,332	0,781	0,538	0,774	0,983	0,803
		$n \geq 3$	0,088	0,718	0,155	0,739	0,251	0,742	0,405	0,771	0,735	0,819
	FLR	$n \leq 2$	0,126	0,741	0,223	0,765	0,360	0,756	0,581	0,762	1,058	0,765
		$n \geq 3$	0,086	0,725	0,153	0,737	0,247	0,747	0,399	0,768	0,724	0,828
	MSN1+	$n \leq 2$	0,173	0,716	0,308	0,743	0,497	0,763	0,807	0,802	1,475	0,705
		$n \geq 3$	0,123	0,743	0,218	0,775	0,353	0,762	0,570	0,764	1,038	0,773
	MSN1+	$n \leq 2$	0,194	0,697	0,344	0,705	0,555	0,697	0,895	0,727	1,604	0,700
		$n \geq 3$	0,121	0,701	0,215	0,727	0,347	0,709	0,561	0,708	1,023	0,738
	MSN2+	$n \leq 2$	0,191	0,745	0,339	0,755	0,548	0,750	0,884	0,780	1,586	0,711
		$n \geq 3$	0,146	0,707	0,260	0,733	0,419	0,746	0,678	0,775	1,231	0,709
	MSN2+	$n \leq 2$	0,233	0,696	0,413	0,714	0,665	0,693	1,066	0,627	1,888	0,599
		$n \geq 3$	0,143	0,687	0,253	0,713	0,409	0,717	0,661	0,732	1,199	0,683

Table 3.12 -  $\mu$  and  $\beta$  values of the fragility model for the as built and retrofitted configuration of modern buildings

		DS1		DS2		DS3		DS4		DS5		
		$\mu$ [g]	$\beta$ [-]	$\mu$ [g]	$\beta$ [-]	$\mu$ [g]	$\beta$ [-]	$\mu$ [g]	$\beta$ [-]	$\mu$ [g]	$\beta$ [-]	
1946-1960	AB	$n \leq 2$	0,150	0,732	0,266	0,760	0,430	0,767	0,696	0,783	1,264	0,704
		$n \geq 3$	0,135	0,748	0,240	0,783	0,387	0,782	0,625	0,800	1,134	0,763
	MSN	$n \leq 2$	0,196	0,750	0,348	0,751	0,561	0,732	0,903	0,747	1,618	0,704
		$n \geq 3$	0,189	0,755	0,335	0,761	0,540	0,759	0,873	0,791	1,569	0,714
	CR	$n \leq 2$	0,170	0,800	0,302	0,818	0,488	0,809	0,792	0,820	1,448	0,702
		$n \geq 3$	0,138	0,737	0,244	0,771	0,395	0,775	0,637	0,790	1,157	0,748
	FLR	$n \leq 2$	0,165	0,774	0,293	0,784	0,474	0,787	0,768	0,807	1,403	0,698
		$n \geq 3$	0,133	0,730	0,236	0,764	0,381	0,760	0,616	0,777	1,118	0,753
	MSN+	$n \leq 2$	0,227	0,750	0,403	0,754	0,650	0,728	1,042	0,671	1,846	0,643
		$n \geq 3$	0,192	0,759	0,340	0,767	0,549	0,756	0,886	0,778	1,590	0,711
	MSN+	$n \leq 2$	0,230	0,695	0,409	0,716	0,659	0,696	1,057	0,634	1,871	0,608
		$n \geq 3$	0,189	0,689	0,335	0,704	0,541	0,707	0,874	0,753	1,571	0,710
1961-1980	AB	$n \leq 2$	0,208	0,739	0,369	0,741	0,595	0,716	0,956	0,699	1,703	0,679
		$n \geq 3$	0,169	0,676	0,300	0,706	0,485	0,736	0,786	0,785	1,437	0,700
	MSN	$n \leq 2$	0,267	0,754	0,474	0,760	0,766	0,753	1,237	0,659	2,199	0,608
		$n \geq 3$	0,200	0,691	0,354	0,694	0,571	0,680	0,919	0,691	1,644	0,683
	CR	$n \leq 2$	0,245	0,745	0,435	0,751	0,702	0,731	1,127	0,642	1,995	0,602
		$n \geq 3$	0,170	0,688	0,301	0,711	0,487	0,724	0,790	0,760	1,444	0,699
	FLR	$n \leq 2$	0,233	0,689	0,413	0,707	0,665	0,690	1,066	0,627	1,888	0,599
		$n \geq 3$	0,159	0,659	0,283	0,687	0,457	0,702	0,740	0,730	1,348	0,685
	MSN+	$n \leq 2$	0,314	0,791	0,556	0,767	0,895	0,756	1,427	0,681	2,451	0,611
		$n \geq 3$	0,207	0,678	0,368	0,689	0,593	0,685	0,953	0,683	1,698	0,671
	MSN+	$n \leq 2$	0,284	0,696	0,504	0,708	0,816	0,714	1,322	0,662	2,368	0,616
		$n \geq 3$	0,196	0,646	0,349	0,657	0,562	0,655	0,906	0,681	1,621	0,682

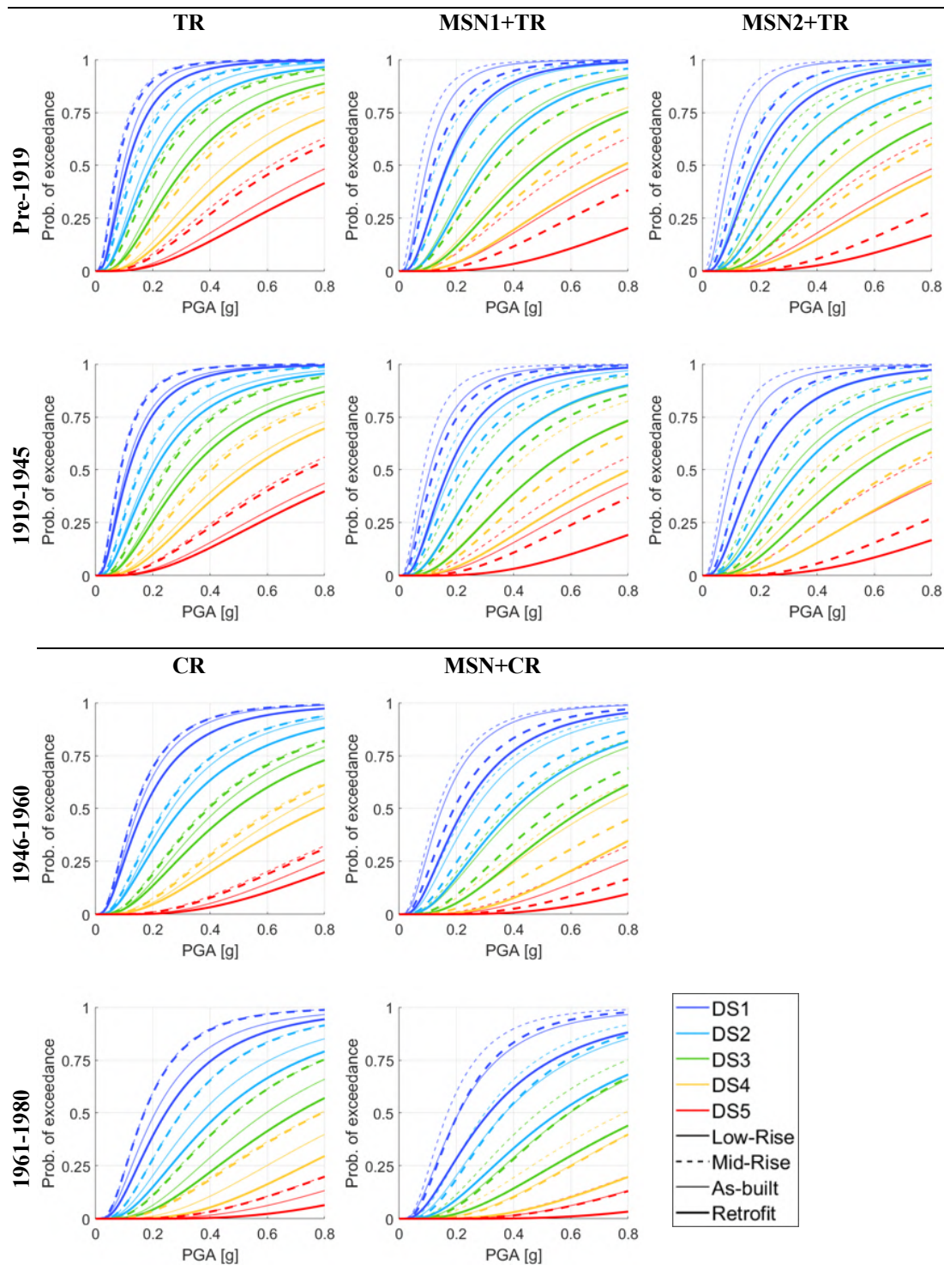


Figure 3.20 - Mitigated fragility curves for TR, MSN1+TR, MSN2+TR, CR, and MSN+CR compared to the as built model

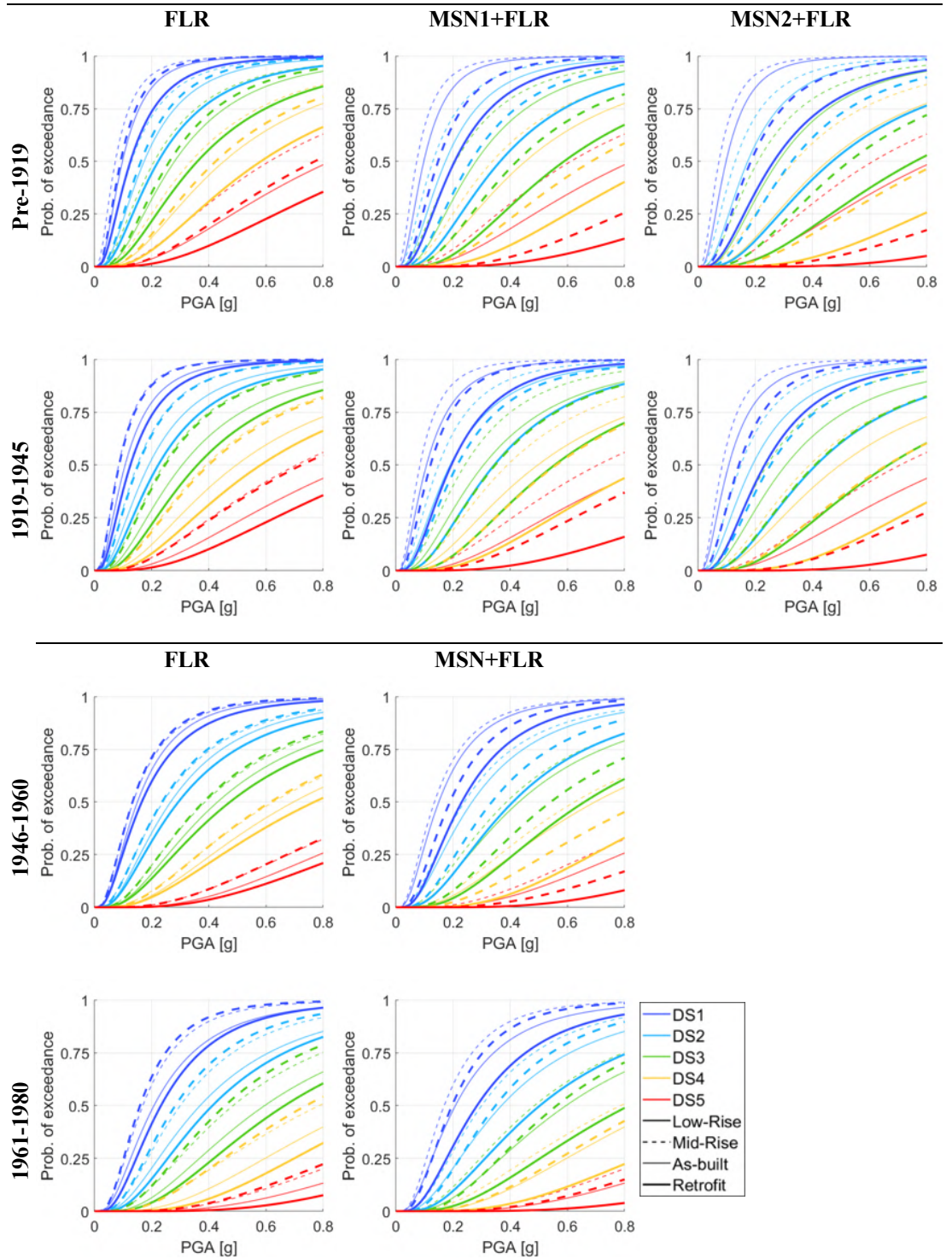


Figure 3.21 – Mitigated fragility curves for FLR, MSN1+FLR, MSN2+FLR, and MSN+FLR compared to the as built model

From these results, it was possible to evaluate the overall improvement brought by different interventions and compare the effectiveness of similar interventions applied to different types of buildings. In Figure 3.22, the percentage increase of  $\mu$  calculated for DS2 are shown as an example. From the histograms, on average, masonry interventions are more effective than tie-rods (or confining rings) and floor

interventions, particularly when applied to mid-rise buildings that, due to the higher masses, are subjected to higher shear actions on the walls. The smaller effectiveness of tie-rods and confining rings is very likely due to the fact that, when the out-of-plane collapses of masonry walls are hindered, than the problem turns into the inadequate strength of the masonry wall. Therefore, although the improvement of the former is significant, the latter start prevailing, and the overall damage of the building is only slightly improved.

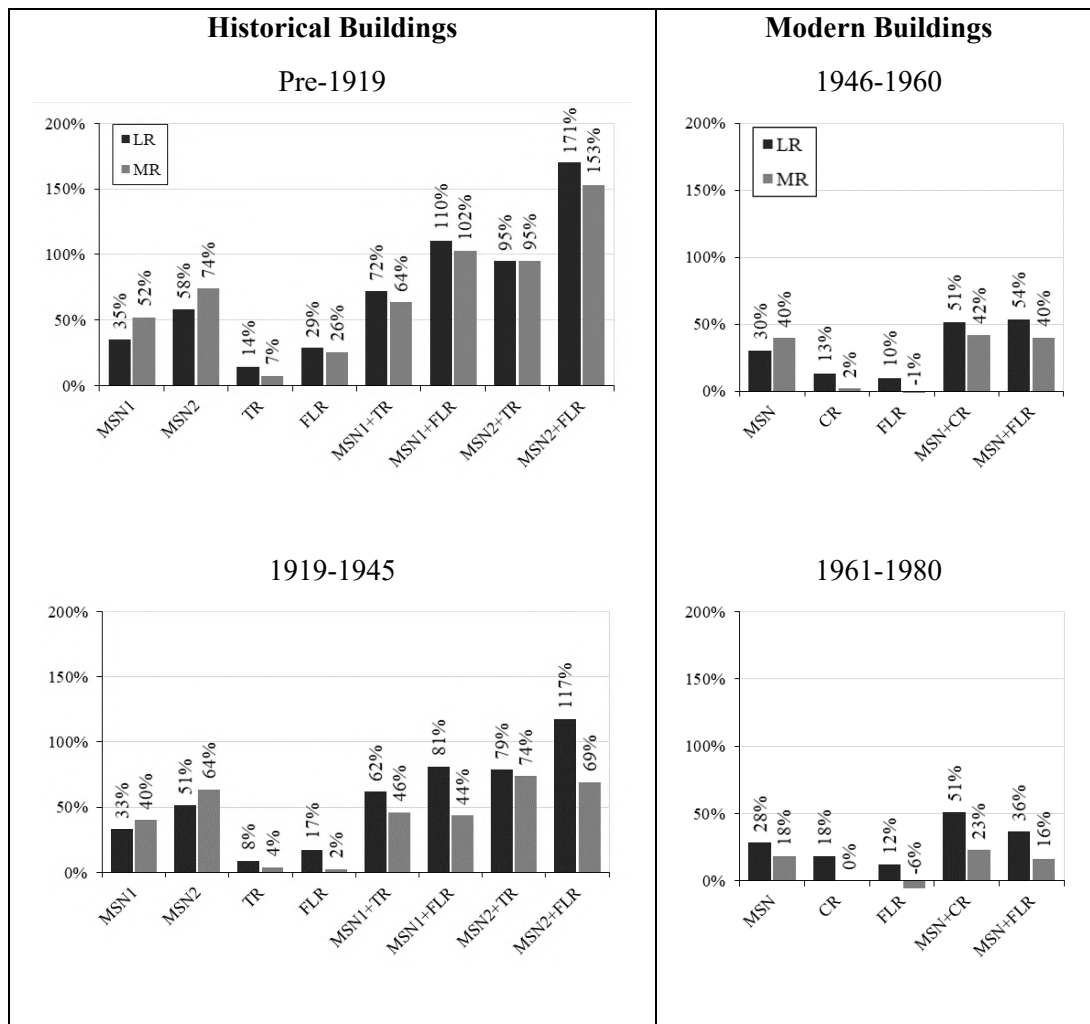


Figure 3.22 - Percentage of increase of  $\mu$  calculated for DS2

It is also interesting to observe that in historical buildings, the interventions on the floors are more effective than the single intervention of tie-rod insertion. This is because the intervention on the floor, as it has been conceived in this study, also consider the presence of diffused connections to the walls, thus improving the behavior towards out-of-plane actions, but only from more refined analyses a better seismic load redistribution among walls could emerge. Conversely, in the case of modern (post-1945) buildings, the interventions on the floors are less effective than the insertion of confining rings, and this is very likely due to a combination of various effects, including the better as-built condition of the modern floor, the increase of masses, hence seismic loads, related to the addition of a new collaborating slab, and the more

beneficial effect of confining elements, considering the absence or low quality of the existing tie-beams. In the case of interventions on floors of modern buildings, it is even observed a general worsening of the behavior of Mid-Rise constructions, probably due to the unfavorable effect of the load increase, not being balanced by a sufficient improvement in stiffness and connections.

Lastly, the improvement obtained by the application of combined interventions is not simply the sum of the improvement obtained for the two interventions applied separately, but it is definitely higher, due to the hindrance or delay of different collapse mechanisms, both in- and out-of-plane, and the overall improvement of the building behavior. As expected, the improvement in case of modern buildings is generally lower than that of historical buildings, because of the better as built condition of the former.

### **3.7. Final remarks**

In this chapter, a methodology for the evaluation of seismic vulnerability has been proposed. The fragility curves presented here are suitable for the estimation of the vulnerability of Italian residential masonry buildings at large scales, considering both their as built configuration and the simulation of possible seismic retrofit interventions. The main difference from creating fragility curves that fit individual case studies is that territorial fragility models need to be representative of building categories that are as homogeneous as possible, and must also rely on features that are clearly identifiable and easy to obtain at a large scale (such as height, material, and construction period, i.e., the parameters that the models presented in this chapter are based on).

These features are of key importance also for the definition of the exposure, which represents the quantity and value of goods (particularly buildings, in this case) and number of people involved in a possible seismic scenario. For example, the economic value of a building might differ according to the material and construction techniques, as well as to the age of the building itself. Moreover, the height of the buildings might give an indication of how many people reside there, thus expressing exposure in terms of human lives that can be affected by an earthquake.

This leads to the consideration that the correct identification of specific building parameters is essential both for the estimation of the exposure of the area under exam, and also for the correct association of a vulnerability indicator. As pointed out in Chapter 2, however, the larger the scale, the more difficult and time-consuming it is to determine the exposure and the vulnerability of an area.

In the next chapter, the automatic procedure for detecting features at territorial scale is presented, which thus allows not only to have an estimate of the exposure of the area under consideration, but also to assess its seismic vulnerability thanks to the model presented in this chapter.



## 4 AUTOMATIC DETECTION AND CHARACTERIZATION OF BUILDINGS AT A TERRITORIAL SCALE

For a risk assessment to produce meaningful results, exposure in the area of concern must be reliably estimated. This first step is necessary to understand how urbanized the area is (how many buildings there are), as well as to identify the building typologies. A good estimate of exposure, especially when it is made for risk assessment purposes, takes into account the different use of buildings, as well as their construction material, construction period, etc. However, estimating exposure can be difficult, especially in urban areas where large-scale surveys are generally expensive and impractical; yet, in those areas, most assets are at stake in the event of a disaster. In order to achieve the goal of collecting building footprints of a specific area, as well as some raw information about buildings, OpenStreetMap tools can be very useful. Furthermore, services that offer street-level images (such as Google Street View) can be employed to retrieve even further information on building taxonomy. Subsequently, Convolutional Neural Networks can be trained and used to associate images of buildings to a certain category. Particularly, an algorithm used to predict the height, material, and construction period of a building based on its street view image is presented in this chapter.

### 4.1. OpenStreetMap module to retrieve building footprints

According to the research mentioned in chapter 2 (specifically, 2.5.1), OpenStreetMaps can be considered very useful for the automatic detection of buildings at a territorial scale.

Specifically in this work, the data that can be offered by OpenStreetMap have been gathered through the Python package OSMnx. With OSMnx it is possible to download geodata from OpenStreetMap and model, project, visualize, and analyze urban geometries. This dependency was firstly presented in Boeing (2017) as a new tool that makes data collection and road network analysis simple, consistent, and automatable, from the perspective of graph theory, transportation, and urban planning. OSMnx offers five important features for researchers: the first one is the automated downloading of policy boundaries and building footprints; the second is the customized and automated downloading and creation of road network data from OpenStreetMap; the third is the algorithmic correction of network topology; the fourth is the ability to save road networks to disk as shapefiles, GraphML, or SVG files; and the fifth is the ability to analyze road networks, including computing routes, projecting and visualizing networks, and calculating metrics and topological measures. These scales include those commonly used in urban planning and traffic studies, as well as advanced scales for the structure and topology of the network. Boeing also published an article in 2020 where he used OSMnx to automatically download and analyze 27,000 U.S. street networks from OpenStreetMap at the metropolitan, municipal, and neighborhood levels, focusing on metrics relevant to graph theory, transportation,

urban design, and morphology, such as structure, connectivity, density, centrality, and resilience. By doing that, he demonstrated that OSMnx is suitable to consistently perform road network analyses with extremely large sample sizes, with excellent network definitions and extents for reproducibility. Lastly, in another work published by Boeing in 2021, OSMnx and data from OpenStreetMap allowed examining street network patterns, orientations, and configurations for several case studies around the world, thus giving important information about different urban fabrics.

OSMnx interacts with OpenStreetMap's APIs (Application Programming Interfaces), which are software intermediaries that allow two applications to communicate with each other. With OSMnx, for example, it is possible to download and model road networks or other networked infrastructures, as well as any other spatial geometry, location boundaries, building footprints, or points of interest. OSMnx relies on other Python packages, notably GeoPandas, which is an open source project that helps manage geospatial data in Python. Thanks to GeoPandas, it is possible to store OSM data as a GeoDataFrame, which is a data structure that organizes data in a 2-dimensional table with rows and columns (similar to a spreadsheet) and has a specific column for the geometry of each object. In this way, OSMnx allows users to obtain maps by city name, polygon, bounding box, or point/address and network distance, and save them as shapefiles, GeoPackages, or GraphML. After retrieving these data, it becomes easier and more practical to perform topological and spatial analyses to automatically calculate urban indicators, visualize road networks as static maps or interactive leaflet web maps, and create diagrams of road networks and building footprints.

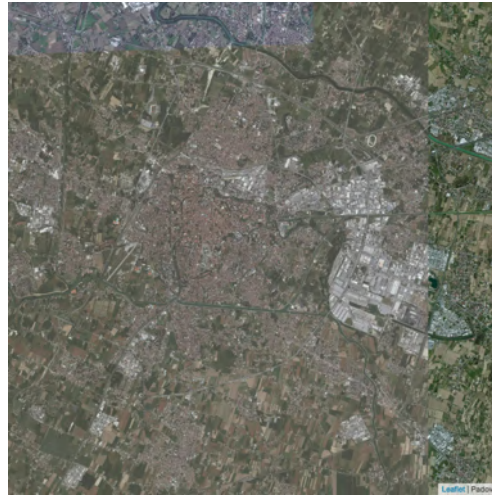
These useful tools that OSMnx offers have been exploited in this project within the Python code explained below, which was developed to retrieve building footprints given a specific satellite image.

To retrieve the desired satellite image, the script provides two input possibilities: the user can search a place by town/municipality, or can enter a pair of coordinates (latitude and longitude) and distance radius  $R$ . In the first case, the program will also return the centroid of the chosen town (in terms of latitude and longitude); in the second case, the program will extract the name of the municipality, region and country to which the chosen area belongs. In both cases, the package used to obtain the missing information is *Nominatim*, a tool to search OSM data by name and address (geocoding) and to generate synthetic addresses of OSM points (reverse geocoding). The code extracts the satellite image through the Static Maps service from the Mapbox API. Mapbox is a mapping and location cloud platform which provides tools to build scalable and customizable maps into websites or web-based applications. The satellite image retrieved through Mapbox is set to be included in a bounding box whose borders are represented by the minimum and maximum latitude and longitude of the selected area, so that all the buildings inside the municipality or within the radius can be visualized.

Figure 4.1 displays two examples of satellite images: Figure 4.1a shows an image extracted for an entire town (Padova), while Figure 4.1b shows an area centered in the point (45.409605, 11.888727) with a radius  $R$  of 300 meters.



Padova (town level)



a)

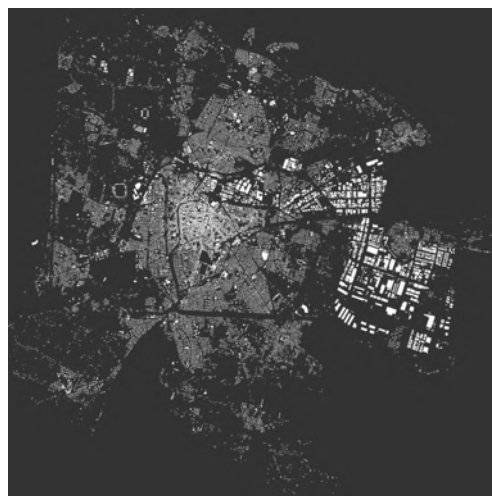
Coordinates: (45.409605, 11.888727),  
R=300 m

b)

Figure 4.1 - Satellite images for a) the town of Padova, b) an area centered in the point of coordinates (45.409605, 11.888727) with a radius of 300 meters

Subsequently, through the dependency OSMnx described above, it is possible to retrieve the footprints of all the buildings that are detected in the input area, thanks to the modules *footprints\_from\_place* or *footprints\_from\_point*, depending on the input choice. In this module, only the footprint type “building” is selected, so that the code only extracts the polygons associated to this type of object. The two maps in Figure 4.2 show the building footprints related to the satellite images shown in Figure 4.1. Other possibilities taken into account by the OSM tags could be “amenity”, “boundary”, “highway”, “landuse”, and “railway”, just to mention a few.

Padova (town level)



a)

Coordinates: (45.409605, 11.888727),  
R=300 m

b)

Figure 4.2 - Building footprints for a) the town of Padova, b) an area centered in the point of coordinates (45.409605, 11.888727) with a radius of 300 meters

This section of the code not only retrieves the building footprints, but also retains their floor area, their centroid (latitude and longitude) and the labels of each building. OpenStreetMap includes the following labels for the key “building”: “accommodation”, “commercial”, “religious”, “civic”, “agricultural”, “sports”, “storage”, “cars”, “power buildings”, “other buildings”. For each possible label, many sub-categories (values) are allowed. All the data obtained are stored in a GeoDataFrame, where each row represents a building and can be accessed and edited via GeoPandas. Figure 4.3 shows the building footprints from Figure 4.2b, with different colors according to their labels.

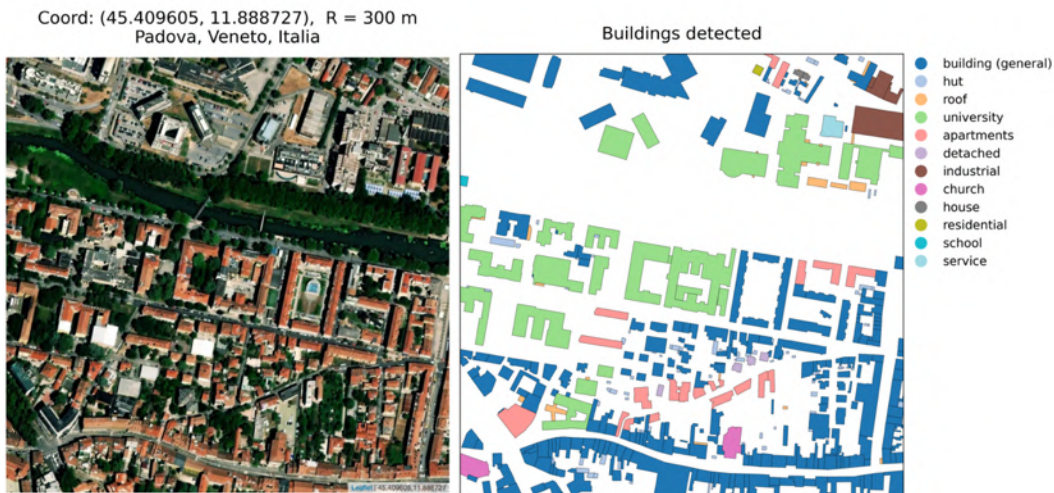


Figure 4.3 - Building footprints and their labels for the area centered in (45.409605, 11.888727) with a radius of 300 meters

Figure 4.4 shows the same type of output, this time for an area centered in (45.965009, 12.653791) with a radius R of 500 meters (located in the town of Pordenone, Friuli-Venezia Giulia, North-East of Italy). This example is presented to prove that the algorithm is completely automatic and works for any set of coordinates and for radii with different amplitudes.

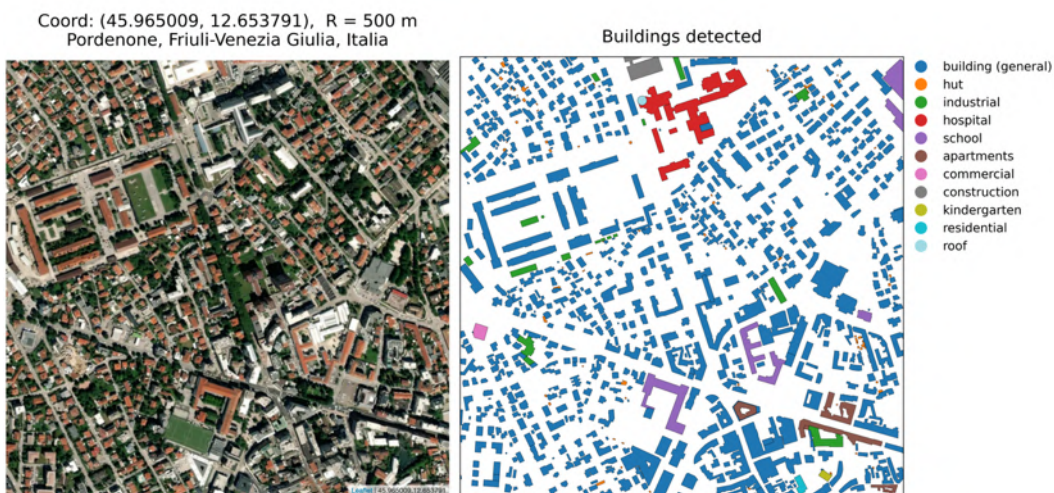


Figure 4.4 - Building footprints and their labels for the area centered in (45.965009, 12.653791) with a radius of 500 meters

In addition, the way in which data are stored makes it easy to filter them. As an example, only residential buildings among the ones detected in Figure 4.3 are shown in colors in Figure 4.5, while other building typologies are plotted in gray. Specifically, the values “building (general)”, “apartments”, “detached”, “house”, “residential”, and “semidetached\_house” have been considered as significant ones for selecting residential buildings only. Again, the same procedure is shown in Figure 4.6 for the buildings detected in Figure 4.4.

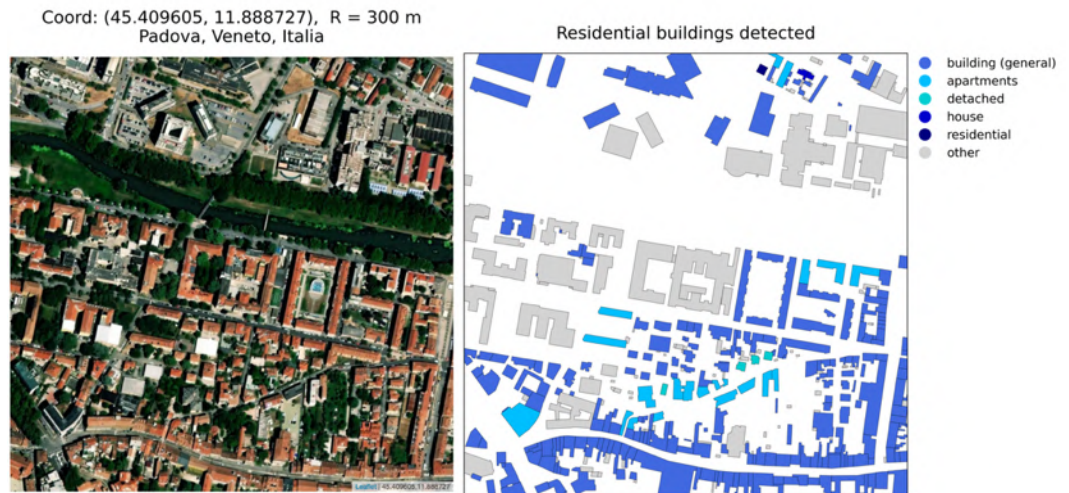


Figure 4.5 - Building footprints and their labels for the area centered in (45.409605, 11.888727) with a radius of 300 meters, where only residential buildings are kept

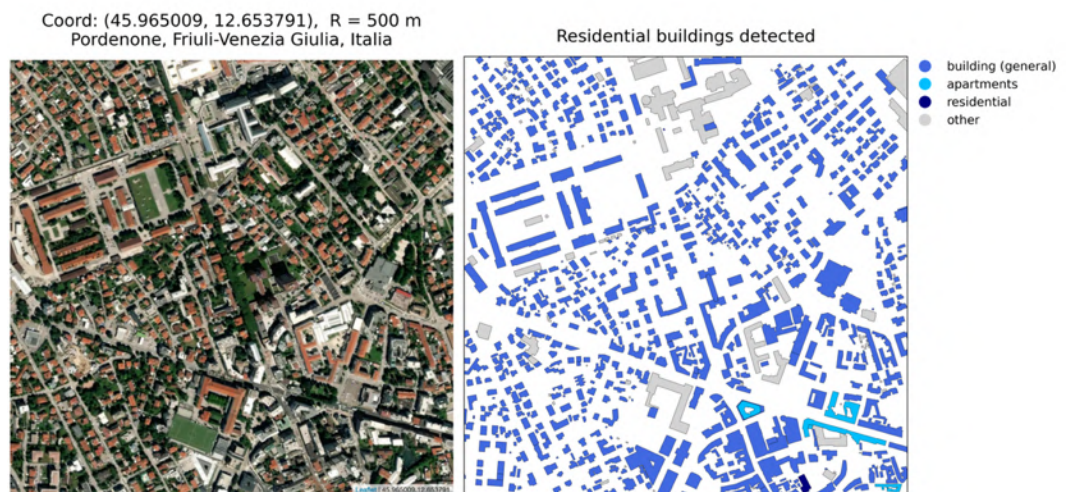


Figure 4.6 - Building footprints and their labels for the area centered in (45.965009, 12.653791) with a radius of 500 meters, where only residential buildings are kept

## 4.2. Google Street View module to retrieve street-level images

As can be seen from what has been shown so far, OpenStreetMap allows us to obtain a lot of valuable information about the buildings belonging to a specific area of interest. It has to be noticed, however, how most of this information regards 2D

features (such as latitude and longitude, floor area, etc.), and even when data that concern other kinds of features are found, they have to be trusted by the user without any possibility of checking. Information about the height of buildings, the disposition of openings, the construction material, just to mention a few examples, simply cannot be derived directly from an aerial image. Fortunately, we now possess tools that make it possible to explore a particular area not only from above, as seen from an airborne image, but also in its 3D complexity: in particular, it has become simple and user-friendly to access street view services, which provide street view images (SVIs), i.e., ground-level panoramic views of cities and other places. As described in chapter 2 (section 2.5.2), among all the possible street view services, Google Street View is definitely the most comprehensive in the world.

Google Street View images can add valuable information to that already obtained from satellite photos and OpenStreetMap. For this reason, an additional module has been implemented to the algorithm based on the OSMnx package described in the previous section, so that additional data can be saved in the GeoDataFrame.

As said before, for each building the centroid is known. Thanks to the Google Street View API, it is possible to automatically obtain the façade picture of a desired building, given its centroid coordinates. Indeed, through the `google_streetview.api` dependency, the user can select the location where the picture has to be retrieved (expressed as a pair of coordinates, latitude and longitude), the size of the output picture, the pitch (vertical angle) and the heading (horizontal angle). Specifically, the angle parameters are defined as follows:

- *pitch*: angle variance (up or down) from the camera's initial default pitch, which is often (but not always) flat horizontal (for example, an image taken on a hill will likely exhibit a default pitch that is not the exact horizontal). The default value is 0, and pitch angles are measured with positive values looking up (to +90 degrees straight up and orthogonal to the default pitch) and negative values looking down (to -90 degrees straight down and orthogonal to the default pitch);
- *heading*: rotation angle around the camera locus in degrees relative from true north. The default angle is 0, and headings are measured clockwise (+90 degrees is true east).

In this work, the default size was chosen, i.e., 640x640 pixels (which is also the maximum size for Google Street View pictures). Also, no heading was specified: each time, a value is calculated that directs the camera towards the specified location (i.e., the façade of the building), from the point at which the closest photograph was taken. For what concerns the pitch, an angle of 5° was selected, so that even taller buildings can fit in the image taken (the default value would be 0°, which usually means flat horizontal). Google Street View sometimes offers the possibility to enter some closed places and to obtain indoor pictures of specific buildings, especially when these are public places or private commercial businesses that have given consent to the acquisition of images. However, these types of pictures are not relevant for the sake of this project, since only photos of façades need to be collected. Therefore, the source has been set to “outdoor” images only.

Please note that it is necessary to have a Google API key in order to access this service from Python. For a monthly volume range between 0 and 100,000 queries, the cost is 0.007 USD per each Static Street View requested (i.e., 7.00 USD per 1,000 Street View images), even though a 200 USD Google Maps Platform credit is available each month for each billing account: this means that each month the user can download more than 28,000 images without incurring any costs, and this limit has never been exceeded throughout the duration of this project.

Each street view image is then saved into a folder then can be accessed later on through the following modules of the algorithm. In Figure 4.7, some examples of street view images associated to the area centered in (45.409605, 11.888727) with a radius of 300 meters are shown, while in Figure 4.8 there are other examples of street view pictures associated to the area centered in (45.965009, 12.653791) with a radius of 500 m. The code could easily acquire the street view pictures of all the building footprints in the image, in a fairly short computational time. For an area where the number of buildings is in the range of hundreds, the computational time to perform this task is under a minute.



Figure 4.7 - Examples of street view images obtained from the coordinates of the building footprints for the area centered in (45.409605, 11.888727) with a radius of 300 meters



Figure 4.8 - Examples of street view images obtained from the coordinates of the building footprints for the area centered in (45.965009, 12.653791) with a radius of 500 meters

Unfortunately, even though Google Street View offers a complete coverage throughout the entire Italian territory, it is however true that some pictures of buildings might not be captured, due to the fact that there may not be a street close to the building that needs to be photographed. This is a limit of Google Street View: the acquisition of images is strictly linked to the presence of a road that can be crossed by a vehicle equipped with a camera. Moreover, many Google Street View images may contain pictures of buildings that are partially hidden or covered by obstacles, such as trees, vehicles, or other objects that prevent the viewer (and the algorithm that will be described in the following sections) from having a clear view of the building façade. These issues are actually very similar to the ones that an inspector may encounter during an actual on-site survey of an urban area (for example, the inability to access certain streets or buildings), and considering that our method is indeed trying to simulate an external survey, it is not surprising that our method has the same shortcomings.

### **4.3. Deep Learning for the recognition of building features**

The previous sections have shown how information about building geometries can be obtained automatically, as well as how it is possible to retrieve street-level pictures of multiple buildings remotely, to simulate the process of an actual direct survey at a territorial scale. Clearly, just collecting images of buildings is not sufficient for carrying out seismic risk assessment of an area: each building must be associated to a certain seismic vulnerability level, so that when considering the seismic hazard and exposure, seismic risk can be evaluated. Even though it could be possible to individually observe each street view picture and assign the building to the right category, this operation becomes unsustainable when dealing with thousands of buildings. Although conducted remotely, such an activity would require an excessive amount of time, comparable to an on-site survey. Nevertheless, in chapter 2 (specifically 2.5) many studies that use Artificial Intelligence for the automatic recognition of image features have been presented. Particularly, in the field of Deep Learning, Convolutional Neural Networks can be trained to identify objects and meaningful parts in a picture, and to associate images to a certain category. In the following sections, the algorithm used to predict the height, material, and construction period of a building based on its Google Street View image is presented.

#### **4.3.1. Convolutional Neural Networks (CNNs): a brief history**

Convolutional Neural Networks (ConvNets, or CNNs for short) form the backbone of many modern computer vision systems. Before explaining how Convolutional Neural Networks work, this section provide some insight into the history of CNNs themselves. In 1959, David Hubel and Torsten Wiesel described “simple cells” and “complex cells” in the human visual cortex, proposing that both types of cells are used in pattern recognition (Hubel and Wiesel, 1959). A simple cell responds to edges and bars with specific orientations, while a complex cell also responds to edges and bars, but differs

from a simple cell because these elements can be moved around in the scene and the cell still responds. This property of complex cells is called spatial invariance. In 1962, Hubel and Wiesel proposed that complex cells achieve spatial invariance by summing the output of multiple simple cells that prefer the same orientation (e.g., horizontal bars) but different receptive fields (e.g., bottom, middle, or top of the image). This concept is found throughout the human visual system and is also the fundamental basis of Convolutional Neural Network models (Hubel and Wiesel, 1962).

In the 1980s, Dr. Kunihiro Fukushima was inspired by Hubel and Wiesel's work on simple and complex cells and proposed the model of the neocognitron. The neocognitron model includes components referred to as S-cells and C-cells. The S-cells are located in the first layer of the model and are connected to the C-cells in the second layer of the model. During this process, the local features extracted in the lower stages are gradually integrated into more global features. The basic idea is to capture the concept "from simple to complex" and turn it into a computational model for visual pattern recognition (Fukushima, 1982). This concept makes it one of the earliest precursor to CNNs, and paved the way for further developments.

The actual first work on modern CNNs however emerged in the 1990s, and it was inspired by the neocognitron. In their paper "Gradient-Based Learning Applied to Document Recognition" (1998), Yann LeCun et al. showed that a CNN model that combines simpler features into increasingly complicated features can be successfully applied to handwritten character recognition. In their work, a CNN called LeNet was trained using the MNIST database of handwritten digits (Figure 4.9). MNIST is a dataset that contains images of handwritten digits paired with their true labels 0, 1, 2, 3, 4, 5, 6, 7, 8, or 9. The goal of the project was the prediction of the digit of a sample image, and then the update of the model's settings based on whether or not it correctly predicted the digit.

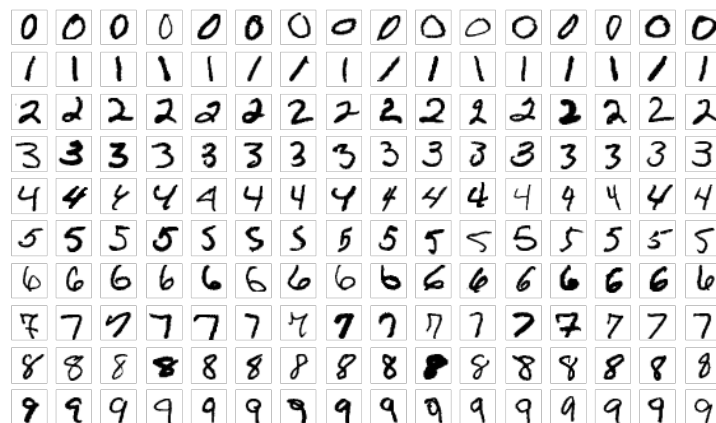


Figure 4.9 - Examples of handwritten digits from the MNIST dataset ([https://it.wikipedia.org/wiki/MNIST\\_database](https://it.wikipedia.org/wiki/MNIST_database))

Throughout the 1990s and early 2000s, researchers carried out further work on CNN models. Particularly, the merit for recent CNN architectures is the ImageNet classification competition called "ImageNet Large Scale Visual Recognition

Challenge (ILSVRC)". Similar to MNIST, ImageNet is a public, freely-available dataset of images and their corresponding true labels. Instead of handwritten digits labeled 0–9, ImageNet focuses on “natural images,” labeled with a variety of descriptors including “strawberry”, “cinema”, and “golden retriever”. The labels were acquired through massive manual labeling. ImageNet currently includes 14,197,122 images (some examples are shown in Figure 4.10). The competition was launched in 2010 and resulted in significant efforts by researchers to benchmark their machine learning and computer vision models on a common dataset, particularly for image classification. In 2012, AlexNet was the first winner of the ImageNet competition, since it achieved a great performance labeling pictures by drastically reducing the error rate. Krizhevsky et al. published the paper “ImageNet Classification with Deep Convolutional Neural Networks” in 2012 describing the model. Since 2012, CNNs have experienced a huge surge in popularity. As a matter of fact, the very next year ZFNet (named after its developers Zeiler and Fergus, 2014) was the new winner of the ImageNet LSVRC. The architecture of ZFNet was the same as AlexNet, but there were a few changes in the hyperparameters, which led to an even better performance of the algorithm. In 2014, one of the most important contributions was the introduction of a new architecture known as VGGNet (Symoniam and Zissermann, 2015), where VGG stands for Visual Geometry Group (Oxford University). The Group was motivated by the idea that by increasing the depth of the algorithm more non-linearities can be modeled. The architecture won the runner-up in the ImageNet challenge in 2014. Great popularity was gained by VGG-16, as well as its deeper variant named VGG-19. In 2014, Google introduced GoogLeNet (Szegedy et al., 2015), which focused on deeper networks but with the objective of greater efficiency to reduce memory usage and computational burden. Its architecture is known as Inception-v1. Inception-v3 and Inception-v4 were also introduced in 2015 and 2016 respectively. He et. al. (2016) from Microsoft Research conceived the idea of “residual blocks”, which are connected to each other in their architecture ResNet. ResNet won 1st place in ILSVRC and COCO 2015 competitions and has continued to be a popular choice for several applications.

Throughout the past several years, CNNs have achieved excellent performance describing natural images (including the datasets ImageNet, CIFAR-10, CIFAR-100, and VisualGenome), performing facial recognition (including CelebA), and analyzing medical images (including chest x-rays, photos of skin lesions, and histopathology slides). The following are some applications of Convolutional Neural Networks in use today:

- *object recognition*: in the last years, sophisticated models such as R-CNN, Fast R-CNN, and Faster R-CNN have been developed, which are the predominant pipeline for many object recognition models used in autonomous vehicles, face recognition, and more;
- *semantic segmentation*: also known as image segmentation, it indicates the task of clustering parts of an image that belong to the same object class. It is a form of pixel-level prediction, since each pixel of an image is assigned to a category;



- *image captioning*: CNNs are also used to write captions for images and videos. This can be used for many applications, such as activity recognition or describing videos and images for people who are visually impaired.



Figure 4.10 - Example images from the ImageNet dataset (<https://becominghuman.ai/transfer-learning-part-3-datasets-and-repositories-cebc644007f4>)

### 4.3.2. Theory of Convolutional Neural Networks

After this brief summary of the history of Convolutional Neural Networks, the technical aspects of these models will now be treated.

A Convolutional Neural Network is a class of neural networks specialized in processing data with a grid-like topology, such as images. A digital image can be conceived as a binary representation of visual data, containing a series of pixels arranged in a grid pattern with pixel values that indicate the color of each pixel. CNNs are deep learning algorithms that can take an input image, assign meaning (learnable weights and biases) to different aspects or objects in the image, and distinguish between them. A CNN is structured so that each one of its layers is able to recognize simpler patterns first (such as lines and curves) and more complex patterns later (faces,

objects, etc.). In other words, the network can be trained to better understand the complexity of the image.

A CNN usually consists of three types of layers: convolutional layer, pooling layer, and fully connected layer.

The convolutional layer is the core building block of the CNN, and it carries most of the computational load of the network. This layer performs a dot product between two matrices, one matrix representing the set of learnable parameters, also called the kernel, and the other matrix representing a portion of the image. The kernel slides over the height and width of the image, creating a two-dimensional representation of the image, called the activation map, which indicates the response of the kernel at each spatial position of the image (Figure 4.11). The sliding size of the kernel is called the stride. Convolution takes advantage of three important ideas that have motivated researchers in computer vision: sparse interaction, parameter sharing, and equivariant representation. Trivial neural network layers use matrix multiplication with a matrix of parameters describing the interaction between the input and output units. This means that each output unit interacts with each input unit. However, in convolutional neural networks, the interaction is sparse. This is achieved by making the kernel smaller than the input. For example, an image may have millions or thousands of pixels, but when it is processed using the kernel, meaningful information can be detected in tens or hundreds of pixels. This means that fewer parameters need to be stored: this not only reduces the memory requirements of the model, but also improves the statistical efficiency. Conventionally, the first convolutional layer is responsible for capturing low-level features such as edges, color, gradient orientation, and so on. With additional layers, the architecture also adapts to the high-level features, understanding the images in their entirety.

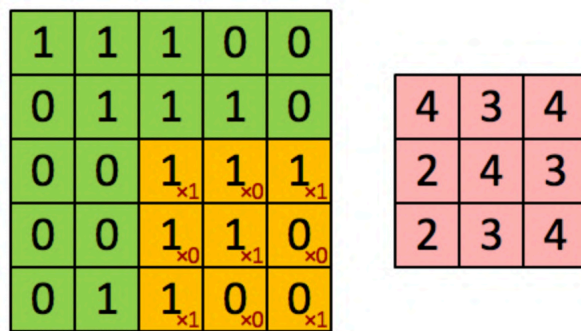


Figure 4.11 - Convoluting a 5x5x1 image with a 3x3x1 kernel to get a 3x3x1 convolved feature

Another essential layer of CNNs is the pooling layer. The pooling layer replaces the output of the network at specific locations by deriving summary statistics of nearby outputs. This helps in reducing the spatial size of the representation, thereby decreasing the computational overhead required. There are several pooling functions, however the two most popular are max pooling and average pooling (Figure 4.12). Max pooling returns the maximum value from the portion of the image covered by the kernel. On the other hand, average pooling provides the average of all values from the portion of the image covered by the kernel. In all cases, pooling provides translational

invariance, meaning that an object is detectable regardless of where it appears in the image.

The convolutional layer and the pooling layer together form the  $n$ -th layer of a convolutional neural network. Depending on the complexity of the images, the number of these layers can be increased to capture low-level details, usually at the cost of more computational power.

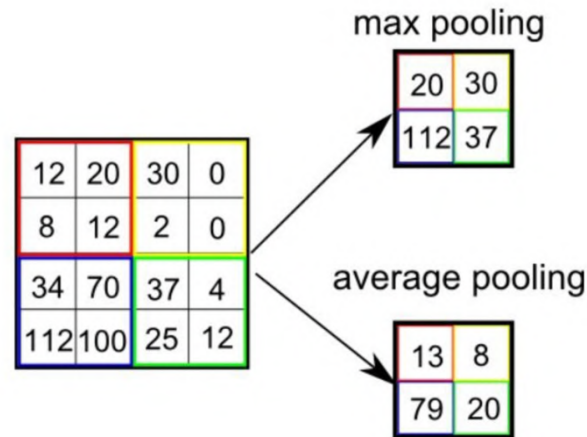


Figure 4.12 - The two main types of pooling: max pooling and average pooling

Next, the final output needs to be flattened for classification purposes. In order to perform this task, the third important type of layer is needed: the fully connected (FC) layer. Neurons in this layer have full connectivity with all neurons in the previous and following layer. The FC layer helps to map the representation between the input and the output, by converting the image into a column vector. Over a range of epochs, the model is able to distinguish between dominant and certain low-threshold features in images and classify them using classification techniques that convert a vector of numbers into a vector of probabilities, such as the softmax activation function. The softmax function is a function that turns a vector of real values into a vector of values that sum to 1.

Since convolution is a linear operation and images are anything but linear, nonlinearity layers are often placed immediately after the convolutional layer to introduce nonlinearity into the activation map. There are several types of nonlinear operations, the best known being: the sigmoid, which takes a real-valued number and flattens it into a range between 0 and 1; tanh, which outputs values to the range  $[-1, 1]$ ; ReLU, which has a threshold to zero. Compared to sigmoid and tanh, ReLU is more reliable and can accelerate convergence by six times.

An example of structure of Convolutional Neural Network is shown in Figure 4.13 (particularly, this is a CNN trained with the dataset MNIST to recognize handwritten digits). Another possible way of visualizing a CNN can be seen in Figure 4.14, where a 3D representation of the layers of a CNN is shown. This network has 1,024 nodes on the bottom layer, six 5x5 (stride 1) convolutional filters in the first hidden layer, followed by sixteen 5x5 (stride 1) convolutional filters in the second hidden layer, then three fully-connected layers, with 120 nodes in the first layer, 100 nodes in the second,

and 10 nodes in the third. The convolutional layers are each followed by a downsampling layer that does 2x2 max pooling (with stride 2). This representation is described by Harley (2015) and can be visualized interactively at <https://www.cs.cmu.edu/~aharley/vis/>.

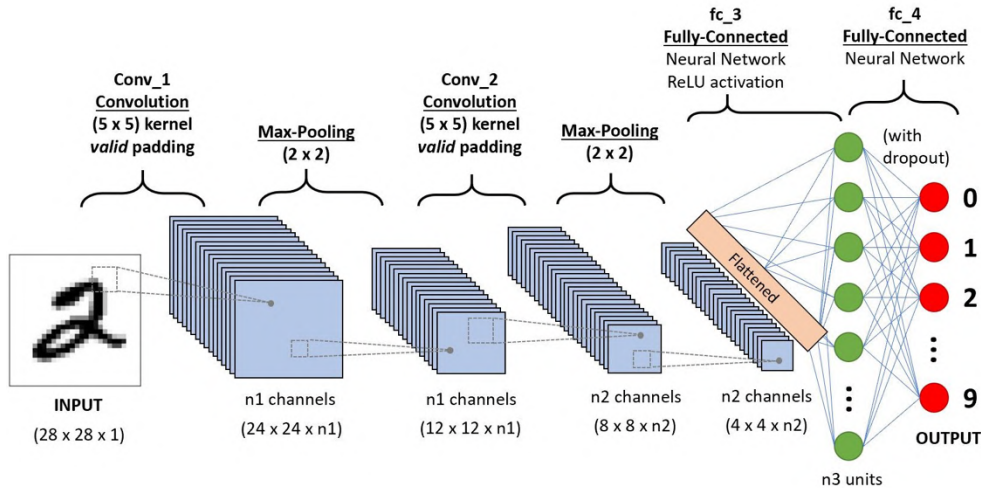


Figure 4.13 - Example of scheme of a CNN



Figure 4.14 - 3D Convolutional Neural Network visualization (Harley, 2015)

#### 4.4. Database of images of Italian residential buildings

In order to train a Convolutional Neural Network, the first step to take is to create a solid and consistent database of images. For this specific work, many images of Italian residential buildings were collected and labeled, according to the different features for which the CNNs needed to be trained: height, material, and construction period. The appropriate number of samples depends on the problem at hand and should be considered individually for each case. However, as a rough rule of thumb, it is recommended to train a CNN algorithm with a dataset of more than 5,000 samples to effectively generalize the problem. It must then be remembered that it is always possible to increase the size of the samples using data augmentation: this method aims

to artificially increase the size of a training dataset by creating modified versions of models (randomly rotating the image, adding reflections, zooming in, adding a color filter, etc.). Data augmentation is a commonly used approach in image processing applications to create variations of images that can improve the network's ability to recognize new images. On the web it is possible to find many datasets that are ready to be used for training CNNs. Some of the most popular are the following:

- MNIST: this dataset has already been mentioned in this chapter, as it represents a milestone in the history of Convolutional Neural Networks. MNIST is a dataset of handwritten digits, which contains a training set of 60,000 examples and a test set of 10,000 examples (for a total of 70,000 images in 10 classes, i.e. the 10 digits from 0 to 9). It has a size of approximately 50 MB;
- ImageNet: also mentioned before, this is a dataset of images that are organized according to the WordNet hierarchy. WordNet contains approximately 100,000 phrases and ImageNet provides around 1,000 images on average to illustrate each phrase. It has a size of 150 GB;
- COCO: large-scale dataset for object detection, segmentation and captioning. It contains 330,000 images (of which more than 200,000 are labeled), 1.5 million object instances, 80 object categories, 5 captions per image, and has a compressed size of 25 GB;
- Open Images: dataset of almost 9 million URLs for images, annotated with image-level labels spanning thousands of classes (more than 5,000). The dataset contains a training set of 9,011,219 images, a validation set of 41,260 images and a test set of 125,436 images, for a compressed size of 500 GB;
- Street View House Numbers (SVHN): real-world image dataset similar to the MNIST dataset, but with more labelled data (over 600,000 images in 10 classes, for a size of 2.5 GB). The data has been collected from house numbers detected via Google Street View;
- CIFAR-10: dataset for image classification, consisting of 60,000 images in 10 classes, with a size of 170 MB;
- Fashion-MNIST: a MNIST-like fashion product database, which contains 60,000 training images and 10,000 test images (size 30 MB). Each image is in gray-scale and associated with a label from 10 classes.

There are also many other datasets that take into account other types of input data. For example, it is possible to find datasets for the natural language processing, which is the application of computational techniques to the analysis and synthesis of natural language and speech. In this case, the dataset will not be composed by images, but rather by text (words, sentences, paragraphs, posts, articles, or even entire books). Also audio/video datasets are available online: these datasets can be composed of audios, sounds, tracks, music samples, speeches, and songs.

Unfortunately, when the aim is to train a Convolutional Neural Network on a very specific task (e.g. on recognizing very specific features on Italian residential buildings, such as in this project), open source datasets are often not sufficient to perform this task. It is therefore required to create and structure an *ad hoc* dataset, in order to have

the best accuracy when predicting features from images that do not belong to the dataset.

There are some useful and practical ways to retrieve images from the web, so that they are automatically downloaded, stored and labeled according to the search parameters. One tool is Microsoft's Bing Image Search API, which is part of Microsoft's Cognitive Services used to bring AI to vision, speech, text, and more to apps and software. This solution allows the user to programmatically download images via a query. Results include thumbnails, full image URLs, publishing website info, and image metadata. It is also possible to apply sorting and filtering options that simplify finding specific results in image searches. Images can also be downloaded with a similar approach that involves Google Images: the images can be obtained through a Python code that gathers the URLs of images through a query. Those methods have been tested to retrieve pictures of buildings that meet certain characteristics and that could be used to train the CNNs, but again the specificity of the problem made it uneasy to take advantage of those tools, however fast and practical they were. Indeed, it should be noticed that the pictures that have to be recognized and predicted by the trained CNNs come from Google Street View. However, when querying pictures of buildings with particular features from the web, it is not always so immediate to retrieve only pictures that can resemble those from Google Street View. As a matter of fact, these algorithms might select pictures that do not have the characteristics of a street view image, i.e., do not look like photographs that were taken by a camera positioned at the street level. Many times drawings, 3D models, schemes, details, or indoor pictures were selected by the search algorithm, despite the fact that specific filters were applied in order to have only photographs. After a visual check of the images that were downloaded by different queries, the amount of pictures that needed to be discarded was too high, so it was considered more efficient to manually collect pictures. Even though this operation might have been more time-consuming, the creation of a robust dataset was deemed of primary importance for reaching the best performance in feature recognition, and thus to achieve the success of the whole project.

Of course, when gathering manually pictures of buildings, it was important to make sure that the buildings were catalogued according to the three parameters of interest, and that the labels were as correct as possible. The level of reliability that could be achieved was regarded as fundamental. For these reasons, the following platforms were considered worthy of use.

#### **4.4.1. Images retrieved from the CARTIS web application**

Firstly, the CARTIS web portal (<http://cartis.plinivs.it/backoffice/login.php>, Figure 4.15) was accessed. This platform collects all the data gathered within CARTIS (Typological-Structural Characterization of the urban compartments), a project that proposes a procedure that involves the construction of regional inventories, obtained through the typological-structural characterization of buildings (Zuccaro et al., 2016). For detailed information about CARTIS, see chapter 2 (paragraph 2.1.3). Particularly, the second level CARTIS forms were the ones that were used to collect pictures and

information about buildings in Italy. As a matter of fact, in the CARTIS web portal these forms are digitally entered online by each research unit who contributed and is still contributing to the CARTIS project (among which we find the University of Padova), and are then accessible to all the other units. It is directly possible to see the main information about the forms that are listed in the portal, such as the code of the form, the Region, Province, Municipality and district to which the form belongs, the type of building surveyed (MUR if masonry building, CAR if made of reinforced concrete), and the state of completion of the form (Figure 4.16).

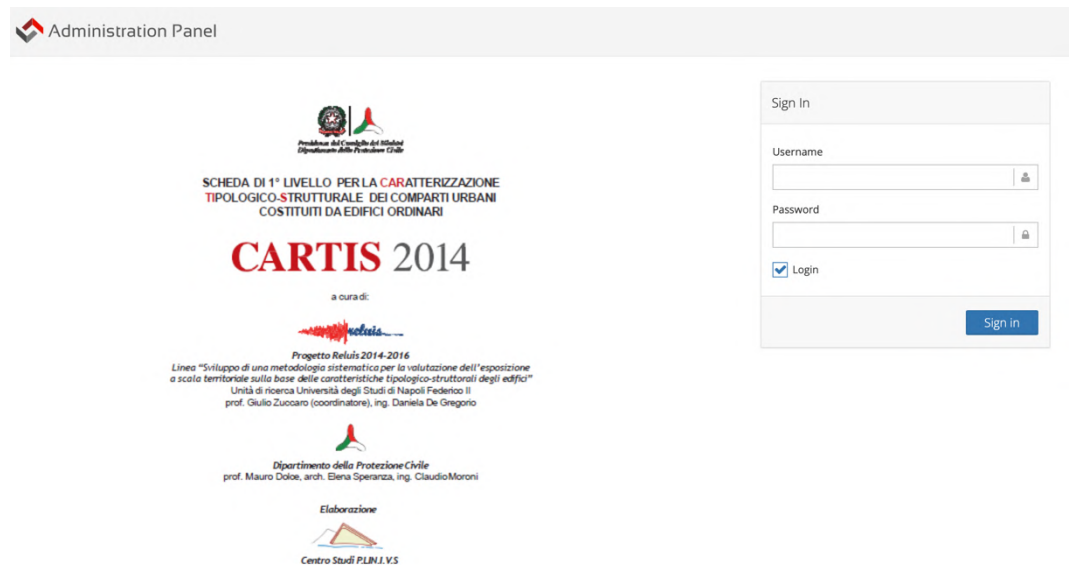


Figure 4.15 - Administration panel of the CARTIS web portal (<http://cartis.plinivis.it/backoffice/login.php>)

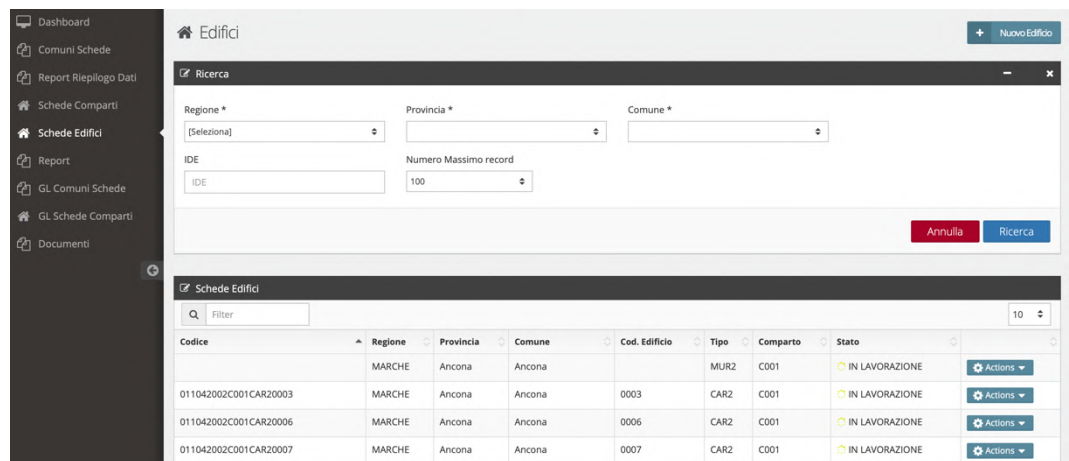


Figure 4.16 - User interface for the second level CARTIS forms in the CARTIS web application

After accessing the form, it is then possible to have further information about the building. What is interesting for the sake of this work is that, among all data inputs, it is possible to find information about the identification of the building, its number of floors, its material, and its construction period. Even more, the compiler has the possibility to attach a picture of the building concerned (this operation is not mandatory, but many compilers provided an image of the building). The images are usually photographs taken from the street level, which makes them suitable to be part

of the database of images through which the CNNs shall be trained. The pictures have to be downloaded one by one, and also the labels have to be associated manually: this makes it a long process, but the amount of images and the quality of information was worth the time spent. Each picture was saved with a univocal code, so that it could be reconducted to its labels. Table 4.1 shows the number of CARTIS forms with an associated picture that could be taken from the web platform. It can be seen that, out of the 2,625 CARTIS forms that were stored in the platform (as of May 2021), 1,264 had an associated picture of the building.

Table 4.1 - Number of second level CARTIS forms obtained from the CARTIS web platform

	<b>Italian Region</b>	<b>N. of forms</b>	<b>N. of forms with picture</b>
1	Abruzzo	104	66
2	Basilicata	50	0
3	Calabria	67	42
4	Campania	500	35
5	Emilia Romagna	109	55
6	Friuli Venezia Giulia	35	0
7	Lazio	10	0
8	Liguria	2	0
9	Lombardia	71	66
10	Marche	500	392
11	Molise	440	38
12	Piemonte	15	13
13	Puglia	12	1
14	Sardegna	0	0
15	Sicilia	104	92
16	Toscana	232	182
17	Trentino Alto Adige	0	0
18	Umbria	125	110
19	Valle D'Aosta	0	0
20	Veneto	249	172
	<b>TOTAL</b>	<b>2,625</b>	<b>1,264</b>

It can be noticed that, although with different amount of pictures, most of the Italian Regions are covered by CARTIS forms with images of buildings. Even though some regions do not present any form, Regions from the same area (Northern, Central, or Southern Italy) are covered. This consideration is essential, since the guideline for the creation of the dataset was the collection of images of buildings belonging to all the possible areas in Italy (e.g., buildings belonging to different Regions, to zones with different altitudes, to different urban areas, etc.). By doing this, the representativeness of the Italian built stock can be maintained, and the neural networks will be able to



better identify images that include any kind of building that can be found in the Italian territory.

For what concerns the labels that were assigned to these pictures, 956 are associated to MUR (masonry buildings), while the other 308 have the CAR code (reinforced concrete). In terms of height, the images contain 678 Low-Rise buildings (i.e., 1 or 2 floors), and 586 Mid-Rise buildings (3 or more floors). Lastly, 597 images belong to the Pre-1919 period, 166 to 1919-1945, 63 to 1946-1960, 241 to 1961-1980, and 197 to Post-1980. Figure 4.17 shows some examples of images downloaded from the CARTIS online platform.



Figure 4.17 - Examples of images downloaded from the CARTIS online database

Furthermore, information about the Italian residential taxonomy also thanks to the direct surveys that had been carried out by the University of Padova within the CARTIS framework. In particular, the research unit of the University of Padova that participated in the CARTIS project worked on the Municipality of Pordenone, in the

Region of Friuli-Venezia Giulia (North-East of Italy) during 2018-2019, publishing the results of the surveys as well as further investigations in the paper by Vettore et al., 2020. Pordenone is a medium-sized town of about 50 thousand inhabitants and 10 thousand buildings (9,171 residential buildings, according to ISTAT 2011), located in the South-West of the Region. In order to facilitate the collection and the management of the data that were requested by CARTIS, a georeferenced (QGIS) multi-level database was created. The specific attribute table (shapefile) with the fields of the CARTIS form allowed an efficient and rapid data entry and the integration of different layers, which are quite useful when dealing with this type of analysis: Google Satellite, CTR, historical cartographies, seismic micro-zonation maps, etc. Furthermore, according to the CARTIS approach, the municipality was divided into nine districts. According to census data (ISTAT 2011), Pordenone counts 3,532 load-bearing masonry buildings (39%), 3,760 r.c. structures (41%) and 1,879 of other typology (20%). Buildings built before 1919 prevail in the central zones, and are typically arranged in clusters, with more or less regular texture, from rough stones and poor mortar to ashlars and bricks with lime mortar, and with traditional timber floors and roofs. On the other hand, the most common types of buildings in the suburbs are the ones built in 1946-1970, made of brick walls and precast r.c. horizontal structures, such as precast joists ('Varese' type) or lightweight hollow bricks with steel bars. Figure 4.18 shows some examples of masonry buildings that can be found in Pordenone, belonging to different construction periods. For a more detailed and in-depth explanation of the various building typologies that were detected in Pordenone, please refer to Vettore et al., 2020.

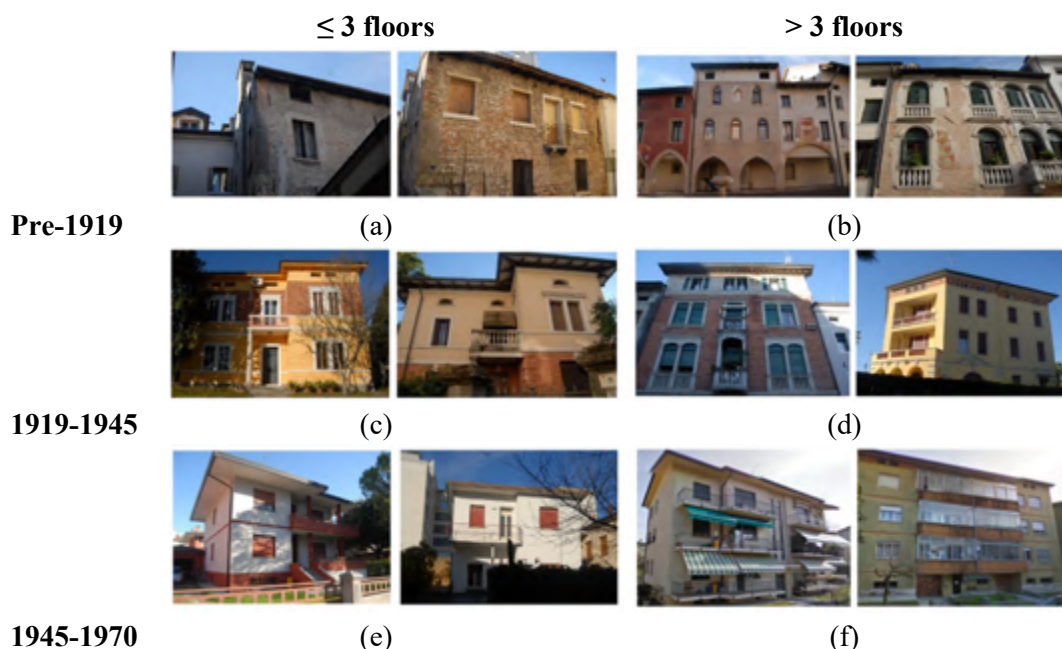


Figure 4.18 - Examples of masonry buildings in Pordenone: a) and b), pre-1919; c) and d), 1919-1945; e) and f), post-1945

As evidenced by Figure 4.18, the extensive two-year survey that was carried out throughout Pordenone allowed the collection of many pictures of different kinds of

buildings, which are all labeled according to the CARTIS parameters (and in these parameters of course we can find the height, the material and the construction period). Not only that, but as mentioned before all the data gathered were then stored in a GIS file, so that all the information was geo-referenced: this means that in case some photographs had not been taken and saved, or some pictures were blurry or not visible from a street level, it was easily possible to go back to the actual building and retrieve the image again, from Google Street View for example, or even more conveniently with the Google Street View API, through the algorithm explained in paragraph 4.2. Thanks to this past work, it was possible to collect in a fairly short amount of time 8,688 pictures of labeled images. The pictures are divided into the following categories: for what concerns their material, 2,354 belong to r.c. and 6,634 belong to masonry; as far as their height is concerned, 4,727 are Low-Rise buildings, while the remaining 3,961 are Mid-Rise buildings; lastly, considering their construction period, 1,843 belong to Pre-1919, 52 to 1919-1945, 3,882 to 1946-1960, 1,407 to 1961-1980 and 1,504 to Post-1980.

#### 4.4.2. Images retrieved from Da.D.O.

Another source from which valuable images of buildings were collected is Da.D.O. (Dolce et al., 2017a, Dolce et al. 2017b, Dolce et al., 2019). Da.D.O. (*Database of Observed Damage*, [http://egeos.eucentre.it/danno\\_osservato/web/danno\\_osservato](http://egeos.eucentre.it/danno_osservato/web/danno_osservato)) is a project funded by the Civil Protection Department, which coordinates its development and scientific content, while the IT development of the platform is carried out by EUCENTRE (European Centre for Training and Research in Earthquake Engineering). The platform was designed to collect, catalogue, and compare data on structural characteristics of buildings, as well as information on seismic damage of ordinary buildings and churches inspected during or following seismic events of national importance (Figure 4.19). Particularly, the contributions to the Da.D.O. - Ordinary Buildings section were offered by the Regions of Abruzzo, Basilicata, Campania, Emilia-Romagna, Friuli Venezia-Giulia, Marche, Molise, Puglia, and Toscana. Specifically, Da.D.O. collects and shows data related to the following Italian earthquakes: Friuli 1976, Irpinia 1980, Abruzzo 1984, Umbria-Marche 1987, Pollino 1998, Molise-Puglia 2002, Emilia 2003, L'Aquila 2009, Emilia 2012, Garfagnana-Lunigiana 2013, Mugello 2019. For each one of these earthquakes, it is possible to download the AeDES form for each building involved in the earthquake and surveyed after that (Figure 4.20). A description of the structure of the AeDES form is provided in chapter 2 (paragraph 2.1.3).

In the AeDES forms, each building is labeled considering its height, material, and construction period, which are the three main characteristics that are sought in the search of images for the dataset. Furthermore, each AeDES form is associated to the coordinates of the buildings it is related to (in terms of latitude and longitude), which makes it practical to retrieve the image of the building through Google Street View, for example. A filter was applied so that only the forms concerning buildings that suffered a D0 damage were downloaded (i.e., only buildings that had no damage, in

order to avoid to collect images of buildings that had incurred severe damage or had even collapsed, thus making them not recognizable for the CNN training process).



Figure 4.19 – User login of Da.D.O. ([http://egeos.eucentre.it/danno\\_osservato/web/danno\\_osservato](http://egeos.eucentre.it/danno_osservato/web/danno_osservato))

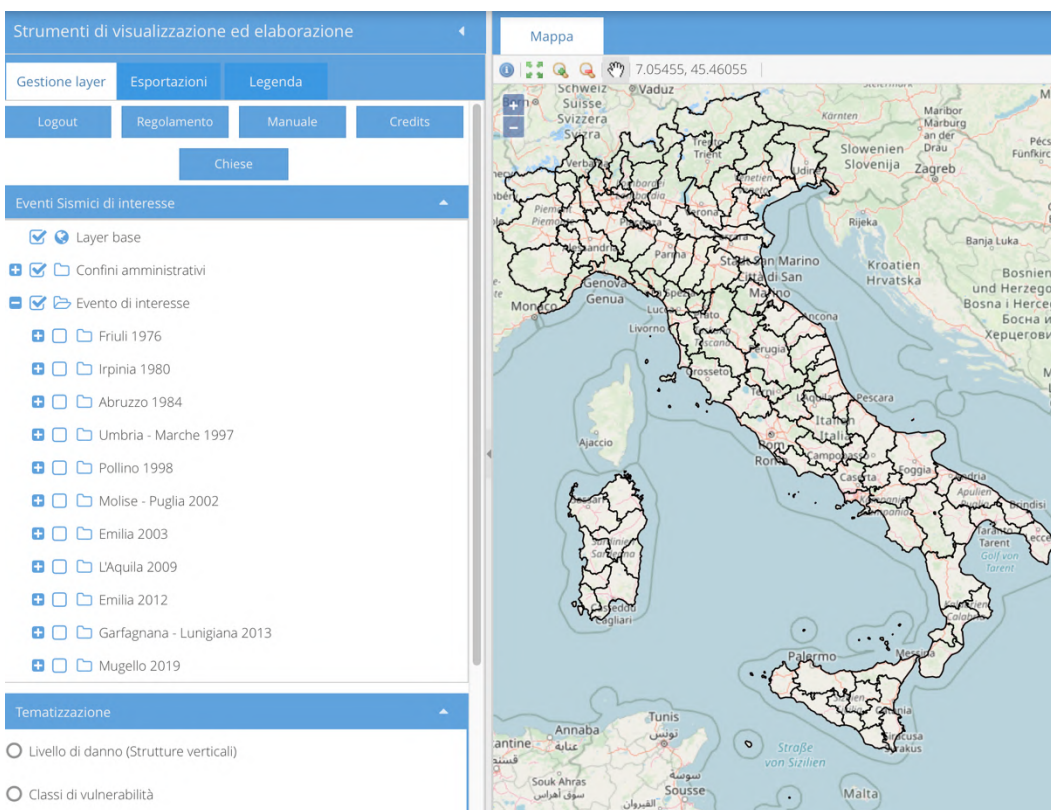


Figure 4.20 – User interface of the Da.D.O. web portal

After applying this filter, the following number of images was obtained for each earthquake survey: 2 for the Friuli 1976 earthquake; 6 for the Irpinia 1980 earthquake; 1,152 for the Umbria-Marche 1997 earthquake; 761 for the Pollino 1998 earthquake; 3,420 for the Molise-Puglia 2002 earthquake; 34 for the Emilia 2003 earthquake; 6,364 for the L’Aquila 2009 earthquake; 1,784 for the Emilia 2012 earthquake; 107 for the

Garfagnana-Lunigiana 2013 earthquake; and lastly 99 for the Mugello 2019 earthquake. The total number of images that could be collected thanks to the Da.D.O. platform is 13,792.

#### **4.4.3. Training, evaluation, and validation sets**

All of the sources mentioned above represent a valid and essential help for the creation of a wide and solid dataset. However, when dealing with such amounts of data it is always preferable to check everything manually, especially when automatic algorithms are utilized to retrieve the pictures (e.g., Google Street View API given the coordinates of a building). As a matter of fact, this may lead to the acquisition of many labeled pictures that do not contain buildings, or where the actual building cannot be seen properly. This is something to be avoided, since it may interfere with the training of the CNNs. For this reason, all the pictures saved in the final folder have been verified, and some pictures have been discarded. This operation led to the selection of a total of 10,000 pictures of buildings that were considered suitable to build the dataset. As said before, each picture had been labeled according to the 3 parameters that were considered useful for the vulnerability assessment of buildings: height, material, and construction period. In this way, it was possible to create 3 different datasets with the same number of images.

Moreover, not all the pictures collected in the dataset are actually used for the training of the CNNs. Some of the pictures are kept for the processes of validation and evaluation. The training set is the set of data that is used to train and make the model learn the hidden features and patterns in the data. In each epoch, the same training data is fed to the neural network architecture repeatedly, and the model continues to learn the features of the data. The validation set is a separate data set from the training set that is used to validate our model performance during training. This validation process provides information that allows tuning the model's hyperparameters and configurations accordingly: the model is trained on the training set, and at the same time, the model evaluation is performed on the validation set after each epoch. The main idea in splitting the data set into a validation set is to avoid overfitting, i.e., the model can classify the samples in the training set very well, but is not able to generalize and make accurate classifications on data it has not seen before. Lastly, the evaluation (or test) set is a separate data set used to test the model after training is complete. This provides an unbiased final performance measure of the model in terms of accuracy and precision. The details of these steps will be explained in the following sections. The splitting of the images into the 3 folders was made by sorting the images in a random way, so that images from different sources could be mixed to avoid the risk that all the images from one source could be used for the training and all the images coming from another source could be used only for the evaluation or validation part. After this randomization, 70% of the pictures was assigned to the folder "training", while 15% ended up in the "validation" folder and the final 15% in the "evaluation" one. There is no fixed rule for deciding how many images are to be destined to the training part, and the percentages are usually chosen through a trial and error process, but according to

previous studies and to other similar datasets, this seemed to be the best solution for the specific case. This splitting was repeated 3 times, for the 3 different features which the CNNs will have to be trained on. In Table 4.2 it is possible to see the number of images belonging to each folder.

Table 4.2 - Splitting of images into training, validation, and evaluation for the 3 features

Feature	Labels	Training	Validation	Evaluation	Total
Height	Low-Rise	4,004	856	856	10,000
	Mid-Rise	2,998	643	643	
Material	Masonry	4,906	1,051	1,051	10,000
	R.C.	2,094	449	449	
Construction period	Pre-1919	1,621	348	348	10,000
	1919-1945	510	109	109	
	1946-1960	2,056	440	440	
	1961-1980	1,826	391	391	
	Post-1980	989	211	211	

As can be seen, within each category the number of images is not always well balanced, meaning that some classes have more images than other (this is particularly evident when observing the number of images associated to each construction period). Usually, the number of images used to train a neural network should be approximately the same, especially if each class has the same probability of being encountered (or if we do not know the probability of meeting each class). However, in this particular case we already know that some building typologies are more likely to be found, and this is also evidenced by the national ISTAT data (ISTAT 2011). To evaluate if the number of images belonging to each class was satisfying, i.e., to see if some classes did not include enough pictures to recognize a specific characteristic, the percentage of images belonging to each class in our dataset has been compared with the percentage of buildings that belong to the same category according to the national census ISTAT 2011. The results of this comparison are shown in Figure 4.21. Particularly, Figure 4.21a exhibits a good correspondence between the percentages of LowRise and MidRise building images utilized in our database and the percentages of LowRise and MidRise buildings according to ISTAT 2011. Regarding the material, ISTAT 2011 not only considers the distinction between masonry and r.c. buildings, but it also takes into account the category “other” (consisting in buildings made of steel, wooden, etc.). Even though the dataset did not consider this additional category, the representativeness of the classes “masonry” and “r.c.” is maintained, as can be seen in Figure 4.21b. Lastly, Figure 4.21c shows the comparison between our database and the ISTAT data for the construction period. This variable was indeed the most critical one, since our dataset contains classes with a number of images that is significantly lower than other classes (this is particularly evident if we compare the 1919-1945 class with the 1946-1960 class). However, Figure 4.21c highlights that the differences in our database are actually very similar to the ones reported in ISTAT, and that the database follows the trend observed at a national level. The main differences consist

in a greater proportion of Pre-1919 and 1946-1960 buildings in our dataset, at the expense of a lower representativeness for buildings belonging to the 1961-1980 and Post-1980 categories. This can be explained considering the fact that many building images have been retrieved from the CARTIS web database, where most of the second level forms had been filed for buildings belonging to historical centers (so usually belonging to the Pre-1919 epoch) or to expansion districts that could be representative of an expansion of the towns, that typically began after the Second World War. These observations can in any case suggest a refinement or an extension of the database, in order to flatten these differences.

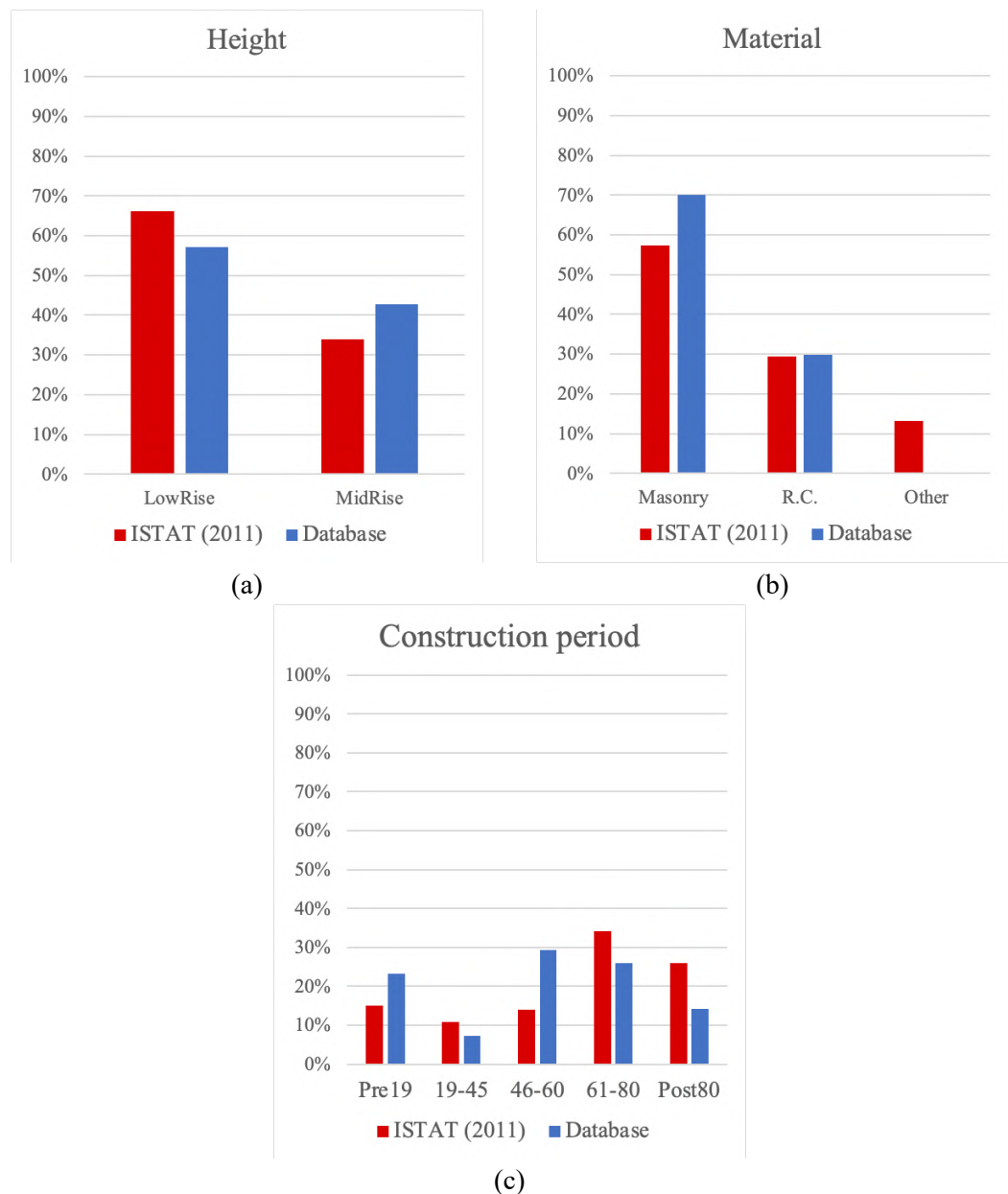


Figure 4.21 – Comparison of building distribution between ISTAT 2011 and our dataset considering the features height, material, and construction period

## **4.5. Training of the CNNs for the prediction of height, material, and construction period**

### **4.5.1. Google Colaboratory**

Now that the dataset is built, it can be used to train the Convolutional Neural Networks. All the codes used are written in Python and have been run on Google Colaboratory. Google Colaboratory (also known as Google Colab), product of Google Research, is a free Jupyter notebook environment that runs in the cloud and can be connected to Google Drive. As of October 2019, the Colaboratory user interface only allows for the creation of notebooks with Python 2 and Python 3 kernels. Python 2, however, reached its end of life on January 1, 2020, and is no longer supported by the Python developer community. Because of that, Colab is in the process of deprecating Python 2 runtimes. Colab allows the execution of Python codes through the browser, and is especially suited to machine learning and data analysis. Colab does not require any setup to use, while providing access free of charge to computing resources including GPUs. This is indeed the main reason why Colab has been used for the execution of the codes, because it makes it possible to run notebooks on a hosted computer that is most-likely better and more powerful than a local machine, leading to faster trainings of CNN models. In particular, Colab currently provides a Tesla T4 GPU. The only downside is that Colab resources, particularly the GPU usage, are not guaranteed and are not unlimited, and the usage limits sometimes fluctuate. This means first of all that notebooks run by connecting to virtual machines that have maximum lifetimes of 12 hours, and also that notebooks will disconnect when left idle for too long, depending on the usage of the specific user. These rules are established in order to prioritize an interactive use, prohibiting actions associated with bulk compute, which would negatively impact other users. It is possible however to avoid this by subscribing to Colab Pro and Pro+, which are services offered with additional charge that do not have the limitations mentioned above, providing priority access to faster GPUs, longer running notebooks and more memory. In any case, for the neural networks that were trained in this study, the thresholds in term of speed and time were never met, so the free version of Google Colab was perfectly sufficient. Another important perk of using Google Colab is that it can be directly connected to Google Drive through the associated Google account, meaning that it is very handy to import data (such as, for example, the pictures of the dataset through which the CNNs are trained), as well as to save the final files where the weights of the neural network models are stored. It is also possible to import data from Github and many other sources, which makes Google Colab very suitable for research purposes.



#### 4.5.2. Transfer learning and fine-tuning

In this section and in the following ones, the core of the code that was used to train the Convolutional Neural Networks that can identify specific parameters from images of buildings will be addressed. The algorithms developed were actually three: one for the prediction of the height (number of stories), which predicts whether a building is a Low-Rise building (1 or 2 stories) or a Mid-Rise building (3 stories or more), one for the prediction of the material, which aims to predict whether a building is made of masonry or reinforced concrete, and the last one for the prediction of the construction period, where the possible age groups are: Pre-1919, 1919-1945, 1946-1960, 1961-1980, and Post-1980. However, since the three scripts are very similar, the pipeline of the code will only be explained once, keeping in mind that in each case the algorithm is trained on the same dataset of pictures, considering though different labels (height, material, construction period). Nonetheless, the small differences among the three codes will be pointed out when necessary.

All the three codes have been written directly in Google Colab notebooks for what concerns the pre-processing of the database and the training; once the models with the weights are saved, they are then used in separate scripts on the local machine to predict the label of pictures that do not belong to the dataset. Google Colab's GPUs were in fact used only to speed up the training process, while when wanting to predict the parameters from pictures that are external to the database, this can be done outside Google Colab.

As mentioned before in this chapter, machine learning offers many different possibilities when the aim is to recognize particular elements in pictures. Among all the possible options, Convolutional Neural Networks have proven to be very useful to perform this kind of task. Nevertheless, even the world of CNNs provides a wide range of different tools that can be combined so that an almost infinite spectrum of choices is available. This is undoubtedly a great resource for the project, but it also poses the question on how to formulate the problem and which solution is the best one. Since many times the answer is not univocal, and many different approaches can lead to similar results, a series of attempts have been made, in a "trial and error" perspective. Finally, the best results have been achieved by using the transfer learning techniques and by fine-tuning it.

As a matter of fact, since so much work has already been carried out in the field of Convolutional Neural Networks, it has become pointless to train an entire CNN from scratch (i.e., with random initialization). Instead, it is common to pretrain a CNN on a very large dataset (e.g. ImageNet), and then use the CNN either as an initialization or a feature extractor for the task of interest. One of the most used Transfer Learning techniques is the one that leverages a CNN as a fixed feature extractor, and then fine-tunes it. More in detail, in this work a CNN is firstly pretrained on ImageNet, then the last fully-connected layer is removed (where the outputs are the 1,000 scores associated to the classes in ImageNet). Consequently, the rest of the CNN is treated as a fixed feature extractor, and a linear classifier (e.g., linear SVM or softmax classifier) can be trained for the new dataset. It is also possible to fine-tune the weights of the

pretrained network by continuing the backpropagation. All the layers of the CNN can be fine-tuned, or some of the early layers can be kept fixed, so that only the higher-level portion of the network is fine-tuned. This is motivated by the observation that the earlier features of a CNN contain more generic features (e.g. edge detectors or color blob detectors) that can be useful to many tasks, but the final layers of the CNN become progressively more specific to the details of the classes contained in the original dataset. In short, fine-tuning corresponds to performing “network surgery”: the final set of FC layers from a pre-trained CNN are removed, and then the head is replaced with a new set of FC layers with random initializations.

This method has been deemed useful to perform the task of recognizing specific features from images of buildings. In this project, a CNN (pre-trained on ImageNet dataset) was taken, and was then fine-tuned to perform image classification and recognize classes it was never trained on. Subsequently, a fine-tuning step was adopted, where the idea was not only to update the CNN architecture, but also to re-train it to learn new object classes.

The process can be summarized in the following steps. The fully connected nodes at the end of the CNN were removed (i.e., where the actual class label predictions are made). These fully connected nodes were then replaced with initialized ones, while the earlier convolutional layers were kept frozen, in order to ensure that any previous features already learned by the CNN are not deleted. With this new configuration, only the new FC layers that are in the head of the CNN were trained. Lastly, the convolutional layers were unfrozen and another training process was carried out.

This procedure takes advantage of a neural network whose layers have already learned rich and discriminative filters, while the brand new FC layers are totally random. If the gradient was allowed to backpropagate from these random values throughout the network, the features that had already been learnt would be potentially destroyed. To tackle this problem, the FC head is trained by itself by freezing all layers in the body of the network. After the FC head has started to learn patterns in our dataset, the training is paused, the body is unfrozen, and it is possible to continue the training.

This fine-tuning technique has proved very powerful to obtain image classifiers on a custom dataset from pre-trained CNNs. The code steps are explained in detail in the following section.

#### **4.5.3. Outline of the script to train the Convolutional Neural Networks**

It is recalled that the CNNs are trained in Google Colab, in order to have a better performance and run the code faster. For this reason, the runtime type must be changed, specifically the hardware acceleration needs to be switched to GPU. It is then possible to check the type of device used through the snippet:

```
from tensorflow.python.client import device_lib
device_lib.list_local_devices()
```

The devices are then printed, and this is an example of the output of these lines of code:

```
[name: "/device:CPU:0"
  device_type: "CPU"
  memory_limit: 268435456
  locality {
  }
  incarnation: 8325539197691550422
  xla_global_id: -1, name: "/device:GPU:0"
  device_type: "GPU"
  memory_limit: 14465892352
  locality {
    bus_id: 1
    links {
    }
  }
  incarnation: 137947544852152167
  physical_device_desc: "device: 0, name: Tesla T4, pci bus id:
0000:00:04.0, compute capability: 7.5"
  xla_global_id: 416903419]
```

In general, during this project, it has always been possible to use the Google Colab Tesla T4, without incurring in any time restriction.

Afterwards, Google Drive has to be mounted in Google Colab. The folders with all the images of the dataset (organized in training, validation, and evaluation folders) had been previously uploaded in Google Drive (as zipped folders). To make Colab connect with Drive, these lines have to be included:

```
from google.colab import drive
drive.mount('/content/drive', force_remount=True)
```

After logging in, Google Colab is allowed to navigate the Drive in which these folders are stored.

Subsequently, all the necessary dependencies are imported. Particularly, TensorFlow plays a crucial role in this code, and many of its features are exploited. TensorFlow is an open source framework developed by Google researchers to run Machine Learning, Deep Learning and other statistical and predictive analyses. TensorFlow is implemented through Keras, an open-source software library that provides a Python interface for artificial neural networks. Among all the possible packages, the following ones are imported:

- preprocessing.image, specifically ImageDataGenerator, which generates batches of tensor image data with real-time data augmentation, as well as other packages to load images;
- VGG-16, the network that was loaded (excluding the head FC layers);
- layers such as Dropout, Flatten, Dense, Input, Model, necessary to create the structure of the CNN architecture;
- SGD optimizer (i.e., gradient descent with momentum optimizer)

Also, other dependencies are imported, in order to manage and visualize the results. The main ones are: numpy, argparse, imutils, pickle, cvs, and os. All these

dependencies are already included in Google Colab, so there was no need to install them.

Once the tools that will be used are imported, it is time to locate the folder with the dataset of images in Google Drive, unzip it, and then create the output folder locally (so that Google Colab can access it directly using its own internal memory, without having to connect to Google Drive each time).

Now, it is necessary to initialize the base path to the new directory that will contain the images after computing the training and testing split. The list of class label names has to be initialized, and the batch size has to be set. The batch size is the number of samples that are passed through to the network at one time. In this work, the batch size is set to 32, as many other works suggest. The reason why this is a good amount of samples is related to computer memory: in fact, choosing a batch size of powers of 2 helps because of the way computer memory works in the GPU. Batches are going to be vectorized and processed in parallel in GPU, and choosing a non-binary (i.e., not in the power of 2) batch size may result in inefficient hence poorer performance. When a large volume of data is involved, small inefficiencies can have a large impact on performance. The specific number must also be calibrated, since using the maximum batch size available on a GPU may not provide the best results, as batch size impacts learning significantly. With smaller batch sizes the estimate of gradient in each epoch is more noisy but it helps the algorithm to avoid local minima. It has to be however taken into account that small batches also make training less efficient, since cost will converge much more slowly. Given all these considerations, a batch size of 32 samples was deemed suitable for this particular project.

Furthermore, the label encoder file path must be initialized, as well as the output directory to where the extracted features will be stored (in CSV file format). Moreover, the paths where the outputs of the model will be saved after training have to be set. Some functions are also defined to visualize images and results. Particularly, one function is intended to plot images (in case pictures are to be viewed), while another function is meant to plot and save the training history (in terms of accuracy and loss). At this point, the image pre-processing phase begins. Firstly, data augmentation is applied, including random rotations, zooms, translations, shears, and flips. The random transformations of the images are not actually added to the original training data, since they are performed in-place, implying that the dataset size does not increase. Of course, these operations concern the training set only, while for the images belonging to validation and evaluation data augmentation is not applied.

After having initialized the data augmentation object, the ImageNet mean subtraction (in RGB order) is defined. This operation consists of a pixel-wise subtraction for all images, so that the data is considered centered. The reason why this step needs to be implemented in the process of training is that each feature should have a similar range of values so that gradients can be comparable. The values are [123.68, 116.779, 103.939] and they are based on the public data from the ImageNet dataset (these three are indeed the mean values of the dataset).

Subsequently, the training, evaluation, and validation generators are initialized so that they can load batches of images from their respective training, evaluation, and

validation splits. Here, the “class mode” has to be selected: “binary” is chosen when the CNN has to predict between only two classes, otherwise the class mode is set to “categorical”. In this lines of the code we find the first difference among the three CNNs that are trained: for predicting height and material, the class mode is binary (Low-Rise vs Mid-Rise, and masonry vs reinforced concrete), while for the prediction of the construction period the categorical mode has to be selected (the classes are indeed five: Pre-1919, 1919-1945, 1946-1960, 1961-1980, Post-1980).

The following part of the code concerns the actual network surgery, which is the main characteristic of transfer learning.

The VGG-16 architecture is loaded (with pre-trained ImageNet weights), omitting the FC layers. It is very practical to load VGG-16 as a base model, since it can be directly accessed through TensorFlow. Moreover, the key:

```
include_top = False
```

allows the exclusion of the last FC layers. As previously mentioned, VGG-16 is a big (around 138 million parameters) but architecturally uniform and simple network, composed of convolutional and max pooling layers, where the input images have a size of 224x224x3 (Symonian and Zissermann, 2015). Particularly, it has 16 layers, and it is formed by convolutional layers with a 3x3 filter, s=1, same padding, and by max pooling layers, 2x2 filter, s=2.

Its structure is shown below:

```
2 conv layers: 64 filters (224x224x64)
Pooling layer: (112x112x64)
2 conv layers: 128 filters (112x112x128)
Pooling layer: (56x56x128)
3 conv layers: 256 filters (56x56x256)
Pooling layer: (28x28x256)
3 conv layers: 512 filters (28x28x512)
Pooling layer: (14x14x512)
3 conv layers: 512 filters (14x14x512)
Pooling layer: (7x7x512)
Fully connected layer: 4096
Fully connected layer: 4096
Softmax: 1000 (total number of final classes)
```

As said before, the last FC layers are however frozen, and a new head of the model that will be placed on top of the base model needs to be constructed. The output of the base model is taken as the new input, and then Flatten, Dense, and Dropout layers are used to form the new head of the model.

Flattening a tensor means to remove all of the dimensions except for one. A Flatten layer in Keras reshapes the tensor to have a shape that is equal to the number of elements contained in the tensor. This corresponds to making a 1d-array of elements.

Dense is used to create fully connected layers, in which every output depends on every input. The activation function has to be selected, and in this case the ReLU and softmax activation functions are chosen. ReLU (rectified linear activation function) is a linear function that outputs the input directly if it is positive, otherwise it will output zero. Softmax instead is generally used in the last output layer and it is a function that converts a vector of numbers into a vector of probabilities, where the probabilities of each value are proportional to the relative scale of each value in the vector. Lastly, the Dropout layer consists in randomly setting a fraction rate of input units to 0 at each update during training time, which helps prevent overfitting.

This new model is then placed on top of the base model, and will become the actual model to be trained.

By setting:

```
layer.trainable = False
```

it is possible to block the layers in the base model. Now the layers in the base model are frozen and they will not be updated during the first training process.

After setting the layers as non-trainable, the model needs to be compiled. Firstly, the optimizer has to be defined. An optimizer is a function that modifies the attributes of the neural network, such as weights and learning rate. Thus, it helps in reducing the overall loss and improving the accuracy. In this case, a SGD (gradient descent with momentum optimizer) is chosen, with learning rate  $lr=1e-4$  and  $momentum=0.9$ .

The learning rate is a tuning parameter in an optimization algorithm that determines the step size at each iteration while moving toward a minimum of a loss function, while momentum is set to speed up the learning rate, by avoiding local minima points so that a global minimum is found. Going into more detail about the learning rate, this is a hyperparameter that controls how much the model needs to be changed in response to the estimated error each time the model weights are updated. Choosing the learning rate is challenging, as a value which is too small may result in a long training process that could get stuck, whereas a value which is too large may result in learning a sub-optimal set of weights or in an unstable training process. The momentum can smooth the progression of the learning algorithm. When a momentum close to 1 is used, such as 0.9 or 0.99, the accuracy of the model on the test dataset appears to be more stable, showing less volatility over the training epochs. It is also possible to use decay for progressively reducing the learning rate (not taken into account in this work).

Secondly, the loss function has to be selected, so that the loss is computed and the network is updated after every iteration until model updates do not bring any improvement in the desired evaluation metric. For what concerns the loss function, a “binary\_crossentropy” is chosen when two classes have to be predicted (so, for the CNNs that predict height and material), while loss is set to “categorical\_crossentropy” when there are more than two classes (in this case, when the construction period has to be predicted).

At this point, the head of the network can be trained while all the other layers are frozen, only updating the weights for the new FC layers, so that they can start to become initialized with actual learned values versus the initial pure random ones.

All the three models have been “warmed up” through 50 epochs. For each epoch, time and speed are evaluated, as well as loss, accuracy, validation loss and validation accuracy.

In machine learning, accuracy is one of the main metrics for evaluating classification models, and it is used to measure the algorithm's performance in an interpretable way. Accuracy represents the proportion of predictions in which the model is correct, i.e., the number of correct predictions over the total number of predictions. Formally, accuracy has the following definition:

$$accuracy = \frac{tp + tn}{tp + fn + fp + tn} \quad (\text{Eq. 4.1})$$

where  $tp$  are the true positive,  $tn$  the true negative,  $fp$  the false positive, and  $fn$  the false negative (see Table 4.3). The definitions of these metrics are explained below:

- True Positive ( $tp$ ): number of predictions where the classifier correctly predicts the positive class as positive;
- True Negative ( $tn$ ): number of predictions where the classifier correctly predicts the negative class as negative;
- False Positive ( $fp$ ): number of predictions where the classifier incorrectly predicts the negative class as positive;
- False Negative ( $fn$ ): number of predictions where the classifier incorrectly predicts the positive class as negative.

Table 4.3 - Graphic representation of the meaning of true positive, false negative, false positive and true negative

		actual value	
		positive	negative
predicted value	positive	true positive ( $tp$ )	false positive ( $fp$ )
	negative	false negative ( $fn$ )	true negative ( $tn$ )

On the other hand, loss is a number that indicates how good or bad the predictions of the model are. If the model's prediction is perfect, the loss is zero; otherwise, the loss becomes greater. The goal of training a model is to find a set of weights and biases that have a small average loss across all examples.

Here the last epoch (number 50) of the first training process for the CNN that is supposed to predict the feature “height” is shown, including the parameters of loss, accuracy, validation loss and validation accuracy.

```
Epoch 50/50
218/218 [=====] - 72s 329ms/step - loss: 0.0040 - accuracy: 0.9991
- val_loss: 0.6683 - val_accuracy: 0.8791
```

The following line shows the same values for the parameter “material”.

```
Epoch 50/50
218/218 [=====] - 79s 363ms/step - loss: 0.0079 - accuracy: 0.9984
- val_loss: 1.2033 - val_accuracy: 0.7921
```

Lastly, the values of loss and accuracy for the last epoch of training of the “construction period” feature are shown below.

```
Epoch 50/50
218/218 [=====] - 60s 276ms/step - loss: 0.0670 - accuracy: 0.9752
- val_loss: 2.8876 - val_accuracy: 0.5163
```

The testing generator is now reset and the network is evaluated after fine-tuning just the network head. This can be done by calculating parameters such as precision, recall, and F<sub>1</sub>-score. Precision (also called positive predictive value) is the fraction of relevant instances among the retrieved instances, while recall (also known as sensitivity) is the fraction of relevant instances that were retrieved. These two parameters can be indicated through the formulas:

$$precision = \frac{tp}{tp + fp} \tag{Eq. 4.2}$$

$$recall = \frac{tp}{tp + fn} \tag{Eq. 4.3}$$

where *tp* indicates the true positives, *fp* the false positive, and *fn* the false negatives (see Table 4.3).

The F<sub>1</sub>-score combines precision and recall of a classifier into a single metric by taking their harmonic mean. It can be computed through:

$$F_1 = \frac{2}{precision^{-1} + recall^{-1}} = 2 \frac{precision \cdot recall}{precision + recall} = \frac{tp}{tp + \frac{1}{2}(fp + fn)} \tag{Eq. 4.4}$$

Figure 4.22, Figure 4.23, and Figure 4.24 show the evaluation of these measures after training the network head only, as well as the graphs of loss and validation throughout this training process.



	precision	recall	f1-score
accuracy			0.86
macro avg	0.86	0.86	0.86
weighted avg	0.86	0.86	0.86

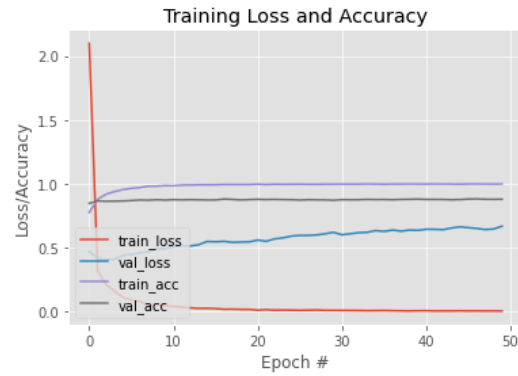


Figure 4.22 - Precision, recall, and F1 score for the parameter "height" after the warmup training

	precision	recall	f1-score
accuracy			0.79
macro avg	0.76	0.70	0.71
weighted avg	0.78	0.79	0.77

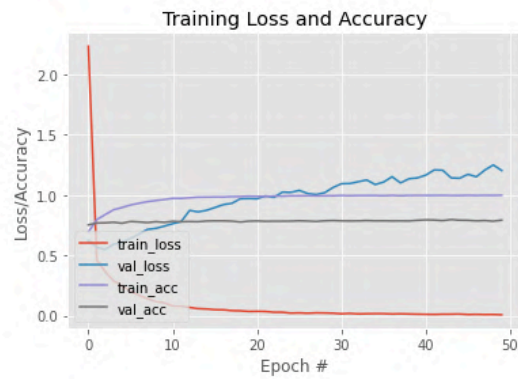


Figure 4.23 - Precision, recall, and F1 score for the parameter "material" after the warmup training

	precision	recall	f1-score
accuracy			0.52
macro avg	0.45	0.42	0.41
weighted avg	0.49	0.52	0.50



Figure 4.24 - Precision, recall, and F1 score for the parameter "construction period" after the warmup training

After allowing the FC Layers to warm up, it is already possible to obtain an accuracy of 86% for the height CNN, an accuracy of 79% for the material CNN, and lastly 52% for the construction period one. The first two CNNs already show a quite respectable accuracy, which goes even evidently above 80% in the case of the “height” parameter. However, the construction period CNN shows an accuracy value that drops to almost 50%: that is of course due to the fact that in this case the CNN is not trained to recognize only two categories (where a 50% accuracy would not be satisfactory), but it has to predict a label among five possible ones. Also, it must be remembered that the size of the dataset stays the same for the three CNNs (the CNNs are indeed trained using the same dataset of building pictures), but while for height and material these pictures are labeled according to two possible categories, for the parameter “construction period” the labels are five, making the number of support images less for some categories, particularly with regards to the 1919-1945 and Post-1980 construction periods (see Table 4.2). Furthermore, compared to height and material, the identification of the construction period of a building is definitely more challenging, and many times even a visual inspection and a detailed survey might fail to correct classify the age of a building. While material and height are usually (even though not always) very clear characteristics that can be easily pointed out just looking at a building façade, the identification of the construction period is often based on smaller details and takes into account features that often overlap between consecutive epochs. This peculiarity will be further discussed at the end of this chapter, where examples for some case study areas are presented.

Now that the head FC layers have been trained and initialized, it is time to unfreeze the final set of convolutional layers and make them trainable. Only the final convolutional block of VGG-16 is unfrozen (not the rest of the network), which means the last three convolutional layers and the last max pooling layer. The model then needs to be recompiled, and also this time a SGD optimizer is used. The model is therefore trained again, fine-tuning both the final set of convolutional layers along with the new set of FC layers. The number of epochs is set to 20, in order not to overfit.

Below it is possible to see the second “unfrozen” training process, where the values of loss, accuracy, validation loss and validation accuracy are shown for the last epoch, i.e., the 20<sup>th</sup> one.

#### Height:

```
Epoch 20/20  
218/218 [=====] - 73s 335ms/step - loss: 0.0024 - accuracy: 0.9991  
- val_loss: 0.6722 - val_accuracy: 0.8920
```

#### Material:

```
Epoch 20/20  
218/218 [=====] - 81s 370ms/step - loss: 0.0081 - accuracy: 0.9977  
- val_loss: 1.3393 - val_accuracy: 0.7894
```

## Construction period:

Epoch 20/20

218/218 [=====] - 62s 286ms/step - loss: 0.0595 - accuracy: 0.9791  
 - val\_loss: 3.1972 - val\_accuracy: 0.5177

The graphs of accuracy and loss are shown also for this new training in Figure 4.25, Figure 4.26, and Figure 4.27.

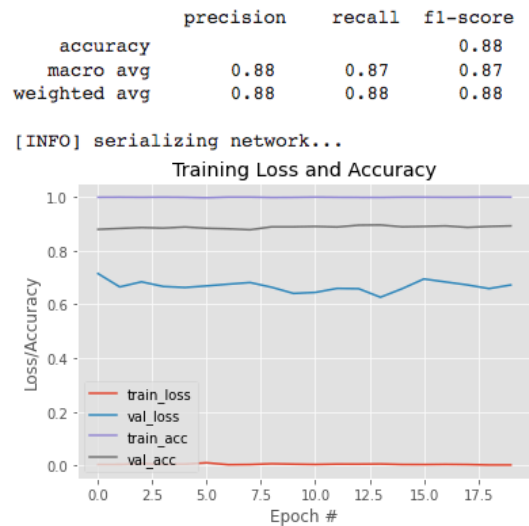


Figure 4.25 - Precision, recall, and F1 score for the parameter "height" after the unfrozen training

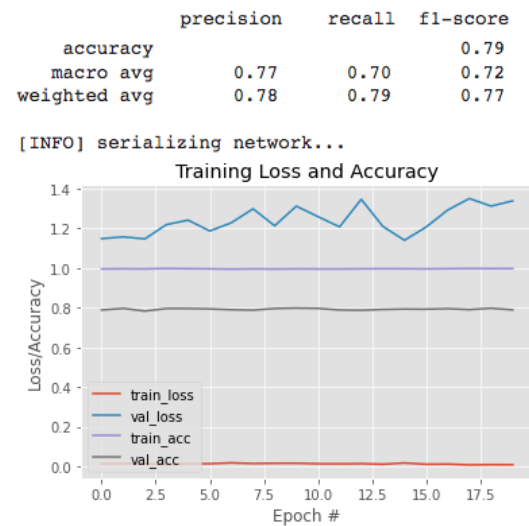


Figure 4.26 - Precision, recall, and F1 score for the parameter "material" after the unfrozen training

	precision	recall	f1-score
accuracy			0.51
macro avg	0.42	0.41	0.39
weighted avg	0.48	0.51	0.48

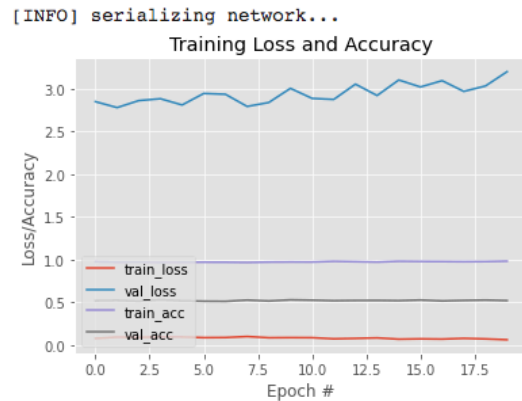


Figure 4.27 - Precision, recall, and F1 score for the parameter "construction period" after the unfrozen training

After the second part of this training process, we can observe a slight but still significant increase in the accuracy of the CNN that is supposed to predict the parameter “height”, while the accuracy for the features “material” and “construction period” do not exhibit strong fluctuations compared to the previous results (when only the FC layers were trained). Overall, the parameters of precision, recall, F<sub>1</sub>-score, and accuracy appear promising and suitable to be used for feature prediction of residential buildings, thus leading to appropriate seismic risk assessments.

At this point, the model can be saved to disk (in this case, in Google Drive), so that it is possible to recall it when we want to predict the labels of brand new images. Once the model is saved in Google Drive, it can be easily exported to the local machine. From this point on, the scripts have been written and executed on the local machine, without using Google Colab anymore.

Three codes have been written in order to predict the height, the material and the construction period of images of buildings, given the weights that were previously computed as a result of the CNN trainings. Of course, each code will access the specific output model. The main packages that are installed and imported for these three codes are `load_model`, dependency imported from `tensorflow.keras` specifically to read the weights of each neural network model, `cv2` (OpenCV) to open and visualize images, as well as other standard packages such as `os`, `numpy`, and `matplotlib`.

Firstly, the image of the building whose feature is to be predicted must be loaded and preprocessed. Particularly, the image needs to be scaled for output purposes: it is necessary to switch from RGB to BGR (since OpenCV loads images in BGR), and most importantly the picture has to be resized to 224x224 pixels (to be consistent with the images on which the CNN had been trained on). The image is then converted to floating points, and a mean subtraction is applied (the same that was applied in the preprocessing phase before training the CNN, with the values [123.68, 116.779, 103.939]). These preprocessing steps are fundamental, since when a prediction script does not provide satisfactory results, most of the times this is due to improper

preprocessing. Typically, having color channels in the wrong order or forgetting to perform mean subtraction can lead to unfavorable results.

Now that the image is correctly preprocessed and read, it is possible to predict its class label, by loading the fine-tuned model and then performing inference to extract the top prediction. This operation can be repeated for multiple buildings, in particular for all the buildings belonging to the area of interest and whose pictures have been collected through the Google Street View API, as explained in section 4.2. The information of each building detected inside the area is already stored in a GeoDataFrame: the prediction for height, material and construction period can be easily added to this spreadsheet in Python, so that each building also has this data associated with it. Figure 4.28 shows some examples of outputs of the three CNNs that have been trained.



Figure 4.28 - Examples of outputs of the three CNNs for the parameters height, material, and construction period

Particularly, pictures of buildings have been retrieved from Google Street View (pictures on which the CNNs had not been trained before), and on the top left of the image it is possible to see the best prediction made by each model, with the score associated to the label. Examples of different buildings are shown, considering the three features (height, material, and construction period) and different categories that can be recognized. For what concerns material, MUR stands for masonry, while CAR stands for reinforced concrete.

#### 4.5.4. Comparison of the CNN predictions with an on-site survey

Other than the internal validation of the Convolutional Neural Networks, that can be assessed at each epoch of the training process, and the evaluation (testing) that can be performed at the end of the training, it can also be useful to compare the predictions of the CNNs on height, material, and construction period with data collected manually during surveys, which can be considered accurate enough for reliable comparison.

As mentioned in section 4.4.1, an extensive survey was conducted during 2018-2019 in the Municipality of Pordenone by the University of Padova, under the CARTIS framework. The data gathered can be leveraged to evaluate whether the neural networks return correct results or not.

In the following images, some comparison are shown between the manual survey of Pordenone and the predictions of the CNNs, for the three parameters height, material, and construction period. Actually, the direct survey carried out in Pordenone allowed the collection of much more detailed information about the residential buildings that compose the urban fabric: for the purposes of this comparison, however, the data have been brought back to the categories that the CNNs can recognize.

Figure 4.29, Figure 4.30, and Figure 4.31 show an example of comparison between the manual survey and the CNN predictions for a central area of Pordenone, right to the north of the historical city center. Particularly, Figure 4.29 focuses on the height of the buildings, where green indicates Low-Rise buildings (1-2- stories), while red indicates Mid-Rise buildings (3 stories or more). Secondly, Figure 4.30 compares the results in terms of material: the footprints in blue represent reinforced concrete buildings, while the ones in brown represent masonry buildings. Lastly, Figure 4.31 compares the predictions for the construction period of buildings, where each color corresponds to one of the possible age categories. The buildings shown in gray are not residential buildings, or their picture could not be retrieved through the Google Street View algorithm. Therefore, the model could not make predictions for the specific building.

Figure 4.32, Figure 4.33, and Figure 4.34 show the same types of comparison for height, material and construction period, but for a different neighborhood in Pordenone (in the northern part of the town, west of the hospital “Santa Maria degli Angeli”).

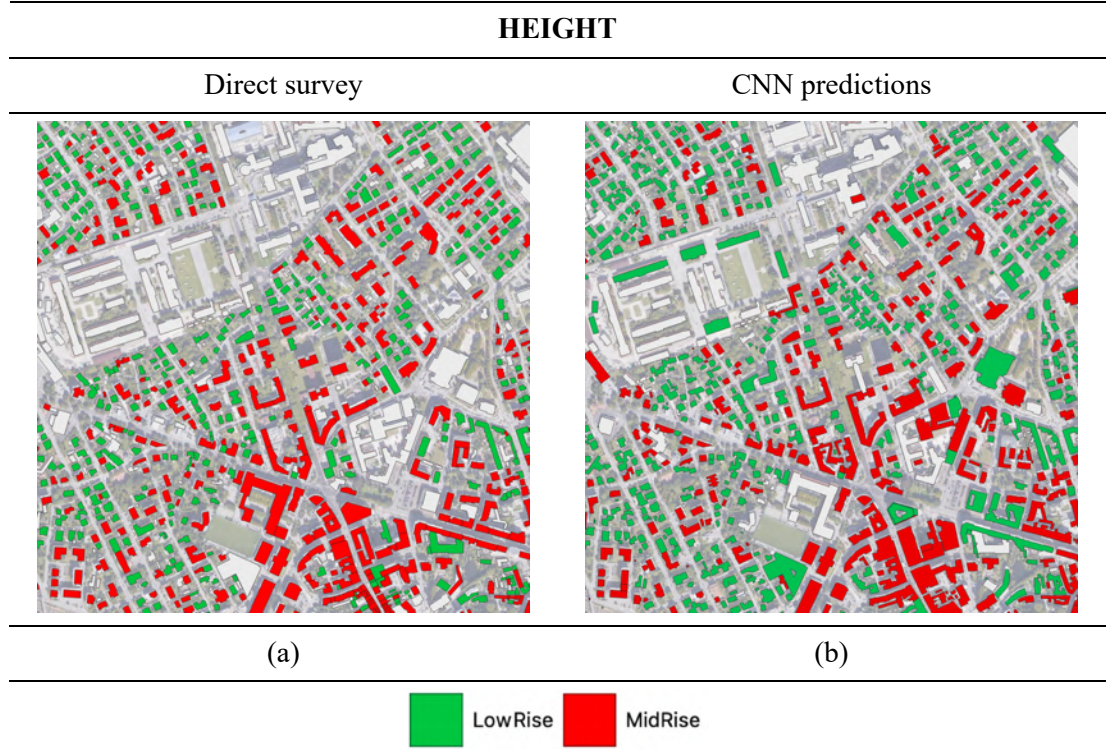


Figure 4.29 - Comparison between direct survey (a) and CNN predictions (b) for the parameter "height", for Pordenone city center

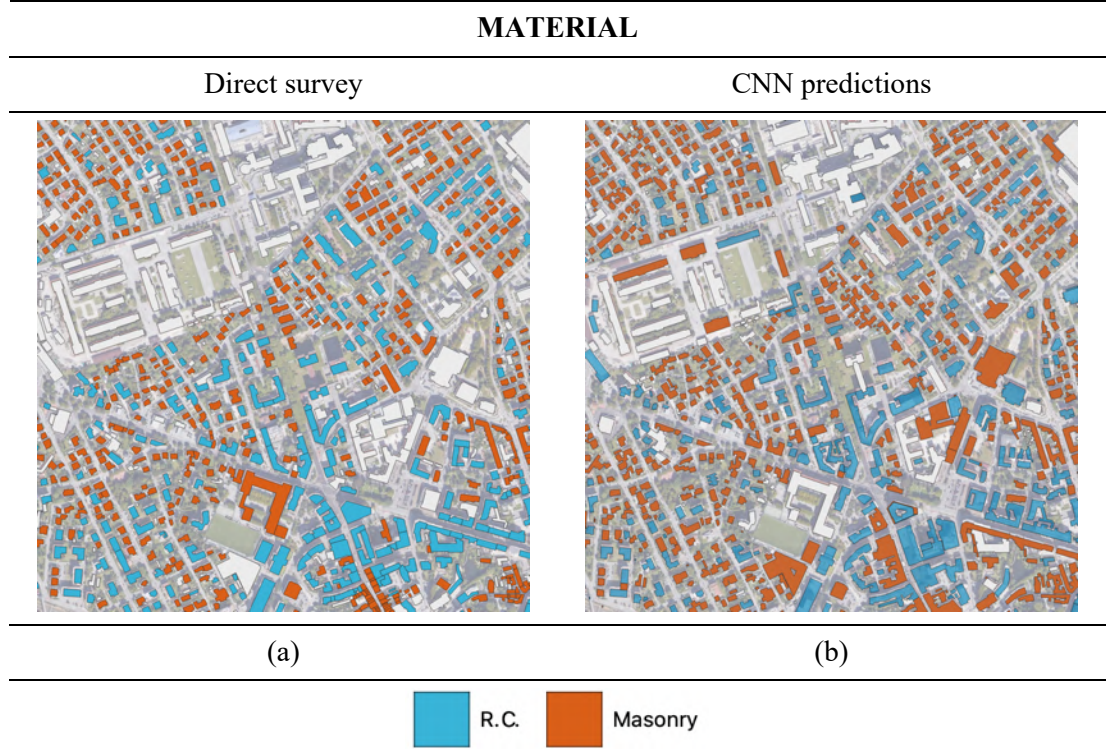


Figure 4.30 - Comparison between direct survey (a) and CNN predictions (b) for the parameter "material", for Pordenone city center

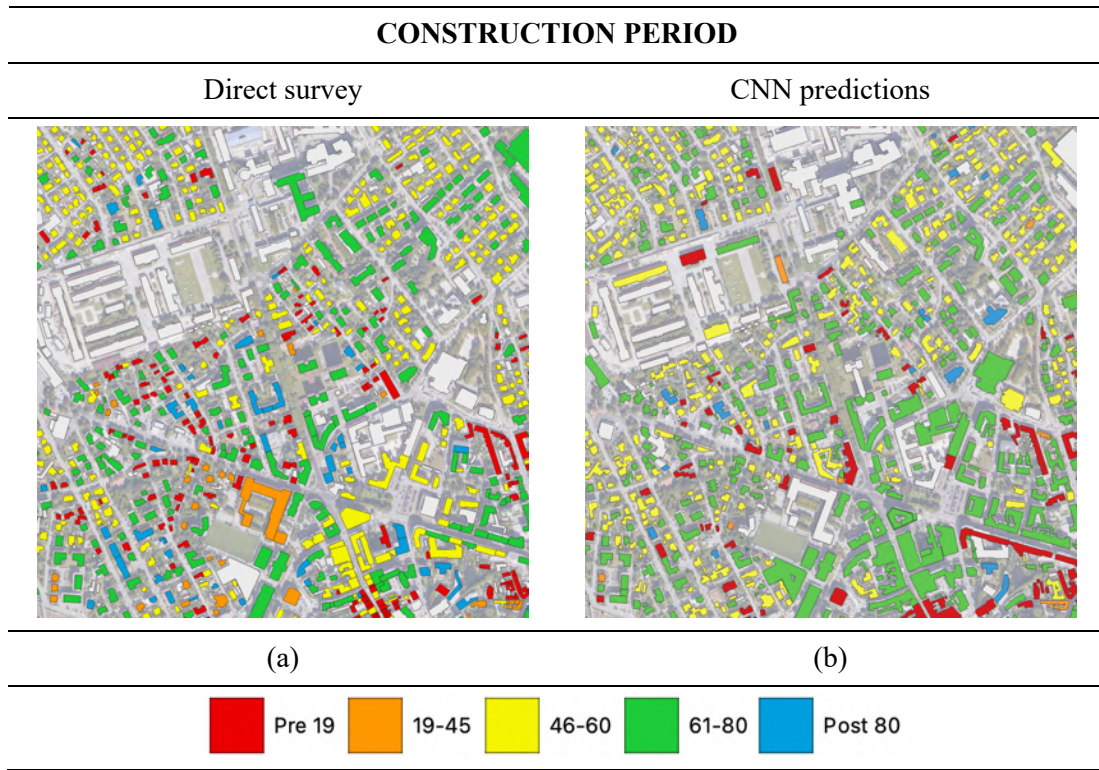


Figure 4.31 - Comparison between direct survey (a) and CNN predictions (b) for the parameter "construction period", for Pordenone city center

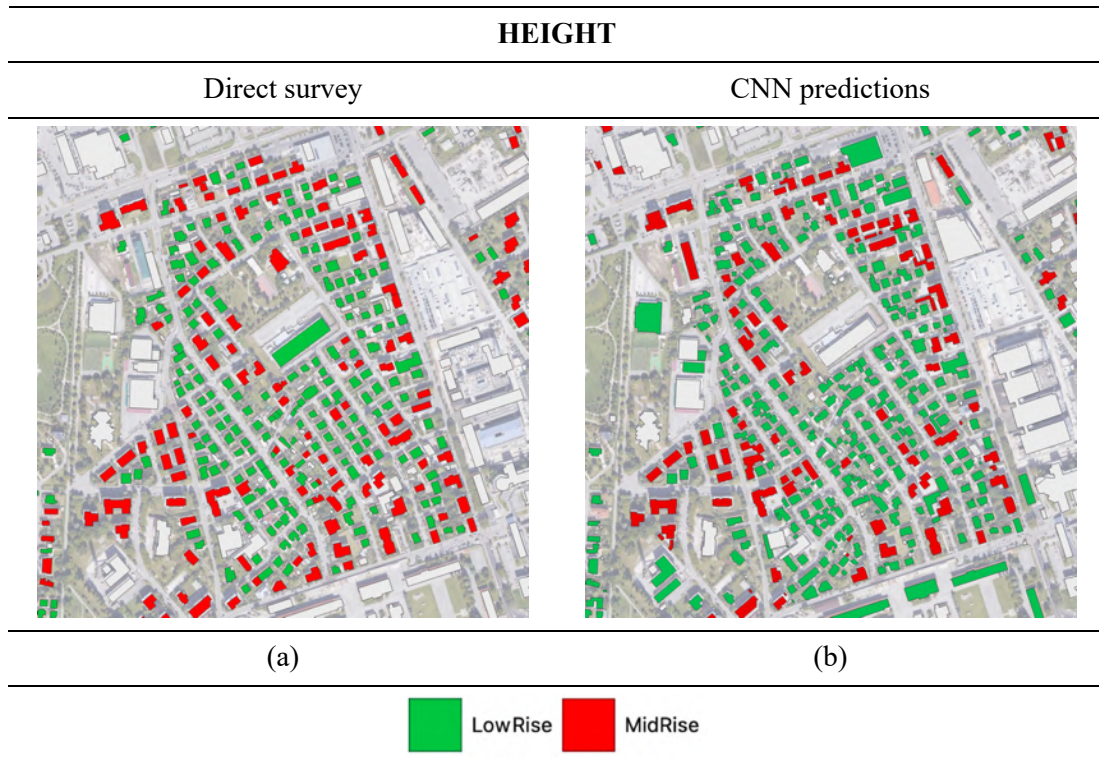


Figure 4.32 - Comparison between direct survey (a) and CNN predictions (b) for the parameter "height", for Pordenone northern area



**MATERIAL**

Direct survey

CNN predictions



(a)

(b)



Figure 4.33 - Comparison between direct survey (a) and CNN predictions (b) for the parameter "material", for Pordenone northern area

**CONSTRUCTION PERIOD**

Direct survey

CNN predictions



(a)

(b)

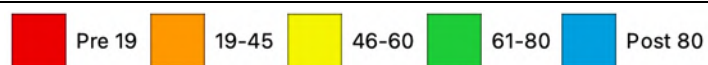


Figure 4.34 - Comparison between direct survey (a) and CNN predictions (b) for the parameter "construction period", for Pordenone northern area

The pictures compared above are shown to have a visual representation of the similarities and differences between the direct survey and the predictions made by the algorithm for some representative areas in Pordenone. However, since both projects take into account the whole town of Pordenone, it is possible to compare the two methods at a larger scale, i.e., at municipality level. Before showing the results of this comparison, some considerations need to be made. First of all, in this work it is assumed that the survey conducted in Pordenone gives the correct data for each single building. Even though this might be very close to reality, given the effort and the time spent for the project, it is not possible to ignore the fact that in such extensive surveys some human errors can occur: whether it is the misidentification of some building characteristics (leading to their incorrect labeling), the wrong classification of residential buildings versus commercial or industrial ones, or even the incorrect data entry in the GIS file where the information was stored. Secondly, as can be noticed (to a certain extent) in the figures shown before, sometimes the footprints derived through OpenStreetMap do not match exactly the ones drawn in the manual survey. This is particularly evident when many close aggregates (clusters) can be found in the same area. This is due to the fact that the survey carried out in Pordenone mainly took into account house numbers, so each polygon corresponds to a different property. On the other hand, the building footprints elaborated by OSM originate from the roof shapes that can be detected from satellite images. For this reason, OSM is not able to separate clusters of residential buildings, and it usually catalogues them as one *relationship* element (since they are often described as a complex polygon with holes inside). This makes the building-by-building comparison slightly more difficult, since many times a one-by-one association cannot be made. In any case, the matching between buildings from the two different sources was performed considering the centroids of buildings, so that each building detected by the OSM algorithm was associated with the building found in the direct survey shapefile, whose centroid was the closest to the OSM building. Once again, this can however represent a source of errors when analyzing the two building samples.

Nevertheless, keeping in mind all these assumptions, Figure 4.35 shows the percentages of correct and wrong predictions of the three CNNs, when compared to the direct survey carried out in Pordenone (Figure 4.35a for the feature “height”, Figure 4.35b for the material, and Figure 4.35c for the construction period).

As can be observed from the three pie charts in Figure 4.35, the correspondence between CNN predictions and on-site survey is very good for material and height, while it seems to worsen for the construction period. Particular attention can be paid to Figure 4.35b, which shows a correct classification of the material of the residential buildings in Pordenone that reaches 76%. These results are perfectly in line with the graphs that were shown in the previous section, where the accuracy of the CNNs for height and material was significantly higher than the accuracy of the CNN that was trained to recognize the construction period. The reasons why this happens have already been discussed (i.e., different number of possible labels, less clear-cut distinctions among categories, etc.).

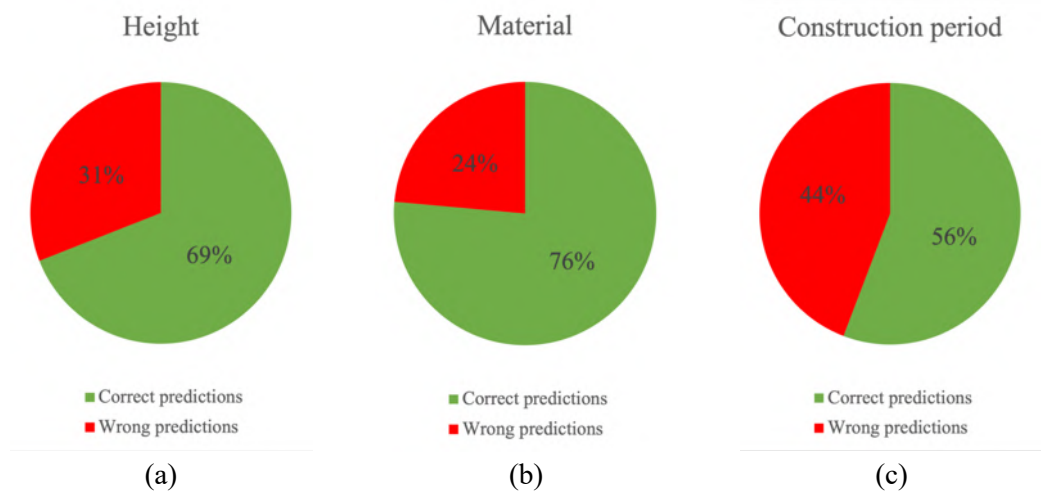


Figure 4.35 – Percentages of correct and wrong predictions of the CNNs for the parameters height (a), material (b), and construction period (c) for the Municipality of Pordenone, when compared to the direct survey

However, while the predictions for height and material can either be right or wrong (0 or 1), the correctness of the classification of the age of a building can be evaluated differently. Indeed, it would not make sense to treat in the same way a prediction that is wrong only by one period (e.g., labeling a Pre-1919 building as a 1919-1945 building) and a prediction that mistakes the age of a building by many decades or even centuries (e.g., labeling a Pre-1919 building as a Post-1980 one). This consideration is even more meaningful if we keep in mind that the aim of this step is to associate each building with the correct fragility set, which relies also on the construction period parameter. Of course, if the construction period predicted by the CNN is very far from the actual one, the fragility model will describe the building behavior in a complete inadequate manner; however, if the error consists only of one construction period, the fragility curves might give only slightly inaccurate results, without being entirely unrepresentative. This observation is perfectly in line with the results presented in Chapter 3, where fragility curves for residential masonry buildings have been presented. When the misassociation of a building with its construction period only consists in one class difference, this might lead to a slight overestimation or underestimation of its seismic behavior (in terms of probability of reaching a certain damage state) that is not supposed to entirely compromise the results of a risk assessment. This is evident when considering the curves shown in Chapter 3 in Figure 3.12, for example, as well as their parameters presented in Table 3.5.

Following this consideration, Figure 4.36 displays the correct predictions versus the wrong predictions for the parameter “construction period” in the town of Pordenone, where the number of epochs deviating from the actual label is differentiated.

For example, if a Post-1980 is labeled as a Pre-1919 building, this will fall into the “4 epochs difference” slice; if a 1919-1945 building is labeled as a Post-1980 building, this will be included in the “3 epochs difference” slice, and so on. Figure 4.36 shows that the percentage of mislabeled building images decreases as the error in terms of “number of epochs” increases. As a matter of fact, most of the images that did not receive a correct prediction for this parameters are actually associated with the next or

previous epoch (“1 epoch difference”). Among all the wrong predictions (that 44% in red in Figure 4.35c), the “1 epoch difference” error represents the 51.4%. This is indeed a promising result, since it suggests that even when the CNN does not label a building correctly, it still associates it with a construction period that will not drastically change the taxonomy of the area under consideration, thus giving a good estimate in terms of exposure and vulnerability. This is particularly true for masonry buildings, as it has been shown in chapter 3 when presenting a fragility model for macro-typologies associated with the same construction periods. For r.c. buildings the errors can be considered more or less critical according to the year of seismic classification of the concerned municipality.

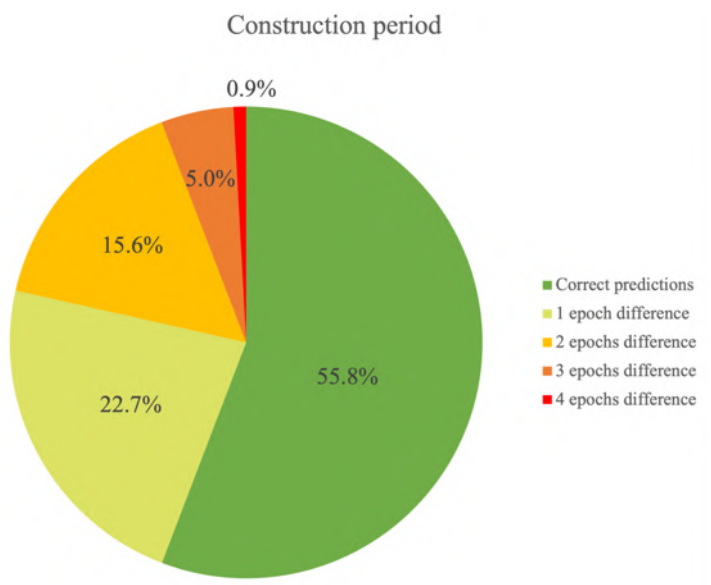


Figure 4.36 – Percentages of correct predictions and predictions with 1, 2, 3, or 4 epochs difference for the Municipality of Pordenone, when compared to the direct survey

Even though these considerations lead to the assumption that the code works well, the prediction errors encountered still leave room to further improvements. With CNNs, it is usually very difficult to establish *a priori* how much the parameters of accuracy can be raised, but previous studies and past works have shown that some techniques can indeed improve the performance of these neural networks. Some examples of strategies and expedients are discussed below.

First of all, the image dataset on which the CNNs are trained might be modified. Since in this case the transfer learning technique is used, it could be possible to take advantage of bigger pre-trained models. However, since this work makes use of the ImageNet database, which is one of the biggest and most popular ones, it is hard to think of a possible improvement in this regard. Nevertheless, the custom dataset also might be refined, particularly by increasing the dataset size or by performing data augmentation.

Furthermore, the algorithm itself could be checked and some modifications might be made. For example, it would be interesting to train the neural networks for different number of epochs (both for the warm up training and the unfrozen training). Although

the number of epochs used in this work are considered sufficient to make the models stable, and usually the performance of a neural network does not experience great changes after a certain epoch, this option should not be discarded. Furthermore, meaningful improvements might be reached by tuning parameters such as learning rate and batch size. This option has already been investigated in this work, since many trials have been conducted before reaching the values presented in this chapter, but of course new combinations might be explored. In addition, it would be possible to try different loss functions and see how they affect the overall performance of the networks. Moreover, in this project a SGD (stochastic gradient descent) optimizer was chosen, but a different optimizer might be used. As a matter of fact, other possibilities are available in literature, such as the Adam optimizer, which uses techniques like momentum and adaptive learning rates for faster training. There are indeed many other optimizers to choose from and experiment with. Lastly, it would be interesting to improve the network architecture or even to try new ones, other than the VGG16 chosen in this study.

Besides possible improvements and future developments that may be included in this work, also further analyses of the results might be carried out.

For example, comparisons across specific sets of buildings could be made, meaning that each building could be individually considered and the predictions on height, material, and construction period should be compared with the data collected manually. This can lead to a better estimation of how much an incorrect classification may affect the assessment of exposure and vulnerability, which could lead to an overestimation or underestimation of seismic damage and risk.

In particular, a focus should be placed on the construction period parameter, which is the one that encounters the highest rate of incorrect predictions. In this way, it could be possible to understand how much this error (which for Pordenone reaches 44%) can affect subsequent risk assessments.

As mentioned above, all the analyses and comparisons made so far apply to the town of Pordenone, and one might think that the error could change considerably if another area is chosen. Although this might be true and of course other towns should be considered in order to further validate the neural network predictions, it should be pointed out that the image database on which the three CNNs have been trained takes into account photos of buildings from all Italian regions, considering larger and smaller municipalities, which are located at the seaside or in mountain areas. For this reason, it is expected that the comparisons are similar for other areas or towns, since the algorithm is intended to work with the same degree of accuracy for every place in Italy. However, in order to prove that this is indeed true, it would be undoubtedly interesting to run the code for municipalities with different characteristics (both in terms of exposure and vulnerability).

What needs to be pointed out, however, is the great benefit that this procedure brings when compared to traditional surveys, especially in terms of time. For the specific case of the town of Pordenone, which counts more than 8'000 residential buildings, the algorithm is able to process satellite images, retrieve Google Street View pictures of each building, and classify them according to height, material, and construction period

in around 2 hours (using a personal laptop, without any additional CPU or GPU). Moreover, all the process is completely automatic, meaning that once the place name “Pordenone” is typed at the beginning of the program, the script does not require any other input from the user. This was indeed the goal that was intended to be pursued: having an automatic and fast method that could replace a direct survey in determining specific building features. The same results took weeks to be achieved through the traditional survey that was carried out in Pordenone, months if we consider the time that was required to digitalize all the data collected in the field.

After these considerations and comparisons, the complete maps of Pordenone with the predictions for height (Figure 4.37), material (Figure 4.38) and construction period (Figure 4.39) for each residential building identified within the municipality are shown. Since the area of concern is quite extensive, especially with respect to the maps shown before, the detail of the representation will probably be lost. However, these maps are more intended to show that the algorithm is able to manage and plot areas of considerable size: of course, when these maps are opened as a shapefile, their visualization is more convenient since it is possible to zoom in and out according to the query needs.

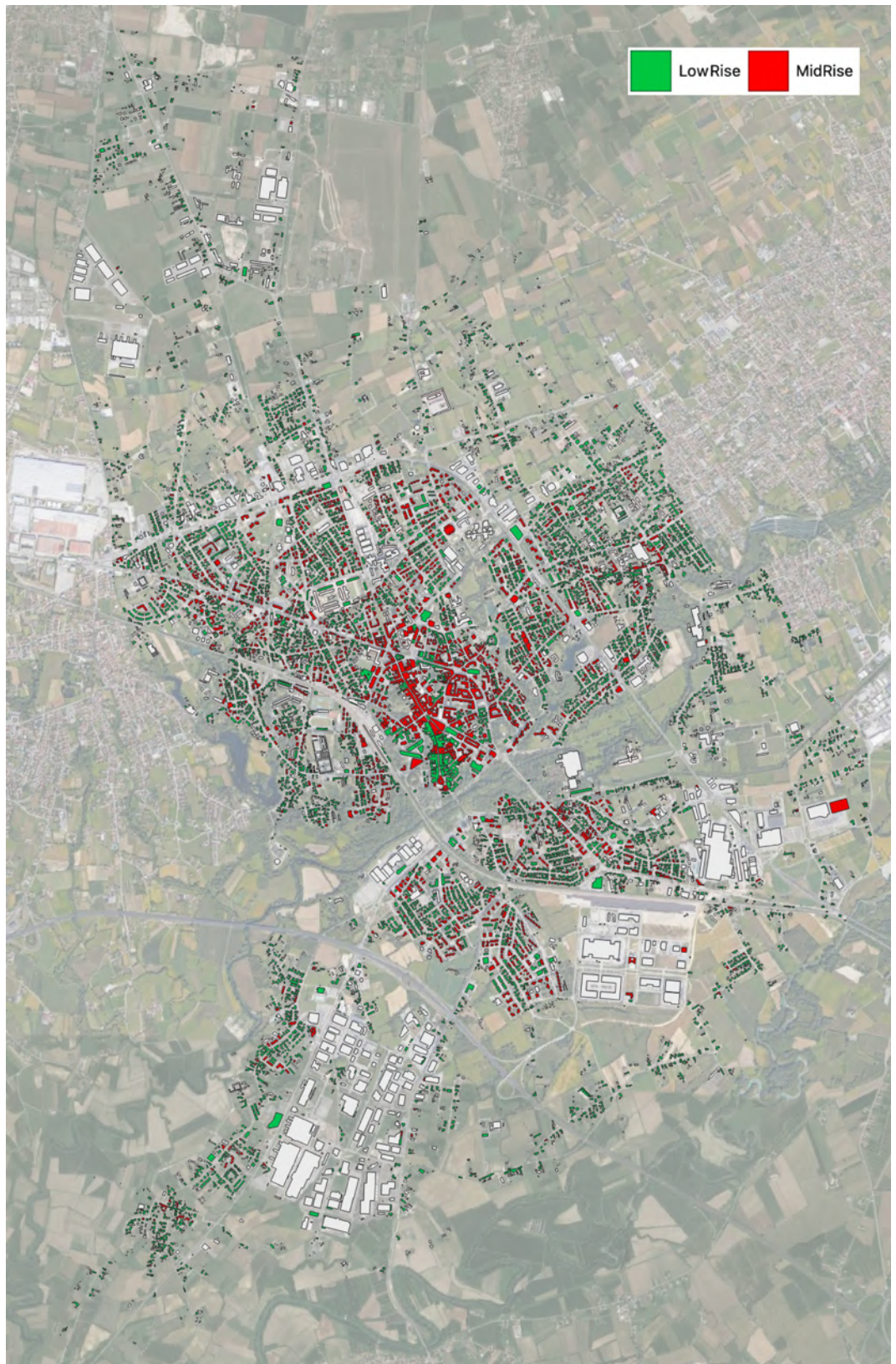


Figure 4.37 - CNN predictions for the parameter "height" for the whole Municipality of Pordenone

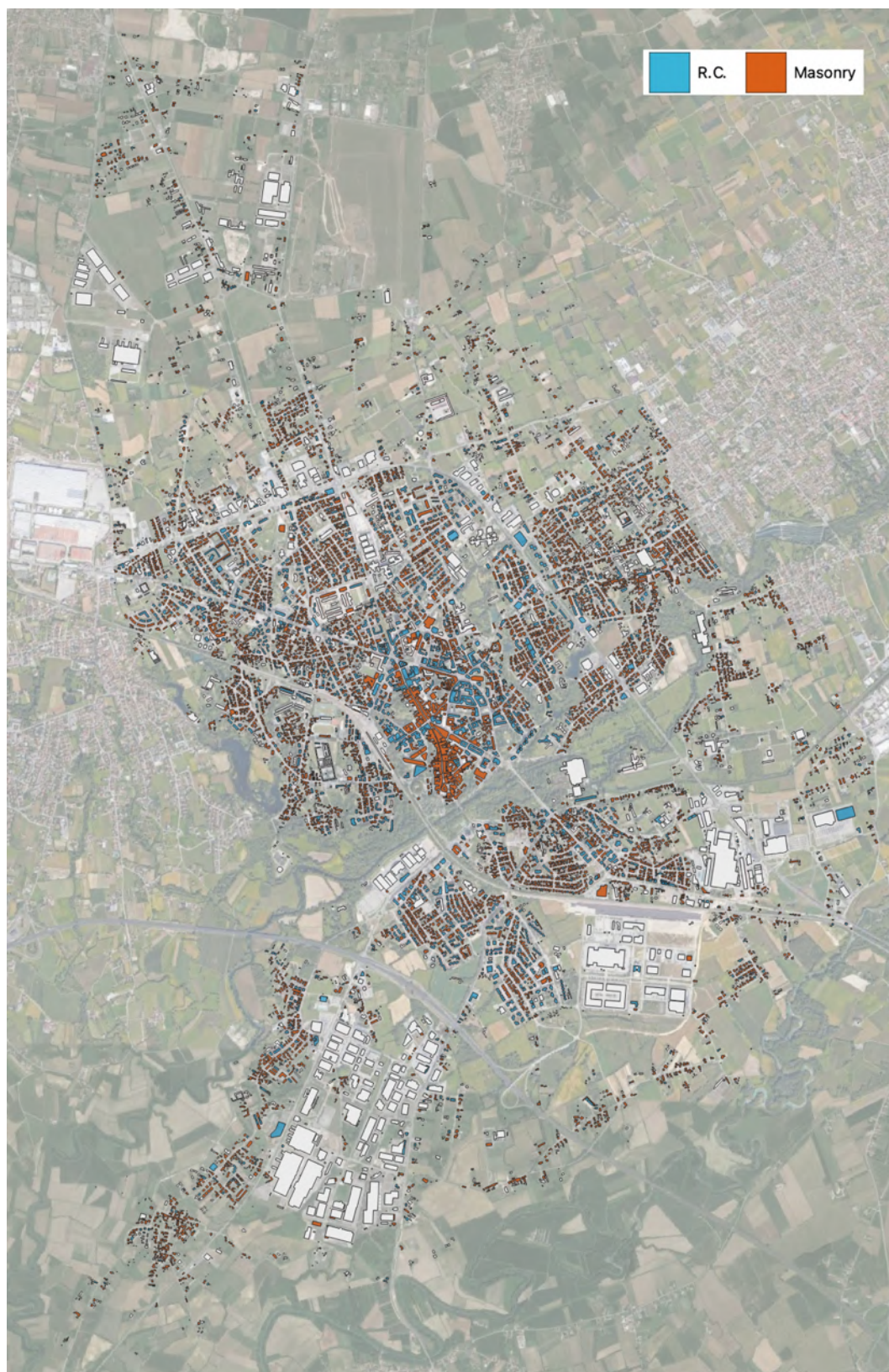


Figure 4.38 - CNN predictions for the parameter "material" for the whole Municipality of Pordenone



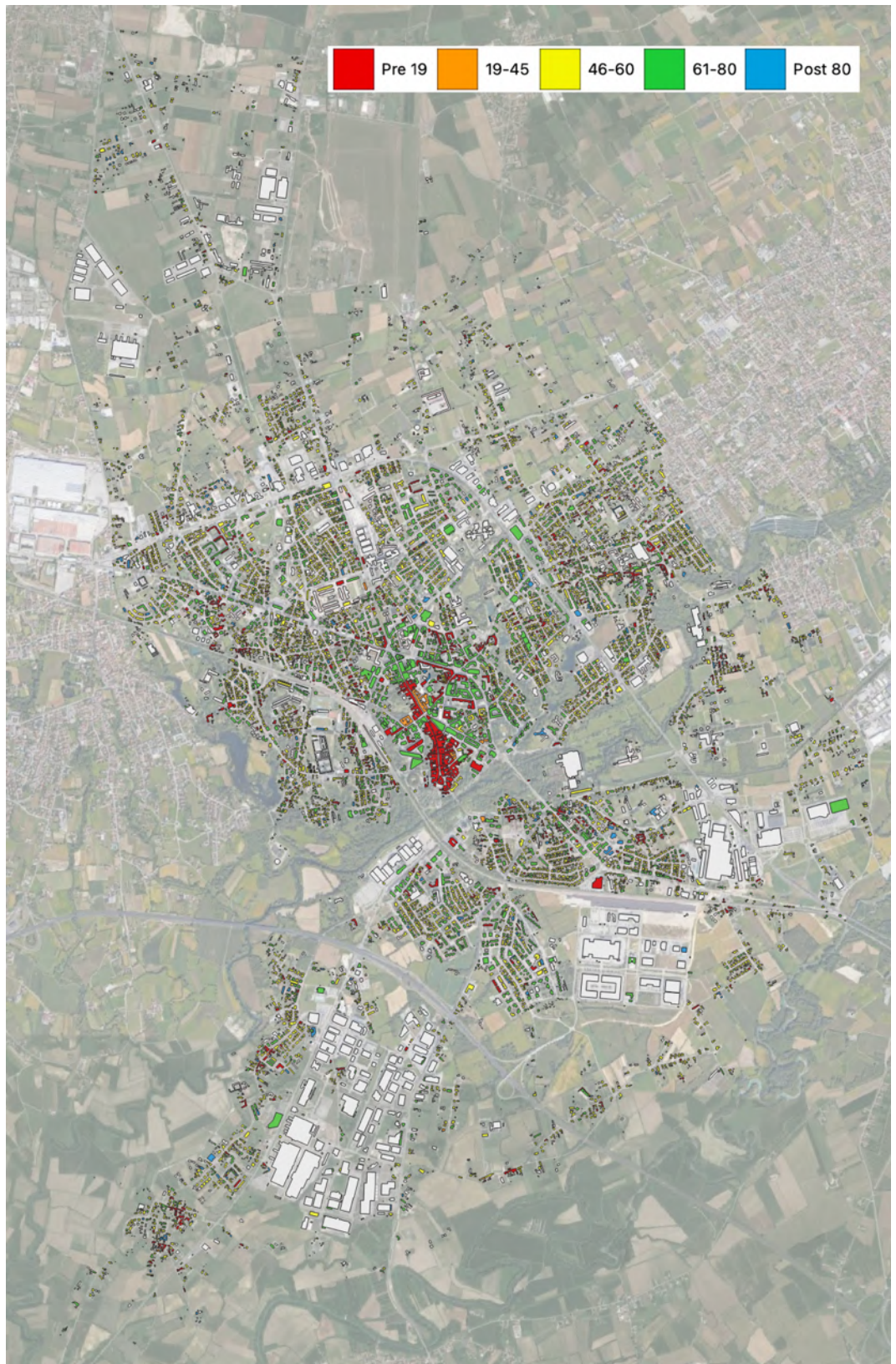


Figure 4.39 - CNN predictions for the parameter "construction period" for the whole Municipality of Pordenone



## 5 SEISMIC RISK CALCULATION PLATFORM

This chapter presents the structure of the seismic risk calculation platform developed in this thesis, which allows the combination of vulnerability and exposure with the seismic hazard of the area of interest, in order to evaluate seismic damage and risk.

Damage is expressed as the probability of reaching or overcoming a certain damage state: when assessing damage at a territorial scale, it is then possible to identify the buildings or areas which are more prone to seismic damage. Risk can then be derived from damage and is usually represented by the possible losses in terms of different indicators, such as repair or reconstruction costs, number of unusable buildings or dwellings, victims, injuries, and displaced people.

This tool might be used for prevention and mitigation of seismic risk by emergency authorities and institutions to manage resources in the aftermath of an earthquake and to select effective emergency measures and recovery plans.

### 5.1. Structure of the platform

In this chapter, the structure of the platform elaborated to compute seismic damage and seismic risk is described. The code is divided in multiple sections or modules, namely the hazard module, the vulnerability module, and lastly the exposure module, containing the consequence matrices that translate damage into risk indicators. As all the other codes developed within this thesis, also the damage and risk calculation algorithms were written in Python.

As said in chapter 4, all the results in terms of building characteristics (mainly geometries, labels, and predictions of height, material, and construction period) can be saved as a shapefile and then visualized in software that supports this type of file format (such as, for example, QGIS). A shapefile can also be easily re-imported in another Python script, since Python possesses packages that allow reading geofiles. This means that the information gathered through the scripts described in chapter 4 can be conveniently retrieved and used in the seismic risk assessment platform. The structure is illustrated below in details.

Firstly, all the necessary dependencies need to be imported. *Pandas* is imported for recollecting the shapefiles with all the building geometries, and for reading the GeoPandas spreadsheets where all the data about buildings are stored. Moreover, the *lognorm* function is imported from the *scipy.stats* package: this dependency is fundamental, considering that we are going to deal with fragility curves that follow lognormal cumulative distributions for what concerns seismic vulnerability. The package *geopy.distance* is also imported, as it represents a helpful tool to calculate distances (in meters or kilometers) between two different geographical points. This operation is used in multiple parts of the script, especially when having to associate a location to a seismic hazard parameter. Lastly, *numpy* and *math* are imported, to perform the main mathematical operations (such as creating arrays or rounding output values).

After having imported the shapefile with all the information about the area analyzed, as it was saved from the previous script, this new script is able to access the data and store them in a GeoDataFrame: essentially, the risk assessment module receives as input data the output data of the previous modules. From now on, the actual computation begins, starting from the assessment of the seismic hazard of the area under consideration, followed by the association of a fragility set for evaluating the seismic vulnerability of each building in the area, and completed by the last module that takes into account exposure and consequence matrices. The final output of this platform is represented by risk indicators such as economic losses, casualties, and impact in terms of usability of buildings and displaced people. Each module is explained and discussed in the following sections.

## 5.2. Seismic hazard module

The first component of risk that is considered by the platform is seismic hazard. The hazard model used in this application is based on the Italian Seismic Hazard map (MPS04) developed by Istituto Nazionale di Geofisica e Vulcanologia (INGV) and adopted at national level with a Civil Protection Ordinance (OPCM 3519/2006; see section 2.1.1). It is the official Italian hazard model (Stucchi et al., 2004, 2011) and provides the seismic action (elastic response spectrum) for 10,751 points of a mesh of 5×5 km covering all the Italian territory. Particularly, MPS04 provides the values of  $a_g$  (maximum horizontal acceleration), FO (maximum value of the amplification factor for the horizontal acceleration spectrum), and  $T_c^*$  (reference value for determining the beginning of the plateau in the horizontal acceleration spectrum), taking into consideration nine return periods ( $T_r = 30, 50, 72, 101, 140, 201, 475, 975, 2475$  years).

The MPS04 grid point closest to the area of interest is selected by the algorithm. Ideally, a particular MPS04 point could be associated with the centroid of each building detected in the area. However, since the points in the MPS04 map are 5 km distant, it is very uncommon for buildings belonging to a small area or a municipality to be referred to different points. Therefore, the code computes the nearest point in the MPS04 grid to the central point of the area of interest (whether it is an area where specific coordinates are selected or the centroid of a municipality). The association to different MPS04 points would make sense only if we were considering a wider area, such as an Italian Province or Region.

Within the hazard module, the platform requires the user to indicate if the damage computation should be performed in terms of conditional or unconditional damage. Conditional damage expresses the expected damage for a specific ground motion (in this case, for a specific PGA). The user is asked to enter the desired return period  $T_r$ , which is associated with a particular PGA value for the nearest point of the grid to the location of interest. On the other hand, unconditional damage does not take into account only one return period (thus one value of ground motion), however it represents the combination of multiple levels of ground motion (for various  $T_r$  values),

taking into account the annual probability of reaching those levels. When computing unconditional damage, an observation time window is chosen (e.g., the next 50 years), and all the possible earthquake scenarios that can occur in the selected time are taken into consideration. Every scenario must be included with its own probability of occurrence in the observation time, as follows:

$$p = 1 - e^{-\left(\frac{T_o}{T_r}\right)} \quad (\text{Eq. 5.1})$$

where  $p$  is the probability that an earthquake with return period  $T_r$  occurs in the observation time. The PGA and its probability of occurrence in the time window selected is calculated for each one of the nine return periods.

In this work, the type of soil was also taken into account for the calculation of seismic hazard. Specifically, the paper by Forte et al. (2019) was considered. Indeed, that work provides maps of seismic classification of near-surface soils for Italy that take into account two sources of information: site-specific measurements and large-scale geological maps. The soil maps were obtained by creating a database of available site-specific surveys covering (unevenly) the entire national territory. From this database, twenty geo-lithological complexes are identified using the available geologic maps, and the surveys are grouped as a function of the geo-lithological complex. The distribution of measured  $VS_{30}$  and  $VS_{eq}$  are then estimated, and medians and standard deviations of such distributions are assumed to be representative of the corresponding complexes.  $VS_{30}$  represents the time-averaged shear-wave velocity (VS) to a depth of 30 meters, while  $VS_{eq}$  derives from a slight modification of the  $VS_{30}$  parameter when considering depths of the bedrock which are less than 30 m. The statistics of these investigations are used to derive the large-scale soil maps. To make the results of the study available, a stand-alone software called SSC-Italy has been developed, and it is publicly downloadable at <http://wpage.unina.it/iuniervo/SSC-Italy.zip>. The results provided by Forte et al. (2019) give a percentage of soil A, soil B, soil C, soil D, and soil E for each Italian municipality. The description of the different types of soils is presented in Table 5.1.

Despite not being adequate substitutes of site-specific studies such as microzonation and local site response analyses, the data provided can be useful for large-scale seismic risk studies. In this project, the percentages of different types of soils for each Italian municipality are derived from Forte et al. (2019) and are saved in an excel file. Subsequently, the Python code retrieves information on the municipality to which the study area belongs (this information has in fact already been extracted from the OSM code described in chapter 4) and associates it with the correct percentages of soil type. The Italian Technical Standards for Constructions (DM 17/01/2018, S.O. No. 8 G.U. 20/02/2018, Italian Ministry of Public Works, 2018) provide guidelines on how to consider this component of hazard by supplying stratigraphic amplification coefficients. These coefficients can be indeed used to calculate the amplification of the ground motion due to soil characteristics. By doing so, it is possible to work with a

more precise parameter that indicates seismic hazard, which takes into consideration the conformation of the area.

Table 5.1 - Description of soil types according to Italian code (Ministry of Public Works, 2018)

<b>Soli Type</b>	<b>Description</b>
Soil A	rocky or very rigid soils
Soil B	soft rocks and deposits of very dense coarse-grained soils or very consistent fine-grained soils
Soil C	deposits of medium dense coarse-grained soils or medium consistent fine-grained soils, with a depth of more than 30 m
Soil D	deposits of poorly dense coarse-grained soils or poorly consistent fine-grained soils, with a depth of more than 30 m
Soil E	soils with characteristics like those defined for categories C or D, with a depth not exceeding 30 m

### 5.3. Seismic vulnerability module

Now that the seismic hazard parameter is defined, vulnerability comes into play. As already stated several times, this work defines vulnerability models making use of fragility curves. The vulnerability module has thus the primary function of loading the fragility curves: for what concerns residential masonry buildings, a detailed description of the vulnerability models that have been developed has already been given in chapter 3. Particularly, the fragility curves presented in Table 3.5 are recalled in case evaluations on buildings in their as built state are to be made; on the other hand, the fragility curves shown in Table 3.11 and Table 3.12 are used when seismic retrofit interventions are taken into consideration. At the current state of this work, the Convolutional Neural Networks can recognize the height, material, and construction period of a building (see chapter 4); unfortunately, they cannot determine whether or not a building has undergone seismic mitigation. Therefore, in this project all the buildings detected are considered in their as built configuration, assuming that none of them has ever experienced a retrofit intervention. As far as reinforced concrete is concerned, we relied on fragility curves from literature. In particular, the model presented in Rosti et al. (2021b) has been deemed reliable and appropriate for this type of analyses on r.c. buildings. The reason why the Rost et al. model has been chosen is that the fragility curves presented in that paper have already been used and validated within the Italian National Risk Assessment document (DPC, 2018) together with the model for masonry described in this thesis, and it has thus been considered eligible for the following large-scale analyses. In Rosti et al. (2021b), empirical fragility curves for reinforced concrete buildings are derived, based on post-earthquake damage data collected in the aftermath of earthquakes occurred in Italy during the period 1976-2012. These data are made available through the online platform Da.D.O., which has already been described in the previous chapters. Among all the earthquake databases,

only the Irpinia 1980 and L'Aquila 2009 ones are considered for further elaborations, as they are the only two that possess an adequate level of completeness for the purposes of the work. The PGA is evaluated from the ShakeMaps provided by the INGV, and six damage levels (from DS0 to DS5) are used for fragility analyses, according to EMS98. The damage levels are obtained from observed damage collected during post-earthquake inspections through existing conversion rules, considering damage to vertical structures and infills. Fragility curves for two vulnerability classes (C2 and D), further subdivided into three classes of building height (Low-Rise, with 1 or 2 stories, Medium-Rise, with 3 or 4 stories, and High-Rise, with 5 stories or more), are obtained. In Rosti et al. (2021b), vulnerability class C2 includes r.c. buildings designed for both gravity and seismic (Pre-1980) loads, while D refers to r.c. buildings with seismic design Post-1980. For this reason, the buildings belonging to construction periods before 1980 have been associated to C2 fragility curves; on the other hand, r.c. buildings belonging to Post-1980 have been associated with D fragility curves. Furthermore, the CNNs developed and described in chapter 4 are not able to distinguish between buildings with 3-4 stories and buildings with 5 stories or more (the neural networks can only categorize Low-Rise buildings, with 1 or 2 stories, and Mid-Rise buildings, with 3 stories or more). For this reason, only the Low-Rise and the Medium-Rise fragility curves have been taken into account; the High-Rise category has not been used in this work in order not to overestimate seismic vulnerability. The median and standard deviation of the curves used within this project for reinforced concrete buildings are shown in Table 5.2.

Table 5.2 -  $\mu$  and  $\beta$  values of the fragility model from Rosti et al. (2021b)

Building macro-typologies		DS1		DS2		DS3		DS4		DS5	
		$\mu$ [g]	$\beta$ [-]	$\mu$ [g]	$\beta$ [-]	$\mu$ [g]	$\beta$ [-]	$\mu$ [g]	$\beta$ [-]	$\mu$ [g]	$\beta$ [-]
Pre-1919	$n \geq 3$	0.1260	0.6930	0.2500	0.6930	0.3970	0.6930	0.8060	0.6930	0.9310	0.6930
	$n \leq 2$	0.2130	0.7900	0.5180	0.7900	0.8570	0.7900	1.3880	0.7900	1.6460	0.7900
1919-1945	$n \geq 3$	0.1260	0.6930	0.2500	0.6930	0.3970	0.6930	0.8060	0.6930	0.9310	0.6930
	$n \leq 2$	0.2130	0.7900	0.5180	0.7900	0.8570	0.7900	1.3880	0.7900	1.6460	0.7900
1946-1960	$n \geq 3$	0.1260	0.6930	0.2500	0.6930	0.3970	0.6930	0.8060	0.6930	0.9310	0.6930
	$n \leq 2$	0.2130	0.7900	0.5180	0.7900	0.8570	0.7900	1.3880	0.7900	1.6460	0.7900
1961-1980	$n \geq 3$	0.1260	0.6930	0.2500	0.6930	0.3970	0.6930	0.8060	0.6930	0.9310	0.6930
	$n \leq 2$	0.2130	0.7900	0.5180	0.7900	0.8570	0.7900	1.3880	0.7900	1.6460	0.7900
Post-1980	$n \geq 3$	0.2530	0.9950	0.7740	0.9950	1.4170	0.9950	2.6820	0.9950	7.3860	0.9950
	$n \leq 2$	0.4220	0.9510	1.1630	0.9510	1.8220	0.9510	3.0240	0.9510	4.4580	0.9510

After entering all the fragility curves into the Python script (for masonry and reinforced concrete), in terms of  $\mu$  and  $\beta$ , those curves need then to be associated to building typologies, according to material, period, and height. This is done by applying a filter to the GeoDataFrame, so that each building is paired with its correct fragility curves. As already mentioned, the fragility curves used in this work are expressed as a function of PGA [g], where each curve represents the probability of reaching or exceeding a particular damage state (DS1, DS2, DS3, DS4, and DS5). It is therefore possible to

read the y-value defined by the curves for the specific value of PGA that has just been computed, and the algorithm can calculate the probability of occurrence for each damage state. A graphic representation of this procedure can be seen in Figure 5.1. In this way, it is possible to assess what is the likelihood for a building to experience a damage state in case an earthquake of a particular intensity occurs.

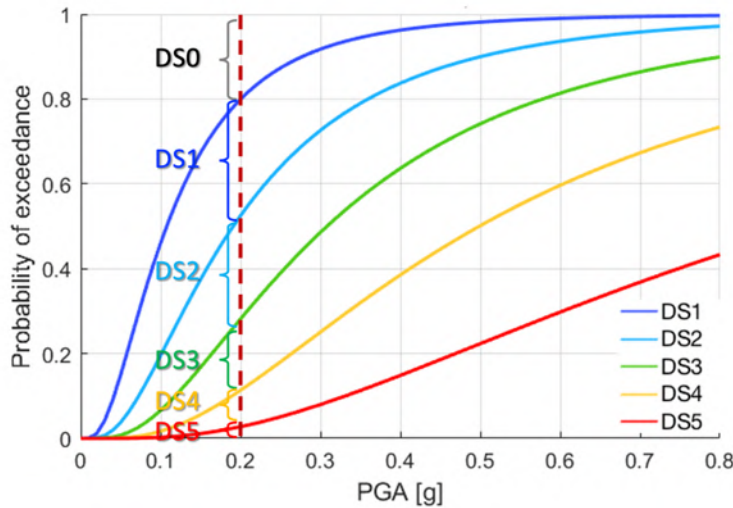


Figure 5.1 – Example of definition of the probability of occurrence for each damage state, given a PGA of 0.2g

This operation is repeated for all the residential buildings in the case study area for which it was possible to retrieve a street view image and predict the parameters of height, material, and construction period: in other words, the damage is calculated for all the buildings that could be associated with a vulnerability model (fragility set). From the probability values of each damage state, it is also possible to calculate the average damage, as:

$$DS_M = \sum_{i=1}^5 i \cdot DS_i \quad (\text{Eq. 5.2})$$

where  $DS_M$  is indeed the average damage and  $DS_i$  represents the probability of occurrence of a damage state. Each damage state is then multiplied by a coefficient  $i$  that goes from 1 (light damage) to 5 (complete collapse). This indicator allows a synthetic representation of damage, suggesting which is the mean damage that a building would incur considering a specific PGA.

### 5.4. Exposure module and consequence matrices

Now that damage is evaluated for each building in the study area, losses can be assessed. When dealing with earthquakes, there are three main categories of losses that should be considered, both from a scientific point of view and for civil protection and emergency management purposes.



Firstly, direct economic losses can be assessed. In order to do so, the economic value of the buildings must be estimated. In this work, a default average value of 1,350 €/m<sup>2</sup> was chosen for masonry and reinforced concrete buildings. Consequently, in order to compute the economic loss that a building may undergo, each damage state is associated with a fraction of the total reconstruction cost. Specifically, Table 5.3 shows the coefficients that represent these percentages, also called damage ratios. For example, for the repair of a building that has reached a DS3 (severe damage), the cost would be 30% of the total reconstruction cost. The value of buildings and the damage ratios were calibrated on the actual repair costs that were monitored in the reconstruction process following the Italian earthquake of L'Aquila 2009 (Di Ludovico et al., 2017a, b, already described in section 2.2).

By multiplying each one of the five damage ratios by the probability of occurrence of the corresponding damage state, it is possible to find a repair cost ratio (RCR) for each damage state. This number represents the percentage of loss due to a particular damage state. Adding together the five partial RCRs, a total RCR can be obtained, describing the most probable loss rate for a building. Ultimately, the total RCR can be multiplied by the total value of the building, thus obtaining the most likely economic loss due to the PGA under consideration. When this operation is reiterated for all the buildings in the area of interest, a value of possible economic loss can be estimated: this can be done for a neighborhood, district, or even municipality.

Table 5.3 – Damage ratios: percentages used for the computation of economic losses

<b>Damage level</b>	<b>Damage ratios (% of total cost)</b>
DS1	2
DS2	10
DS3	30
DS4	60
DS5	100

Furthermore, the number of casualties is another important risk indicator that needs to be considered, especially when dealing with the deployment of emergency services during the rescue phase. As for the economic value of buildings, the human exposure has to be assessed. This is in fact quite simple when we consider an entire municipality, since there are many sources from which the number of total population can be retrieved. In this work, the ISTAT (2011) data were used: even though they do not refer to the current year, they have proven to be reliable when considering population and family statistics. However, when we perform risk analyses on a smaller area, which may not be defined by political or administrative boundaries, it might not be trivial to estimate the amount of population that belongs there. In order to have an approximation of the number of people that might live in a fraction of municipality, the population density was calculated from ISTAT, and then the number of people was calculated based on the total built up area. By doing so, the number of people living in a particular building can be estimated, and the total number of people belonging to the

area of interest can be assessed. At this point, the number of injuries or fatalities can be evaluated. Also for this risk indicator, some coefficients can be associated to each damage state, as a percentage of people.

As described in Dolce et al. (2019), there are several references for estimating expected fatalities after earthquakes. The original idea of Coburn and Spence (1992) has been further developed and updated by several authors based on the local context and taking into account observational data after significant earthquakes worldwide (Spence and So, 2011). An example for Italy can be found in Zuccaro and Cacace (2011). In any case, all the works emphasize the high uncertainty of these estimates, due to several factors that can influence the actual impacts (presence of occupants in different times of the day and year, damage and mechanisms of partial or total collapse of the buildings, effectiveness of rescue measures, etc.). The likelihood of injury or death to building occupants is generally evaluated as a function of the level of damage suffered by the building. It is assumed that the ratio of injuries and deaths is significant only for damage levels DS4 and DS5, the most severe. Table 5.4 lists the standard coefficients for fatalities and injuries, where the values were calibrated using the literature cited above. It was assumed that the number of fatalities is equal to the one percent of people living in buildings that have reached damage level DS4 (very severe damage) plus the ten percent of people living in buildings that have reached a DS5 (collapse). The calculation for the injured follows a similar method, with different percentages for DS4 and DS5.

Table 5.4 - Percentages used for the computation of casualties (fatalities and injuries)

<b>Damage level</b>	<b>Fatalities (% of people)</b>	<b>Injuries (% of people)</b>
DS1	0	0
DS2	0	0
DS3	0	0
DS4	1	5
DS5	10	30

Lastly, a section of the code is dedicated to the evaluation of the usability of buildings and the consequent number of displaced people. Table 5.5 shows the coefficients that relate damage states to building impact, i.e., the percentage of damaged buildings that corresponds to the selected impact. In this work, each damage state can be associated with different outcomes in terms of usability: the building can be considered usable, not usable in a short or in a long time span, or collapsed. These outcomes are related to the damage states according to particular percentages, which sum up to 100% for each damage state.

In this way, it is possible to assess what will be the state of a building after a seismic event of given PGA, and thus predict the condition of an area or town in terms of usability. Going even deeper, it is possible to have an estimate of how many displaced people there may be after the earthquake, which will lead to a better understanding of how many safety workers and infrastructures should be deployed for such an

emergency. In order to compute this indicator, people living in buildings that are considered collapsed or not usable in a short or long time span are counted as displaced, while people belonging to usable buildings are not counted in. The sum of all the displaced people can give an important information on the impact of the earthquake, when the aim is to take care of homeless people in the aftermath of the event.

Table 5.5 - Percentages used for the computation of building usability

Damage level	Usable (%)	Not usable in a short time span (%)	Not usable in a long time span (%)	Collapsed (%)
DS1	100	0	0	0
DS2	60	40	0	0
DS3	0	40	60	0
DS4	0	0	100	0
DS5	0	0	0	100

The general framework described in this last section is graphically summarized in Figure 5.2, where the main steps that lead from the definition of damage to the assessment of the different risk indicators are shown.

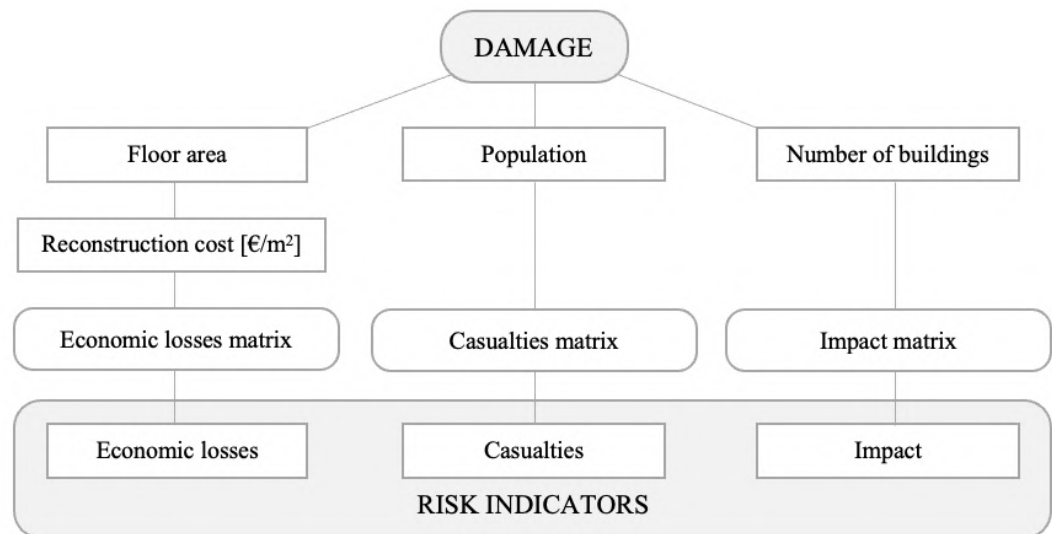


Figure 5.2 - General framework for risk assessment

Although the information that can be retrieved from this procedure are fundamental for the definition of risk, it has to be reminded that these are only partial indicators, and that many other factors should be taken into account (such as indirect economic losses, just to cite one). However, since the focus of this work is put on residential buildings, direct economic losses, casualties and impact can already give a good representation of risk at a territorial scale.

In this chapter, the architecture of the platform and the different modules that compose the platform itself have been presented. In the following chapter, some real case studies

will be shown, where this procedure is applied to different areas in Italy. Damage maps will be produced in terms of conditional and unconditional damage, as well as risk maps expressing the risk indicators mentioned in this chapter.

## 6 RESULTS

This chapter presents all possible results that can be derived within the scope of this thesis project. As a matter of fact, what is presented below is the outcome of the combination of all the findings that have been discussed in the previous chapters. Results can be provided both in terms of conditional damage or risk (i.e., considering a specific return period, thus a single seismic intensity) and unconditional damage or risk (i.e., for a time window). The outcomes are presented mainly through damage or risk maps, but also through histograms, pie charts, and tables. Additionally, this chapter is supposed to highlight the versatility and automation of the procedure: for this reason, different case study areas in terms of geographic locations and territorial scales are presented. Moreover, other works and tools are used to validate the procedure and the platform developed in this thesis: specifically, on site damages surveys are compared to the predictions of damage made by the algorithm, while risk indicators are compared with the result provided by an external platform for risk assessment. Lastly, a simulation of the effect of different seismic mitigation strategies is performed, in order to understand the possible benefit of seismic retrofit at a territorial scale.

### 6.1. Damage maps

The damage maps presented in this section are intended to show what is the probability of reaching the possible damage states (from DS1, slight damage, to DS5, collapse) for each building identified in a specific area. Moreover, following the calculation presented in Equation 5.2, it is also possible to visualize the average damage of each building. These maps are presented at a local scale up to a municipality scale. In addition, the results provided in terms of average damage are then compared with the results of a project carried out after the 2016 Central Italy earthquakes, where the seismic damage of the buildings in the Municipality of Castelsantangelo sul Nera (Province of Macerata, Marche Region) was surveyed on site and a damage state was associated to each building. This validation gives an indication on the quality of the estimates provided by the prediction algorithm, highlighting its strengths and weaknesses.

#### 6.1.1. Conditional damage maps

As mentioned in chapter 5, conditional damage is a representation of damage that takes into account only one return period, thus one ground motion intensity (in this case, one value of PGA expressed in  $g$ ). In the following maps, some examples of conditional damage are shown in the Municipality of Pordenone for a return period of 475 years. Regarding the PGA that was taken into account to run the simulations, the point belonging to the MPS04 grid that was closer to the center of the area under investigation was used (see chapter 5 for more details on the seismic hazard maps that

were used in this project). Moreover, the type of soil of the area was also taken into consideration, according to the maps provided by Forte et al. (2019). For Pordenone, the soil is deemed to consist of 79% soil B, and 21% soil C. As a result of all these considerations, the PGA associated to a return period of 475 years (i.e., for a seismic scenario that has 10% probability of exceedance in 50 years) for the areas of interest is 0.2381 g. All the simulations on conditional damage are then run assuming this value of PGA, for the whole Municipality of Pordenone.

As an example, Figure 6.1 and Figure 6.3 show the probability of reaching or exceeding a certain damage state for Pordenone city center and Pordenone northern area, respectively. These areas are the same presented in chapter 4 (from Figure 4.29 to Figure 4.34). The damage states DS1 (slight damage), DS3 (severe damage), and DS5 (collapse) are shown. As can be seen, for a seismic scenario with a return period of 475 years most of the buildings have a probability of reaching a DS1 that exceeds 50%, including a consistent amount of buildings that exhibit a probability higher than 75%. This is particularly evident for Pordenone central area, where the configuration of the area is heterogeneous with many vulnerable buildings. On the other hand, predictions seem more homogeneous within Pordenone northern area, due to the greater similarity of the buildings. For what concerns the maps related to DS3, it is still possible to detect some buildings that have a probability of more than 25% of reaching this damage state, and only very few of them exceed 50%. With respect to the DS5 maps, no building appears to have a probability which is higher than 25% of reaching collapse, both in Pordenone center and in Pordenone northern area.

Figure 6.5 shows the same type of results for the whole Municipality of Pordenone. Even though with this kind of visualization the level of detail might get lost, it is still possible to identify the area of the town which may be more prone to seismic damage, and the degree of probability of reaching the different damage states.





Figure 6.1 - Damage maps DS1, DS3, and DS5 for Tr = 475 years in Pordenone city center

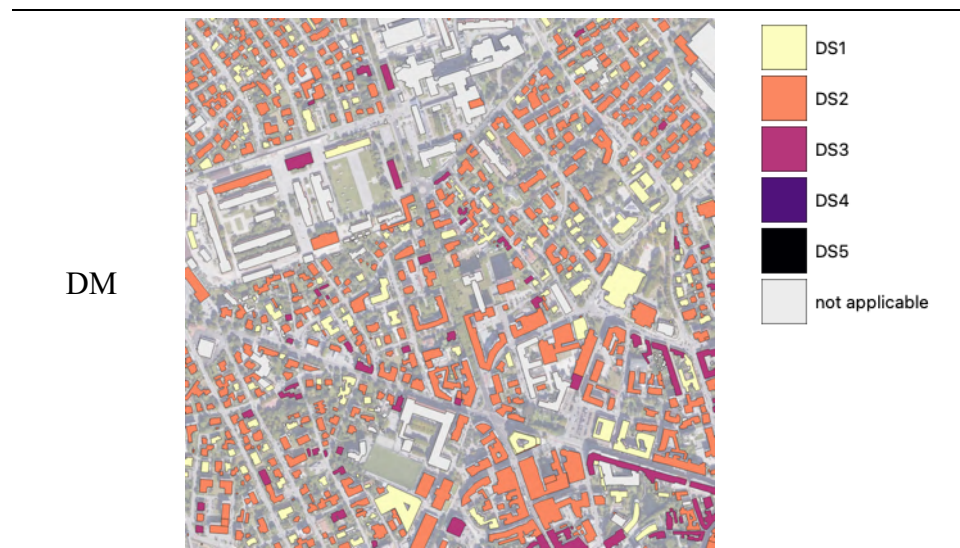
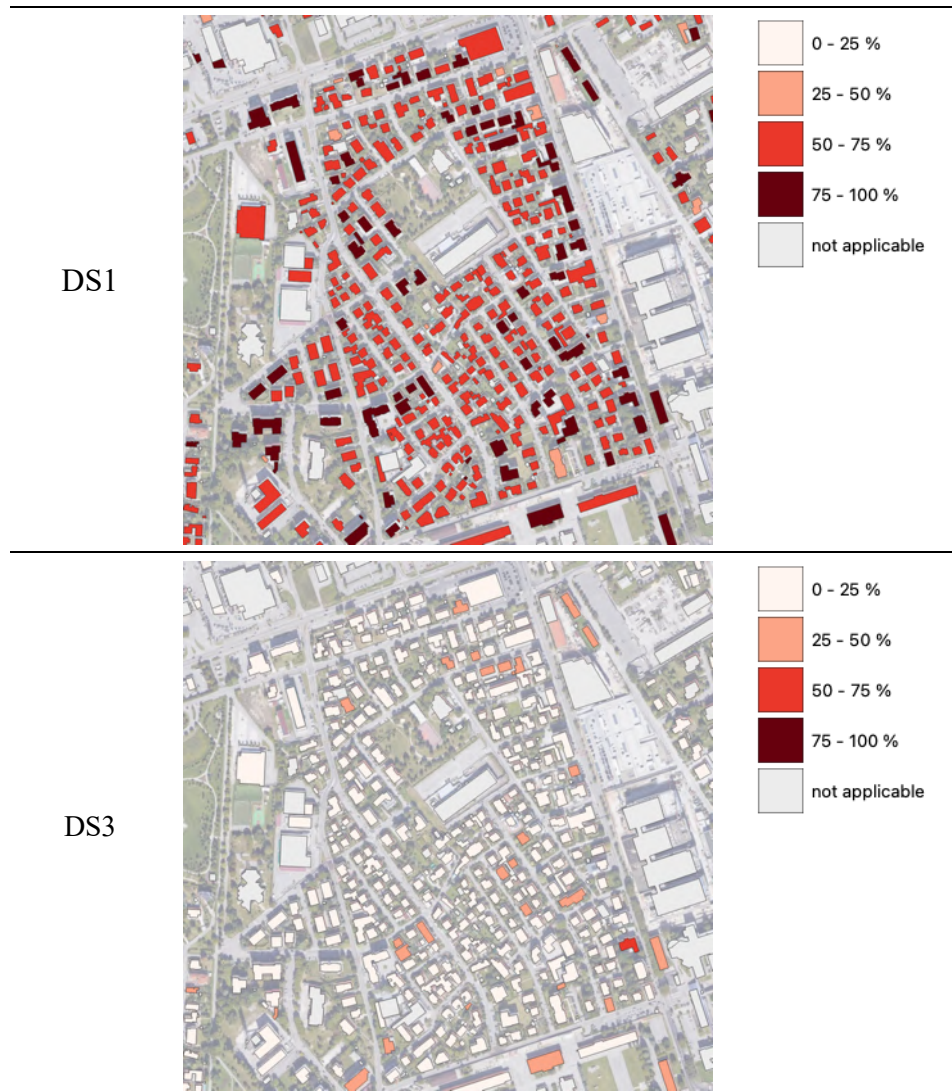


Figure 6.2 - Average damage map for Tr = 475 years in Pordenone city center

Figure 6.2, Figure 6.4, and Figure 6.6 show the maps that express the average damage calculated with Equation 5.2, as explained in chapter 5. Figure 6.2 and Figure 6.4 show a predominant damage equal to DS2 (moderate damage), despite a considerable amount of buildings associated to an average damage of DS1 and DS3. When looking at the map in Figure 6.6, it is possible to see that in the historical center of Pordenone most of the buildings have an average damage equal to DS3 and even DS4 in some cases, while in other parts of the town it is more likely to incur lower damage levels, such as DS1 or DS2.





DS5

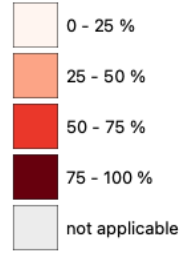


Figure 6.3 - Damage maps DS1, DS3, and DS5 for  $T_r = 475$  years in Pordenone northern area

DM

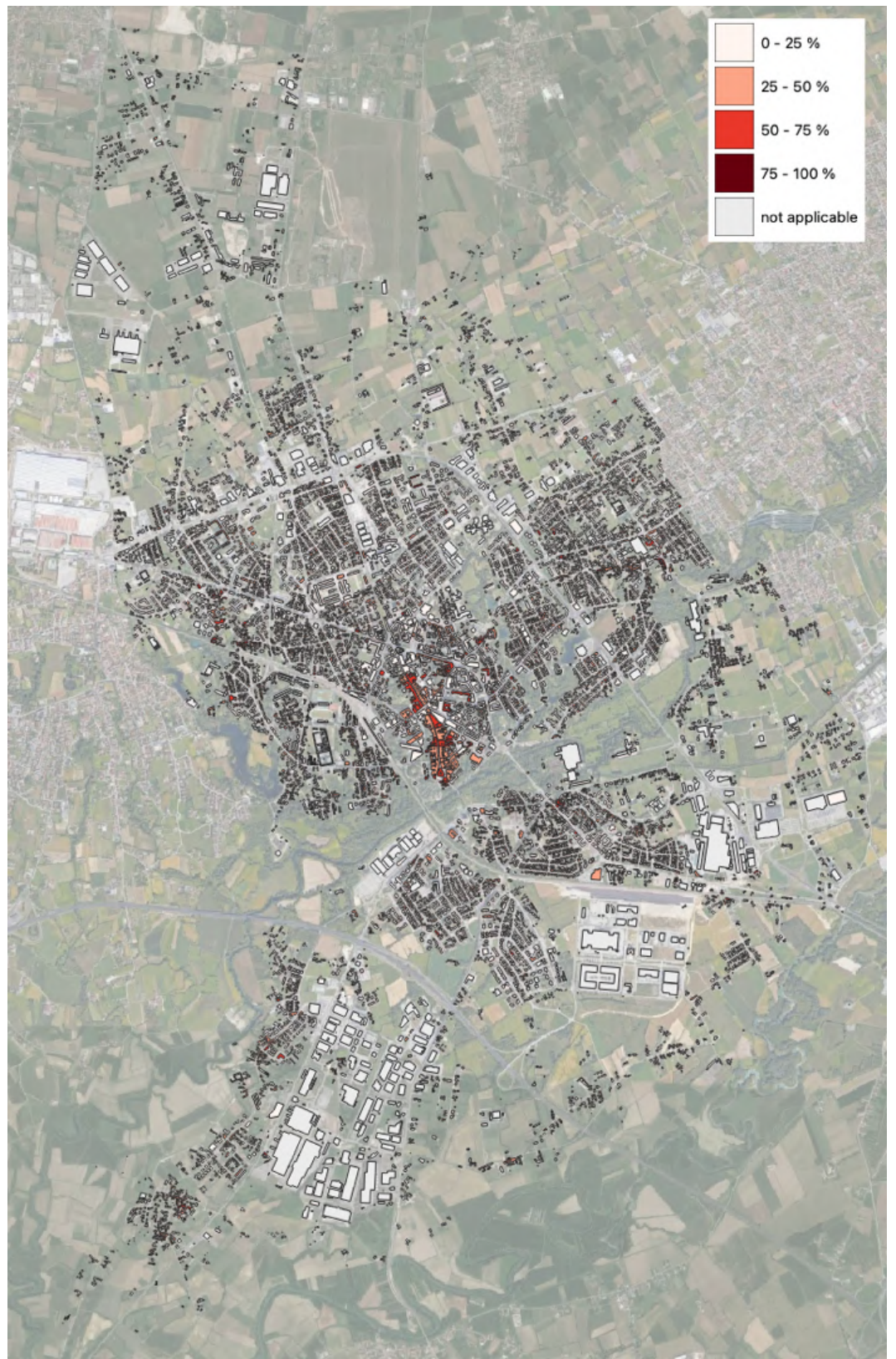


Figure 6.4 - Average damage map for  $T_r = 475$  years in Pordenone northern area

DS1



DS3



DS5



Figure 6.5 - Damage maps DS1, DS3, and DS5 for  $T_r = 475$  years in the Municipality of Pordenone



Figure 6.6 - Average damage map for  $T_r = 475$  years in the Municipality of Pordenone

### 6.1.2. Unconditional damage maps

Other simulations are then performed for the same areas (Pordenone city center, Pordenone northern area, and the whole Municipality), this time for unconditional damage. When dealing with unconditional damage, all the available return periods need to be taken into account, also considering their probability of occurrence within the time window of prediction (see chapter 5). In this case, a time window of 50 years has been selected. The PGAs associated with the different return periods for the areas considered are displayed in Table 6.1. Also in this case, the composition of soil for the town of Pordenone was taken into consideration.

Table 6.1 – PGAs associated with each return period for the town of Pordenone

Return period [years]	PGA [g]
30	0.0668
50	0.0865
72	0.1034
101	0.1224
140	0.1425
201	0.1673
475	0.2381
975	0.2982
2475	0.3860

Compared to conditional damage maps shown in the previous section (relating to a return period of 475 years), the unconditional damage maps shown below exhibit a lower degree of damage, in terms of percentage of exceedance of different damage states (Figure 6.7, Figure 6.9, and Figure 6.11) and also in terms of average damage (Figure 6.8, Figure 6.10, and Figure 6.12). Particularly, for a time window of 50 years only few buildings seem to have a probability of reaching a DS1 greater than 50%, while most of the buildings are in the 25-50% range. As already noticed before, also Figure 6.11 shows that the historical buildings in the city center of Pordenone are the most likely to reach a DS1, while for other parts of the town the probability of reaching this damage state decreases. When considering higher damage states such as DS3 and DS5, no building appears to have a probability to reach these DSs that falls out of the 0-25% range.

With respect to the average damage maps, it is possible to see that most of the buildings are associated with a DS1 damage, with some exceptions falling into DS2. This is particularly evident in Figure 6.12, where most of the buildings are associated with a DS1, other than the ones in the city center, which are mostly associated with a DS2.

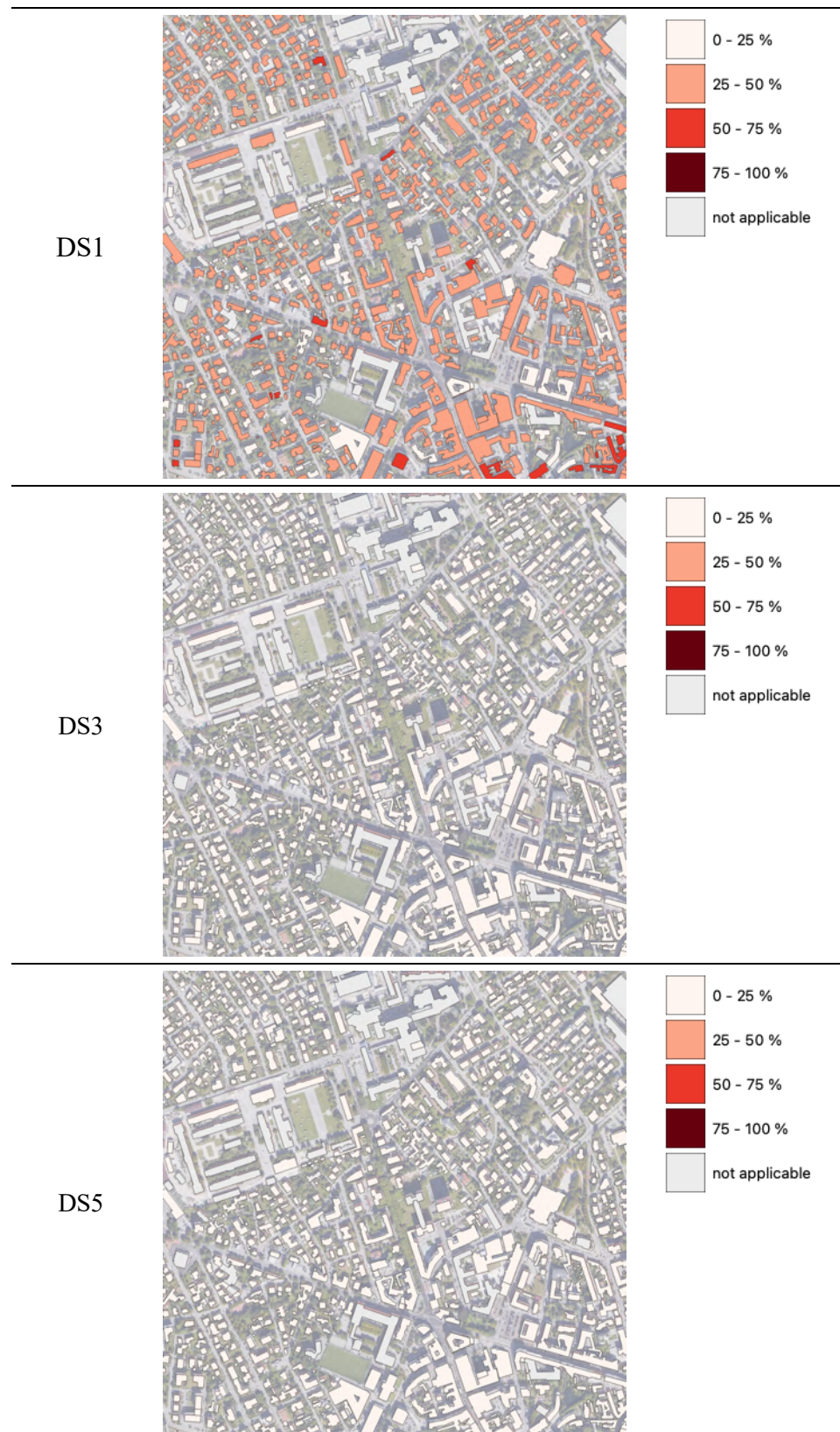


Figure 6.7 - Damage maps DS1, DS3, and DS5 for a time window of 50 years in Pordenone city center



Figure 6.8 - Average damage map for a time window of 50 years in Pordenone city center







Figure 6.9 - Damage maps DS1, DS3, and DS5 for a time window of 50 years in Pordenone northern area

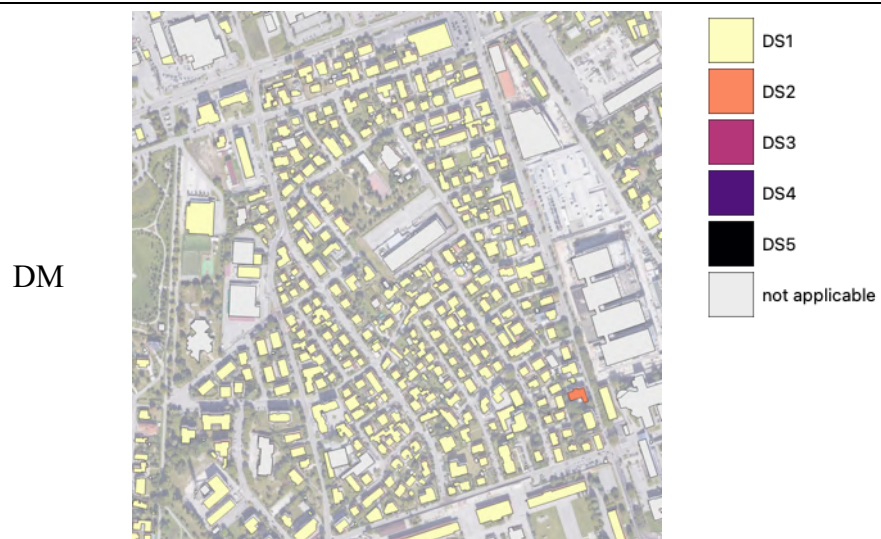


Figure 6.10 - Average damage map for a time window of 50 years in Pordenone northern area

DS1



DS3



DS5



Figure 6.11 - Damage maps DS1, DS3, and DS5 for a time window of 50 years in the Municipality of Pordenone

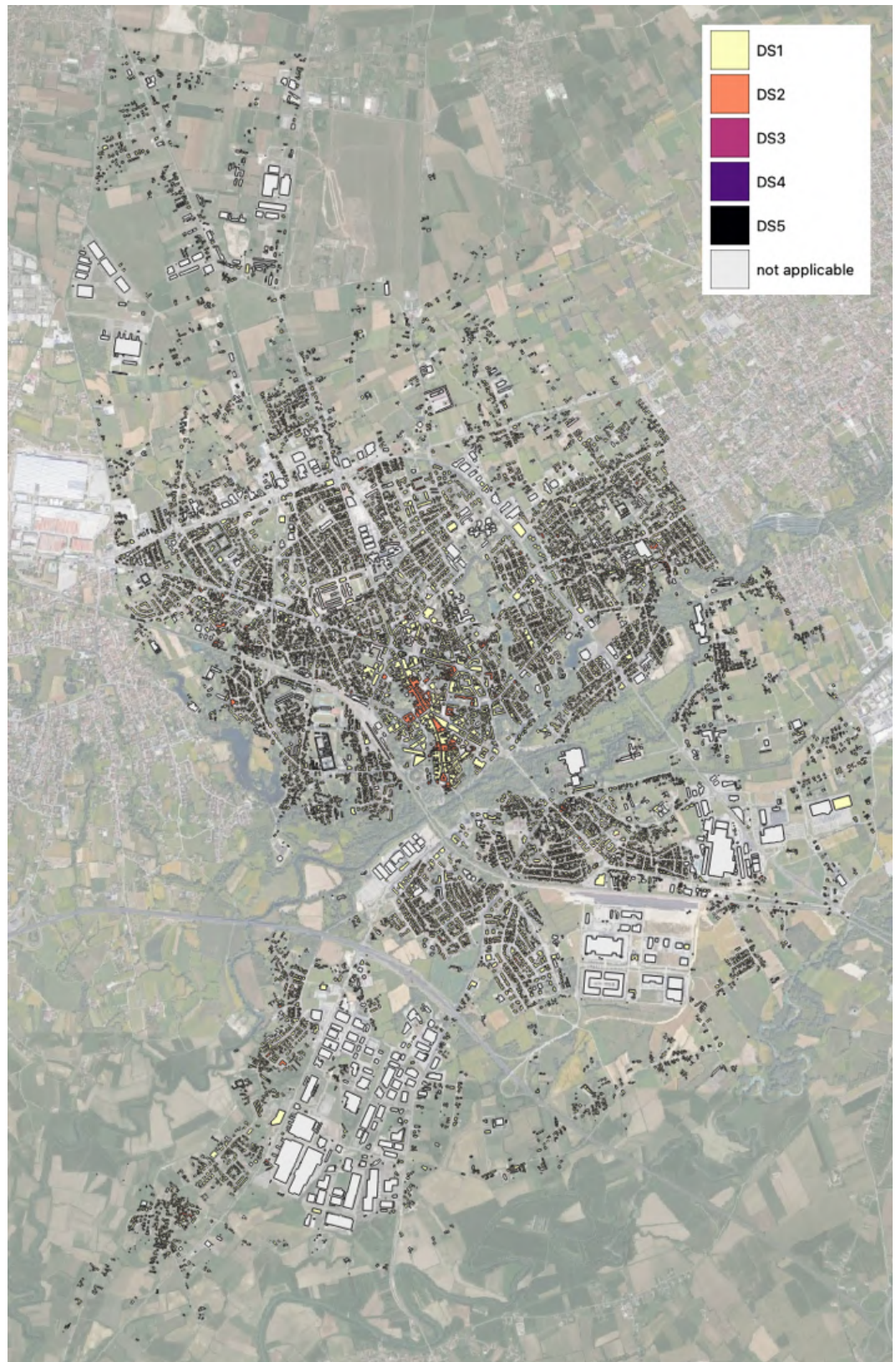


Figure 6.12 - Average damage map for a time window of 50 years in the Municipality of Pordenone

### 6.1.3. Damage maps validation

In order to have a validation of the results presented so far, the work carried out by Valluzzi et al. (2021a) was leveraged. In this study, framed within the 2019-2021 DPC-ReLUIIS Project with the financial support of the China-Italy International Research Centre for Protection of Historical Architectures and Cultural Relics (CIPAR), Guangzhou University, over 2'300 case studies (i.e., structural units/buildings) belonging to 20 villages struck by the 2016 Central Italy earthquake were analyzed by a multi-level survey procedure proposed by the University of Padova. The damage was studied in terms of local macro-seismic intensity and calculated by comparing the influence of several features such as configuration, building aggregation, geometric and architectural details, horizontal and vertical structural components, and materials. For the sake of this comparison, one of the villages is examined in detail, namely Castelsantangelo sul Nera (Province of Macerata, Marche Region), and the results in term of EMS98 damage that were surveyed and reported in Valluzzi et al. (2021a) are then compared with the predictions of damage derived from the algorithm developed in this thesis (in terms of average damage).

Castelsantangelo sul Nera was founded in the 13th century as a walled village on a hill on the border between the dominions of Visso, to which it belonged, and Norcia. It is situated at 780 meters above sea level on the flank of Mount Cornaccione. According to Vettore et al. (2022), 147 structural units (SUs) can be identified in Castelsantangelo sul Nera. Of these, the six churches are excluded from the statistics, as well as 33 buildings that were not evaluated due to their secondary nature (garages and rural warehouses, demolished buildings or ruins) or because they were inaccessible at the time of the surveys. This led to the identification and survey of 108 SUs, focused on retrieving information on agglomeration shape, masonry quality, horizontal structures, structural interventions, and damage level. The town of Castelsantangelo sul Nera was repeatedly hit by the seismic swarm that began on October 26, 2016.

For this work, the definition of damage levels is essential to compare the DSs surveyed with the ones predicted by the risk calculation platform. Primarily, the PGA that caused damages in Castelsantangelo sul Nera needs to be correctly identified, so that the simulation can be as close as possible as the real scenario surveyed on site. This step already poses some problems, as it is not always so obvious to assess the exact level of PGA that is experienced by a building. This is due to multiple reasons: first, seismographs are sparse and not always close to the epicenter of the earthquake (or to the area under analysis); second, site and soil effects can deeply influence the intensity of ground motion, even within short distances; then, this case presents an even more challenging issue, since as mentioned before the damage suffered by buildings was not caused by a single earthquake, but by a seismic swarm, that might have caused an accumulation of damage in the buildings. For the reasons cited above, it is clear that is not so trivial to associate a damage level with a univocal PGA. Nonetheless, some official sources have been leveraged in order to obtain a value of PGA which could be as close as possible as the real ground shaking experienced by the buildings in

Castelsantangelo sul Nera in 2016. In this study, the PGA was obtained through an interpolation of the ShakeMaps (Russo et al., 2022) considering the centroid of Castelsantangelo sul Nera and referring to the most severe event among the three main events (August 24, October, 26, and October 30, 2016). Following this procedure, the value of PGA that was associated with the Municipality of Castelsantangelo sul Nera was equal to 0.541 g.

Another difference that can be noticed between the two different methodologies of damage evaluation (direct survey vs prediction) is that the detection of the buildings is not always the same. Even though most of the times the shapes and the floor areas do not have significant differences, occasionally the subdivision of buildings might not be comparable. This difference between the algorithm and a direct survey has also been addressed in chapter 4: while the automatic algorithm relies on satellite images (thus on the identification of roof shapes), a direct survey might be more precise and identify more structural units. Due to this further division, sometimes the level of damage cannot be unambiguously comparable between the two methods.

Moreover, it has to be recalled that the algorithm can associate a building with a specific damage state by computing its average damage. The value (which usually has a decimal part) needs then to be converted into an integer number that indicates the damage state. In this work, this has been carried out by rounding the average damage: this operation however might lead to incorrect estimates of damage, especially when the average damage falls between two damage limits. For the same reason, it is very hard (if not impossible) to catch the extreme damage levels, i.e., DS0 (no damage) and DS5 (collapse). This is again due to the fact the algorithm calculates the damage level as an average damage, meaning that it takes into consideration all the possible damage states that a PGA might lead to, with their own probabilities. It is therefore difficult to obtain a value that can be rounded to 0 or to 5, since there is always a percentage of slight, moderate, or severe damage that pulls these extreme cases towards the middle of the EMS98 scale.

Bearing in mind these considerations, it is nonetheless possible to compare the damage states surveyed on site after the earthquake with the predictions made by the algorithm. Figure 6.13 shows the two damage maps one next to the other: Figure 6.13a refers to the direct survey, while Figure 6.13b is related to the results provided by the algorithm (rounded average damage). Although the two maps already highlight similarities and differences between the two methods, it is perhaps easier to visualize the same results in the form of pie charts, where each slice represents the percentage of buildings associated with a damage state. This is indeed presented in Figure 6.14, where Figure 6.14a regards the direct survey, while Figure 6.14b refers to the predicted damage. First, it is possible to notice what has already been mentioned about the prediction of extreme damage levels (DS0 and DS5), since Figure 6.14b exhibits neither. Other than this difference, the percentages of the other damage states seem comparable and of the same order.

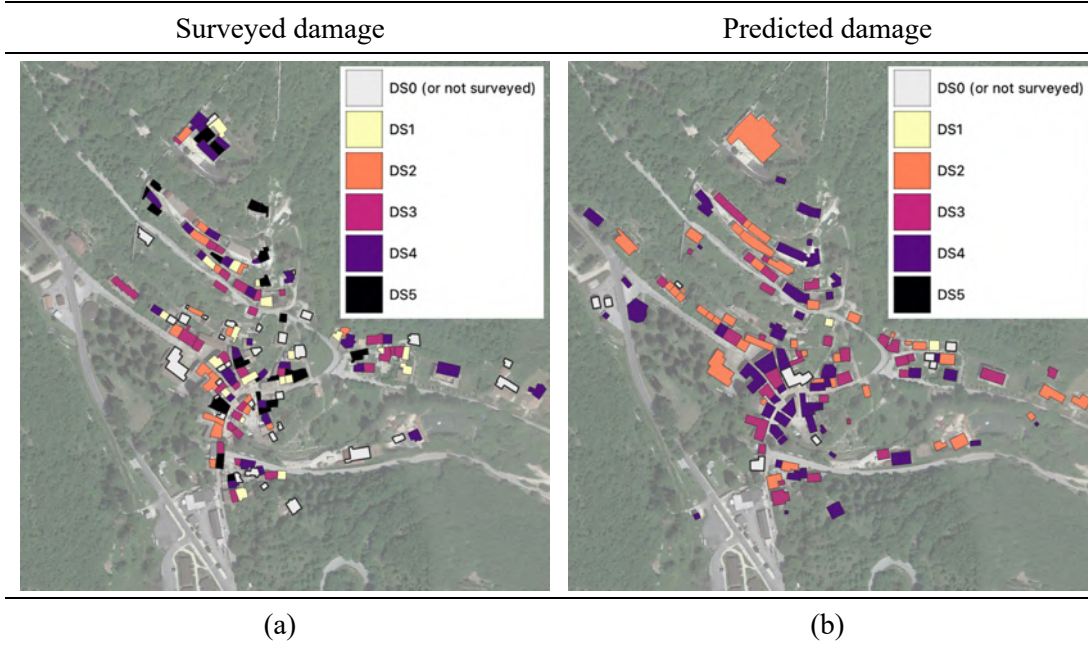


Figure 6.13 – Damage in Castelsantangelo sul Nera assessed during a direct survey (a) and predicted by the algorithm (b)

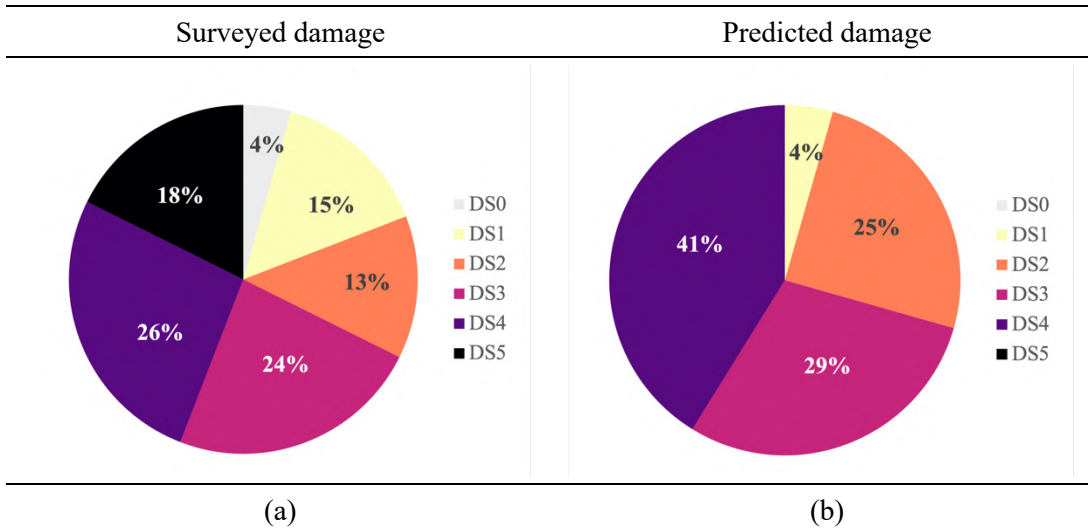


Figure 6.14 – Percentages of damage states in Castelsantangelo sul Nera assessed during a direct survey (a) and predicted by the algorithm (b)

Even when the damage is not properly identified, it is however useful to see how much the algorithm is wrong compared to the direct survey, i.e., of how many damage states the algorithm is mistaken. Figure 6.15 shows indeed that while 67% of buildings are associated with the same damage level of the direct survey by the algorithm, even in the cases where the damage state is not correctly identified the error is one class of damage (23%) or two classes (only 10%). No more than a difference of two damage states has been encountered in this validation example.



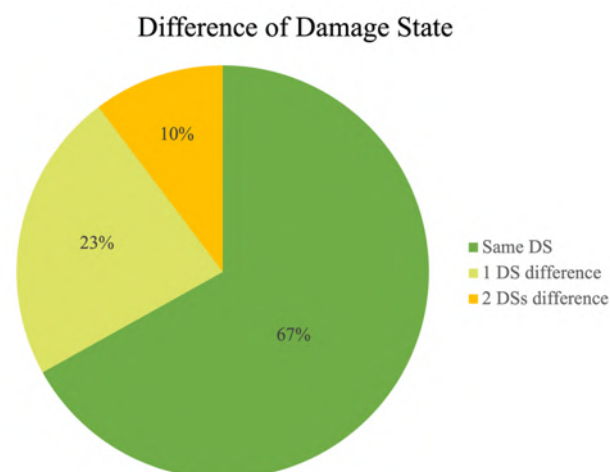


Figure 6.15 - Percentages of correct predictions and predictions with 1 or 2 damage states difference for the Municipality of Castelsantangelo sul Nera when compared to the direct survey

## 6.2. Risk maps

Another important output of this project is the elaboration of seismic risk maps. The process implemented in the risk platform has been explained in detail in chapter 5: here only the key concepts are recalled. In summary, the damage maps created (of which some examples have been shown in the previous section) can be used to elaborate risk maps through consequence matrices that relate damage to possible losses. The losses that can be computed are economic losses (i.e., reconstruction and repair cost), human losses (i.e., casualties), impact on buildings (i.e., usability), and displaced people. All these indicators are of extreme importance and utility when civil protection institutions have to face emergencies, because they give an idea of how much workforce needs to be deployed to deal with the crisis. Furthermore, these results are very useful even in the absence of an actual seismic event, as they can predict the effect of particular scenarios and therefore help with the operations of preparedness and prevention.

In the following sections, conditional and unconditional risk maps are presented (along the same line of the damage maps presented above). These maps will focus on economic losses, usability of buildings, and displaced people. Moreover, a validation is presented, where the results of this project in terms of risk are compared to the ones derivable from IRMA (Italian Risk MAPs), the online platform developed by Eucentre already described in section 2.3. The results provided by this platform have a similar form to that of the platform described in this thesis, so it was possible to compare the outputs and point out similarities and differences between two platforms that have the same purpose, i.e., the definition of risk. Lastly, considering the fact that in chapter 3 not only fragility curves for the as built configuration have been presented, but also mitigated ones taking into account several retrofit strategies, it is possible to simulate the implementation at a local scale of different seismic retrofit interventions, so that their benefit can be assessed. This step may prove very useful in case that more

vulnerable areas need to be retrofitted at a diffuse scale, since this output can provide guidance on how to intervene and what degree of effectiveness could be expected.

### 6.2.1. Conditional risk maps

The conditional risk maps presented in this section reflect the conditional damage maps shown in paragraph 6.1.1. Also in this case, all the simulations have been conducted assuming a PGA that has a return period of 475 years. For the Municipality of Pordenone, this means a PGA of 0.2381 g.

First, the risk maps that represent the possible economic losses for such a seismic scenario are displayed. Figure 6.16, Figure 6.17, and Figure 6.18 show the economic losses for the central area of Pordenone, the northern area of Pordenone, and for the whole Municipality, respectively. These maps highlight the different ranges of repair or reconstruction costs for each building belonging to that area. Unlike damage maps, where only seismic hazard and seismic vulnerability come into play, in this case also exposure plays an important role. As a matter of fact, the risk indicator of economic losses is really the combination of the hazard to which the building is subjected, the building vulnerability, and its exposure, defined as the total cost of the building depending on its total area (as explained in chapter 5). The effect of exposure can be seen in these maps, since it is possible to notice how smaller buildings are usually in the lower ranges of economic losses, while bigger buildings are more likely to belong to the higher ranges. Clearly, looking at these maps, it is impossible to separate the influence of exposure from the influence of vulnerability: the same level of economic losses might be attained by smaller buildings that possess a higher vulnerability, as well as by bigger buildings with a lower vulnerability level. Of course, also seismic hazard plays a crucial role in the assessment of economic losses: however, given the fact that in this work the whole Municipality of Pordenone was associated with a single value of PGA, the effect of hazard is not relevant in these maps. Nonetheless, if two areas in Italy were to be compared, the difference between the seismic hazard of the two places would be fundamental and would greatly affect the estimated economic losses.

Figure 6.18 gives an overall view of the possible economic losses in the whole town of Pordenone. Once again, being the map at a town scale, it might not be possible to distinguish each and every building, but this representation can give a general idea of the severity of economic losses in different areas or neighborhoods of the town. It can be seen that the historical city center might suffer the most significant losses in the whole town: this is due to the vulnerability and exposure of the buildings that belong to that area.

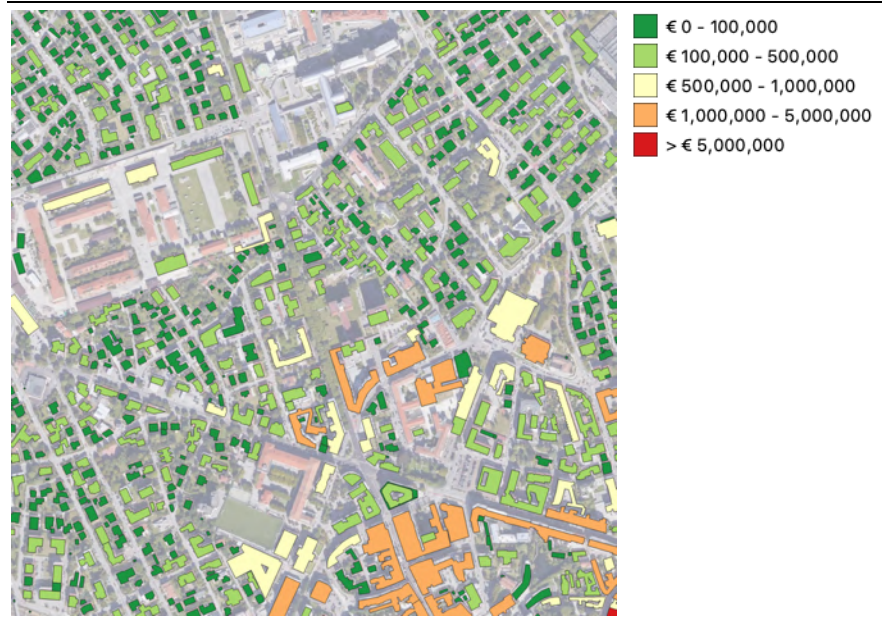


Figure 6.16 – Economic losses for  $Tr = 475$  years in Pordenone city center

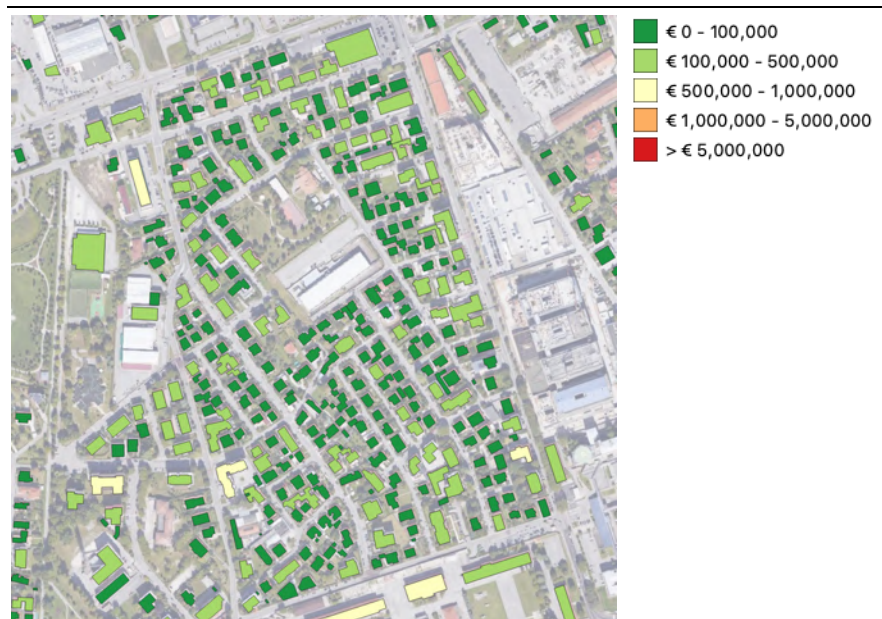


Figure 6.17 - Economic losses for  $Tr = 475$  years in Pordenone northern area



Figure 6.18 - Economic losses for  $T_r = 475$  years in the Municipality of Pordenone

Furthermore, risk maps that show the impact on buildings (i.e., usability) can be produced. These maps intend to display whether a building is still supposed to be usable after the earthquake, or whether on the other hand it is no longer usable (the

possibilities are: unusable in a short period, unusable in a long period, or collapsed). Figure 6.19 and Figure 6.20 show these results for different areas in Pordenone, while Figure 6.21 refers to the whole Municipality. The outputs only give as options “usable” or “unusable in a long period”: this is due to the fact that unusability in a short period is an intermediate state which has a very low probability of occurrence (see the values presented in Table 5.5 in chapter 5, which are used by the risk platform to compute the impact on buildings). For the same reason, it is very difficult to catch the collapsed building, since it is an extreme condition that the percentages used do not seem to capture.

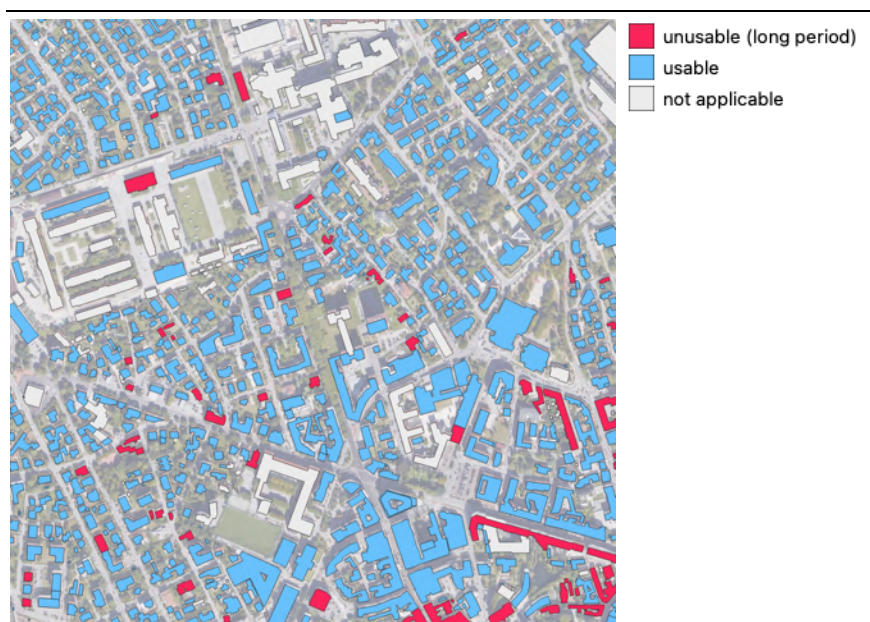


Figure 6.19 - Usability of buildings for  $T_r = 475$  years in Pordenone city center

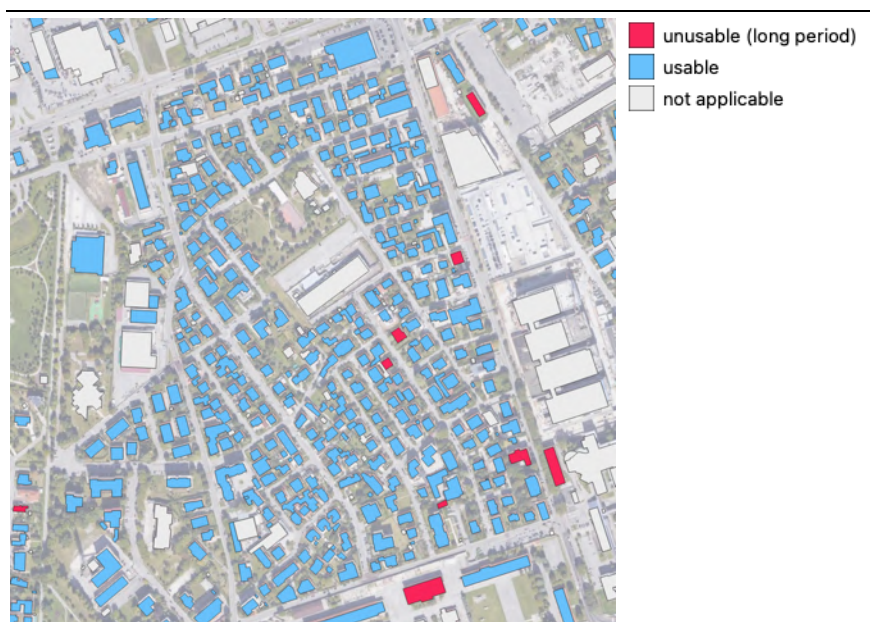


Figure 6.20 - Usability of buildings for  $T_r = 475$  years in Pordenone northern area



Figure 6.21 - Usability of buildings for  $T_r = 475$  years in the Municipality of Pordenone

Nevertheless, looking at Figure 6.21 it is clear how the historical center would be completely unusable in a long period in case an earthquake with a return period of 475 years occurred: this strongly highlights the high vulnerability of that neighborhood.

Another important risk indicator that can be evaluated is the number of displaced people. As explained in chapter 5, this parameter is calculated by estimating the possible number of residents in each building (from the total number of citizens in the town and considering the density of population), and then considering whether the building is usable or not in the aftermath of the earthquake under consideration. This can give an estimation of the number of people who might need a temporary or permanent shelter and who might need assistance from the civil protection organizations. Figure 6.22, Figure 6.23, and Figure 6.24 show the results of this evaluation for the town of Pordenone.

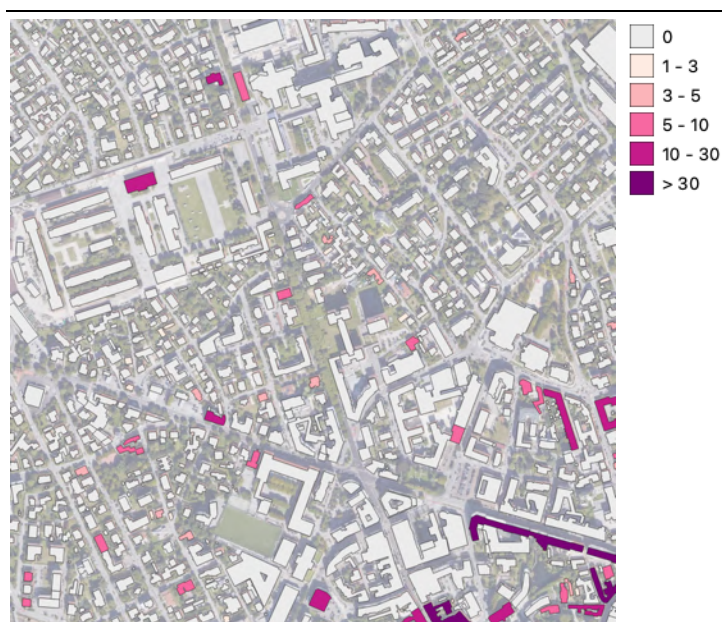


Figure 6.22 - Displaced people for  $T_r = 475$  years in Pordenone city center

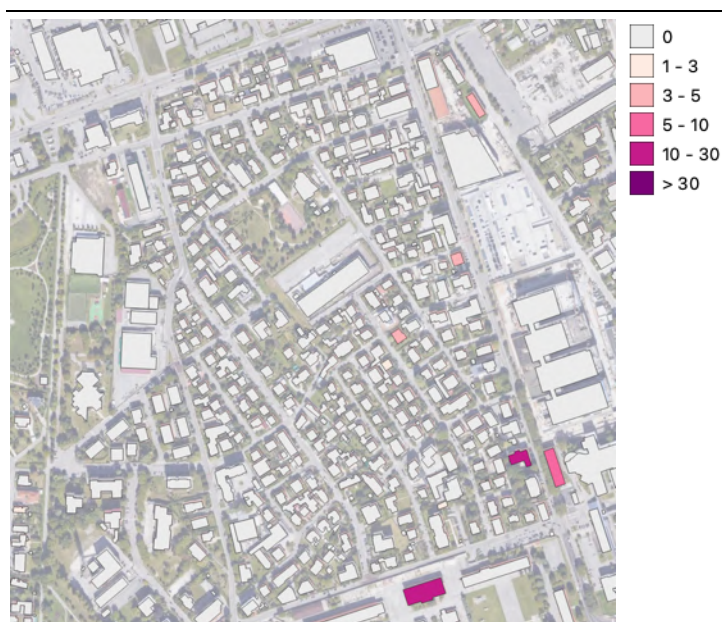


Figure 6.23 - Displaced people for  $T_r = 475$  years in Pordenone northern area



Figure 6.24 - Displaced people for  $T_r = 475$  years in the Municipality of Pordenone

Figure 6.24 points out that in most buildings of the historical center the number of people per building that might be displaced exceeds the value of 30. To give an order



of magnitude, the total number of displaced in Pordenone after an earthquake with return period 475 years exceeds the value of 5,000.

### 6.2.2. Unconditional risk maps

Following the structure presented in section 6.1.2., some analyses of unconditional risk have been carried out. Also in this case, a time window of 50 years has been selected, and the risk indicators of economic losses, impact and displaced people are shown below. Figure 6.25, Figure 6.26, and Figure 6.27 show the economic losses that can be produced by all the possible earthquakes that may occur in 50 years.



Figure 6.25 - Economic losses for a time window of 50 years in Pordenone city center



Figure 6.26 - Economic losses for a time window of 50 years in Pordenone northern area



Figure 6.27 - Economic losses for a time window of 50 years in the Municipality of Pordenone

As can be seen, the range of losses is slightly lower than the one resulting from a conditional analysis for a return period of 475 years. This is due to the fact that the effects of all the earthquakes that can happen in a selected time window are scaled by

their probability of occurrence in that interval: that is to say, earthquakes with very high return period (e.g., 2475 years) are indeed included in the computation of risk with great values of PGA, however the probability of occurrence of such earthquakes is very low in a time frame of 50 years.

The same aspect is noticeable in the results referring to usability (Figure 6.28, Figure 6.29, and Figure 6.30) and displaced people (Figure 6.31, Figure 6.32, and Figure 6.33). Even more in these two last cases, the unconditional risk computation fails to detect any unusable buildings or displaced people in 50 years in the town of Pordenone.

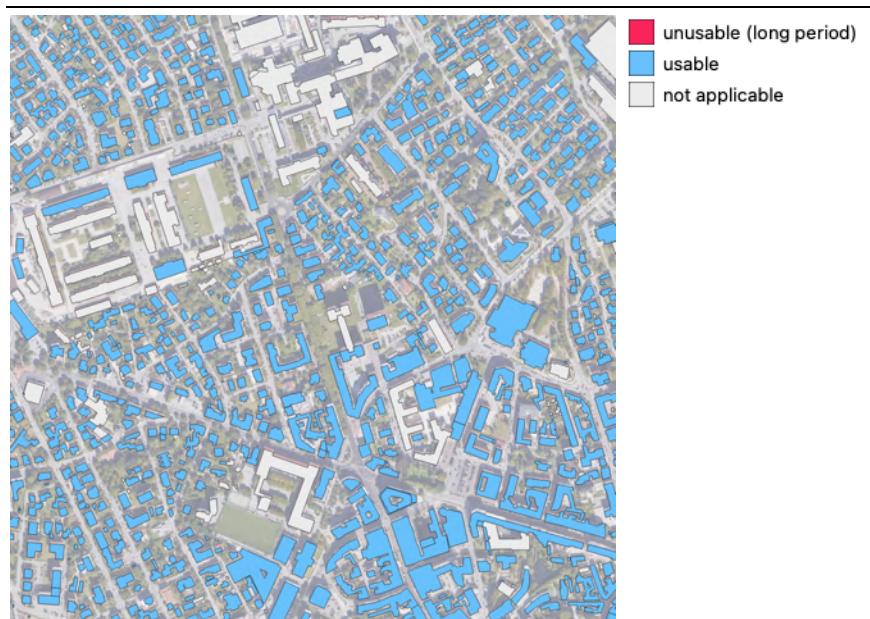


Figure 6.28 – Usability of buildings for a time window of 50 years in Pordenone city center



Figure 6.29 - Usability of buildings for a time window of 50 years in Pordenone northern area



Figure 6.30 - Usability of buildings for a time window of 50 years in the Municipality of Pordenone

The reason why this occurs is because the earthquakes that have more weight in an unconditional evaluation of risk are the ones that have very low return periods, thus very low PGAs. Even though they contribute to the increase of the economic losses (even slight damages produce repair costs), they might not lead to unusable buildings, therefore no displaced people are predicted.

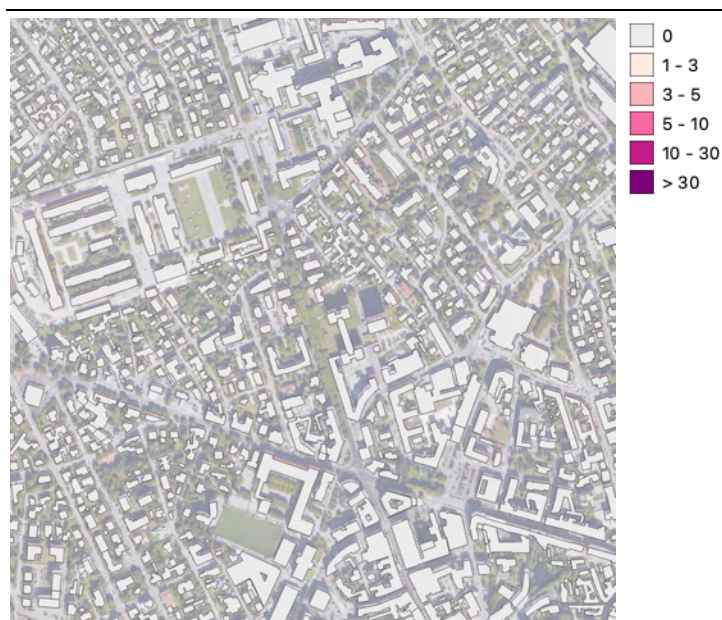


Figure 6.31 - Displaced people for a time window of 50 years in Pordenone city center



Figure 6.32 - Displaced people for a time window of 50 years in Pordenone northern area



Figure 6.33 - Displaced people for a time window of 50 years in the municipality of Pordenone

### 6.2.3. Risk maps validation

As stated before, also for what concerns risk estimates an evaluation was performed. In order to do so, the values of the considered risk indicators provided by the risk calculation platform developed in this thesis have been compared with the ones available in IRMA (Borzi et al. 2021b, described in section 2.3). The seismic hazard used in the platform is the MPS04 hazard model developed by the INGV, which is the same hazard model that is implemented within the platform described in this project. IRMA can also take into account the distribution of different soils across Italy according to the study of Forte et al. (2019), which is the same considered in our platform. IRMA then allows the users to upload different vulnerability databases as well as different sets of fragility curves on the platform. For what concerns seismic vulnerability, the fragility curves described in chapter 3 (masonry fragility curves) and chapter 5 (reinforced concrete fragility curves) have been given as vulnerability inputs; these curves were the same utilized in the risk platform of this project. The main difference between the two platforms relies on the definition of exposure: while for the platform of this work exposure is taken into account considering building by building (evaluated from satellite images and online maps and then assessed through Convolutional Neural Networks as described in chapter 4), IRMA on the other hand defines exposure from the national data provided by ISTAT, the Italian National Institute of Statistics. ISTAT, however, supplies data at a national, regional, provincial, or municipal level at most: this means that the IRMA platform is not able to give results that consider territorial scales which are smaller than the municipal scale. With regard to the typology of results, as well as the platform here developed, also IRMA combines the different exposure databases with all possible sets of fragility curves, so that the user can create maps with conditional damage (i.e., the return period is selected) or unconditional damage (i.e., an observation time window is selected). These maps can be converted into risk maps with consequence matrices, which are the same used in this work (see chapter 5). This makes the outputs of the two platforms easily comparable.

In this validation phase, the town of Pordenone was chosen as a case study. As already mentioned, it is not possible to compare the result that our platform provides for each building, since IRMA gives aggregate results at a municipality level, therefore the outputs of the two platforms were compared in an aggregate way, considering the entire Municipality.

Since exposure is the component of risk that is calculated differently by the two platforms, a preliminary evaluation of exposure is carried out. The results of this evaluation are presented in Table 6.2: it is recalled that these analyses only take into account residential buildings. As can be seen, there is a considerable difference between the total area of buildings detected, and consequently between the building total values (the value in IRMA is around 40% of the one in the risk platform). This is mainly due to the fact that the data provided by ISTAT is described as “area of dwellings occupied by residents”, while our platform takes into account the whole area of a building as detected in OpenStreetMap, and then multiplies the area by the number

of floors identified according to the prediction of the CNN concerning the height. This may lead to an underestimation of the total built up area in the IRMA platform, and therefore to a different evaluation of exposure in terms of economic value. On the other hand, the number of people detected by the two platforms is essentially the same, due to the fact that both platforms make use of ISTAT data to retrieve this exposure parameter.

Table 6.2 - Difference of exposure in Pordenone between the risk calculation platform and IRMA

<b>Exposure</b>	<b>IRMA</b>	<b>Risk calculation platform</b>	<b>Ratio [%]</b>
Total building area	2,251,608	5,424,185	41.51%
Total building value	3,039,670,800 €	7,322,650,039 €	41.51%
Number of people	49,982	49,569	99.17%

Prosecuting on with the comparison in terms on risk, the case of conditional risk for an earthquake of return period equal to 475 years was considered. The results are shown in Table 6.3. As can be seen, the expected economic losses take on different values between the two platforms, where the losses predicted by IRMA are almost half of the losses expected according to our platform: this is clearly due to the difference in the definition of building exposure highlighted in Table 6.2. Also the number of victims and injuries show some differences, which might seem surprising since the values of exposure in terms of number of people is perfectly comparable between the two platforms. This however comes from the different approach that the two platforms have: while IRMA considers the Municipality as a whole, thus calculating the possible casualties at a municipality scale, our platform performs the same computation at a building level. This can lead to differences in approximation and rounding that result in significant differences.

Table 6.3 - Difference of conditional risk (Tr=475 years) in Pordenone between the risk calculation platform and IRMA

<b>Risk indicators</b>	<b>IRMA</b>	<b>Risk calculation platform</b>	<b>Ratio [%]</b>
Economic losses	476,306,009 €	919,712,000 €	51.79%
Victims	238	395	60.25%
Injuries	767	1763	43.51%

The same comparison has been carried out for the unconditional risk, considering a time window of 50 years. The values and ratios are shown in Table 6.4. In this case, the two platforms return results that are very similar and, most importantly, stand in the same order of magnitude. It is indeed important to recall that the purpose of these platforms, especially when they are dealing with larger scales such as municipality scales, is mainly to provide results that can reflect the actual outcomes of possible real seismic scenarios, bearing in mind that these results need to be read at a territorial scale.



Table 6.4 - Difference of unconditional risk (time window 50 years) in Pordenone between the risk calculation platform and IRMA

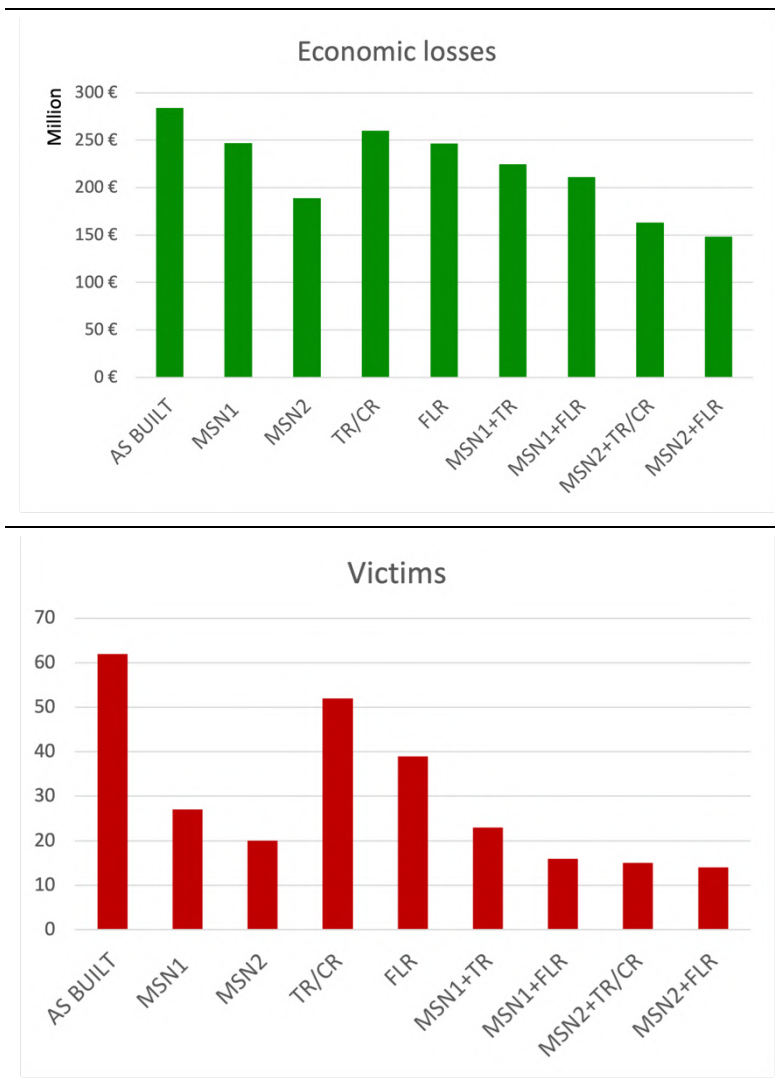
<b>Risk indicators</b>	<b>IRMA</b>	<b>Risk calculation platform</b>	<b>Ratio [%]</b>
Economic losses	264,401,256 €	283,920,370 €	93.13%
Victims	93	62	150.00%
Injuries	302	332	90.96%

#### 6.2.4. Risk assessment in case of retrofitted scenarios

The last section of this chapter is dedicated to the simulation of possible retrofit strategies in the buildings in Pordenone, in order to assess their effectiveness. In order to carry out these analyses, the retrofitted fragility models presented in chapter 3 have been used. It is recalled that the fragility curves developed in this project only refer to masonry buildings: for this reason, reinforced concrete buildings have always been considered in their as built state, while the vulnerability of masonry buildings has been modified according to the type of intervention implemented.

Here the selected interventions are briefly listed (they are also summarized in Table 3.9 in chapter 3): for masonry buildings belonging to Pre-1919 and 1919-1945 construction periods, two stages of masonry strengthening have been assumed (MSN1 and MSN2), the addition of tie-rods (TR) and the stiffening of floors (FLR). For buildings belonging to 1946-1960, 1961-1980, and Post-1980 only one stage of masonry strengthening has been considered (MSN, comparable to the MSN2 of the previous construction periods), as well as the addition of confining rings (CR) and the stiffening of floors (FLR). Combined interventions carried out on masonry walls and on horizontal diaphragms or connections have also been considered, such as MSN1+TR, MSN+FLR, MSN2+TR/CR, and MSN2+FLR. The simulations were run in the risk platform for the whole town of Pordenone without changing any parameter other than the fragility curves, in order to assess their pure effect on risk indicators. Figure 6.34 shows the results for economic losses, victims, and injuries in the town of Pordenone after an unconditional risk analysis with a time window of 50 years. Each histogram shows as the first bar the risk indicator value for the case in which all the buildings are in their as built configuration, while the following bars show the same risk indicator in case that all the masonry buildings in Pordenone underwent that specific retrofit intervention. The same results can also be visualized through histograms that present the economic losses, victims, and injuries as a percentage of the initial as built configuration. This histograms are shown in Figure 6.35. From these graphs it is possible to perceive the level of effectiveness (and benefit, to a certain extent) of the different retrofit strategies. For example, the addition of tie-rods (TR) usually is less effective, reducing economic losses by 8%, victims by 16% and injuries by 14% compared to the as built state. The most effective intervention includes the two stages of masonry strengthening and the stiffening of floors (MSN2+FLR). This intervention, in a time span of 50 years, may lead to a decrease of economic losses of 48% compared to the as built condition, as well as 77% less victims and 59% less

injuries. Clearly, these considerations are not sufficient to carry out proper cost-benefit analysis: for example, although the addition of tie-rods does not seem very effective, it is however true that this kind of retrofit strategy is usually the less expensive one, and it is also one of the easiest one to be implemented, especially at a large scale. In order to perform evaluations that can actually be helpful for a targeted mitigation plan at a territorial scale, the costs of interventions need also to be taken into account, as well as the different targets that interventions may have.



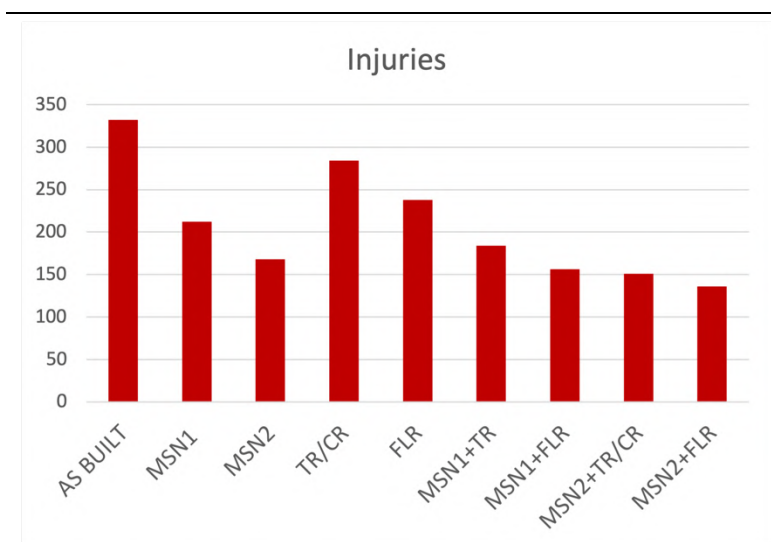
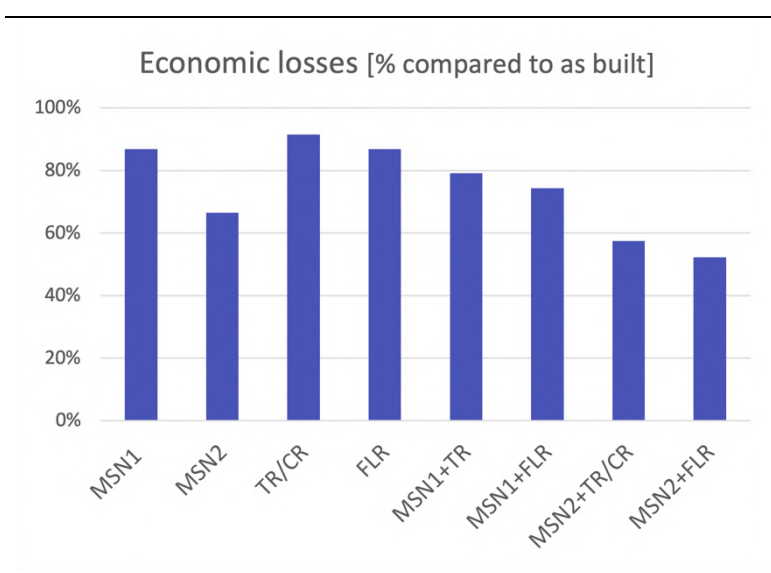


Figure 6.34 - Effect on economic losses, victims, and injuries for different retrofit strategies in Pordenone (50 years)



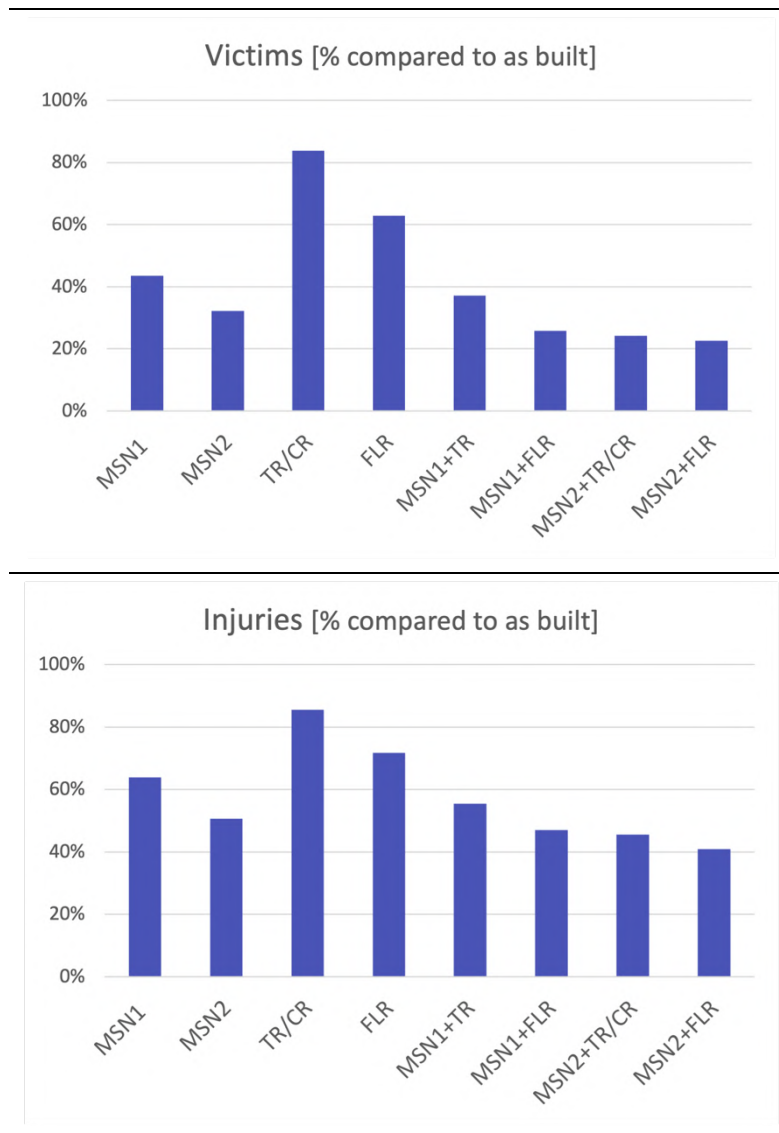


Figure 6.35 - Effect on economic losses, victims, and injuries for different retrofit strategies in Pordenone (50 years) as percentage of the as built configuration

## 7 CONCLUSIONS AND FUTURE DEVELOPMENTS

### 7.1. Conclusions

This thesis explored the possibility of performing seismic risk analyses in a remote and automatic way.

First, a review of the state of the art in the field of earthquake engineering is presented, with particular focus on seismic fragility assessment and the use of machine learning techniques for the evaluation of exposure. The literature review has shown that some research gaps are still existing, particularly the need for a national fragility model that can be representative for all the possible Italian building typologies, as well as for a methodology to remotely and automatically evaluate exposure and associate buildings with their appropriate vulnerability. This thesis directly addresses these issues and is suggesting solutions to overcome them.

The first part of this thesis is indeed dedicated to the derivation of a fragility model for Italian residential masonry buildings of general validity within the national territory. The model can describe not only masonry buildings in their as built condition, but also takes into account the possible variation of fragility in case seismic retrofit interventions are applied to the same buildings. The model has proven to be representative for the Italian building typologies: this is justified by the validation performed by comparing the model output estimates with the real damage surveys carried out after L'Aquila earthquake in 2009. The success in the elaboration of this fragility model has proven that is reasonable to develop large scale vulnerability models, and that these can also give indications on the level of mitigation that retrofit intervention can bring to buildings.

As for the automatic identification and categorization of buildings in order to define exposure, this work has shown that it is possible to detect buildings at a territorial scale from satellite images and online map services with a very good level of detail. Furthermore, street view images can be utilized to remotely retrieve pictures of buildings, thus simulating an external direct survey. These tools are fundamental for a rapid evaluation of exposure at large scale, since they drastically reduce costs and time necessary for the surveys. Subsequently, Deep Learning techniques, particularly Convolutional Neural Networks, have proven to be successful in the correct identification of specific building features, such as height, material, and construction period. Although these are just basic data regarding the building configuration, they are however fundamental for the definition of the exposure, as well as for the association of a correct fragility model to the building itself. This gives a considerable help in surveying buildings automatically, for the purpose of large-scale risk estimates. The outputs of the models and methods developed in this thesis are ultimately used within a seismic risk calculation platform, which was specifically developed for the purposes of this project. This platform includes different modules that eventually provide damage and risk estimates: the results produced seem very promising, also

considering the good match with past real case scenarios and with other risk calculation tools.

Lastly, the final part of this thesis has given an insight of another potential of this work: thanks to the development of mitigated fragility curves, it is possible to assess the economic benefit that a retrofit strategy can bring at a territorial scale. When this result is integrated with the cost of the interventions, as well as with all the consequences that the mitigation can bring, it is then possible to carry out cost-benefit analysis and select the best strategy for an effective mitigation plan.

All these considerations suggest that the whole methodology developed within this thesis can represent a valid tool for civil protection, insurance companies, and any other public or private organization involved in risk management. Indeed, the tool provided by this work can not only assess seismic damage and risk for specific earthquake scenarios, but gives also the possibility to make forecasts and projections over varying time windows. The results that this platform can offer give important indications on how many human and economic resources are expected to be deployed in the emergency phases after different earthquake scenarios: this information is usually not known by the above-mentioned authorities and agencies. Moreover, these results can also assist emergency planners in making sure that even in case of earthquakes that lead to the interruption of almost all the urban functions, the urban settlement can still preserve its strategic emergency functions, its accessibility and the connection with the territorial context.

## **7.2. Future developments**

Since this work is composed by different interconnected modules, it also leaves space to improvements and future developments.

First of all, even though the developed fragility model has proven its robustness at a national level, it is however true that a better representation of vulnerability could be given by different models calibrated on specific geographical areas. Therefore, future studies will aim to refine the macro-typological classification, with particular attention to geographical representativeness, in order to provide several regional model that can be more representative of the built stock at a local scale. The goal is indeed to develop increasingly reliable territorial-scale damage assessment tools, necessary for risk management purposes. Moreover, the same methodology for deriving fragility curves for residential masonry buildings could be adapted to other building typologies, i.e., consisting of other materials, such as residential r.c. buildings, or even belonging to completely different building classes, such as industrial buildings, schools, churches and religious buildings, monumental buildings, etc. In these cases, of course the software or tools used to perform the analyses should be appropriate for the building typology under consideration. There is already research that is working towards this direction, and this suggests a possible integration or adaptation of the external work within the platform developed in this project, in order to attain a more exhaustive vulnerability assessment of the whole built stock.

The steps that concern the automatic identification of building features are also open to further developments. Preliminarily, the database of buildings used to train the neural networks can be increased but most importantly improved, selecting only the most representative building pictures for recognizing the specific features. This could lead to better results in terms of accuracy when training the Convolutional Neural Networks. Furthermore, other neural networks that detect additional features might be developed, particularly for the characteristics that influence seismic vulnerability and for which specific fragility models have been built on. The same procedure could be implemented also for other building typologies, so that particular features that are meaningful for the definition of their seismic vulnerability are recognized. As a possible extension of this work, when parameters are impossible to be retrieved from pictures that only show the external façade of a building, statistical methods (such as Bayesian methods) might be developed to associate unknown variables to distributions of known parameters.

Finally, deeper studies on consequence matrices that correlate damage to risk indicators are to be carried out. Research is putting a lot of focus on this topic, since institutions are asking for more precise estimations of the possible losses caused by earthquakes. The evaluation of these data and coefficients is not trivial at all, since it requires considerations on many aspects that contribute to the definition of losses caused by a seismic event and that are often inherently affected by uncertainties.

In conclusion, the same framework and the same platform could serve as a basis for the assessment of other natural risks, such as floods, landslides, windstorms, etc., taking into account the proper refinements to include appropriate hazard and vulnerability models, as well as an ad hoc evaluation of exposure.

## **ACKNOWLEDGEMENTS**

I would like to thank the ReLUIIS consortium (Consorzio della Rete dei Laboratori Universitari di Ingegneria Sismica e Strutturale, particularly the ReLUIIS-DPC 2019-2021 project) for the continuous and intense discussions on seismic risk subjects, which gave several insights for the development of this thesis, and the DPC (Dipartimento della Protezione Civile) for the opportunity to include me and my research team in a work of such great scope.

I would like to say thank you to Eucentre (European Centre for Training and Research in Earthquake Engineering) for giving me access to the IRMA platform, without which I would not have been able to achieve the results of this thesis.

I would also like to thank professors Francesco Pesavento, Bernhard Schrefler, Timon Rabczuk, and the Bauhaus Universität of Weimar, Germany, where I spent the first year of my PhD program under the European project BESTOFRAC and where I had time to shape this project and grow as a researcher.



## REFERENCES

- Abdelrahim, E. M. D., Mansour, R. F., & Al-Marghilnai, A. (2017). Shadow Detection and Geo-tagged Image Information Based Strategic Infrastructure Characterization. <https://doi.org/10.48550/arXiv.1709.08375>
- ACI 549.6R-20. (2020). *Guide to Design and Construction of Externally Bonded Fabric-Reinforced Cementitious Matrix (FRCM) and Steel-Reinforced Grout (SRG) Systems for Repair and Strengthening Masonry Structures*. ACI: Farmington Hills, MI, USA. ISBN 9781641951203
- Adeli, H., & Jiang, X. (2006). Dynamic fuzzy wavelet neural network model for structural system identification. *Journal of Structural Engineering*, 132(1), 102–111. [https://doi.org/10.1061/\(ASCE\)0733-9445\(2006\)132,1\(102\)](https://doi.org/10.1061/(ASCE)0733-9445(2006)132,1(102))
- Akbas, B., Shen, J., & Sabol, T.A. (2011). Estimation of seismic-induced demands on column splices with a neural network model. *Applied Soft Computing*, 11(8), 4820-4829. <https://doi.org/10.1016/j.asoc.2011.06.019>
- Akhani, M., Kashani, A. R., M, M., & Gandomi, A. H. (2019). A hybrid computational intelligence approach to predict spectral acceleration. *Measurement*, 138, 578–589. <https://doi.org/10.1016/j.measurement.2019.02.054>
- Akkar, S., Sandikkaya, M.A., Sxenyurt, M, Sisi, A.A., Ay, B., Traversa, P., Douglas, J., Cotton, F., Luzi, L., Hernandez, B., & Godey, S. (2014). Reference database for seismic ground-motion in Europe (RESORCE). *Bulletin of Earthquake Engineering*, 12(1), 311–339. <https://doi.org/10.1007/s10518-013-9506-8>
- Al-Habashna, A. (2020). Reports on Special Business Projects An Open-source System for Building-height Estimation using Street-view Images, Deep Learning, and Building Footprints. 18, 1–24. [www.statcan.gc.ca](http://www.statcan.gc.ca)
- Alavi, A.H., & Gandomi, A.H. (2011). Prediction of principal ground-motion parameters using a hybrid method coupling artificial neural networks and simulated annealing. *Computers and Structures*, 89, 2176-2194. <https://doi.org/10.1016/j.compstruc.2011.08.019>
- Alavi, A.H., Gandomi, A.H., Modaresnezhad. M, & Mousavi, M. (2011). New ground-motion prediction equations using multi expression programming. *Journal of Earthquake Engineering*, 15(4), 511-536. <https://doi.org/10.1080/13632469.2010.526752>
- Albert, A., Kaur, J., & Gonzalez, M. C. (2017). Using convolutional networks and satellite imagery to identify patterns in urban environments at a large scale. *Proceedings of the ACM SIGKDD International Conference on Knowledge Discovery and Data Mining, Part F1296*, 1357–1366. <https://doi.org/10.1145/3097983.3098070>

- Alimoradi, A., & Beck, J.L. (2015). Machine-learning methods for earthquake ground motion analysis and simulation. *Journal of Engineering Mechanics*, 141(4), 04014147. [https://doi.org/10.1061/\(ASCE\)EM.1943-7889.0000869](https://doi.org/10.1061/(ASCE)EM.1943-7889.0000869)
- Allali, S. A., Abed, M., & Mebarki, A. (2018). Post-earthquake assessment of buildings damage using fuzzy logic. *Engineering Structures*, 166, 117–127. <https://doi.org/10.1016/j.engstruct.2018.03.055>
- AlShawa, O., Liberatore, D., & Sorrentino, L. (2019). Dynamic One-Sided Out-Of-Plane Behavior of Unreinforced-Masonry Wall Restrained by Elasto-Plastic Tie-Rods. *International Journal of Architectural Heritage*, 13(3), 340–357. <https://doi.org/10.1080/15583058.2018.1563226>
- Alvanitopoulos, P.F., Andreadis, I., & Elenas, A. (2010). Neuro-fuzzy techniques for the classification of earthquake damages in buildings. *Measurement*, 43(6), 797–809. <https://doi.org/10.1016/j.measurement.2010.02.011>
- Amiri, G.G., Khorasani, M., Hessabi, R.M., & Amrei, S.A.R. (2010). Ground-motion prediction equations of spectral ordinates and arias intensity for Iran. *Journal of Earthquake Engineering* 14(1), 1–29. <https://doi.org/10.1080/13632460902988984>
- Ancheta, T.D., Darragh, R.B., Stewart, J.P., Seyhan, E., Silva, W.J., Chiou, B.S.J., Wooddell, K.E., Graves, R.W., Kottke, A., Boore, D.M., Kishida, T. & Donahue, J. (2014). NGA-West2 database. *Earthquake Spectra*, 30(3), 989–1005. <https://doi.org/10.1193/070913EQS197M>
- Aoki, T., Ceravolo, R., Stefano, A., Genovese, C., & Sabia, D. (2002). Seismic vulnerability assessment of chemical plants through probabilistic neural networks. *Reliability Engineering and System Safety*, 77(3), 263–268. [https://doi.org/10.1016/S0951-8320\(02\)00059-5](https://doi.org/10.1016/S0951-8320(02)00059-5)
- Araújo, A. S., Oliveira, D. V., & Lourenço, P. B. (2014). Numerical study on the performance of improved masonry-to-timber connections in traditional masonry buildings. *Engineering Structures*, 80, 501–513. <https://doi.org/10.1016/j.engstruct.2014.09.027>
- Arévalo, V., González, J., Valdes, J., & Ambrosio, G. (2006). Detecting shadows in QuickBird satellite images. *International Archives of the Photogrammetry, Remote Sensing and Spatial Information Sciences - ISPRS Archives*, 36(May).
- Arosio, G. (1941). *Enciclopedia del costruttore edile*. Hoepli. (in Italian)
- Askan, A., & Yucemen, M. S. (2010). Probabilistic methods for the estimation of potential seismic damage, Application to reinforced concrete buildings in Turkey. *Structural Safety*, 32(4), 262-271. <https://doi.org/10.1016/j.strusafe.2010.04.001>
- Baggio, C., Bernardini, A., Colozza, R., Corazza, L., Della Bella, M., Di Pasquale, G., Dolce, M., Goretti, A., Martinelli, A., Orsini, G., Papa, F., & Zuccaro, G. (2014). Manuale per la compilazione della scheda di primo livello di rilevamento

danno, pronto intervento e agibilità per edifici ordinari nell'emergenza post-sismica (AEDES). (in Italian)

- Baggio, C., Bernardini, A., Colozza, R., Corazza, L., Della Bella, M., Di Pasquale, G., Dolce, M., Goretti, A., Martinelli, A., Orsini, G., Papa, F., & Zuccaro, G. (2007). Field Manual for post-earthquake damage and safety assessment and short term countermeasures (AeDES) (M. Rota & A. Goretti, Trans.). *Joint Research Centre*.
- Bakhshi, H., Bagheri, A., Ghodrati Amiri, G., & Barkhordari, M.A. (2014). Estimation of spectral acceleration based on neural networks. *Proceedings of the Institution of Civil Engineers - Structures and Buildings*, 167(8), 457–468. <https://doi.org/10.1680/stbu.12.00059>
- Ballarini, I., Corgnati, S. P., & Corrado, V. (2014). Use of reference buildings to assess the energy saving potentials of the residential building stock, The experience of TABULA project. *Energy Policy*, 68, 273–284. <https://doi.org/10.1016/j.enpol.2014.01.027>
- Bani-Hani, K., & Ghaboussi, J. (1998). Neural networks for structural control of a benchmark problem, active tendon system. *Earthquake Engineering and Structural Dynamics*, 27(11), 1225-1245. [https://doi.org/10.1002/\(SICI\)1096-9845\(1998110\)27:11<1225::AID-EQE780>3.0.CO;2-T](https://doi.org/10.1002/(SICI)1096-9845(1998110)27:11<1225::AID-EQE780>3.0.CO;2-T)
- Bani-Hani, K., & Sheban, M.A. (2006). Semi-active neuro-control for base-isolation system using magnetorheological (MR) dampers. *Earthquake Engineering and Structural Dynamics*, 35(9), 1119-1144. <https://doi.org/10.1002/eqe.574>
- Bani-Hani, K., Ghaboussi, J., & Schneider, S.P. (1999a). Experimental study of identification and control of structures using neural network. Part 1, Identification. *Earthquake Engineering and Structural Dynamics*, 28(9), 995-1018. [https://doi.org/10.1002/\(SICI\)1096-9845\(199909\)28:9<995::AID-EQE851>3.0.CO;2-8](https://doi.org/10.1002/(SICI)1096-9845(199909)28:9<995::AID-EQE851>3.0.CO;2-8)
- Bani-Hani, K., Ghaboussi, J., & Schneider, S.P. (1999b). Experimental study of identification and control of structures using neural network. Part 2, Control. *Earthquake Engineering and Structural Dynamics*, 28(9), 1019-1039. [https://doi.org/10.1002/\(SICI\)1096-9845\(199909\)28:9<1019::AID-EQE852>3.0.CO;2-X](https://doi.org/10.1002/(SICI)1096-9845(199909)28:9<1019::AID-EQE852>3.0.CO;2-X)
- Barbat, A.H., Pujades, L.G., & Lantada, N. (2008). Seismic damage evaluation in urban areas using the capacity spectrum method, Application to Barcelona. *Soil Dynamics and Earthquake Engineering*, 28(10-11), 851–865. <https://doi.org/10.1016/j.soildyn.2007.10.006>
- Barrington-Leigh, C., & Millard-Ball, A. (2017). The world's user-generated road map is more than 80% complete. *PLoS ONE*, 12(8), 1–20. <https://doi.org/10.1371/journal.pone.0180698>

- Bartlett, S.F., & Youd, T.L. (1995). Empirical prediction of liquefaction-induced lateral spread. *Journal of Geotechnical Engineering*, 121(4), 316-329. [https://doi.org/10.1061/\(ASCE\)0733-9410\(1995\)121:4\(316\)](https://doi.org/10.1061/(ASCE)0733-9410(1995)121:4(316))
- Baziar, M.H., & Ghorbani, A. (2005). Evaluation of lateral spreading using artificial neural networks. *Soil Dynamics and Earthquake Engineering*, 25(1), 1-9. <https://doi.org/10.1016/j.soildyn.2004.09.001>
- BELICE project (2018). Manual of ASR1. Wide area assessment process.
- Benedetti, D., & Petrini, V. (1984). On seismic vulnerability of masonry buildings, proposal of an evaluation procedure. *L'industria delle Costruzioni*, 18(149), 66-78.
- Bernardini, A. (2000). *La vulnerabilità degli edifici. Valutazione a scala nazionale della vulnerabilità sismica degli edifici ordinari*. CNR-Gruppo Nazionale Difesa Terremoti. (in Italian)
- Bernardini, A., & Tonon, F. (2004). Aggregation of evidence from random and fuzzy sets. *ZAMM Journal of Applied Mathematics and Mechanics*, 84(10–11), 700–709. <https://doi.org/10.1002/zamm.200410145>
- Bernardini, A., Gori, M., & Modena, C. (1990). Application of coupled analytical models and experimental knowledge to seismic vulnerability analyses of masonry buildings. In A. Koridze, *Earthquake damage evaluation and vulnerability analysis of building structures*. (Vol. 3, pp. 161–180). Oxon: Omega Scientific.
- Bernardini, A., Lagomarsino, S., Mannella, A., Martinelli, A., Milano, L., & Parodi, S. (2010). Forecasting seismic damage scenarios of residential buildings from rough inventories: A case-study in the Abruzzo Region (Italy). *Proceedings of the Institution of Mechanical Engineers, Part O: Journal of Risk and Reliability*, 224(4), 279–296. <https://doi.org/10.1243/1748006XJRR305>
- Bernardini, A., Valluzzi, M. R., Modena, C., D'Ayala, D., & Speranza, E. (2008). Vulnerability assessment of the historical masonry building typologies of Vittorio Veneto (NE Italy). *Bollettino Di Geofisica Teorica Ed Applicata*, 49(3–4), 463–483.
- Bezak, P. (2016). Building recognition system based on deep learning. *2016 3rd International Conference on Artificial Intelligence and Pattern Recognition, AIPR 2016*, 159–163. <https://doi.org/10.1109/ICAIPR.2016.7585230>
- Biljecki, F., Ledoux, H., & Stoter, J. (2017). Generating 3D city models without elevation data. In *Computers, Environment and Urban Systems* (Vol. 64). <https://doi.org/10.1016/j.compenvurbsys.2017.01.001>
- Bird, J. F., Bommer, J. J., H, C., & Pinho, R. (2006). Modelling liquefaction-induced building damage in earthquake loss estimation. *Soil Dynamics and Earthquake Engineering*, 26(1), 15–30. <https://doi.org/10.1016/j.soildyn.2005.10.002>

- Bishop, C.M. (2006). Pattern Recognition and Machine Learning (eds. Jordan, M., Kleinberg, J., Scholkopf, B.), New York, Springer.
- Boeing, G. (2017). OSMnx, New methods for acquiring, constructing, analyzing, and visualizing complex street networks. *Computers, Environment and Urban Systems*, 65, 126–139. <https://doi.org/10.1016/j.compenvurbsys.2017.05.004>
- Boeing, G. (2020). A multi-scale analysis of 27,000 urban street networks, Every US city, town, urbanized area, and Zillow neighborhood. *Environment and Planning B, Urban Analytics and City Science*, 47(4), 590-608. <https://doi.org/10.1177/2399808318784595>
- Boeing, G. (2021). Spatial information and the legibility of urban form, Big data in urban morphology. *International Journal of Information Management*, 56(September 2019), 102013. <https://doi.org/10.1016/j.ijinfomgt.2019.09.009>
- Boore, D.M., & Atkinson, G.M. (2008). Ground-motion prediction equations for the average horizontal component of PGA, PGV, and 5%-damped PSA at spectral periods between 0.01 s and 10.0 s. *Earthquake Spectra*, 24(1), 99–138. <https://doi.org/10.1193/1.2830434>
- Boore, D.M., Stewart, J.P., Seyhan, E., & Atkinson, G.M. (2014). NGA-West2 equations for predicting PGA, PGV, and 5% damped PSA for shallow crustal earthquakes. *Earthquake Spectra* 30(3), 1057–1085. <https://doi.org/10.1193/070113EQS184M>
- Borri, A., Castori, G., & Corradi, M. (2011). Shear behavior of masonry panels strengthened by high strength steel cords. *Construction and Building Materials*, 25(2), 494–503. <https://doi.org/10.1016/j.conbuildmat.2010.05.014>
- Borri, A., Corradi, M., Castori, G., & Molinari, A. (2019). Stainless steel strip – A proposed shear reinforcement for masonry wall panels. *Construction and Building Materials*, 211, 594–604. <https://doi.org/10.1016/j.conbuildmat.2019.03.197>
- Borri, A., Sisti, R., Corradi, M., & Giannantoni, A. (2016). Experimental analysis of masonry ring beams reinforced with composite materials. In C. Modena, F. da Porto, & M. R. Valluzzi (Eds.), *Brick and Block Masonry* (0 ed., pp. 717–726). CRC Press. <https://doi.org/10.1201/b21889-90>
- Borzi, B., Faravelli, M., Di Meo, A. (2021a). Application of the SP-BELA methodology to RC residential buildings in Italy to produce seismic risk maps for the national risk assessment. *Bulletin of Earthquake Engineering*, 19, 3185–3208. <https://doi.org/10.1007/s10518-020-00953-6>
- Borzi, B., Onida, M., Faravelli, M., Polli, D., Pagano, M., Quaroni, D., Cantoni, A., Speranza, E., & Moroni, C. (2021b). IRMA platform for the calculation of damages and risks of Italian residential buildings. *Bulletin of Earthquake Engineering*, 19(8), 3033–3055. <https://doi.org/10.1007/s10518-020-00924-x>

- Bostrom, A., French, S., & Gottlieb, S. (2008). Risk Assessment, Modeling and Decision Support. Risk, Governance and Society, eds. Springer, ISBN 978-3-540-71158-2.
- Boulanger, R.W., & Idriss, I.M. (2014). CPT and SPT based liquefaction triggering procedures. Report No. UCD/CGM-14/01, April. Davis, CA, University of California at Davis.
- Box, G.E.P., & Hunter, J.S. (1957). Multi-factor experimental designs for exploring response surfaces. *The Annals of Mathematical Statistics*, 28, 195–241.
- Bozorgvar, M., & Zahrai, S.M. (2019). Semi-active seismic control of buildings using MR damper and adaptive neural-fuzzy intelligent controller optimized with genetic algorithm. *Journal of Vibration and Control*, 25(2), 273-285. <https://doi.org/10.1177/1077546318774502>
- Bozzoni, F., & Lai, C.G. (2017). Tools for rapid seismic response assessment of strategic facilities under GIS environment, applications to Italian seaports and embankment dams. *Proceedings of the 3rd International conference on performance-based design in earthquake geotechnical engineering*. Vancouver, British Columbia, Canada, July 16-19, 2017.
- Bozzoni, F., Chiarolla, S., & Lai, C.G. (2015). Valutazione della risposta sismica di dighe in terra della Regione Campania mediante approcci semplificati. *Progettazione Sismica*, 6, 49–67.
- Braga, F., Dolce, M., & Liberatore, D. (1982). A statistical study on damaged buildings and an ensuing review of the MSK-76 scale. *Proceedings of the 7th European Conference on Earthquake Engineering*, Athens, Greece.
- Braga, F., Gigliotti, R., Monti, G., Morelli, F., Nuti, C., Salvatore, W., & Vanzi, I. (2014). Speedup of post earthquake community recovery, the case of precast industrial buildings after the Emilia 2012 earthquake. *Bulletin of Earthquake Engineering*, 12(5), 2405–2418. <https://doi.org/10.1007/s10518-014-9583-3>
- Branco, J. M., & Tomasi, R. (2014). Analysis and Strengthening of Timber Floors and Roofs. In A. Costa, J. M. Guedes, & H. Varum (Eds.), *Structural Rehabilitation of Old Buildings* (Vol. 2, pp. 235–258). Springer Berlin Heidelberg. [https://doi.org/10.1007/978-3-642-39686-1\\_8](https://doi.org/10.1007/978-3-642-39686-1_8)
- Brown, A.S., & Yang, H.T.Y. (2001). Neural networks for multiobjective adaptive structural control. *Journal of Structural Engineering*, 127(2), 203-210. [https://doi.org/10.1061/\(ASCE\)0733-9445\(2001\)127:2\(203\)](https://doi.org/10.1061/(ASCE)0733-9445(2001)127:2(203))
- Brzev, S., Scawthorn, C., Charleson, A.W., Allen, L., Greene, M., Jaiswal, K., & Silva, V. (2013). GEM building taxonomy version 2.0. GEM Technical Report 2013-02 V1.0.0. Pavia, Italy, GEM Foundation.

- Buratti, N., Ferracuti, B., & Savoia, M. (2010). Response Surface with random factors for seismic fragility of reinforced concrete frames. *Structural Safety*, 32(1), 42–51. <https://doi.org/10.1016/j.strusafe.2009.06.003>
- Burton, H. V, Sreekumar, S., Sharma, M., & Sun, H. (2017). Estimating aftershock collapse vulnerability using mainshock intensity, structural response and physical damage indicators. *Structural Safety*, 68, 85–96. <https://doi.org/10.1016/j.strusafe.2017.05.009>
- Cacace, F., Zuccaro, G., De Gregorio, D., & Perelli, F. L. (2018). Building Inventory at National scale by evaluation of seismic vulnerability classes distribution based on Census data analysis: BINC procedure. *International Journal of Disaster Risk Reduction*, 28, 384–393. <https://doi.org/10.1016/j.ijdrr.2018.03.016>
- Cai, B. Y., Li, X., Seiferling, I., & Ratti, C. (2018). Treepedia 2.0, Applying Deep Learning for Large-Scale Quantification of Urban Tree Cover. *Proceedings - 2018 IEEE International Congress on Big Data, BigData Congress 2018 - Part of the 2018 IEEE World Congress on Services*, 49–56. <https://doi.org/10.1109/BigDataCongress.2018.00014>
- Calabrese, A., & Lai, C.G. (2013). Fragility functions of blockwork wharves using artificial neural networks. *Soil Dynamics and Earthquake Engineering*, 52, 88–102. <https://doi.org/10.1016/j.soildyn.2013.05.002>
- Calderini, C., Vecchiattini, R., Battini, C., & Piccardo, P. (2016). Mechanical and metallographic characterization of iron tie-rods in masonry buildings: An experimental study. In *Structural Analysis of Historical Constructions: Anamnesis, Diagnosis, Therapy, Controls*. CRC Press.
- Calvi, G. M., Pinho, R., Magenes, G., Bommer, J. J., Restrepo-Vélez, L. F., & Crowley, H. (2006). Development of seismic vulnerability assessment methodologies over the past 30 years. *ISET Journal of Earthquake Technology*, 43(3), 75-104.
- Calvi, G.M. (1999). A displacement-based approach for vulnerability evaluation of classes of buildings. *Journal of Earthquake Engineering*, 3(3), 411-438. <https://doi.org/10.1080/13632469909350353>
- Campostrini, G. P., Taffarel, S., Bettiol, G., Valluzzi, M. R., Da Porto, F., & Modena, C. (2018). A Bayesian approach to rapid seismic vulnerability assessment at urban scale. *International Journal of Architectural Heritage*, 12(1), 36–46. <https://doi.org/10.1080/15583058.2017.1370506>
- Cantalupi, A. (1862). *Instituzioni pratiche sull'arte di costruire le fabbriche civili*. Galli e Omodei. (in Italian)
- Capozucca, R. (2010). Experimental FRP/SRP–historic masonry delamination. *Composite Structures*, 92(4), 891–903. <https://doi.org/10.1016/j.compstruct.2009.09.029>

- Carbonara, P. (1954). *Trattato di architettura pratica*. Utet. (in Italian)
- Cardellicchio, A., Ruggieri, S., Leggieri, V., & Uva, G. (2022). View VULMA: Data Set for Training a Machine-Learning Tool for a Fast Vulnerability Analysis of Existing Buildings. *Data*, 7(1). <https://doi.org/10.3390/data7010004>
- Carpanese, P., Follador, V., Donà, M., & da Porto, F. (2022). Effectiveness of seismic mitigation strategies for the Italian masonry building heritage. *XIX ANIDIS Conference, Seismic Engineering in Italy*, Turin, Italy, September 11-15, 2022.
- Carpanese, P., Follador, V., Donà, M., & da Porto, F. (2022). Efficacia di strategie di mitigazione sismica per il patrimonio edilizio italiano in muratura. *40° convegno nazionale GNGTS*. Trieste, Italy, June 27-29, 2022. (in Italian)
- Carpanese, P., Follador, V., Saler, E., & da Porto, F. (2021). Seismic risk assessment for the Italian residential masonry built stock and effectiveness of different mitigation strategies. *8th ECCOMAS Thematic Conference on Computational Methods in Structural Dynamics and Earthquake Engineering (COMPADYN 2021)*, Athens, Greece, June 27–30, 2021.
- Carreño, M.L., Cardona, O.D., & Barbat, A.H. (2010). Computational tool for post-earthquake evaluation of damage in buildings. *Earthquake Spectra*, 26(1), 63–86. <https://doi.org/10.1193/1.3282885>
- Casapulla C., Giresini L., Argiento L.U., & Maione A. (2019). Nonlinear static and dynamic analysis of rocking masonry corners using rigid macro-block modelling. *International Journal of Structural Stability and Dynamics*, 19(11), 1- 32. <https://doi.org/10.1142/S0219455419501372>
- Casapulla, C., Argiento, L.U., da Porto, F., & Bonaldo, D. (2016). The relevance of frictional resistances in out-of-plane mechanisms of block masonry structures. Proceedings of the 16th International Brick and Block Masonry Conference (IBMAC 2016), 119-127. Padova, Italy, 26-30 June 2016.
- Cascardi, A., Leone, M., & Aiello, M. A. (2020). Transversal joining of multi-leaf masonry through different types of connector: Experimental and theoretical investigation. *Construction and Building Materials*, 265, 120733. <https://doi.org/10.1016/j.conbuildmat.2020.120733>
- Castagno, J., & Atkins, E. (2018). Roof shape classification from LiDAR and satellite image data fusion using supervised learning. *Sensors (Switzerland)*, 18(11). <https://doi.org/10.3390/s18113960>
- Ceccarini, I. (1952). *Composizione della casa*. Hoepli. (in Italian)
- Cescatti, E., Porto, F. da, Modena, C., & Casarin, F. (2016). *Ties in historical constructions: Typical features and laboratory tests*. Structural Analysis of Historical Constructions, Leuven, Belgium.



- Chang, C., & Roschke, P. (1998). Neural network modeling of a magnetorheological damper. *Journal of Intelligent Material Systems and Structures*, 9, 755-764. <https://doi.org/10.1177/1045389X9800900908>
- Chiou, B., Darragh, R., Gregor, N., & Silva, W. (2008). NGA project strong-motion database. *Earthquake Spectra*, 24(1), 23–44. <https://doi.org/10.1193/1.2894831>
- Chiru-Danzer, M., Juang, C. H., Christopher, R.A. & Suber, J. (2001). Estimation of liquefaction-induced horizontal displacements using artificial neural networks. *Canadian Geotechnical Journal*, 38(1), 200–207. <https://doi.org/10.1139/t00-087>
- CNR-DT 215/2018. (2020). *Istruzioni per la Progettazione, l'Esecuzione ed il Controllo di Interventi di Consolidamento Statico mediante l'utilizzo di Compositi Fibrorinforzati a Matrice Inorganica*. (in Italian)
- Coburn, A., & Spence, R. (1992). Earthquake protection. *Bulletin of the New Zealand Society for Earthquake Engineering*. <https://doi.org/10.5459/bnzse.e.27.2.163>
- Coburn, A.W., Spence, R.J.S., & Pomonis, A. (1992). Factors determining human casualty levels in earthquakes, Mortality prediction in building collapse. Proceedings of Earthquake Engineering - 10th World Conference Balkema, Rotterdam, 1992, 5989–5994.
- Comber, A., Umezaki, M., Zhou, R., Ding, Y., Li, Y., Fu, H., Jiang, H., & Tewkesbury, A. (2012). Using shadows in high-resolution imagery to determine building height. *Remote Sensing Letters*, 3(7), 551–556. <https://doi.org/10.1080/01431161.2011.635161>
- Conte, J. P., Durrani, A.J., & Shelton, R. O. (1994). Seismic response modeling of multi-story buildings using neural networks. *Journal of Intelligent Material Systems and Structures*, 5(3), 392–402. <https://doi.org/10.1177/1045389X9400500312>
- Contento, A., Gardoni, P., Egidio, A., and Di De Leo, A.M. (2017). Probability models to assess the seismic safety of rigid block-like structures and the effectiveness of two safety devices. *Procedia Engineering*, 199, 1164–1169. <https://doi.org/10.1016/j.proeng.2017.09.312>
- Corradi, M., Borri, A., Castori, G., & Sisti, R. (2014). Shear strengthening of wall panels through jacketing with cement mortar reinforced by GFRP grids. *Composites Part B: Engineering*, 64, 33–42. <https://doi.org/10.1016/j.compositesb.2014.03.022>
- Corradi, M., Borri, A., Poverello, E., & Castori, G. (2017). The use of transverse connectors as reinforcement of multi-leaf walls. *Materials and Structures*, 50(2), 114. <https://doi.org/10.1617/s11527-016-0977-3>
- Corradi, M., Tedeschi, C., Binda, L., & Borri, A. (2008). Experimental evaluation of shear and compression strength of masonry wall before and after

- reinforcement: Deep repointing. *Construction and Building Materials*, 22(4), 463–472. <https://doi.org/10.1016/j.conbuildmat.2006.11.021>
- Corrado, V., Ballarini, I., & Corgnati, S. P. (2014). *Typology Approach for Building Stock, National scientific report on the TABULA activities in Italy* (Issue June 2009).
- Corsanego, A., & Petrini, V. (1990). Seismic vulnerability of buildings, work in progress, Proceedings SEISMED Workshop on Seismic Vulnerability and Risk Assessment, Trieste, 577–598.
- Criminisi, A., Reid, I., & Zisserman, A. (2000). Single view metrology. *International Journal of Computer Vision*, 40(2), 123–148. <https://doi.org/10.1023/A:1026598000963>
- Crowley, H., Colombi, M., Crempien, J., et al. (2010). GEM1 seismic risk report.
- Cubrinovski, M., Winkley, A., Haskell, J., Palermo, A., Wotherspoon, L., Robinson, K., Bradley, B., Brabhakaran, P., & Hughes, M. (2014). Spreading-induced damage to short-span bridges in Christchurch, New Zealand. *Earthquake Spectra*, 30(1), 57–83. <https://doi.org/10.1193/030513EQS063M>
- Curioni, G. (1868). *L'arte del fabbricare*. Augusto Federico Negro Editore. (in Italian)
- D'Ayala, D. (1998). *The use of bed joint reinforcement to improve the performance of historic masonry buildings*. 320–326.
- D'Ayala, D., & Speranza, E. (2003). Definition of collapse mechanisms and seismic vulnerability of masonry structures. *Earthquake Spectra*, 19(3), 479–509. <https://doi.org/10.1193/1.1599896>
- da Porto, F., Lagomarsino, S., Cattari, S., Follador, V., Carpanese, P., Donà, M., Alfano, S. (2022). Fragility curves of as-built and retrofitted masonry buildings in Italy. *3rd European Conference on Earthquake Engineering and Seismology (3ECEES)*. Bucharest, Romania, September 4-9, 2022.
- da Porto, F., Munari, M., Prota, A., & Modena, C. (2013). Analysis and repair of clustered buildings: Case study of a block in the historic city centre of L'Aquila (Central Italy). *Construction and Building Materials*, 38, 1221–1237. <https://doi.org/10.1016/j.conbuildmat.2012.09.108>
- da Porto, F., Valluzzi, M. R., Munari, M., Modena, C., Arède, A., & Costa, A. A. (2018). Strengthening of Stone and Brick Masonry Buildings. In A. Costa, A. Arède, & H. Varum (Eds.), *Strengthening and Retrofitting of Existing Structures* (Vol. 9, pp. 59–84). Springer Singapore. [https://doi.org/10.1007/978-981-10-5858-5\\_3](https://doi.org/10.1007/978-981-10-5858-5_3)
- De Felice, G., & Giannini, R. (2010). An efficient approach for seismic fragility assessment with application to old reinforced concrete bridges. *Journal of*

- Earthquake Engineering*, 14(2), 231-251.  
<https://doi.org/10.1080/13632460903086028>
- de Felice, G., De Santis, S., Garmendia, L., Ghiassi, B., Larrinaga, P., Lourenço, P. B., Oliveira, D. V., Paolacci, F., & Papanicolaou, C. G. (2014). Mortar-based systems for externally bonded strengthening of masonry. *Materials and Structures*, 47(12), 2021–2037. <https://doi.org/10.1617/s11527-014-0360-1>
- De Grandis, S., Domaneschi, M., & Perotti, F. (2009). A numerical procedure for computing the fragility of NPP components under random seismic excitation. *Nuclear Engineering and Design*, 239(11), 2491-2499. <https://doi.org/10.1016/j.nucengdes.2009.06.027>
- De Lautour, R.O., & Omenzetter, P. (2009). Prediction of seismic-induced structural damage using artificial neural networks. *Engineering Structures*, 31(2), 600-606. <https://doi.org/10.1016/j.engstruct.2008.11.010>
- De Stefano, A., Sabia, D., & Sabia, L. (1999). Probabilistic neural networks for seismic damage mechanisms prediction. *Earthquake Engineering & Structural Dynamics*, 28(8), 807-821. [https://doi.org/10.1002/\(SICI\)1096-9845\(199908\)28:8<807::AID-EQE838>3.0.CO;2-#](https://doi.org/10.1002/(SICI)1096-9845(199908)28:8<807::AID-EQE838>3.0.CO;2-#)
- Deb, K., Pratap, A., Agarwal, S., & Meyarivan, T. (2002). A fast and elitist multiobjective genetic algorithm: NSGA-II. *IEEE Transactions on Evolutionary Computation*, 6(2), 182–197. <https://doi.org/10.1109/4235.996017>
- Del Vecchio, C., Di Ludovico, M., & Prota, A. (2020). Repair costs of reinforced concrete building components, From actual data analysis to calibrated consequence functions. *Earthquake Spectra*, 36, 353–377. <https://doi.org/10.1177/8755293019878194>
- Del Vecchio, C., Di Ludovico, M., Pampanin, S., & Prota, A. (2018). Repair costs of existing rc buildings damaged by the l'Aquila earthquake and comparison with FEMA P-58 predictions. *Earthquake Spectra*, 34, 237–263. <https://doi.org/10.1193/122916EQS257M>
- Demartinos, K., & Dritsos, S. (2006). First-level pre-earthquake assessment of buildings using fuzzy logic. *Earthquake Spectra*, 22(4), 865-885. <https://doi.org/10.1193/1.2358176>
- Derras, B., Bard, P.Y., & Cotton, F. (2014). Towards fully data driven ground-motion prediction models for Europe. *Bulletin of Earthquake Engineering*, 12(1), 495–516. <https://doi.org/10.1007/s10518-013-9481-0>
- Dhanya, J., & Raghukanth, S.T.G. (2018). Ground motion prediction model using artificial neural network. *Pure and Applied Geophysics*, 175(3), 1035–1064. <https://doi.org/10.1007/s00024-017-1751-3>

- Di Ludovico, M., De Martino, G., Prota, A., Manfredi, G., & Dolce, M. (2022). Relationships between empirical damage and direct/indirect costs for the assessment of seismic loss scenarios. *Bulletin of Earthquake Engineering*, 20, 229–254. <https://doi.org/10.1007/s10518-021-01235-5>
- Di Ludovico, M., Prota, A., Moroni, C., Manfredi, G., & Dolce, M. (2017a). Reconstruction process of damaged residential buildings outside historical centres after the L'Aquila earthquake, part I - "light damage" reconstruction. *Bulletin of Earthquake Engineering*, 15(2), 667-692. <https://dx.doi.org/10.1007/s10518-016-9877-8>
- Di Ludovico, M., Prota, A., Moroni, C., Manfredi, G., & Dolce, M. (2017b). Reconstruction process of damaged residential buildings outside historical centres after the L'Aquila earthquake, part II - "heavy damage" reconstruction. *Bulletin of Earthquake Engineering*, 15(2), 693-729. <https://dx.doi.org/10.1007/s10518-016-9979-3>
- Di Meo, A., Borzi, B., Quaroni, D., Onida, M., & Pasquale, V. (2018). Real time damage scenario and seismic risk assessment of Italian roadway network. *Proceedings of the 16th European conference on earthquake engineering*, Thessaloniki, Greece, 18-21 June 2018.
- Di Pasquale, G., & Goretti, A. (2001). Functional and economic vulnerability of residential buildings affected by recent Italian earthquakes. *Proceedings of the 'X Convegno Nazionale di Ingegneria Sismica.'* X ANIDIS, Potenza-Matera, Italy.
- Di Pasquale, G., Orsini, G., & Romeo, R. W. (2005). New developments in seismic risk assessment in Italy. *Bulletin of Earthquake Engineering*, 3, 101-128. <https://doi.org/10.1007/s10518-005-0202-1>
- Di Sivo, M. (1981). *Normativa e tipologia dell'abitazione popolare, l'origine e lo sviluppo nelle leggi della casa dal 1902 al 1980*. Alinea Editrice. (in Italian)
- Diaz Plata, E.D., & Arguello, H. (2016). An algorithm to estimate building heights from Google street-view imagery using single view metrology across a representational state transfer system. *Proceedings of the SPIE, Volume 9868, Baltimore, Maryland, United States, April 17-21, 2016*. <https://doi.org/10.1117/12.2224312>
- Dimitrov, A., & Golparvar-Fard, M. (2014). Vision-based material recognition for automated monitoring of construction progress and generating building information modeling from unordered site image collections. *Advanced Engineering Informatics*, 28(1), 37–49. <https://doi.org/10.1016/j.aei.2013.11.002>
- Dizhur, D., Wei, S., Giaretton, M., Schultz, A. E., Ingham, J. M., & Giongo, I. (2021). Testing of URM wall-to-diaphragm through-bolt plate anchor connections. *Earthquake Spectra*, 37(1), 304–323. <https://doi.org/10.1177/8755293020944187>

- Dolce, M., & Goretti, A. (2015). Building damage assessment after the 2009 Abruzzi earthquake. *Bulletin of Earthquake Engineering*, 13(8), 2241–2264. <https://doi.org/10.1007/s10518-015-9723-4>
- Dolce, M., & Moroni, C. (2005). La Valutazione della vulnerabilità e del rischio sismico degli edifici pubblici mediante le procedure VC (Vulnerabilità c.a.) e VM (Vulnerabilità muratura). (in Italian)
- Dolce, M., Prota, A., Borzi, B., da Porto, F., Lagomarsino, S., Magenes, G., Moroni, C., Penna, A., Polese, M., Speranza, E., Verderame, G. M., & Zuccaro, G. (2021). Seismic risk assessment of residential buildings in Italy. *Bulletin of Earthquake Engineering*, 19(8), 2999–3032. <https://doi.org/10.1007/s10518-020-01009-5>
- Dolce, M., Speranza, E., Giordano, F., & Bocchi, F. (2017b). Da.D.O – A web-based tool for analyzing and comparing post-earthquake damage database relevant to national seismic events since 1976. *ANIDIS 2017 Pistoia*, 1976(September), SG03.347-357.
- Dolce, M., Speranza, E., Giordano, F., Borzi, B., Bocchi, F., Conte, C., Meo, A. Di, Faravelli, M., & Pascale, V. (2019). Observed damage database of past Italian earthquakes, The Da.D.O. WebGIS. *Bollettino Di Geofisica Teorica Ed Applicata*, 60(2), 141–164. <https://doi.org/10.4430/bgta0254>
- Dolce, M., Speranza, E., Giordano, F., Borzi, F., Conte, C., Di Meo, A., Faravelli, M., & Pascale, V. (2017a). La Piattaforma web-GIS Da.D.O per la Consultazione e la comparazione del danno osservato in eventi sismici di rilevanza nazionale dal 1976. *Gngts 2017*, 2016(2001), 30. (in Italian)
- Donà, M., Bizzaro, L., Carturan, F., & da Porto, F. (2019). Effects of Business Recovery Strategies on Seismic Risk and Cost-Effectiveness of Structural Retrofitting for Business Enterprises. *Earthquake Spectra* 35(4), 1795–1819. <https://doi.org/10.1193/041918EQS098M>
- Donà, M., Carpanese, P., Follador, V., & da Porto, F. (2019). Derivation of mechanical fragility curves for macro-typologies of Italian masonry buildings. *Proceedings of the 7th International Conference on Computational Methods in Structural Dynamics and Earthquake Engineering (COMPdyn 2015)*, 1691–1706. <https://doi.org/10.7712/120119.7029.19172>
- Donà, M., Carpanese, P., Follador, V., da Porto, F., Sbrogiò, L., & Xu L. (2020). Seismic fragility and risk of Italian residential masonry heritage. *17th International Brick and Block Masonry Conference (IB2MaC 2020)*, Krakow, Poland, July 5-8, 2020.
- Donà, M., Carpanese, P., Follador, V., Sbrogiò, L., & da Porto, F. (2021). Mechanics-based fragility curves for Italian residential URM buildings. *Bulletin of Earthquake Engineering*, 19(8), 3099–3127. <https://doi.org/10.1007/s10518-020-00928-7>
- Donghi, D. (1905). *Manuale dell'architetto*. Utet. (in Italian)

- Douglas, J. (2003). Earthquake ground motion estimation using strong-motion records, A review of equations for the estimation of peak ground acceleration and response spectral ordinates. *Earth- Science Reviews*, 61(1–2), 43–104. [https://doi.org/10.1016/S0012-8252\(02\)00112-5](https://doi.org/10.1016/S0012-8252(02)00112-5)
- DPC - Italian Civil Protection Department of the Presidency of the Council of Ministers (2018). National risk assessment - Overview of the potential major disasters in Italy, seismic, volcanic, tsunami, hydro-geological/hydraulic and extreme weather, droughts and forest fire risks, pp. 1 – 137
- Dubois, C., Thiele, A., & Hinz, S. (2016). Building detection and building parameter retrieval in InSAR phase images. *ISPRS Journal of Photogrammetry and Remote Sensing*, 114, 228–241. <https://doi.org/10.1016/j.isprsjprs.2016.02.009>
- Dukes, J., Mangalathu, S., Padgett, J.E., & DesRoches, R. (2018). Development of a bridge-specific fragility methodology to improve the seismic resilience of bridges. *Earthquake and Structures*, 15(3), 253–261. <https://doi.org/10.12989/eas.2018.15.3.253>
- Ebad Sichani, M., Padgett, J.E., & Bisadi, V. (2018). Probabilistic seismic analysis of concrete dry cask structures. *Structural Safety*, 73, 87-98. <https://doi.org/10.1016/j.strusafe.2018.03.001>
- Elnashai, A.S., Di Sarno, L. (2010). Fundamentals of earthquake engineering, from source to fragility, 2nd Edition. Wiley, ISBN, 978-1-118-67892-3.
- Elwood, E., & Corotis, R.B. (2015). Application of fuzzy pattern recognition of seismic damage to concrete structures. *ASCE-ASME Journal of Risk and Uncertainty in Engineering Systems, Part A, Civil Engineering*, 1(4), 04015011. <https://doi.org/10.1061/AJRUA6.0000831>
- Fabris, M., Achilli, V., Campostrini, G. P., & Modena, C. (2013). *L'aerofotogrammetria digitale per la stima delle caratteristiche strutturali degli edifici*.
- Faccioli, E., & Cauzzi, C. (2006). Macroseismic intensities for seismic scenarios estimated from instrumentally based correlations. *Proceedings First European Conference on Earthquake Engineering and Seismology*, paper number 569.
- Faravelli, M., Borzi, B., Di Meo, A., & Polli, D. (2017). A mechanic based model for definition of seismic risk and real time damage scenario of buildings. *Proceedings of the 6th international conference on computational methods in structural dynamics and earthquake engineering, COMPDYN 2017*, Rhodes Island, Greece, 15-17 June 2017, 637–651.
- Faravelli, M., Borzi, B., Pagano, M., & Quaroni, D. (2018). Using OpenQuake to define seismic risk and real time damage scenario in Italy. *Proceedings of the 16th European conference on earthquake engineering*, Thessaloniki, Greece, 18-21 June 2018.

- Farfani, H. A., Behnamfar, F., & Fathollahi, A. (2015). Dynamic analysis of soil-structure interaction using the neural networks and the support vector machines *Expert Systems with Applications*, 42(22), 8971–8981. <https://doi.org/10.1016/j.eswa.2015.07.053>
- FEMA - Federal Emergency Management Agency (2003). HAZUS-MH MR4 technical manual. The National Institute of Building Sciences, Federal Emergency Management Agency, <https://www.fema.gov/>
- Ferrario, E., Pedroni, N., Zio, E., & Lopez-Caballero, F. (2017). Bootstrapped artificial neural networks for the seismic analysis of structural systems. *Structural Safety*, 67, 70-84. <https://doi.org/10.1016/j.strusafe.2017.03.003>
- Ferreira, T.M., Maio, R. & Vicente, R. (2017) Seismic vulnerability assessment of the old city centre of Horta, Azores: calibration and application of a seismic vulnerability index method. *Bulletin of Earthquake Engineering*, 15, 2879–2899. <https://doi.org/10.1007/s10518-016-0071-9>
- Ferrini, M., Melozzi, A., Pagliuzzi, A., & Scarparolo, S. (2003). Rilevamento della Vulnerabilità Sismica degli Edifici in Muratura - Manuale per la Compilazione della Scheda GNDT/CNR di II Livello. Versione modificata Regione Toscana (in Italian)
- Fleischmann, M. (2019). *momepy*, Urban morphology measuring toolkit. *Journal of Open Source Software*, 4 (43). 1807. ISSN 2475-9066 (<https://doi.org/10.21105/joss.01807>)
- Fleischmann, M., Feliciotti, A., Romice, O., & Porta, S. (2020). Morphological tessellation as a way of partitioning space, Improving consistency in urban morphology at the plot scale. *Computers, Environment and Urban Systems*, 80, 101441. <https://doi.org/10.1016/j.compenvurbsys.2019.101441>
- Follador, V., Donà, M., Carpanese, P., & da Porto, F. (2021). Fragility curves for Italian residential masonry buildings with retrofit interventions. *8th ECCOMAS Thematic Conference on Computational Methods in Structural Dynamics and Earthquake Engineering (COMPDYN 2021)*, Athens, Greece, June 27–30, 2021. <https://doi.org/10.7712/120121.8698.18819>
- Forte, G., Chioccarelli, E., De Falco, M., Cito, P., Santo, A., & Iervolino, I. (2019). Seismic soil classification of Italy based on surface geology and shear-wave velocity measurements. *Soil Dynamics and Earthquake Engineering*, 122(March), 79–93. <https://doi.org/10.1016/j.soildyn.2019.04.002>
- Fu, J., Liao, G., Yu, M., Li, P., & Lai, J. (2016). NARX neural network modeling and robustness analysis of magnetorheological elastomer isolator. *Smart Materials and Structures*, 25(12), 1-17. <https://doi.org/10.1088/0964-1726/25/12/125019>
- Fukushima, K. (1980). Neocognitron, A self-organizing neural network model for a mechanism of pattern recognition unaffected by shift in position. *Biological Cybernetics*, 36(4), 193–202. <https://doi.org/10.1007/BF00344251>

- Gandomi, A. H., Alavi, A. H., M, M., & Tabatabaei, S. M. (2011). A hybrid computational approach to derive new ground-motion prediction equations. *Engineering Applications of Artificial Intelligence*, 24(4), 717–732. <https://doi.org/10.1016/j.engappai.2011.01.005>
- Gao, Y., & Mosalam, K.M. (2018). Deep transfer learning for image-based structural damage recognition. *Computer-Aided Civil and Infrastructure Engineering*, 33(9), 748-768. <https://doi.org/10.1111/mice.12363>
- García, S.R., Romo, M.P., & Botero, E. (2008). A neurofuzzy system to analyze liquefaction-induced lateral spread. *Soil Dynamics and Earthquake Engineering*, 28(3), 169-180. <https://doi.org/10.1016/j.soildyn.2007.06.014>
- Gattesco, N., Franceschinis, R., & Zorzini, F. (2011). La guida tecnica - Caratterizzazione progressiva della vulnerabilità sismica Allegato II - Metodi di calcolo semplificato, Trieste, Italy.
- German, S., Brilakis, I., & DesRoches, R. (2012). Rapid entropy-based detection and properties measurement of concrete spalling with machine vision for post-earthquake safety assessments. *Advanced Engineering Informatics*, 26(4), 846-858. <https://doi.org/10.1016/j.aei.2012.06.005>
- German, S., Jeon, J.-S., Zhu, Z., Bearman, C., Brilakis, I., DesRoches, R., & Lowes, L. (2013). Machine vision-enhanced postearthquake inspection. *Journal of Computing in Civil Engineering*, 27(6), 622-634. [https://doi.org/10.1061/\(ASCE\)CP.1943-5487.0000333](https://doi.org/10.1061/(ASCE)CP.1943-5487.0000333)
- Ghaboussi, J., & Joghataie, A. (1995). Active control of structures using neural networks. *Journal of Engineering Mechanics*, 121(4), 555-567. [https://doi.org/10.1061/\(ASCE\)0733-9399\(1995\)121:4\(555\)](https://doi.org/10.1061/(ASCE)0733-9399(1995)121:4(555))
- Ghosh, J., & Sood, P. (2016). Consideration of time-evolving capacity distributions and improved degradation models for seismic fragility assessment of aging highway bridges. *Reliability Engineering and System Safety*, 154, 197-218. <https://doi.org/10.1016/j.ress.2016.06.001>
- Ghosh, J., Padgett, J.E., & Duenas-Osorio, L. (2013). Surrogate modeling and failure surface visualization for efficient seismic vulnerability assessment of highway bridges. *Probabilistic Engineering Mechanics*, 34, 189-199. <https://doi.org/10.1016/j.probengmech.2013.09.003>
- Ghosh, J., Rokneddin, K., Padgett, J.E., & Duenas-Osorio, L. (2014). Seismic reliability assessment of aging highway bridge networks with field instrumentation data and correlated failures, I, Methodology. *Earthquake Spectra*, 30(2), 795-817. <https://doi.org/10.1193/040512EQS155M>
- Ghosh, S., Roy, A., & Chakraborty, S. (2018). Support vector regression based metamodeling for seismic reliability analysis of structures. *Applied Mathematical Modelling*, 64, 584-602. <https://doi.org/10.1016/j.apm.2018.07.054>



- Giaretton, M., Dizhur, D., Garbin, E., Ingham, J., & da porto, F. (2018). In-Plane Strengthening of Clay Brick and Block Masonry Walls Using Textile-Reinforced Mortar. *Journal of Composites for Construction*, 22. [https://doi.org/10.1061/\(ASCE\)CC.1943-5614.0000866](https://doi.org/10.1061/(ASCE)CC.1943-5614.0000866)
- Giaretton, M., Valluzzi, M. R., Mazzon, N., & Modena, C. (2017). Out-of-plane shake-table tests of strengthened multi-leaf stone masonry walls. *Bulletin of Earthquake Engineering*, 15(10), 4299–4317. <https://doi.org/10.1007/s10518-017-0125-7>
- Gill, S., Ghesquiere, F., Anderson, E., & Holmes, C. (2009). The central American probabilistic risk assessment (CAPRA). a regional SDI for disaster risk reduction.
- Giovinazzi, S., & Lagomarsino, S. (2004). A macroseismic method for the vulnerability assessment of buildings. Proceedings of the 13th World Conference on Earthquake Engineering, Vancouver, B.C., Canada, August 1-6, 2004 Paper No. 896.
- Giuriani, E., Marini, A., & Plizzari, G. (2005). Experimental Behavior of Stud Connected Wooden Floors Undergoing Seismic Action / Untersuchung des Verhaltens von mit Bolzen verbundenen Holzdecken unter seismischer Belastung. *Restoration of Buildings and Monuments*, 11(1), 3–24. <https://doi.org/10.1515/rbm-2005-5924>
- GNDT-SSN (1994). Scheda di esposizione e vulnerabilità e di rilevamento danni di primo livello e secondo livello (muratura e cemento armato). (in Italian)
- Goh, A.T.C. (1994). Seismic liquefaction potential assessed by neural networks. *Journal of Geotechnical Engineering*, 120(9), 1467-1480. [https://doi.org/10.1061/\(ASCE\)0733-9410\(1994\)120:9\(1467\)](https://doi.org/10.1061/(ASCE)0733-9410(1994)120:9(1467))
- Goh, A.T.C. (1996). Neural-network modeling of CPT seismic liquefaction data. *Journal of Geotechnical Engineering*, 122(1), 70-73. [https://doi.org/10.1061/\(ASCE\)0733-9410\(1996\)122:1\(70\)](https://doi.org/10.1061/(ASCE)0733-9410(1996)122:1(70))
- Goh, A.T.C., & Goh, S.H. (2007). Support vector machines, Their use in geotechnical engineering as illustrated using seismic liquefaction data. *Computers and Geotechnics*, 34(5), 410-421. <https://doi.org/10.1016/j.compgeo.2007.06.001>
- Gong, L., Wang, C., Wu, F., Zhang, J., Zhang, H., & Li, Q. (2016). Earthquake-induced building damage detection with post-event sub-meter VHR TerraSAR-X staring spotlight imagery. *Remote Sensing*, 8(11), 1-21. <https://doi.org/10.3390/rs8110887>
- Grimaz, S., Cucchi, F., Slejko, D., Gattesco, N., Pipan, M., Barazza, F., Biolchi, S., Franceschinis, R., Garcia, J., Malisan, P., Moretti, A., Prizzon, S., Rebez, A., Santulin, M., Zini, L., Zorzini, F. (2011). Decision-making supports for seismic risk mitigation of schools at a regional scale, the ASSESS project. *30° Convegno Nazionale Gruppo Nazionale di Geofisica della Terra Solida*, 375–380, Trieste, Italy.

- Grünthal, G. (1998). European Macroseismic Scale. Chaiers du Centre Européen de Géodynamique et de Séismologie, vol. 15 Luxembourg
- Guenzi, C. (Ed.). (1981). *L'arte di edificare. Manuali in Italia 1750–1950*. BE - MA editrice. (in Italian)
- Gülkan, P., & Kalkan, E. (2002). Attenuation modeling of recent earthquakes in Turkey. *Journal of Seismology*, 6(3), 397–409. <https://doi.org/10.1023/A:1020087426440>
- Güllü, H., and Erxcelebi, E. (2007). A neural network approach for attenuation relationships, An application using strong ground motion data from Turkey. *Engineering Geology*, 93(3–4), 65–81. <https://doi.org/10.1016/j.enggeo.2007.05.004>
- Guo, Z., Shao, X., Xu, Y., Miyazaki, H., Ohira, W., & Shibasaki, R. (2016). Identification of village building via Google Earth images and supervised machine learning methods. *Remote Sensing*, 8(4). <https://doi.org/10.3390/rs8040271>
- Gutenberg, B. & Richter, C.F. (1942). Earthquake magnitude, intensity, energy and acceleration. *Bulletin of the Seismological Society of America*, 32(3), 163-191. <https://doi.org/10.1785/BSSA0320030163>
- Gutenberg, B., & Richter, C.F. (1956). Earthquake magnitude, intensity, energy and acceleration (Second paper). *Bulletin of the Seismological Society of America*, 46(2), 105-145. <https://doi.org/10.1785/BSSA0460020105>
- Hamze-Ziabari, S.M., & Bakhshpoori, T. (2018). Improving the prediction of ground motion parameters based on an efficient bagging ensemble model of M5# and CART algorithms. *Applied Soft Computing Journal*, 68, 147-161. <https://doi.org/10.1016/j.asoc.2018.03.052>
- Hancilar, U., Tuzun, C., Yenidogan, C., & Erdik, M. (2010). ELER software, a new tool for urban earthquake loss assessment. *Natural Hazards and Earth System Sciences*, 10, 2677–2696. <https://doi.org/10.5194/nhess-10-2677-2010>
- Hanna, A.M., Ural, D., & Saygili, G. (2007). Neural network model for liquefaction potential in soil deposits using Turkey and Taiwan earthquake data. *Soil Dynamics and Earthquake Engineering*, 27(6), 521-540. <https://doi.org/10.1016/j.soildyn.2006.11.001>
- Hansapinyo, C., Latcharote, P., & Limkatanyu, S. (2020) Seismic Building Damage Prediction From GIS-Based Building Data Using Artificial Intelligence System. *Frontiers in Built Environment*, 6, 576919. <https://doi.org/10.3389/fbuil.2020.576919>
- Harirchian, E., Jadhav, K., Kumari, V., & Lahmer, T. (2021) ML-EHSAPP: a prototype for machine learning-based earthquake hazard safety assessment of

- structures by using a smartphone app, *European Journal of Environmental and Civil Engineering*, 1-21, <https://doi.org/10.1080/19648189.2021.1892829>.
- Hariri-Ardebili, M.A., & Pourkamali-Anaraki, F. (2018). Simplified reliability analysis of multi hazard risk in gravity dams via machine learning techniques. *Archives of Civil and Mechanical Engineering*, 18(2), 592-610. <https://doi.org/10.1016/j.acme.2017.09.003>
- Harley, A. W. (2015). An interactive node-link visualization of convolutional neural networks. *Lecture Notes in Computer Science (Including Subseries Lecture Notes in Artificial Intelligence and Lecture Notes in Bioinformatics)*, 9474, 867–877. [https://doi.org/10.1007/978-3-319-27857-5\\_77](https://doi.org/10.1007/978-3-319-27857-5_77)
- He, K., Zhang, X., Ren, S., & Sun, J. (2016). Deep residual learning for image recognition. *Proceedings of the IEEE Computer Society Conference on Computer Vision and Pattern Recognition*, 2016-Decem, 770–778. <https://doi.org/10.1109/CVPR.2016.90>
- Hecht, R., Meinel, G., & Buchroithner, M. (2015). Automatic identification of building types based on topographic databases—a comparison of different data sources. *International Journal of Cartography*, 1(1), 18–31. <https://doi.org/10.1080/23729333.2015.1055644>
- Hermosilla, T., Ruiz, L. A., Recio, J. A., & Estornell, J. (2011). Evaluation of automatic building detection approaches combining high resolution images and LiDAR data. *Remote Sensing*, 3(6), 1188–1210. <https://doi.org/10.3390/rs3061188>
- Hershberger, J. (1956). A comparison of earthquake acceleration with intensity ratings. *Bulletin of the Seismological Society of America*, 46(4), 317–320. <https://doi.org/10.1785/BSSA0460040317>
- Ho, T.K. (1995). Random decision forests. *Proceedings of 3rd international conference on document analysis and recognition*, Montreal, QC, Canada, 14–16 August, 278–282.
- Hoang, N.D., & Bui, D.T. (2018). Predicting earthquake-induced soil liquefaction based on a hybridization of kernel Fisher discriminant analysis and a least squares support vector machine, A multi-dataset study. *Bulletin of Engineering Geology and the Environment*, 77(1), 191-204. <https://doi.org/10.1007/s10064-016-0924-0>
- Hosmer, D.W., & Lemeshow, S. (2000). *Applied Logistic Regression*. 2nd ed. New York, John Wiley.
- Housner, G.W., Bergman, L.A., Caughey, T.K., Chassiakos, A.G., Claus, R.O., Masri, S.F., Skelton, R.E., Soong, T.T., Spencer, B.F., & Yao, J.T.P. (1997). Structural control, Past, present, and future. *Journal of Engineering Mechanics*, 123(9), 897-971. [https://doi.org/10.1061/\(ASCE\)0733-9399\(1997\)123:9\(897\)](https://doi.org/10.1061/(ASCE)0733-9399(1997)123:9(897))

- Huang, C.S., Hung, S.L., Wen, C.M. & Tu, T.T. (2003). A neural network approach for structural identification and diagnosis of a building from seismic response data. *Earthquake Engineering and Structural Dynamics*, 32(2), 187-206. <https://doi.org/10.1002/eqe.219>
- Huang, G., Qiu, W., & Zhang, J. (2017). Modelling seismic fragility of a rock mountain tunnel based on support vector machine. *Soil Dynamics and Earthquake Engineering*, 102, 160-171. <https://doi.org/10.1016/j.soildyn.2017.09.002>
- Huang, H., & Burton, H.V. (2019). Classification of in-plane failure modes for reinforced concrete frames with infills using machine learning. *Journal of Building Engineering*, 25, 100767. <https://doi.org/10.1016/j.jobbe.2019.100767>
- Hubel, D.H., & Wiesel, T.N. (1959). Receptive fields of single neurones in the cat's striate cortex. *J Physiol.* 1959 Oct;148(3),574-91. <https://doi.org/10.1113/jphysiol.1959.sp006308>
- Hubel, D.H., & Wiesel, T.N. (1962). Receptive fields, binocular interaction and functional architecture in the cat's visual cortex. *J Physiol.* 1962 Jan;160(1),106-54. <https://doi.org/10.1113/jphysiol.1962.sp006837>
- Hung, S.L., Huang, C.S., Wen, C.M., & Hsu, Y.C. (2003). Nonparametric identification of a building structure from experimental data using wavelet neural network. *Computer-aided Civil and Infrastructure Engineering*, 18(5), 356–368. <https://doi.org/10.1111/1467-8667.t01-1-00313>
- Iannelli, G.C., & Dell'Acqua, F. (2017). Extensive Exposure Mapping in Urban Areas through Deep Analysis of Street-Level Pictures for Floor Count Determination. *Urban Sci.* 2017, 1, 16. <https://doi.org/10.3390/urbansci1020016>
- Idriss, I.M., & Boulanger, R.W. (2006). Semi-empirical procedures for evaluating liquefaction potential during earthquakes. *Soil Dynamics and Earthquake Engineering*, 26, 115–130. <https://doi.org/10.1016/j.soildyn.2004.11.023>
- Italian Government (1962), Law no. 1684 of 1962/11/25 (GU no. 326 of 1962/12/22), *Provvedimenti per l'edilizia, con particolari prescrizioni per le zone sismiche.* (in Italian)
- Italian Ministry of Infrastructures (1986). DM 1986/01/24 (GU no. 108 of 1986/05/12), *Norme Tecniche relative alle costruzioni antisismiche.* (in Italian)
- Italian Ministry of Infrastructures (1996). DM 1996/01/16 (GU no. 29 of 1996/02/05), *Norme tecniche relative ai criteri generali di verifica di sicurezza delle costruzioni e dei carichi e sovraccarichi.* (in Italian)
- Italian Ministry of Infrastructures (2009). Circolare no. 617 of 2009/02/02 (GU 2009/02/26, Suppl. Ordinario no.27), *Istruzioni per l'applicazione delle 'Nuove norme tecniche per le costruzioni' di cui al decreto ministeriale 14 gennaio 2008.* (in Italian)

- Italian Ministry of Infrastructures and Transports (2019). Circolare no. 7 C.S.LL.PP. of 2009/01/21 (GU n.35 del 11-2-2019 - Suppl. Ordinario n. 5), *Istruzioni per l'applicazione dell'«Aggiornamento delle "Norme tecniche per le costruzioni"» di cui al decreto ministeriale 17 gennaio 2018*. (in Italian)
- Italian Ministry of Infrastructures. (1987). DM 1987/11/20 (GU no. 285 of 1987/12/05), *Norme Tecniche per la progettazione, esecuzione e collaudo degli edifici in Muratura e per il loro consolidamento*. (in Italian)
- Italian Ministry of Public Works (2018). Technical Standards for Construction, approved by Ministerial Decree of 17/01/2018 and published in the Official Gazette no. 42 of 20/02/2018.
- Italian Royal Decree RD no. 193 of 1909/04/18 (GU no. 95 of 1909/04/22), *Norme tecniche ed igieniche obbligatorie per le riparazioni, ricostruzioni e nuove costruzioni degli edifici pubblici e privati nei Comuni colpiti dal Terremoto del 28 dicembre 1908 o da altri precedenti*. (in Italian)
- Italian Royal Decree RD no. 2089 of 1924/10/23 (GU no.303 of 1924/12/30), *Norme tecniche ed igieniche per le riparazioni, ricostruzioni e nuove costruzioni degli edifici pubblici e privati nei Comuni o frazioni di comune dichiarati zone sismiche*. (in Italian)
- Italian Royal Decree RD no. 640 of 1935/03/25 (GU no. 120 of 1935/05/22), *Nuovo testo delle norme tecniche di edilizia con speciali prescrizioni per le località colpite dai terremoti*. (in Italian)
- Jeng, C.H., & Mo, Y.L. (2004). Quick seismic response estimation of prestressed concrete bridges using artificial neural networks. *Journal of Computing in Civil Engineering*, 18(4), 360-372. [https://doi.org/10.1061/\(ASCE\)0887-3801\(2004\)18:4\(360\)](https://doi.org/10.1061/(ASCE)0887-3801(2004)18:4(360))
- Jeon, J. S., Mangalathu, S., Song, J., & Desroches, R. (2019). Parameterized seismic fragility curves for curved multi-frame concrete box-girder bridges using Bayesian parameter estimation. *Journal of Earthquake Engineering*, 23, 954–979. <https://doi.org/10.1080/13632469.2019.1342291>
- Jiao, P., & Alavi, A. H. (2020). Artificial intelligence in seismology, Advent, performance and future trends. *Geoscience Frontiers*, 11(3), 739–744. <https://doi.org/10.1016/j.gsf.2019.10.004>
- Joghataie, A., & Farrokh, M. (2008). Dynamic analysis of nonlinear frames by Prandtl neural networks. *Journal of Engineering Mechanics*, 134(11), 961-969. [https://doi.org/10.1061/\(ASCE\)0733-9399\(2008\)134:11\(961\)](https://doi.org/10.1061/(ASCE)0733-9399(2008)134:11(961))
- Jolliffe, I.T. (2002). *Principal Component Analysis* (Springer Series in Statistics). 2nd ed. New York, Springer.

- Juang, C.H., & Chen, C.J. (1999). CPT-based liquefaction evaluation using artificial neural networks. *Computer-Aided Civil and Infrastructure Engineering*, 14(3), 221-229. <https://doi.org/10.1111/0885-9507.00143>
- Jumlesha, S. K., Sk, K. B., Satyanarayana, C., Srinivas, M. N., Ramanaiah, M. V, Babu, K., Ch, S., & P, S. K. (2012). Automatic Urban Feature Extraction Using. *International Journal of Engineering Research and Applications (IJERA)*, 2(3), 221–225.
- Kadhim, N., & Mourshed, M. (2018). A shadow-overlapping algorithm for estimating building heights from VHR satellite images. *IEEE Geoscience and Remote Sensing Letters*, 15(1), 8–12. <https://doi.org/10.1109/LGRS.2017.2762424>
- Kalagri, A., Miltiadou-Fezans, A., & Vintzileou, E. (2010). Design and evaluation of hydraulic lime grouts for the strengthening of stone masonry historic structures. *Materials and Structures*, 43(8), 1135–1146. <https://doi.org/10.1617/s11527-009-9572-1>
- Kameshwar, S., & Padgett, J.E. (2014). Multi-hazard risk assessment of highway bridges subjected to earthquake and hurricane hazards. *Engineering Structures*, 78, 154-166. <https://doi.org/10.1016/j.engstruct.2014.05.016>
- Kameshwar, S., & Padgett, J.E. (2018). Effect of vehicle bridge interaction on seismic response and fragility of bridges. *Earthquake Engineering and Structural Dynamics*, 47(3), 697-713. <https://doi.org/10.1002/eqe.2986>
- Kang, J., Körner, M., Wang, Y., Taubenböck, H., & Zhu, X. X. (2018). Building instance classification using street view images. *ISPRS Journal of Photogrammetry and Remote Sensing*, 145, 44–59. <https://doi.org/10.1016/j.isprsjprs.2018.02.006>
- Kappos, A. J., Panagopoulos, G., Panagiotopoulos, C., & Penelis, G. (2006). A hybrid method for the vulnerability assessment of R/C and URM buildings. *Bulletin of Earthquake Engineering*, 4(4), 391–413. <https://doi.org/10.1007/s10518-006-9023-0>
- Karimi, I., Khaji, N., Ahmadi, M.T., & Mirzayee, M. (n.d.). System identification of concrete gravity dams using artificial neural networks based on a hybrid finite element-boundary element approach. *Engineering Structures*, 32(11), 3583–3591. <https://doi.org/10.1016/j.engstruct.2010.08.002>
- Kárník, V., Schenková, Z., & Schenk, V. (1984). Vulnerability and the MSK scale. *Engineering Geology*, 20(1-2), 161-168. [https://doi.org/10.1016/0013-7952\(84\)90051-6](https://doi.org/10.1016/0013-7952(84)90051-6)
- Kaveh, A., T, B., & Hamze-Ziabari, S. M. (2016). Derivation of new equations for prediction of principal ground-motion parameters using M5# algorithm. *Journal of Earthquake Engineering*, 20(6), 910–930. <https://doi.org/10.1080/13632469.2015.1104758>

- Kawasumi, H. (1951). Measures of earthquakes danger and expectancy of maximum intensity throughout Japan as inferred from the seismic activity in historical times. *Bulletin of the Earthquake Research Institute*, Tokyo University, Tokyo, 469-482.
- Kaya, Z. (2016). Predicting liquefaction-induced lateral spreading by using neural network and neuro- fuzzy techniques. *International Journal of Geomechanics*, 16(4), 4015095. [https://doi.org/10.1061/\(ASCE\)GM.1943-5622.0000607](https://doi.org/10.1061/(ASCE)GM.1943-5622.0000607)
- Kerh, T., & Ting, S.B. (2005). Neural network estimation of ground peak acceleration at stations along Taiwan high-speed rail system. *Engineering Applications of Artificial Intelligence*, 18(7), 857–866. <https://doi.org/10.1016/j.engappai.2005.02.003>
- Khodabandolehlou, H., Pekcan, G., Fadali, M.S., & Salem, M.M.A. (2018). Active neural predictive control of seismically isolated structures. *Structural Control and Health Monitoring*, 25(1), 1-15. <https://doi.org/10.1002/stc.2061>
- Khosravikia, F., P, C., & Nagy, Z. (2019). Artificial neural network-based framework for developing ground-motion models for natural and induced earthquakes in Oklahoma, Kansas, and Texas. *Seismological Research Letters*, 90(2A), 604–613. <https://doi.org/10.1785/0220180218>
- Khosravikia, F., Potter, A., Prakhov, V., Zalachoris, G., Cheng, T., Tiwari, A., Clayton, P., Cox, B., Rathje, E., Williamson, E., Paine, J. & Frohlich, C. (2018). Seismic Vulnerability and Post-event Actions for Texas Bridge Infrastructure. Austin, TX, The University of Texas at Austin.
- Kia, A., & Sensoy, S. (2014). Classification of earthquake-induced damage for R/C slab column frames using multiclass SVM and its combination with MLP neural network. *Mathematical Problems in Engineering* 2014; 734072. <https://doi.org/10.1155/2014/734072>
- Kohestani, V.R., & Ardakani, M.H. (2015). Evaluation of liquefaction potential based on CPT data using random forest. *Natural Hazards*, 79(2), 1079-1089. <https://doi.org/10.1007/s11069-015-1893-5>
- Köhler, P., Müller, M., Sanders, M., & Wächter, J. (2006). Data management and GIS in the center for disaster management and risk reduction technology (CEDIM), from integrated spatial data to the mapping of risk. *Natural Hazards and Earth System Sciences*, 6(4). <https://doi.org/10.5194/nhess-6-621-2006>
- Koutsourelakis, P. S. (2010). Assessing structural vulnerability against earthquakes using multi- dimensional fragility surfaces, A Bayesian framework. *Probabilistic Engineering Mechanics*, 25(1), 49–60. <https://doi.org/10.1016/j.probengmech.2009.05.005>
- Kramer, S.L. (1996). *Geotechnical Earthquake Engineering*, Prentice-Hall, New Jersey.

- Krishnamoorthy, A., Bhat, S., & Bhasari, D. (2017). Radial basis function neural network algorithm for semi-active control of base-isolated structures. *Structural Control and Health Monitoring*, 24(10), 1-11. <https://doi.org/10.1002/stc.1984>
- Krizhevsky, A., Sutskever, I., & Hinton, G.E. (2012). ImageNet Classification with Deep Convolutional Neural Networks. *NIPS'12, Proceedings of the 25th International Conference on Neural Information Processing Systems - Volume 1, December 2012*, 1097–1105. <https://doi.org/10.1145/3065386>
- Lagaros, N. D., Tsompanakis, Y., Psarropoulos, P.N., & Georgopoulos, E. C. (2009). Computationally efficient seismic fragility analysis of geostuctures. *Computers and Structures*, 87 (19-20), 1195-1203. <https://doi.org/10.1016/j.compstruc.2008.12.001>
- Lagaros, N.D., & Fragiadakis, M. (2007). Fragility assessment of steel frames using neural networks. *Earthquake Spectra*, 23(4), 735-752. <https://doi.org/10.1193/1.2798241>
- Lagomarsino, S., & Cattari, S. (2014). Fragility Functions of Masonry Buildings. In K. Pitilakis, H. Crowley, & A. M. Kaynia (Eds.), *SYNER-G: Typology Definition and Fragility Functions for Physical Elements at Seismic Risk* (Vol. 27, pp. 111–156). Springer Netherlands. [https://doi.org/10.1007/978-94-007-7872-6\\_5](https://doi.org/10.1007/978-94-007-7872-6_5)
- Lagomarsino, S., & Giovinazzi, S. (2006). Macroseismic and mechanical models for the vulnerability and damage assessment of current buildings. *Bulletin of Earthquake Engineering*, 4(4), 415–443. <https://doi.org/10.1007/s10518-006-9024-z>
- Lagomarsino, S., Cattari, S. & Ottonelli, D. (2021). The heuristic vulnerability model, fragility curves for masonry buildings. *Bulletin of Earthquake Engineering*, 19, 3129–3163. <https://doi.org/10.1007/s10518-021-01063-7>
- Lagomarsino, S., Cattari, S., & Ottonelli, D. (2015). *Derivazione di curve di fragilità empiriche per classi tipologiche rappresentative del costruito Aquilano sulla base dei dati del danno dell'evento sismico del 2009. Research Project DPC-ReLUIS, PR1 (Strutture in muratura), WP6 (Vulnerabilità delle costruzioni in muratura a scala territoriale)—Task 6.3.*
- Lattanzi, D., Miller, G. R., Eberhard, M.O., & Haraldsson, O. S. (2015). Bridge column maximum drift estimation via computer vision. *Journal of Computing in Civil Engineering*, 30(4), 04015051. [https://doi.org/10.1061/\(ASCE\)CP.1943-5487.0000527](https://doi.org/10.1061/(ASCE)CP.1943-5487.0000527)
- Laupheimer, D., & Haala, N. (2018). Deep Learning for the Classification of Building Facades. 38. *Wissenschaftlich-Technische Jahrestagung Der DGPF Und PFGK18 Tagung in München*, 19, 701–709. <https://doi.org/10.1016/j.autcon.2021.104016>



- LeCun, Y., Bottou, L., Bengio, Y., & Haffner, P. (1998). Gradient-based learning applied to document recognition. *Proceedings of the IEEE*, 86(11), 2278–2323. <https://doi.org/10.1109/5.726791>
- Lee, H.J., Jung, H.J., Cho, S.W., & Lee, I.W. (2008). An experimental study of semiactive modal neuro-control scheme using MR damper for building structure. *Journal of Intelligent Material Systems and Structures* 19(9), 1005-1015. <https://doi.org/10.1177/1045389X07083024>
- Lee, H.J., Yang, G., Jung, H.J., Spencer, B.F., & Lee, I.W. (2006). Semi-active neurocontrol of a base-isolated benchmark structure. *Structural Control and Health Monitoring*, 13(2-3), 682-692. <https://doi.org/10.1002/stc.105>
- Li, Y., Chen, Y., Rajabifard, A., Khoshelham, K., & Aleksandrov, M. (2018). Estimating building age from google street view images using deep learning. *Leibniz International Proceedings in Informatics, LIPIcs*, 114(40), 1–7. <https://doi.org/10.4230/LIPIcs.GIScience.2018.40>
- Liasis, G., & Stavrou, S. (2016). Satellite images analysis for shadow detection and building height estimation. *ISPRS Journal of Photogrammetry and Remote Sensing*, 119, 437–450. <https://doi.org/10.1016/j.isprsjprs.2016.07.006>
- Liel, A. B., Haselton, C. B., Deierlein, G.G., & Baker, J. W. (2009). Incorporating modeling uncertainties in the assessment of seismic collapse risk of buildings. *Structural Safety*, 31(2), 197–211. <https://doi.org/10.1016/j.strusafe.2008.06.002>
- Liu, Z., & Tesfamariam, S. (2012). Prediction of lateral spread displacement, Data-driven approaches. *Bulletin of Earthquake Engineering*, 10(5), 1431-1454. <https://doi.org/10.1007/s10518-012-9366-7>
- Liu, Z., & Zhang, Z. (2018). Artificial neural network based method for seismic fragility analysis of steel frames. *KSCCE Journal of Civil Engineering*, 22(2), 708-717. <https://doi.org/10.1007/s12205-017-1329-8>
- Llamas, J., Lerones, P. M., Medina, R., Zalama, E., & Gómez-García-Bermejo, J. (2017). Classification of architectural heritage images using deep learning techniques. *Applied Sciences (Switzerland)*, 7(10), 1–26. <https://doi.org/10.3390/app7100992>
- Luo, H., & Paal, S.G. (2018). Machine learning-based backbone curve model of reinforced concrete columns subjected to cyclic loading reversals. *Journal of Computing in Civil Engineering*, 32(5), 04018042. [https://doi.org/10.1061/\(ASCE\)CP.1943-5487.0000787](https://doi.org/10.1061/(ASCE)CP.1943-5487.0000787)
- Luo, H., & Paal, S.G. (2019). A locally weighted machine learning model for generalized prediction of drift capacity in seismic vulnerability assessments. *Computer-Aided Civil and Infrastructure Engineering*, 34, 935-950. <https://doi.org/10.1111/mice.12456>

- Magenes, G., Penna, A., Senaldi, I. E., Rota, M., & Galasco, A. (2014). Shaking Table Test of a Strengthened Full-Scale Stone Masonry Building with Flexible Diaphragms. *International Journal of Architectural Heritage*, 8(3), 349–375. <https://doi.org/10.1080/15583058.2013.826299>
- Mahajan, N., Patil, D., Kotkar, A., & Wasnik, K. (2019). Prediction of building structure age using machine learning. *International Journal of Advance Research, Ideas and Innovations in Technology*, 5(3), ISSN: 2454-132X
- Mahmoudi, S.N., & Chouinard, L. (2016). Seismic fragility assessment of highway bridges using support vector machines. *Bulletin of Earthquake Engineering*, 14(6), 1571-1587. <https://doi.org/10.1007/s10518-016-9894-7>
- Maltezos, E., Doulamis, N., Doulamis, A., & Ioannidis, C. (2017). Deep convolutional neural networks for building extraction from orthoimages and dense image matching point clouds. *Journal of Applied Remote Sensing*, 11(04), 1. <https://doi.org/10.1117/1.jrs.11.042620>
- Mangalathu, S., & Burton, H.V. (2019). Deep learning-based classification of earthquake-impacted buildings using textual damage descriptions. *International Journal of Disaster Risk Reduction*, 36, 101111. <https://doi.org/10.1016/j.ijdr.2019.101111>
- Mangalathu, S., & Jeon, J. S. (2019a). Machine learning-based failure mode recognition of circular reinforced concrete bridge columns, Comparative study. *Journal of Structural Engineering*, 145(10), 04019104. [https://doi.org/10.1061/\(ASCE\)ST.1943-541X.0002402](https://doi.org/10.1061/(ASCE)ST.1943-541X.0002402)
- Mangalathu, S., & Jeon, J. S. (2019b). Stripe-based fragility analysis of concrete bridge classes using machine learning techniques. *Earthquake Engineering & Structural Dynamics*, 48, 1238-1255. <https://doi.org/10.1002/eqe.3183>
- Mangalathu, S., & Jeon, J.S. (2018). Classification of failure mode and prediction of shear strength for reinforced concrete beam-column joints using machine learning techniques. *Engineering Structures*, 160, 85-94. <https://doi.org/10.1016/j.engstruct.2018.01.008>
- Mangalathu, S., Heo, G., & Jeon, J.S. (2018a). Artificial neural network based multi-dimensional fragility development of skewed concrete bridge classes. *Engineering Structures*, 162, 166-176. <https://doi.org/10.1016/j.engstruct.2018.01.053>
- Mangalathu, S., Jeon, J.S., & DesRoches, R. (2018b). Critical uncertainty parameters influencing seismic performance of bridges using Lasso regression. *Earthquake Engineering and Structural Dynamics*, 47(3), 784-801. <https://doi.org/10.1002/eqe.2991>
- Mannella, A., Di Ludovico, M., Sabino, A., Prota, A., Dolce, M., & Manfredi, G. (2017). Analysis of the population assistance and returning home in the

- reconstruction process of the 2009 L'aquila earthquake. *Sustainability*, 9(8), 1395. <https://doi.org/10.3390/su9081395>
- Maragno, D., Fontana, M. D., & Musco, F. (2020). Mapping heat stress vulnerability and risk assessment at the neighborhood scale to drive Urban adaptation planning. *Sustainability (Switzerland)*, 12(3). <https://doi.org/10.3390/su12031056>
- Margottini, C., Molin, D., & Serva, L. (1992). Intensity versus ground motion: A new approach using Italian data. *Engineering Geology*, 33(1), 45–58. [https://doi.org/10.1016/0013-7952\(92\)90034-V](https://doi.org/10.1016/0013-7952(92)90034-V)
- Marini, A., Cominelli, S., Zanotti, C., & Giuriani, E. (2018). Improved natural hydraulic lime mortar slab for compatible retrofit of wooden floors in historical buildings. *Construction and Building Materials*, 158, 801–813. <https://doi.org/10.1016/j.conbuildmat.2017.10.010>
- Mazzon, N., Valluzzi, M. R., Aoki, T., & Garbin, E. (2009). *Shaking Table Tests on Two Multi-Leaf Stone Masonry Buildings*. 11th Canadian Masonry Symposium, Toronto, Canada.
- Mazzotti, C., Savoia, M., Chinni, C., & Perri, G. (2013). Una metodologia speditiva per la valutazione di vulnerabilità sismica di edifici in muratura e calcestruzzo armato (in Italian). <https://doi.org/10.7414/PS.4.2.95-112>
- Menichini, G., Nistri, V., Boschi, S., Del Monte, E., Orlando, M., & Vignoli, A. (2022). Calibration of vulnerability and fragility curves from moderate intensity Italian earthquake damage data. *International Journal of Disaster Risk Reduction*, 67. <https://doi.org/10.1016/j.ijdr.2021.102676>
- Mesgar, M.A.A., & Jalilvand, P. (2017). Vulnerability analysis of the urban environments to different seismic scenarios, residential buildings and associated population distribution modelling through integrating dasymetric mapping method and GIS. *Procedia engineering*, 198, 454-466. <https://doi.org/10.1016/j.proeng.2017.07.100>
- Misra, P., Avtar, R., & Takeuchi, W. (2018). Comparison of digital building height models extracted from AW3D, TanDEM-X, ASTER, and SRTM digital surface models over Yangon City. *Remote Sensing*, 10(12). <https://doi.org/10.3390/rs10122008>
- Mitra, N., Mitra, S., & Lowes, L. N. (2011). Probabilistic model for failure initiation of reinforced concrete interior beam-column connections subjected to seismic loading. *Engineering Structures*, 33(1), 154–162. <https://doi.org/10.1016/j.engstruct.2010.09.029>
- Mitropoulou, C.C., & Papadrakakis, M. (2011). Developing fragility curves based on neural network IDA predictions. *Engineering Structures*, 33(12), 3409-3421. <https://doi.org/10.1016/j.engstruct.2011.07.005>

- Modena, C., Casarin, F., da Porto, F., & Munari, M. (2010). L'Aquila 6th April 2009 Earthquake: Emergency and Post-emergency Activities on Cultural Heritage Buildings. In M. Garevski & A. Ansal (Eds.), *Earthquake Engineering in Europe* (Vol. 17, pp. 495–521). Springer Netherlands. [http://link.springer.com/10.1007/978-90-481-9544-2\\_20](http://link.springer.com/10.1007/978-90-481-9544-2_20)
- Modena, C., Casarin, F., Mazzon, N., Munari, M., Panizza, M., & Valluzzi, M. R. (2009). Structural interventions on historical masonry buildings: Review of Eurocode 8 provisions in the light of the Italian experience. In E. Cosenza (Ed.), *Eurocode 8 Perspectives from the Italian Standpoint* (pp. 225–236). Doppiavoce.
- Modena, C., Pineschi, F., & Valluzzi, M. R. (2000). *Valutazione della vulnerabilità sismica di alcune classi di strutture esistenti. Sviluppo e valutazione di metodi di rinforzo*. Cnr-Gruppo Nazionale Per La Difesa Dai Terremoti.
- Modena, C., Valluzzi, M. R., da Porto, F., & Casarin, F. (2011). Structural Aspects of The Conservation of Historic Masonry Constructions in Seismic Areas: Remedial Measures and Emergency Actions. *International Journal of Architectural Heritage*, 5(4–5), 539–558. <https://doi.org/10.1080/15583058.2011.569632>
- Mohammadnejad, A. K., Mousavi, S. M., Torabi, M., M, M., & Alavi, A. H. (2012). Robust attenuation relations for peak time-domain parameters of strong ground motions. *Environmental Earth Sciences*, 67(1), 53–70. <https://doi.org/10.1007/s12665-011-1479-9>
- Molas, G.L., & Yamazaki, F. (1995). Neural networks for quick earthquake damage estimation. *Earthquake Engineering & Structural Dynamics*, 24(4), 505-516. <https://doi.org/10.1002/eqe.4290240404>
- Molina, S., Lang, D.H., & Lindholm, C.D. (2010). SELENA, an open-source tool for seismic risk and loss assessment using a logic tree computation procedure. *Computers & Geosciences*, 36(3), 257–269. <https://doi.org/10.1016/j.cageo.2009.07.006>
- Moosavi, V. (2017). *Urban morphology meets deep learning, Exploring urban forms in one million cities, town and villages across the planet*. 1–10. <http://arxiv.org/abs/1709.02939>
- Moreira, S., Oliveira, D. V., Ramos, L. F., Lourenço, P. B., Fernandes, R. P., & Guerreiro, J. (2012). *Experimental study on the seismic behavior of masonry wall-to-floor connections*. 15 WCEE, Lisbon, Portugal.
- Moreira, S., Ramos, L. F., Oliveira, D. V., & Lourenço, P. B. (2015). Design Parameters for Seismically Retrofitted Masonry-To-Timber Connections: Injection Anchors. *International Journal of Architectural Heritage*. <https://doi.org/10.1080/15583058.2015.1113339>
- Moretti, B. (1946). *Ville. 68 Esempi di ville e case di campagna*. Hoepli. (in Italian)

- Moretti, B. (1947). *Case d'abitazione in Italia*. Hoepli. (in Italian)
- Morfidis, K., & Kostinakis, K. (2017). Seismic parameters' combinations for the optimum prediction of the damage state of R/C buildings using neural networks. *Advances in Engineering Software*, *106*, 1-16. <https://doi.org/10.1016/j.advengsoft.2017.01.001>
- Morfidis, K., & Kostinakis, K. (2018). Approaches to the rapid seismic damage prediction of r/c buildings using artificial neural networks. *Engineering Structures*, *165*, 120-141. <https://doi.org/10.1016/j.engstruct.2018.03.028>
- Moss, R. E., Seed, R. B., Kayen, R. E., Stewart, J. P., Kiureghian, A., & Cetin, K. O. (2006). CPT-based probabilistic and deterministic assessment of in situ seismic soil liquefaction potential. *Journal of Geotechnical and Geoenvironmental Engineering*, *132*(8), 1032-1051. [https://doi.org/10.1061/\(ASCE\)1090-0241\(2006\)132:8\(1032\)](https://doi.org/10.1061/(ASCE)1090-0241(2006)132:8(1032))
- Mou, L., & Zhu, X. X. (2018). IM2HEIGHT, Height Estimation from Single Monocular Imagery via Fully Residual Convolutional-Deconvolutional Network. 1–13. <http://arxiv.org/abs/1802.10249>
- Munari, M. (2009). *Sviluppo di procedure per valutazioni sistematiche di vulnerabilità sismica di edifici esistenti in muratura* [PhD thesis]. Università degli Studi di Padova, Scuola di Dottorato in “Studio e Conservazione dei Beni Archeologici e Architettonici”. (in Italian)
- Murphy, J.R., & O'Brien, L.J. (1977). The correlation of peak ground acceleration amplitude with seismic intensity and other physical parameters. *Bulletin of the Seismological Society of America*, *67*(3), 877–915. <https://doi.org/10.1785/BSSA0670030877>
- Murphy, K.P. (2012). *Machine Learning, A Probabilistic Perspective*. Chance Encounters, Probability in Education. Cambridge, MA, London, The MIT Press.
- Musson, R.M.W., Grünthal, G., & Stucchi, M. (2010). The comparison of macroseismic intensity scales. *Journal of Seismology*, *14*, 413-428. <https://doi.org/10.1007/s10950-009-9172-0>
- Nakamura, M., Masri, S. F., Chassiakos, A.G., & CauGhey, T. K. (1998). A method for non-parametric damage detection through the use of neural networks. *Earthquake Engineering and Structural Dynamics*, *27*, 997–1010. [https://doi.org/10.1002/\(SICI\)1096-9845\(199809\)27:9<997::AID-EQE771>3.0.CO;2-7](https://doi.org/10.1002/(SICI)1096-9845(199809)27:9<997::AID-EQE771>3.0.CO;2-7)
- National Institute of Building Sciences (1999). *Earthquake loss estimation methodology HAZUS99*, Technical manual, vol I–III. Federal Emergency Management Agency, Washington, DC.

- Neuhausen, M., Obel, M., Martin, A., Mark, P., & König, M. (2018). Window detection in facade images for risk assessment in tunneling. *Visualization in Engineering*, 6(1), 1–16. <https://doi.org/10.1186/s40327-018-0062-9>
- Neumann, F. (1954). *Earthquake Intensity and Related Ground Motion*, University Press, Seattle, Washington.
- Neves, L. C., & Giongo, I. (2021). Retrofitting of Traditional Timber Floors. In J. Branco, P. Dietsch, & T. Tannert (Eds.), *Reinforcement of Timber Elements in Existing Structures* (Vol. 33, pp. 221–245). Springer International Publishing. [https://doi.org/10.1007/978-3-030-67794-7\\_11](https://doi.org/10.1007/978-3-030-67794-7_11)
- Oliveira, D. V., Silva, R. A., Garbin, E., & Lourenço, P. B. (2012). Strengthening of three-leaf stone masonry walls: An experimental research. *Materials and Structures*, 45(8), 1259–1276. <https://doi.org/10.1617/s11527-012-9832-3>
- Oommen, T., & Baise, L.G. (2010). Model development and validation for intelligent data collection for lateral spread displacements. *Journal of Computing in Civil Engineering*, 24(6), 467-477. [https://doi.org/10.1061/\(ASCE\)CP.1943-5487.0000050](https://doi.org/10.1061/(ASCE)CP.1943-5487.0000050)
- OPCM 3274/2003 (2003). Primi elementi in materia di criteri generali per la classificazione sismica del territorio nazionale e di normative tecniche per le costruzioni in zona sismica (in Italian). Off. Gazzette Ital. Repub. N°105 8th May 2003.
- Ordinance of the President of the Council of Ministers 3519 of April 28, 2006, Annex 1b. Reference seismic hazard for the national territory.
- Ormea, G. B. (1951). *La teoria e la pratica delle costruzioni*. Hoepli. (in Italian)
- Paal, S. G., Jeon, J.-S., Brilakis, I., & DesRoches, R. (2014). Automated damage index estimation of reinforced concrete columns for post-earthquake evaluations. *Journal of Structural Engineering*, 141(9), 4014228. [https://doi.org/10.1061/\(ASCE\)ST.1943-541X.0001200](https://doi.org/10.1061/(ASCE)ST.1943-541X.0001200)
- Pal, M. (2006). Support vector machines-based modelling of seismic liquefaction potential. *International Journal for Numerical and Analytical Methods in Geomechanics*, 30(10), 983-996. <https://doi.org/10.1002/nag.509>
- Pan, Y., Agrawal, A.K., & Ghosn, M. (2007). Seismic fragility of continuous steel highway bridges in New York State. *Journal of Bridge Engineering*, 12(6), 689-699. [https://doi.org/10.1061/\(ASCE\)1084-0702\(2007\)12:6\(689\)](https://doi.org/10.1061/(ASCE)1084-0702(2007)12:6(689))
- Pang, Y., Dang, X., & Yuan, W. (2014). An artificial neural network based method for seismic fragility analysis of highway bridges. *Advances in Structural Engineering*, 17(3), 413-428. <https://doi.org/10.1260/1369-4332.17.3.413>

- Panza, G.F., Cazzaro, R. & Vaccari F. (1997). Correlation between macroseismic intensities and seismic ground motion parameters. *Annals of Geophysics*, 40(5), 1371- 1382. <https://doi.org/10.4401/ag-3872>
- Park, J., & Towashiraporn, P. (2014). Rapid seismic damage assessment of railway bridges using the response-surface statistical model. *Structural Safety*, 47, 1-12. <https://doi.org/10.1016/j.strusafe.2013.10.001>
- Partovi, T., Krauß, T., Arefi, H., Omidalizarandi, M., & Reinartz, P. (2014). Model-driven 3D building reconstruction based on integration of DSM and spectral information of satellite images. *International Geoscience and Remote Sensing Symposium (IGARSS)*, July 2015, 3168–3171. <https://doi.org/10.1109/IGARSS.2014.6947150>
- Penna, A., Morandi, P., Rota, M., Manzini, C. F., da Porto, F., & Magenes, G. (2014). Performance of masonry buildings during the Emilia 2012 earthquake. *Bulletin of Earthquake Engineering*, 12(5), 2255–2273. <https://doi.org/10.1007/s10518-013-9496-6>
- Perlovsky, L. (2000). *Neural Networks and Intellect, Using Model-Based Concepts*. 1st ed. Oxford, Oxford University Press.
- Perotti, F., Domaneschi, M., & De Grandis, S. (2013). The numerical computation of seismic fragility of base-isolated nuclear power plants buildings. *Nuclear Engineering and Design*, 262, 189-200. <https://doi.org/10.1016/j.nucengdes.2013.04.029>
- Peyk-Herfeh, M., & Shahbahrani, A. (2014). Evaluation of adaptive boosting and neural network in earthquake damage levels detection. *International Journal of Computer Applications*, 100(3), 23-29. <https://doi.org/10.1016/j.nucengdes.2013.04.029>
- Piazza, M., Baldessari, C., & Tomasi, R. (2008). *The role of in-plane floor stiffness in the seismic behaviour of traditional buildings*. 14th world conference on earthquake engineering, Beijing, China.
- Pirhadi, N., Tang, X., Q, Y., & Kang, F. (2018). A new equation to evaluate liquefaction triggering using the response surface method and parametric sensitivity analysis. *Sustainability*, 11(1), 1–24. <https://doi.org/10.3390/su11010112>
- Pittore, M., & Wieland, M. (2013). Toward a rapid probabilistic seismic vulnerability assessment using satellite and ground-based remote sensing. *Natural Hazards*, 68(1), 115–145. <https://doi.org/10.1007/s11069-012-0475-z>
- Ploeger, S.K., Elsabbagh, A., Saatcioglu, M., & Sawada, M. (2016). Development of the CanRisk earthquake injury model. *Natural Hazards*, 80(2), 1171-1194. <https://doi.org/10.1007/s11069-015-2017-y>

- Podestà, S., & Scandolo, L. (2019). Earthquakes and Tie-Rods: Assessment, Design, and Ductility Issues. *International Journal of Architectural Heritage*, 13(3), 329–339. <https://doi.org/10.1080/15583058.2018.1563239>
- Polese, M., Ludovico, M. Di, Prota, A., Tocchi, G., & Gaetani d'Aragona, M. (2019). Utilizzo della scheda Cartis per aggiornamento dell'inventario ed effetto sulle stime di vulnerabilità a scala territoriale. *Proceedings of the 'XVIII Convegno Nazionale di Ingegneria Sismica' (XVIII ANIDIS)*. Ascoli Piceno, Italy, September 15-19, 2019.
- Quelhas, B., Cantini, L., Guedes, J. M., da Porto, F., & Almeida, C. (2014). Characterization and Reinforcement of Stone Masonry Walls. In A. Costa, J. M. Guedes, & H. Varum (Eds.), *Structural Rehabilitation of Old Buildings* (Vol. 2, pp. 131–155). Springer Berlin Heidelberg. [https://doi.org/10.1007/978-3-642-39686-1\\_5](https://doi.org/10.1007/978-3-642-39686-1_5)
- Raimbault, J. and Perret, J. (2019). Generating urban morphologies at large scales. *2019 Conference on Artificial Life Proceedings*, 179–186. <https://doi.org/10.48550/arXiv.1903.06807>
- Rajeev, P., & Tesfamariam, S. (2012). Seismic fragilities for reinforced concrete buildings with consideration of irregularities. *Structural Safety*, 39, 1-13. <https://doi.org/10.1016/j.strusafe.2012.06.001>
- Raju, P. L. N., Chaudhary, H., & Jha, A. K. (2014). Shadow analysis technique for extraction of building height using high resolution satellite single image and accuracy assessment. *International Archives of the Photogrammetry, Remote Sensing and Spatial Information Sciences - ISPRS Archives*, 40(8), 1185–1192. <https://doi.org/10.5194/isprsarchives-XL-8-1185-2014>
- Ramakrishnan, D., Singh, T. N., Purwar, N., Barde, K. S., A, G., & Gupta, S. (2008). Artificial neural network and liquefaction susceptibility assessment, A case study using the 2001 Bhuj earthquake data, Gujarat, India. *Computational Geosciences*, 12(4), 491–501. <https://doi.org/10.1007/s10596-008-9088-8>
- Rao, M.M., & Datta, T.K. (2006). Modal seismic control of building frames by artificial neural network. *Journal of Computing in Civil Engineering*, 20(1), 69-73. [https://doi.org/10.1061/\(ASCE\)0887-3801\(2006\)20:1\(69\)](https://doi.org/10.1061/(ASCE)0887-3801(2006)20:1(69))
- Rashidi, A., Sigari, M. H., Maghiar, M., & Citrin, D. (2016). An analogy between various machine-learning techniques for detecting construction materials in digital images. *KSCCE Journal of Civil Engineering*, 20(4), 1178–1188. <https://doi.org/10.1007/s12205-015-0726-0>
- Ravi Kiran, A., Reddy, G.R., & Agrawal, M.K. (2019). Seismic fragility analysis of pressurized piping systems considering ratcheting, A case study. *International Journal of Pressure Vessels and Piping*, 169(412), 26-36. <https://doi.org/10.1016/j.ijpvp.2018.11.013>



- Restrepo-Velez, L.F., & Magenes, G. (2004). Simplified procedure for the seismic risk assessment of unreinforced masonry buildings. *Proceedings of the 13th World Conference on Earthquake Engineering – WCEE*. Vancouver, B.C., Canada, August 1-6, 2004, Paper No. 2561.
- Ricci, P., Risi, M. T., Verderame, G.M., & Manfredi, G. (2013). Influence of infill distribution and design typology on seismic performance of low- and mid-rise RC buildings. *Bulletin of Earthquake Engineering*, 11(5), 1585-1616. <https://doi.org/10.1007/s10518-013-9453-4>
- Richter, C. F. (1935). An instrumental earthquake magnitude scale. *Bulletin of the Seismological Society of America*, 25(1), 1-32. ISSN 0037-1106.
- Richter, C. F. (1958). *Elementary seismology*, San Francisco, W. H. Freeman, 768.
- Rinaldin, G., Miniussi, C., & Amadio, C. (2019). Cyclic behavior of masonry walls strengthened by tie rods. *Engineering Structures*, 184, 287–300. <https://doi.org/10.1016/j.engstruct.2019.01.103>
- Robinson, D., Fulford, G., & Dhu, T. (2005). EQRM, geoscience Australia's earthquake risk model, Technical manual, version 3.0
- Rosser, J. F., Boyd, D. S., Long, G., Zakhary, S., Mao, Y., & Robinson, D. (2019). Predicting residential building age from map data. *Computers, Environment and Urban Systems*, 73(July 2018), 56–67. <https://doi.org/10.1016/j.compenvurbsys.2018.08.004>
- Rosti, A., Del Gaudio, C., Rota, M., Ricci, P., Di Ludovico, M., Penna, A., & Verderame, G. M. (2021b). Empirical fragility curves for Italian residential RC buildings. *Bulletin of Earthquake Engineering*, 19(8), 3165–3183. <https://doi.org/10.1007/s10518-020-00971-4>
- Rosti, A., Rota, M., & Penna, A. (2021a). Empirical fragility curves for Italian URM buildings. *Bulletin of Earthquake Engineering*, 19, 3057–3076. <https://doi.org/10.1007/s10518-020-00845-9>
- Rota, M., Penna, A., & Magenes, G. (2010). A methodology for deriving analytical fragility curves for masonry buildings based on stochastic nonlinear analyses. *Engineering Structures*, 32(5), 1312–1323. <https://doi.org/10.1016/j.engstruct.2010.01.009>
- Rota, M., Penna, A., & Magenes, G. (2014). A framework for the seismic assessment of existing masonry buildings accounting for different sources of uncertainty. *Earthquake Engineering Structural Dynamics*, 43, 1045–1066. <https://doi.org/10.1002/eqe.2386>
- Rota, M., Penna, A., & Strobbia, C. L. (2008). Processing Italian damage data to derive typological fragility curves. *Soil Dynamics and Earthquake Engineering*, 28(10–11), 933–947. <https://doi.org/10.1016/j.soildyn.2007.10.010>

- Ruggieri, S., Cardellicchio, A., Leggieri, V., & Uva, G. (2021). Machine-learning based vulnerability analysis of existing buildings. *Automation in Construction*, 132(September). <https://doi.org/10.1016/j.autcon.2021.103936>
- Russo, E., Felicetta, C., D'Amico, M. C., Sgobba, S., Lanzano, G., Mascandola, C., Pacor, F., & Luzi, L. (2022). Italian ACcelerometric Archive (ITACA), version 3.2. Istituto Nazionale di Geofisica e Vulcanologia (INGV). <https://doi.org/10.13127/itaca.3.2>
- Saadi, S., & Bensaibi, M. (2012). *Detection of Buildings Height Using Satellite Monoscopic Image*. August, 2–4. <https://doi.org/10.13140/2.1.4985.6005>
- Saha, S.K., Matsagar, V., & Chakraborty, S. (2016). Uncertainty quantification and seismic fragility of base-isolated liquid storage tanks using response surface models. *Probabilistic Engineering Mechanics*, 43, 20–35. <https://doi.org/10.1016/j.probengmech.2015.10.008>
- Salehi, H., & Burgueño, R. (2018). Emerging artificial intelligence methods in structural engineering. *Engineering Structures*, 171, 170–189. <https://doi.org/10.1016/j.engstruct.2018.05.084>
- Samuel, A.L. (1959). Some studies in machine learning using the game of checkers. *IBM Journal of Research and Development*, 3(3), 210-229. <https://10.1147/rd.33.0210>
- Sandoli, A., Lignola, G.P., Calderoni, B., & Prota, A. (2021). Fragility curves for Italian URM buildings based on a hybrid method. *Bulletin of Earthquake Engineering*, 19, 4979–5013. <https://doi.org/10.1007/s10518-021-01155-4>
- Saretta, Y., Sbrogiò, L., & Valluzzi, M. R. (2021a). Seismic response of masonry buildings in historical centres struck by the 2016 Central Italy earthquake. Calibration of a vulnerability model for strengthened conditions. *Construction and Building Materials*, 299, 123911. <https://doi.org/10.1016/j.conbuildmat.2021.123911>
- Saretta, Y., Sbrogiò, L., & Valluzzi, M. R. (2021b). Assigning the macroseismic vulnerability classes to strengthened ordinary masonry buildings: An update from extensive data of the 2016 Central Italy earthquake. *International Journal of Disaster Risk Reduction*, 62, 102318. <https://doi.org/10.1016/j.ijdrr.2021.102318>
- Sbrogiò, L., Saretta, Y., Molinari, F., & Valluzzi, M. R. (2022). Multilevel Assessment of Seismic Damage and Vulnerability of Masonry Buildings (MUSE-DV). in Historical Centers, Development of a Mobile Android Application. *Sustainability*, 14(12), 7145. <https://doi.org/10.3390/su14127145>
- Schirmer, P. M., & Axhausen, K. W. (2016). A multiscale classification of urban morphology. *Journal of Transport and Land Use*, 9(1), 101–130. <https://doi.org/10.5198/jtlu.2015.667>

- Senaldi, I., Magenes, G., Penna, A., Galasco, A., & Rota, M. (2014). The Effect of Stiffened Floor and Roof Diaphragms on the Experimental Seismic Response of a Full-Scale Unreinforced Stone Masonry Building. *Journal of Earthquake Engineering*, 18(3), 407–443. <https://doi.org/10.1080/13632469.2013.876946>
- Seo, J., & Linzell, D.G. (2010). Probabilistic vulnerability scenarios for horizontally curved steel I-girder bridges under earthquake loads. *Transportation Research Record, Journal of the Transportation Research Board* 2202, 206-211. <https://doi.org/10.3141/2202-24>
- Seo, J., & Linzell, D.G. (2012). Horizontally curved steel bridge seismic vulnerability assessment. *Engineering Structures*, 34, 21-32. <https://doi.org/10.1016/j.engstruct.2011.09.008>
- Seo, J., & Linzell, D.G. (2013). Use of response surface metamodels to generate system level fragilities for existing curved steel bridges. *Engineering Structures*, 52, 642-653. <https://doi.org/10.1016/j.engstruct.2013.03.023>
- Seo, J., & Park, H. (2017). Probabilistic seismic restoration cost estimation for transportation infrastructure portfolios with an emphasis on curved steel I-girder bridges. *Structural Safety* 65, 27-34. <https://doi.org/10.1016/j.strusafe.2016.12.002>
- Seo, J., Duenas-Osorio, L., Craig, J.I., & Goodno, B.J. (2012). Metamodel-based regional vulnerability estimate of irregular steel moment-frame structures subjected to earthquake events. *Engineering Structures*, 45, 585–597. <https://doi.org/10.1016/j.engstruct.2012.07.003>
- Silva, B., Dalla Benetta, M., da Porto, F., & Valluzzi, M. R. (2014). Compression and Sonic Tests to Assess Effectiveness of Grout Injection on Three-Leaf Stone Masonry Walls. *International Journal of Architectural Heritage*, 8(3), 408–435. <https://doi.org/10.1080/15583058.2013.826300>
- Silva, M.S., & Garcia, L. (2001). Earthquake damage assessment based on fuzzy logic and neural networks. *Earthquake Spectra*, 17(1), 89-112. <https://doi.org/10.1193/1.1586168>
- Silva, V., Brzev, S., Scawthorn, C., Yepes, C., Dabbeek, J., & Crowley, H. (2022). A Building Classification System for Multi-hazard Risk Assessment. *International Journal of Disaster Risk Science*, 13(2), 161–177. <https://doi.org/10.1007/s13753-022-00400-x>
- Silva, V., Jaiswal, K., Graeme, W., & Crowley, H. (2014). Global Assessment Of Human Losses Due To Earthquakes. 2nd European Conference on Earthquake Engineering and Seismology. Istanbul, Turkey, August 2014. <https://doi.org/10.13140/2.1.1996.4161>
- Simões, A., Milošević, J., Meireles, H., Bento, R., Cattari, S., & Lagomarsino, S. (2015). Fragility curves for old masonry building types in Lisbon, *Bulletin of*

*Earthquake Engineering*, 13, 3083–3105. <https://doi.org/10.1007/s10518-015-9750-1>

- Simonyan, K., & Zisserman, A. (2015). Very deep convolutional networks for large-scale image recognition. *3rd International Conference on Learning Representations, ICLR 2015 - Conference Track Proceedings*, 1–14. <https://arxiv.org/abs/1409.1556>
- Smith, V., Malik, J., & Culler, D. (2013). Classification of sidewalks in street view images. *2013 International Green Computing Conference Proceedings, IGCC 2013*, 0–5. <https://doi.org/10.1109/IGCC.2013.6604476>
- Sorrentino, L., Cattari, S., da Porto, F., Magenes, G., & Penna, A. (2019). Seismic behaviour of ordinary masonry buildings during the 2016 central Italy earthquakes. *Bulletin of Earthquake Engineering*, 17(10), 5583–5607. <https://doi.org/10.1007/s10518-018-0370-4>
- Spence R.J.S., & So, E.K.M. (2011). Human casualties in earthquakes, modelling and mitigation, *Proceedings of the Ninth Pacific Conference on Earthquake Engineering, Building an Earthquake-Resilient Society*. Auckland, New Zealand, April 14-16, 2011.
- Spence, R., & So, E. (2011). Human casualties in earthquakes, modelling and mitigation. *Proceedings of the Ninth Pacific Conference on Earthquake Engineering Building an Earthquake-Resilient Society*, 224, 1–13. [www.ornl.gov/sci/landscan](http://www.ornl.gov/sci/landscan)
- Stucchi, M., Meletti, C., Montaldo, V., Akinci, A., Faccioli, E., Gasperini, P., Malagnini, L., & Valensise, G. (2004). Pericolosità sismica di riferimento per il territorio nazionale MPS04. Istituto Nazionale di Geofisica e Vulcanologia (INGV). <https://doi.org/10.13127/sh/mps04/ag>.
- Stucchi, M., Meletti, C., Montaldo, V., Crowley, H., Calvi, G. M., & Boschi, E. (2011). Seismic hazard assessment (2003-2009). for the Italian building code. *Bulletin of the Seismological Society of America*, 101(4), 1885–1911. <https://doi.org/10.1785/0120100130>
- Subasri, R., Suresh, S., & Natarajan, A.M. (2014). Discrete direct adaptive ELM controller for active vibration control of nonlinear base isolation buildings. *Neurocomputing*, 129, 246-256. <https://doi.org/10.1016/j.neucom.2013.09.035>
- Szegedy, C., Liu, W., Jia, Y., Sermanet, P., Reed, S., Anguelov, D., Erhan, D., Vanhoucke, V., & Rabinovich, A. (2015). Going deeper with convolutions. *Proceedings of the IEEE Computer Society Conference on Computer Vision and Pattern Recognition*, 07-12-June, 1–9. <https://doi.org/10.1109/CVPR.2015.7298594>
- Taffarel, S. (2016). *Metodi speditivi per la valutazione della vulnerabilità sismica del costruito storico: Approccio all'incertezza nelle forme di aggregazione complessa a diversa scala* [PhD Thesis]. Università degli Studi di Padova,

Corso di Dottorato di Ricerca in “Storia, Critica e Conservazione dei Beni Culturali.” (in Italian)

- Taffarel, S., Campostrini, G. P., Rosato, L., Marson, C., da Porto, F., & Modena, C. (2016). The application of a Bayesian approach to assess the seismic vulnerability of historical centers. *Structural Analysis of Historical Constructions: Anamnesis, Diagnosis, Therapy, Controls - Proceedings of the 10th International Conference on Structural Analysis of Historical Constructions, SAHC 2016*, 1225–1230. <https://doi.org/10.1201/9781315616995-166>
- Tezcan, J. & Cheng, Q. (2012). Support vector regression for estimating earthquake response spectra. *Bulletin of Earthquake Engineering*, 10(4), 1205-1219. <https://doi.org/10.1007/s10518-012-9350-2>
- Theodulis, N. P. & Papazachos B.C. (1992). Dependence of strong ground motion on magnitude-distance, site geology and macroseismic intensity for shallow earthquake in Greece, I, Peak horizontal acceleration, velocity and displacement. *Soil Dynamics and Earthquake Engineering*, 11, 387-402. [https://doi.org/10.1016/0267-7261\(92\)90003-V](https://doi.org/10.1016/0267-7261(92)90003-V)
- Thomas, S., Pillai, G.N. & Pal, K. (2017). Prediction of peak ground acceleration using e-SVR, n-SVR and Ls-SVR algorithm. *Geomatics, Natural Hazards and Risk*, 8(2), 177-193. <https://doi.org/10.1080/19475705.2016.1176604>
- Thomas, S., Pillai, G.N., Pal, K., & Jagtap, P. (2016). Prediction of peak ground acceleration using e-SVR, n-SVR and Ls-SVR algorithm. *Geomatics, Natural Hazards and Risk*, 8(2), 177–193. <https://doi.org/10.1016/j.asoc.2015.12.013>
- Tomažević, M., Klemenc, I., & Weiss, P. (2009). Seismic upgrading of old masonry buildings by seismic isolation and CFRP laminates: A shaking-table study of reduced scale models. *Bulletin of Earthquake Engineering*, 7(1), 293–321. <https://doi.org/10.1007/s10518-008-9086-1>
- Tomažević, M., Lutman, M., & Weiss, P. (1996). Seismic Upgrading of Old Brick-Masonry Urban Houses: Tying of Walls with Steel Ties. *Earthquake Spectra*, 12(3), 599–622. <https://doi.org/10.1193/1.1585898>
- Tooke, T. R., Coops, N. C., & Webster, J. (2014). Predicting building ages from LiDAR data with random forests for building energy modeling. *Energy and Buildings*, 68(PARTA), 603–610. <https://doi.org/10.1016/j.enbuild.2013.10.004>
- Trifunac, M. & Brady, A. (1975). On the correlation of seismic intensity scales with the peaks of the recorded ground motion. *Bulletin of the Seismological Society of America*, 65(1), 139–162. <https://doi.org/10.1785/BSSA0650010139>
- Tsompanakis, Y., Lagaros, N.D., Psarropoulos, P.N., & Georgopoulos, E.C. (2009). Simulating the seismic response of embankments via artificial neural networks. *Advances in Engineering Software*, 40(8), 640-651. <https://doi.org/10.1016/j.advengsoft.2008.11.005>

- Ülgen, D., & Engin, H.K. (2007). A study of CPT based liquefaction assessment using artificial neural networks. *Proceedings of the 4th international conference on earthquake geotechnical engineering*, Thessaloniki, 25-28 June, paper no. 1219, pp. 1-12. New York, Springer.
- United Nations International Strategy for Disaster Reduction (2015). Sendai Framework for Disaster Risk Reduction 2015-2030. [https://www.unisdr.org/files/43291\\_sendaiframeworkfordrren.pdf](https://www.unisdr.org/files/43291_sendaiframeworkfordrren.pdf)
- Vafaei, M., Adnan, A.B., and Rahman, A.B.A. (2013). Real-time seismic damage detection of concrete shear walls using artificial neural networks. *Journal of Earthquake Engineering*, 17(1), 137-154. <https://doi.org/10.1080/13632469.2012.713559>
- Vafaei, M., Adnan, A.B., and Rahman, A.B.A. (2014). A neuro-wavelet technique for seismic damage identification of cantilever structures. *Structure and Infrastructure Engineering*, 10(12), 1666-1684. <https://doi.org/10.1080/15732479.2013.849746>
- Valluzzi, M. R. (2009). *User Manual of Vulnus 4.0, original program by Bernardini Gori A, Modena R C, Vb version edited by Valluzzi MR, with contributions by Benincà G, Barbetta E, Munari M.* (in Italian)
- Valluzzi, M. R., Binda, L., & Modena, C. (2005). Mechanical behaviour of historic masonry structures strengthened by bed joints structural repointing. *Construction and Building Materials*, 19(1), 63–73. <https://doi.org/10.1016/j.conbuildmat.2004.04.036>
- Valluzzi, M. R., da Porto, F., & Modena, C. (2004). Behavior and modeling of strengthened three-leaf stone masonry walls. *Materials and Structures*, 37(3), 184–192. <https://doi.org/10.1007/BF02481618>
- Valluzzi, M. R., Garbin, E., Dalla Benetta, M., & Modena, C. (2008). *Experimental assessment and modelling of in-plane behaviour of timber floors*. VI Int. Conf. on Structural Analysis of Historical Constructions (SAHC08), Bath, United Kingdom.
- Valluzzi, M. R., Munari, M., Modena, C., Binda, L., Cardani, G., & Saisi, A. (2007). Multilevel Approach to the Vulnerability Analysis of Historic Buildings in Seismic Areas Part 2: Analytical Interpretation of Mechanisms for Vulnerability Analysis and Structural Improvement. *Restoration of Buildings and Monuments*, 13(6), 427–442. <https://doi.org/10.1515/rbm-2007-6172>
- Valluzzi, M. R., Sbrogiò, L., Saretta, Y., & Wenliuhan, H. (2021a). Seismic Response of Masonry Buildings in Historical Centres Struck by the 2016 Central Italy Earthquake. Impact of Building Features on Damage Evaluation. *International Journal of Architectural Heritage*, 1–26. <https://doi.org/10.1080/15583058.2021.1916852>

- Valluzzi, M., Garbin, E., Benetta, M., & Modena, C. (2010). *In-plane strengthening of timber floors for the seismic improvement of masonry buildings*. 11th World Conference on Timber Engineering 2010, WCTE 2010.
- Valluzzi, M., Sbrogiò, L., & Saretta, Y. (2021b). Intervention Strategies for the Seismic Improvement of Masonry Buildings Based on FME Validation: The Case of a Terraced Building Struck by the 2016 Central Italy Earthquake. *Buildings*, 11(9), 404. <https://doi.org/10.3390/buildings11090404>
- Vapnik, V. (1998). *Statistical Learning Theory*. 1st ed. New York, John Wiley & Sons.
- Verderame, G. M., Ricci, P., Luca, F., Del Gaudio, C., & Risi, M. T. (2014). Damage scenarios for RC buildings during the 2012 Emilia (Italy) earthquake. *Soil Dynamics and Earthquake Engineering*, 66, 385–400. <https://doi.org/10.1016/j.soildyn.2014.06.034>
- Vettore, M., Donà, M., Carpanese, P., Follador, V., da Porto, F., & Valluzzi, M. R. (2020). A Multilevel Procedure at Urban Scale to Assess the Vulnerability and the Exposure of Residential Masonry Buildings, The Case Study of Pordenone, Northeast Italy. *Heritage*, 3(4), 1433–1468. <https://doi.org/10.3390/heritage3040080>
- Vettore, M., Saretta, Y., Sbrogiò, L., & Valluzzi, M. R. (2022). A New Methodology for the Survey and Evaluation of Seismic Damage and Vulnerability Entailed by Structural Interventions on Masonry Buildings, Validation on the Town of Castelsantangelo sul Nera (MC), Italy. *International Journal of Architectural Heritage*, 16(2), 182–207. <https://doi.org/10.1080/15583058.2020.1766159>
- Vintzileou, E., & Miltiadou-Fezans, A. (2008). Mechanical properties of three-leaf stone masonry grouted with ternary or hydraulic lime-based grouts. *Engineering Structures*, 30(8), 2265–2276. <https://doi.org/10.1016/j.engstruct.2007.11.003>
- Wald, D. J., Quitoriano, V., Heaton, T.H., & Kanamori H. (1999). Relations between Peak Ground Acceleration, Peak Ground Velocity, and Modified Mercalli Intensity in California. *Earthquake Spectra*, 15(3), 557-564. <https://doi.org/10.1193/1.1586058>
- Wang, C., Yu, Q., Law, K. H., McKenna, F., Yu, S. X., Taciroglu, E., Zsarnóczay, A., Elhaddad, W., & Cetiner, B. (2021). Machine learning-based regional scale intelligent modeling of building information for natural hazard risk management. *Automation in Construction*, 122(February). <https://doi.org/10.1016/j.autcon.2020.103474>
- Wang, J., & Rahman, M.S. (1999). A neural network model for liquefaction-induced horizontal ground displacement. *Soil Dynamics and Earthquake Engineering*, 18(8), 555-568. [https://doi.org/10.1016/S0267-7261\(99\)00027-5](https://doi.org/10.1016/S0267-7261(99)00027-5)
- Wang, Z., Pedroni, N., Zentner, I., & Zio, E. (2018). Seismic fragility analysis with artificial neural networks, Application to nuclear power plant equipment.

- Engineering Structures*, 162, 213-225.  
<https://doi.org/10.1016/j.engstruct.2018.02.024>
- Wen, Q., Jiang, K., Wang, W., Liu, Q., Guo, Q., Li, L., & Wang, P. (2019). Automatic building extraction from google earth images under complex backgrounds based on deep instance segmentation network. *Sensors (Switzerland)*, 19(2), 1–16.  
<https://doi.org/10.3390/s19020333>
- Wen, Y. K., Ghaboussi, J., Venini, P., & Nikzad, K. (1995). Control of structures using neural networks. *Smart Materials and Structures*, 4(1A), 149-157.  
<https://doi.org/10.1088/0964-1726/4/1A/018>
- Whitman, R. V., Reed, J.W., & Hong, S.T. (1973). Earthquake Damage Probability Matrices. *Proceedings of the 5th World Conference on Earthquake Engineering*, Vol. 2, Rome, 2531-2540.
- Wieland, M., & Pittore, M. (2014). Performance evaluation of machine learning algorithms for urban pattern recognition from multi-spectral satellite images. *Remote Sensing*, 6(4), 2912–2939. <https://doi.org/10.3390/rs6042912>
- Wieland, M., Pittore, M., Parolai, S., Zschau, J., Moldobekov, B., & Begaliev, U. (2012). Estimating building inventory for rapid seismic vulnerability assessment, Towards an integrated approach based on multi-source imaging. *Soil Dynamics and Earthquake Engineering*, 36, 70–83.  
<https://doi.org/10.1016/j.soildyn.2012.01.003>
- Wieland, M., Torres, Y., Pittore, M., & Benito, B. (2016). Object-based urban structure type pattern recognition from Landsat TM with a Support Vector Machine. *International Journal of Remote Sensing*, 37(17), 4059–4083.  
<https://doi.org/10.1080/01431161.2016.1207261>
- Wu, Z., Xu, B., & Yokoyama, K. (2002). Decentralized parametric damage detection based on neural networks. *Computer-Aided Civil and Infrastructure Engineering*, 17(3), 175-184. <https://doi.org/10.1111/1467-8667.00265>
- Xia, P. Q. (2003). An inverse model of MR damper using optimal neural network and system identification. *Journal of Sound and Vibration*, 266(5), 1009–1023.  
[https://doi.org/10.1016/S0022-460X\(02\)01408-6](https://doi.org/10.1016/S0022-460X(02)01408-6)
- Xie, Y., & DesRoches, R. (2019). Sensitivity of seismic demands and fragility estimates of a typical California highway bridge to uncertainties in its soil-structure interaction modeling. *Engineering Structures*, 189, 605-617.  
<https://doi.org/10.1016/j.engstruct.2019.03.115>
- Xie, Y., Ebad Sichani, M., Padgett, J. E., & DesRoches, R. (2020). The promise of implementing machine learning in earthquake engineering, A state-of-the-art review. *Earthquake Spectra*, 36(4), 1769–1801.  
<https://doi.org/10.1177/8755293020919419>



- Xu, B., Wu, Z., Chen, G., & Yokoyama, K. (2004). Direct identification of structural parameters from dynamic responses with neural networks. *Engineering Applications of Artificial Intelligence*, 17(8), 931-943. <https://doi.org/10.1016/j.engappai.2004.08.010>
- Xu, B., Wu, Z., Yokoyama, K., Harada, T., & Chen, G. (2005). A soft post-earthquake damage identification methodology using vibration time series. *Smart Materials and Structures*, 14(3), 116-124. <https://doi.org/10.1088/0964-1726/14/3/014>
- Xu, Y., Lu, X., Tian, Y., & Huang, Y. (2022). Real-Time Seismic Damage Prediction and Comparison of Various Ground Motion Intensity Measures Based on Machine Learning. *Journal of Earthquake Engineering*, 26(8), 4259-4279. <https://doi.org/10.1080/13632469.2020.1826371>
- Xu, Z.D., & Guo, Y.Q. (2008). Neuro-fuzzy control strategy for earthquake-excited nonlinear magnetorheological structures. *Soil Dynamics and Earthquake Engineering*, 28(9), 717-727. <https://doi.org/10.1016/j.soildyn.2007.10.013>
- Xu, Z.D., Shen, Y.P., & Guo, Y.Q. (2003). Semi-active control of structures incorporated with magnetorheological dampers using neural networks. *Smart Materials and Structures*, 12(1), 80-87. <https://doi.org/10.1088/0964-1726/12/1/309>
- Yakut, O., & Alli, H. (2011). Neural based sliding-mode control with moving sliding surface for the seismic isolation of structures. *Journal of Vibration and Control*, 17(14), 2103-2116. <https://doi.org/10.1177/1077546310395964>
- Yan, Y., & Huang, B. (2022). Estimation of building height using a single street view image via deep neural networks. *ISPRS Journal of Photogrammetry and Remote Sensing*, 192, 83-98, ISSN 0924-2716. <https://doi.org/10.1016/j.isprsjprs.2022.08.006>
- Yao, Y., Liang, H., Li, X., Zhang, J., & He, J. (2017). Sensing urban land-use patterns by integrating Google Tensorflow and scene-classification models. *International Archives of the Photogrammetry, Remote Sensing and Spatial Information Sciences - ISPRS Archives*, 42(2W7), 981-988. <https://doi.org/10.5194/isprs-archives-XLII-2-W7-981-2017>
- Yazdi, A. J., Haukaas, T., Yang, T., & Gardoni, P. (2016). Multivariate fragility models for earthquake engineering. *Earthquake Spectra*, 32(1), 441-461. <https://doi.org/10.1193/061314EQS085M>
- Youd, T.L., Hansen, C.M., & Bartlett, S.F. (2002). Revised multilinear regression equations for prediction of lateral spread displacement. *Journal of Geotechnical and Geoenvironmental Engineering*, 128(12), 1007-1017. [https://doi.org/10.1061/\(ASCE\)1090-0241\(2002\)128:12\(1007\)](https://doi.org/10.1061/(ASCE)1090-0241(2002)128:12(1007))
- Yuan, J., & Cheriyyadat, A. M. (2016). Combining maps and street level images for building height and facade estimation. *Proceedings of the 2nd ACM SIGSPATIAL*

- Workshop on Smart Cities and Urban Analytics, UrbanGIS 2016.*  
<https://doi.org/10.1145/3007540.3007548>
- Yun, H. B., Tasbighoo, F., Masri, S. F., Caffrey, J. P., Wolfe, R. W., N, M., & Black, C. (2008). Comparison of modeling approaches for full-scale nonlinear viscous dampers. *JVC/Journal of Vibration and Control*, 14(1-2), 51-76.  
<https://doi.org/10.1177/1077546307079396>
- Zeiler, M. D., & Fergus, R. (2014). Visualizing and understanding convolutional networks. *Lecture Notes in Computer Science (Including Subseries Lecture Notes in Artificial Intelligence and Lecture Notes in Bioinformatics)*, 8689 LNCS(PART 1), 818–833. [https://doi.org/10.1007/978-3-319-10590-1\\_53](https://doi.org/10.1007/978-3-319-10590-1_53)
- Zeppelzauer, M., Despotovic, M., Sakeena, M., Koch, D., & Döller, M. (2018). Automatic prediction of building age from photographs. *ICMR 2018 - Proceedings of the 2018 ACM International Conference on Multimedia Retrieval*, 3206060(c), 126–134. <https://doi.org/10.1145/3206025.3206060>
- Zhang, F., Zhou, B., Liu, L., Liu, Y., Fung, H. H., Lin, H., & Ratti, C. (2018). Measuring human perceptions of a large-scale urban region using machine learning. *Landscape and Urban Planning*, 180(August), 148–160.  
<https://doi.org/10.1016/j.landurbplan.2018.08.020>
- Zhang, J., Sato, T., Iai, S., & Hutchinson, T. (2008). A pattern recognition technique for structural identification using observed vibration signals, Linear case studies. *Engineering Structures*, 30(5), 1439-1446.  
<https://doi.org/10.1016/j.engstruct.2007.08.006>
- Zhang, Y., & Burton, H.V. (2019). Pattern recognition approach to assess the residual structural capacity of damaged tall buildings. *Structural Safety*, 78, 12-22.  
<https://doi.org/10.1016/j.strusafe.2018.12.004>
- Zhang, Y., Burton, H.V., Sun, H., & Shokrabadi, M. (2018). A machine learning framework for assessing post-earthquake structural safety. *Structural Safety*, 72, 1-16. <https://doi.org/10.1016/j.strusafe.2017.12.001>
- Zhao, Y., Qi, J., & Zhang, R. (2019). CBHE, Corner-based Building Height Estimation for Complex Street Scene Images. *WWW '19, The World Wide Web Conference, May 2019*, 2436–2447. <https://doi.org/10.1145/3308558.3313394>
- Zhou, K., Lindenbergh, R., & Gorte, B. (2019). Automatic shadow detection in urban very-high-resolution images using existing 3D models for free training. *Remote Sensing*, 11(1). <https://doi.org/10.3390/rs11010072>
- Zobin, V. M., Melnik, O. E., González, M., Macedo, O., & Bretón, M. (2010). Swarms of microearthquakes associated with the 2005 Vulcanian explosion sequence at Volcan de Colima, Mexico. *Geophysical Journal International*, 182(2), 808-828.  
<https://doi.org/10.1111/j.1365-246X.2010.04647.x>

- Zuccaro, G., & Cacace, F. (2011). Seismic Casualty Evaluation, The Italian Model, an Application to the L'Aquila 2009 Event. In, Spence, R., So, E., Scawthorn, C. (eds). Human Casualties in Earthquakes. *Advances in Natural and Technological Hazards Research*, vol 29. Springer, Dordrecht. [https://doi.org/10.1007/978-90-481-9455-1\\_12](https://doi.org/10.1007/978-90-481-9455-1_12)
- Zuccaro, G., Dolce, M., De Gregorio, D., Speranza, E., & Moroni, C. (2016). La Scheda Cartis Per La Caratterizzazione Tipologico- Strutturale Dei Comparti Urbani Costituiti Da Edifici Ordinari. Valutazione dell'esposizione in analisi di rischio sismico. *Gngts 2015, May 2019*, 281–287. (in Italian)
- Zuccaro, G., Perelli, F.L., De Gregorio, D., & Cacace, F. (2021). Empirical vulnerability curves for Italian masonry buildings, evolution of vulnerability model from the DPM to curves as a function of acceleration. *Bulletin of Earthquake Engineering*, 19, 3077–3097. <https://doi.org/10.1007/s10518-020-00954-5>